Georgia Water Resources Institute
Annual Technical Report
FY 2010

Introduction

The Georgia Water Resources Institute (GWRI) aims to provide interdisciplinary research, education, technology transfer, and information dissemination, and works collaboratively with various local, state, and federal agencies. At the state and local levels, GWRI collaborates with and supports the Georgia Environmental Protection Division/Georgia Department of Natural Resources, water and power utilities, environmental organizations and citizen groups, and lake associations. At the national level, GWRI collaborative efforts with the California Energy Commission, California Department of Water Resources, National Oceanic and Atmospheric Administration, U.S. Army Corps of Engineers, U.S. Bureau of Reclamation, U.S. Geological Survey, U.S. Environmental Protection Agency, and U.S. Fish and Wildlife Service. Finally, GWRI has a significant international research and educational program in Europe, Africa, China, Middle East, and South America with support from the U.S. Agency for International Development, World Bank, Food and Agriculture Organization of the United Nations, and other international organizations. In all its programs, the Institute strives to bring to bear expertise from a variety of disciplines, including civil and environmental engineering, atmospheric sciences, agriculture, oceanography, forestry, ecology, economics, and public policy.

This year's funded activities include:

RESEARCH PROJECTS

(1) Multi-Scale Investigation of Seawater Intrusion and Application in Coastal Georgia, Jian Luo PI, Georgia Institute of Technology, sponsored by USGS under grant # 2006P17 (Fund #R9261).

(2) Assessing the impacts of a major wildfire in the Okefenokee Swamp on mercury levels in resident Macroinvertebrates and Mosquitofish, Darold Batzer PI, University of Georgia, sponsored by USGS under grant #1266663 (Fund #R7113.

(3) Temporal and Micro-site Variation in Flow Characteristics in Estuarine Habitats, Donald Webster and Marc Weissburg, sponsored by USGS under grant #1266663 (Fund R7113).

(4) Assessment of Endocrine Disruption in Fish and Estrogenic Potency of Waters in Georgia, Robert Bringolf, University of Georgia, sponsored by USGS under grant #1266663 (Fund R7113).

(5) Operational Multi-scale Forecast and Reservoir Management in Northern California, Aris Georgakakos PI, Georgia Institute of Technology, sponsored by NOAA through the Hydrologic Research Center under grant #2006N95.

(6) Integrated Forecast and Reservoir Management (INFORM) for Northern California, Phase II: Operational Implementation, Aris Georgakakos PI, Georgia Institute of Technology, sponsored by California-Nevada River Forecast Center, California Department of Water Resources, California Energy Commission under grant #2006Q15.

(7) Technical Assistance in Water Resource Planning, Aris Georgakakos PI, Georgia Institute of Technology, sponsored by Georgia Department of Natural Resources/ Environmental Protection Division under grant #2006R69.

(8) Technical Assistance for Water Resources Planning in the State of Georgia, Aris Georgakakos PI, Georgia Institute of Technology, sponsored by Georgia Environmental Protection Division under grant #2006Q13.

EDUCATIONAL INITIATIVES

The Africa Water Resources Institute for Education and Applied Research (AWARE) is a joint institute established by the Georgia Institute of Technology (GT) and the University of Pretoria (UP), through the Georgia Water Resources Institute (GWRI) and the University of Pretoria Water Institute (UPWI). This is the first such initiative between major American and African Universities and focuses on interdisciplinary graduate education, applied research, and technology transfer in the areas of water, energy, and environmental resources planning and management. AWARE was officially launched on June 19, 2008, and is based at the UP campus in Pretoria, South Africa. The first AWARE programs include a Joint Masters Degree Program in Water Resources Management and a Professional Continuing Education Program for water and hydropower professionals.

PROFESSIONAL AND POLICY IMPACT

Georgia: GWRI continues to provide technical assistance to the Georgia Department of Natural Resources in relation to the state water planning process. GWRI's River Basin Planning Tool (RBPT) was developed specifically for this purpose and is now being applied to assess water supply availability and gaps in various Georgia basins. The results are communicated to 12 Water Councils that have been formed across the state. GWRI provides training to state engineers and their contractors who are involved in these assessments. The RBPT is further developed as more specific assessment needs arise in the planning process. In addition to the Georgia Tech River Basin Planning Tool, GWRI has completed a comprehensive study on the impacts of climate change for the Apalachicola-Chattahoochee-Flint River Basin shared with Alabama and Florida. The study indicates that droughts will most likely intensify having serious implications on water supply, energy generation, and ecological flows. The study is now being expanded to include all Georgia basins.

California:

Similar work, collaboratively with the Hydrologic Research Center in San Diego, has focused on climate change impacts on the Northern California water resources system (including the Sacramento and San Joaquin River basins). While the nature of the changes is different, due to hydrologic significance of snow melt, the findings are equally important regarding the need for mitigation and adaptation measures. With funding from the California Energy Commission and the Department of Water Resources, GWRI and HRC have just initiated a second project phase which aims at finalizing and transferring the forecast-decision tools and evaluating alternative climate and demand change mitigation measures.

International:

GWRI continues its collaboration with the Democratic Republic of the Congo (DRC), helping raise funding for a comprehensive assessment and development program. The program focuses on water, environmental, and energy development, as well as institutional and legal reforms, and is a collaborative effort with the United Nations Development Program and the DRC Ministry of the Environment. The plan was recently presented to the World Bank and is under funding consideration.

Research Program Introduction

None.

Multi-Scale Investigation of Seawater Intrusion and Application in Coastal Georgia

Basic Information

Title:	Multi-Scale Investigation of Seawater Intrusion and Application in Coastal Georgia
Project Number:	2007GA165G
Start Date:	4/1/2008
End Date:	9/30/2011
Funding Source:	104G
Congressional District:	5th
Research Category:	Ground-water Flow and Transport
Focus Category:	Groundwater, Hydrology, Models
Descriptors:	
Principal Investigators:	Jian Luo, Jian Luo

Publications

1. Lu, C., Kitanidis, P.K., Luo, J. (2009), Effects of kinetic mass transfer and transient flow conditions on widening mixing zones in coastal aquifers, Water Resour. Res., 45, W12402, doi:10.1029/2008WR007643.
2. Lu, C., Gong, R., Luo, J. (2009), Analysis of stagnation points for a pumping well in recharge areas, J. Hydrol., 373, 442-452.
3. Lu, C., Luo, J. (2010), Boundary condition effects on estimating maximum groundwater withdrawal in coastal aquifers, J. Hydrol., submitted.
4. Lu, C., Luo, J. (2010), Dynamics of freshwater-seawater mixing zone development in dual-domain formations, Water Resour. Res., submitted.
5. Lu, C., Kitanidis, P.K., Luo, J., Mixing enhanced by kinetic mass transfer and dynamic forces in coastal aquifers, Eos Trans. AGU, 90(52), Fall Meet. Suppl., Abstract H32C-05, San Francisco, CA, Dec. 14-18, 2009
6. Lu, C., Kitanidis, P.K., Luo, J. (2009), Effects of kinetic mass transfer and transient flow conditions on widening mixing zones in coastal aquifers, Water Resour. Res., 45, W12402, doi:10.1029/2008WR007643.
7. Lu, C., Gong, R., Luo, J. (2009), Analysis of stagnation points for a pumping well in recharge areas, J. Hydrol., 373, 442-452.
8. Lu, C., Luo, J. (2010), Boundary condition effects on estimating maximum groundwater withdrawal in coastal aquifers, J. Hydrol., submitted.
9. Lu, C., Luo, J. (2010), Dynamics of freshwater-seawater mixing zone development in dual-domain formations, Water Resour. Res., submitted.
10. Lu, C., Kitanidis, P.K., Luo, J., Mixing enhanced by kinetic mass transfer and dynamic forces in coastal aquifers, Eos Trans. AGU, 90(52), Fall Meet. Suppl., Abstract H32C-05, San Francisco, CA, Dec. 14-18, 2009
11. Lu, C., Du, P., Chen, Y., Luo, J. (2011). Recovery Efficiency of Aquifer Storage and Recovery (ASR) with Mass Transfer Limitation, Water Resources Res., (in revision)
12. Chen, Y., Lu, C., Luo, J. (2011). Solute Transport in Transient Divergent Flow, Water Resources Res., (in review).
13. Lu, C., Luo, J., Effects of Aquifer Stratification on Freshwater-Seawater Mixing-Zone Development, EOS Trans., AGU, Fall Meet. Suppl., Abstract H43A-1206, San Francisco, CA, Dec. 13-17, 2010.

Report as of FY2010 for 2007GA165G: " Multi-Scale Investigation of Seawater Intrusion and Application in Coastal Georgia"

Students Supported

Ph.D. student: Lu, Chunhui, Yiming Chen

Journal Publications

Lu, C., Kitanidis, P.K., Luo, J. (2009), Effects of kinetic mass transfer and transient flow conditions on widening mixing zones in coastal aquifers, *Water Resour. Res.*, 45, W12402, doi:10.1029/2008WR007643.

Lu, C., Gong, R., Luo, J. (2009), Analysis of stagnation points for a pumping well in recharge areas, *J. Hydrol.*, 373, 442-452.

Lu, C., Luo, J. (2010), Dynamics of freshwater-seawater mixing zone development in dual-domain formations, *Water Resour. Res.*, 46, W11601, doi:10.1029/2010WR009344.

Lu, C., Du, P., Chen, Y., Luo, J. (2011), Recovery efficiency of aquifer storage and recovery (ASR) with mass transfer limitation, *Water Resour. Res.*, in revision.

Lu, C., Luo, J. (2011), Boundary condition effects on estimating maximum groundwater withdrawal in coastal aquifers, *Ground Water*, in revision.

Chen, Y., Lu, C., Luo, J. (2011), Solute transport in transient divergent flow, *Water Resour. Res.*, in review.

Conference

Lu, C., Kitanidis, P.K., Luo, J., Mixing enhanced by kinetic mass transfer and dynamic forces in coastal aquifers, *Eos Trans. AGU*, 90(52), Fall Meet. Suppl., Abstract H32C-05, San Francisco, CA, Dec. 14-18, 2009.

Lu, C., Luo, J., Effects of aquifer stratification on freshwater-seawater mixing- zone development, *EOS Trans. AGU*, Fall Meet. Suppl., Abstract H43A-1206, San Francisco, CA, Dec. 13-17, 2010.

Report Follows

In the following report, the research conducted in FY2010 is presented. Research completed or published in previous years are not included.

Chap. 1

Recovery efficiency of aquifer storage and recovery (ASR) with mass transfer limitation

Abstract

Aquifer storage recovery (ASR) is an effective strategy for water resources management and has been widely used in many contaminated and saline aquifers. However, its recovery efficiency (RE) may be significantly affected by mass transfer limitations. A numerical model is developed to simulate ASR performance by combining the convergent and divergent dispersion models with a first-order mass transfer model. By analyzing the concentration history at the pumping well, we obtain simple and effective relationships for investigating ASR efficiency under various mass transfer parameters, including capacity ratio and mass transfer timescale, and operational parameters, including injection durations and well pumping rates. Based on such relationships, one can conveniently determine whether a site with mass transfer limitations is appropriate or not for ASR and how many ASR cycles are required for achieving a positive RE. Results indicate that the immobile domain may function as a contaminant source or sink or both during the recovery phase and RE usually improves with well flow rate, the decrease of capacity ratio, and the ASR cycles. However, RE is a non-monotonic function of the mass transfer timescale and the injection duration. A critical timescale is given for quantifying this non-monotonic behavior. When the injection period is greater than such a critical value, increasing injection period results in a higher RE. Contrarily, when the injection period is less than the critical value, increasing the injection period may even yield a lower RE.

1 Introduction

Aquifer storage and recovery (ASR) is an effective technology for optimal management of water resources. ASR involves injecting fresh water into aquifers through a well (or a cluster of wells) when additional water is available (storage), and pumping water out from the same or adjacent wells when needed (recovery). The injection, storage and recovery process forms one cycle of ASR (see Figure 1). Interest in ASR has been growing in the face of declining groundwater levels caused by excessive exploitation, increasing vulnerability of surface water supplies to contamination, and salinization of groundwater resources in coastal and offshore environments [e.g., *Eastwood and Stanfield*, 2001; *Almulla et al.*, 2005; *Pyne*, 2005; *Lowry and Anderson*, 2006; *Culkin et al.*, 2008; *Vandenbohede et al.*, 2008]. Specifically, ASR avoids the construction of large and expensive reservoirs, prevents easy loss of freshwater resources, and provides a cost-effective solution to water resources management. In addition, the development of environmentally friendly ASR systems can alleviate land subsidence and act as a hydraulic barrier against saltwater intrusion in coastal regions [e.g., *Shammas*, 2008].

The performance of an ASR system is generally quantified by the recovery efficiency (RE), defined as the quantity of stored water that can be recovered without further treatment divided by the total quantity injected [*Kimbler et al.*, 1975]. It is not uncommon that RE may be significantly lower than 100% for ASR systems installed in an initially non-potable aquifer due to the mixing between the injected fresh water and originally-contaminated groundwater [e.g., *Eastwood and Stanfield*, 2001; *Lowry and Anderson*, 2006]. Primary mechanisms that may influence the RE of an ASR system are those that can introduce or enhance mixing in the subsurface, including density-gradient driven convection, dispersion and diffusion, heterogeneity of the aquifers, rate-limited mass transfer, and others [e.g., *Kuman and Kimbler*, 1970; *Moulder*, 1970; *Merritt*, 1986; *Maliva et al.*, 2006; *Ward et al.*, 2007, 2008, 2009; *Lu et al.*, 2009]. For example, numerical studies of three ASR field sites in Wisconsin, USA showed that dispersive mixing was an important process affecting the RE and a larger longitudinal dispersivity would lead to a much lower RE due to enhanced mixing [*Lowry*, 2004; *Lowry and Anderson*, 2006]. Among all these mechanisms, rate-limited mass transfer, referring to non-equlibrium mass exchange between relatively mobile and immobile or solid phases, was recognized as a potential key factor that may control the RE of an ASR system [*Eastwood and Stanfield*, 2001; *Culkin et al.*, 2008]. In geologic formations exhibiting dual-domain behavior, e.g., mobile-immobile domains such as media consisting of fractures and matrices, preferential flow paths and low permeability zones, injection of potable water may break the local geochemical equilibrium in the subsurface and cause dissolution and desorption of chemical constituents from matrices and rocks, which may contaminate the injected potable water and potentially release more toxic compounds. *Culkin et al.* [2008] observed significant salinity rebounds during the storage phase in ASR field experiments in Charleston, South Carolina, USA, which was successfully characterized by a dual-domain mass transfer model. Thus, prior to the significant depletion of the immobile domain or the solid phase, one would always expect a low RE.

Although the prevalent existence of mass transfer behavior in natural aquifers has been recognized [e.g., *Coats and Smith*, 1964; *van Genuchten and Wierenga*, 1976] and many numerical and analytical solutions have been developed to simulate divergent and convergent dispersion with mass transfer limitations [e.g., *Chen*, 1985, 1986; *Goltz and Oxley*, 1991; *Moench*, 1995], the effectiveness and efficiency of ASR subject to mass transfer limitations remains unknown. In particular, there are no guidelines to determine the likelihood of ASR being successful with mass transfer limitations and to optimize ASR operational parameters. The present study numerically and analytically investigates the efficiency of an ASR system in dual-domain aquifers with mass transfer limitations under various hydrogeologic and operational conditions. Simple and effective relationships between transport parameters and ASR operational parameters are derived to quantify the effectiveness and ascertain the potential of ASR systems with mass transfer limitations. Specific questions to be answered by the present research are as follows: (1) how can we determine whether a site is appropriate or not for ASR with mass transfer limitations and identify when mass-transfer limitations are important; (2) what is the effect of mass transfer parameters and ASR operational parameters on ASR performance; and (3) how many cycles are needed for an ASR system to perform well?

2 Numerical Model

Figure 1 shows the conceptual model of a typical ASR system with a fully-penetrated pumping well installed in a confined, homogeneous, isotropic aquifer. The three-dimensional domain is modeled by a two-dimensional axisymmetric cross-section. The vertical axis of rotation is located at the pumping well. The medium consists of overlapped mobile and immobile domains, which have a uniform initial contaminant concentration of c_0 . The mass transfer process between the mobile and immobile domain is described by a first-order mass transfer model. An ASR cycle consists of an injection, resting (storage) and extraction (recovery) phase. The groundwater velocity is assumed to be steady state during each phase and the transition period between two phases is neglected [*Harvey et al.*, 1994]. During the injection phase, fresh water is injected into the aquifer and a concentration front moves away from the pumping well. During the storage phase, no flow occurs but the concentration profile may be altered by mass transfer between the mobile and immobile domain. During the recovery phase, stored water is extracted via the same pumping well and the concentration front moves toward the pumping well. For simplicity, we assume that the injection flow rate and the recovery rate are the same and the flow field is static during the storage phase. These assumptions are reasonable in practice and were adopted in many other studies [e.g., *Ward et al.*, 2007, 2008]. By neglecting regional flow and density effects, the problem can be described as one-dimensional transport in radial coordinates. It has been known that both regional flow and density effects may significantly influence the RE because regional flow may alter the shape of the water body in the subsurface during the storage phase and density effects may enhance solute mixing [e.g., *Ward et al.*, 2007, 2008]. However, these two mechanisms are not the focus of the present research. The RE is evaluated by setting a criterion of the average concentration of extracted water at the

pumping well, such as the U.S. EPA potable-water standard. In the absence of dispersion and mass transfer, i.e., advection is the only transport process, the ASR system is completely reversible and the RE is 1. With dispersion and mass transfer, the mixing enhancement is not reversible, and hence the injection and extraction phase are not identically reversed and the RE is less than 1.

2.1 Governing Equations

In radial coordinates, the conceptual model can be described by one-dimensional dual-domain advective-dispersive transport and a first-order mass transfer model [e.g., *Bear*, 1979; *Chen*, 1985]:

Mobile domain:

$$\begin{aligned} &\textbf{Injection and recovery phase :} \quad \theta_m \tfrac{\partial c_m}{\partial t} + \theta_{im} \tfrac{\partial c_{im}}{\partial t} = -\theta_m v \tfrac{\partial c_m}{\partial r} + \tfrac{1}{r} \tfrac{\partial}{\partial r}\left(\theta_m r \alpha_L |v| \tfrac{\partial c_m}{\partial r}\right), \quad r > r_w \\ &\textbf{Storage phase :} \quad \theta_m \tfrac{\partial c_m}{\partial t} + \theta_{im} \tfrac{\partial c_{im}}{\partial t} = 0, \quad r > r_w \end{aligned} \tag{1}$$

Immobile domain:

$$\tfrac{\partial c_{im}}{\partial t} = \alpha\left(c_m - c_{im}\right), \quad r > r_w \tag{2}$$

where t [T] is the time; r [L] is the radial distance from the well center; r_w [L] is the well radius; θ_m [-] and θ_{im} [-] are porosities of the mobile and immobile domain, respectively; c_m [M/L^3] and c_{im} [M/L^3] are dissolved solute concentrations in the mobile and immobile domain, respectively; α_L [L] is the longitudinal dispersivity; v [L/T] is the pore fluid velocity; $|v|$ represents the absolute magnitude of v ; and α [$1/T$] is the first-order mass transfer rate coefficient. Eqs. (Eq. pumping) and (Eq. storage) assumes that lateral mixing caused by molecular diffusion is negligible.

The steady-state velocity is given by:

$$\begin{aligned} &\textbf{Injection and recovery phase :} \quad v = \pm \tfrac{q}{2\pi\theta_m r}, \quad r > r_w \\ &\textbf{Storage phase :} \quad v = 0 \end{aligned} \tag{3}$$

where q [L^2/T] is the specific pumping rate (positive sign for injection and negative for extraction), defined as the flow rate per unit length of aquifer thickness. Substituting Eq. (3) into Eq. (1) yields:

$$\begin{aligned} &\textbf{Injection phase :} \quad \theta_m \tfrac{\partial c_m}{\partial t} + \theta_{im} \tfrac{\partial c_{im}}{\partial t} = -\tfrac{q}{2\pi r} \tfrac{\partial c_m}{\partial r} + \tfrac{q\alpha_L}{2\pi r} \tfrac{\partial^2 c_m}{\partial r^2}, \quad r > r_w \\ &\textbf{Recovery phase :} \quad \theta_m \tfrac{\partial c_m}{\partial t} + \theta_{im} \tfrac{\partial c_{im}}{\partial t} = \tfrac{q}{2\pi r} \tfrac{\partial c_m}{\partial r} + \tfrac{q\alpha_L}{2\pi r} \tfrac{\partial^2 c_m}{\partial r^2}, \quad r > r_w \end{aligned} \tag{4}$$

The boundary conditions are given by:

$$\textbf{Injection phase :}\quad c_m(r\to\infty,t)=c_{im}(r\to\infty,t)=c_0,\quad \left(vc_m-\alpha_L|v|\frac{\partial c_m}{\partial r}\right)_{r=r_w}=0$$
$$\textbf{Recovery phase :}\quad c_m(r\to\infty,t)=c_{im}(r\to\infty,t)=c_0,\quad \left.\frac{\partial c_m}{\partial r}\right|_{r=r_w}=0 \qquad (5)$$

where c_0 [M/L^3] is the initial background concentration. For injection of fresh water, the boundary condition assumes zero mass flux during the injection phase. For ASR systems with stream water or reclaimed wastewater injection [e.g., *Sheng*, 2005], a non-zero input flux may be defined. Note the boundary conditions for the extraction phase are the same at the pumping well as previous radial pumping problems, but are different at the inifinite distance [e.g., *Chen and Woodside*, 1988; *Harvey et al.*, 1994], in which the concentrations at the infinite distance are 0, representing a finite contaminant plume length. This is because such problems only involved extraction phases with or without storage phases, which resulted in a trivial solution of concentration c_0 for an infinite plume. However, for ASR systems, such a problem does not occur because extraction phases always follow injection and storage phases, which result in nonuniform concentration distributions at the beginning of extraction phases.

The final concentration distribution at the end of each cycle is used as the initial concentration distribution at the start of the subsequent cycle:

$$c_m(r,t=0)=c_{m0}(r),\quad c_{im}(r,t=0)=c_{im0}(r) \qquad (6)$$

where the time is reset for each ASR cycle. $c_{m0}(r)$ and $c_{im0}(r)$ are not constant functions and vary for different phases and different ASR cycles. For the first injection phase, $c_{m0}(r)$ and $c_{im0}(r)$ are equal to c_0 .

2.2 Dimensional Analysis

We introduce the following dimensionless groups:

- Concentration:

$$c_m^*=\frac{c_m}{c_0},\ c_{im}^*=\frac{c_{im}}{c_0} \qquad (7)$$

- Spatial distance:

$$R=\frac{r}{\alpha_L},\ R_0=\frac{r_w}{\alpha_L} \qquad (8)$$

- Mass transfer coefficients:

$$\textbf{Capacity ratio}: \beta = \frac{\theta_{im}}{\theta_m}$$
$$\textbf{Mass transfer timescale}: \tau_{im} = \frac{1}{\alpha} \quad (9)$$

where τ_{im} [T] is a dimensional parameter.

- ASR operational parameters:

$$\textbf{Time}: \tau = \frac{t}{\tau_{im}}$$
$$\textbf{Pumping rate}: \phi = \frac{q}{\theta_m \pi \alpha_L^2 \alpha}$$
$$\textbf{Injection duration}: T_i = \frac{t_i}{\tau_{im}} \quad (10)$$
$$\textbf{Storage duration}: T_s = \frac{t_s}{\tau_{im}}$$
$$\textbf{Recovery duration}: T_e = \frac{t_e}{\tau_{im}}$$

where t_i , t_s and t_e are the actual time periods of the injection, storage and extraction phase. All these time periods are normalized by the mass transfer timescale.

By substituting the velocity function given by Eq. (velocity) and the defined dimensionless groups into Eqs. (1) and (2), the governing equations for an ASR system can be transformed into:

Mobile domain:

$$\textbf{Injection phase}: \frac{\partial c_m^*}{\partial \tau} + \beta \frac{\partial c_{im}^*}{\partial \tau} = \frac{\phi}{2R}\left(-\frac{\partial c_m^*}{\partial R} + \frac{\partial^2 c_m^*}{\partial R^2} \right), \quad R > R_0 \,\&\, 0 < \tau \le T_i$$
$$\textbf{Storage phase}: \frac{\partial c_m^*}{\partial \tau} + \beta \frac{\partial c_{im}^*}{\partial \tau} = 0, \quad R > R_0 \,\&\, T_i < \tau \le T_i + T_s$$
$$\textbf{Recovery phase}: \frac{\partial c_m^*}{\partial \tau} + \beta \frac{\partial c_{im}^*}{\partial \tau} = \frac{\phi}{2R}\left(\frac{\partial c_m^*}{\partial R} + \frac{\partial^2 c_m^*}{\partial R^2} \right), \quad R > R_0 \,\&\, T_i + T_s < \tau \le T_i + T_s + T_e$$

(11)

Immobile domain:

$$\frac{\partial c_{im}^*}{\partial \tau} = c_m^* - c_{im}^*, \qquad R > R_0 \quad (12)$$

Correspondingly, the boundary and initial conditions become:

$$\begin{aligned} &\textbf{Injection phase :} \quad c_m^*(R\to\infty,\tau) = c_{im}^*(R\to\infty,\tau) = 1, \quad \left(c_m^* - \frac{\partial c_m^*}{\partial R}\right)\Big|_{R=R_0} = 0 \\ &\textbf{Recovery phase :} \quad c_m^*(R\to\infty,\tau) = c_{im}^*(R\to\infty,\tau) = 1, \quad \frac{\partial c_m}{\partial R}\Big|_{R=R_0} = 0 \end{aligned} \quad (13)$$

and

$$c_{m0}^* = \frac{c_{m0}(r)}{c_0}, \quad c_{im0}^* = \frac{c_{im0}(r)}{c_0} \quad (14)$$

Our definition of dimensionless groups follows the previous study for intermittent extraction of contaminant plume [*Harvey et al.*, 1994]. Other dimensionless systems are also available for mass transfer models [e.g., *van Genuchten and Wierenga*, 1976; *Goltz and Oxley*, 1991]. The advantage of the defined dimensionless parameters is that the time is normalized by the mass transfer timescale, which is particularly useful for studying the storage phase. In addition, Eqs. (Injection) - (Immobile) are also valid for linear rate-limited sorption processes by modifying dimensionless groups accordingly [*Harvey et al.*, 1994].

2.3 Numerical Solution

Analytical solutions in Laplace domain have been derived for radial injection and extraction problems [e.g., *Chen*, 1985, 1986, 1987; *Chen and Woodside*, 1988; *Moench*, 1989, 1995; *Goltz and Oxley*, 1991; *Huang and Goltz*, 2006; *Huang et al.*, 2010]. Such analytical solutions have been used to analyze tracer tests in convergent and divergent radial flow fields [e.g., *Novakowski*, 1992; *Moench*, 1995; *Becker and Charbeneau*, 2000], decontamination by pumping with rate-limited sorption or mass transfer [e.g., *Goltz and Oxley*, 1991; *Harvey et al.*, 1994], and single-well push-pull tracer tests [*Huang et al.*, 2010]. For the injection and recovery phase, the proposed ASR model is a combination of radial dispersion in convergent and divergent flow fields and rate-limited mass transfer, which can be readily solved by modifying the available solutions. For the storage phase, analytical solutions in time domain are given by [*Harvey et al.*, 1994]:

$$\begin{aligned} c_m^*(\tau) &= -\frac{c_{im0}^* - c_{m0}^*}{1+\beta}\beta\exp\left[-(1+\beta)\tau\right] + \frac{\beta c_{im0}^* + c_{m0}^*}{1+\beta} \\ c_{im}^*(\tau) &= \frac{c_{im0}^* - c_{m0}^*}{1+\beta}\exp\left[-(1+\beta)\tau\right] + \frac{\beta c_{im0}^* + c_{m0}^*}{1+\beta} \end{aligned} \quad 915)$$

where c_{m0}^* and c_{im0}^* are the initial concentrations at the beginning of the storage phase. In addition, numerical codes, such as MT3DMS and SUTRA, are also available for

modeling axisymmetric solute transport by adjusting transport parameters to account for the cylindrical geometry [*Langevin*, 2008]. In the present research, we use Matlab built-in *ode* solvers to solve Eqs. (Injection) - (Immobile), which yield satisfactory results comparing with analytical solutions (see Supplementary Material).

3 Evaluation of ASR Performance

The performance of an ASR system is evaluated by the RE, which is defined as [*Kimbler et al.*, 1975]:

$$RE = \frac{V_r\left(c_m^*(R_0) < c_{crit}^*\right)}{V_i} \quad (16)$$

where c_{crit}^* is the critical concentration normalized by c_0, V_r is the volume of recovered water through the pumping well that satisfies the predefined standard, and V_i is the total volume of injected fresh water. Certainly, RE increases with c_{crit}^*, i.e., more water can be recovered for lower-standard quality requirements. We here assume $c_{crit}^* = 0.1$, which represents that the initial contaminant concentration is 10 times of the criterion. During the recovery phase, if the extracted concentration becomes greater than c_{crit}^*, the pumping will be terminated because the extracted water will need further aboveground treatment.

Other than the critical concentration c_{crit}^*, which is a function of the initial contaminant concentration and the predefined criterion, RE is affected by both transport parameters, including dispersion and mass transfer coefficients, and ASR operational parameters, including durations of injection, storage and extraction phase and well flow rates. At a selected site where transport parameters are fixed and are a function of the hydrogeology, the optimization of ASR operational parameters is the major problem. Furthermore, in regions of stable seasonal fluctuations in freshwater resources availability, the durations of injection, storage and extraction phase are relatively constant and well pumping rates are the most flexible parameter to control. For simplicity, we assume $t_i = t_s = t_e$, i.e., equal durations of injection, storage and extraction phase, representing a 4-month time period for each phase for a yearly-based ASR cycle. To analyze the ASR performance at different hypothetical sites, we vary three dimensionless parameters: β, T_i and ϕ, in which β is controlled by the mass transfer capacity or the size of the immobile domain, T_i is influenced by the mass transfer timescale, i.e., the first-order mass transfer rate coefficient and the immobile porosity, given constant pumping periods, and ϕ is influenced by the well pumping rate, mass transfer coefficients and dispersivity.

4 Results and Discussion

4.1 Single ASR Cycle

Figure 2 shows the RE of a single ASR cycle at different β, T_i and ϕ. The tested parameter ranges are: $\beta \sim 10^{-1} - 10^{1}$, $T_i \sim 10^{-1} - 10^{1}$, and $\phi \sim 10^{0} - 10^{5}$, in which $\beta = 0.1$ represents small portion of immobile domain (~9%) and $\beta = 10$ large portion of immobile domain (~91%) and $T_i = 0.1$ represents a large mass transfer timescale comparing with pumping periods and a small mass transfer rate coefficient and $T_i = 10$ represents a small mass transfer timescale and a large mass transfer rate coefficient. If we consider an aquifer thickness 20 m, $\alpha_L = 1$ m, and $\theta_m = 0.3$, the examined range of ϕ corresponds to the actual pumping rate [0.0157 m^3/d, 1.57×10^3 m^3/d] for $T_i = 0.1$ and [1.57 m^3/d, 1.57×10^5 m^3/d] for $T_i = 10$, respectively. The major information delivered by Figure 2 is summarized in the following:

1) RE generally increases with the well pumping rate given β and T_i except for cases with zero RE.

2) In many combinations of β and T_i, RE remains zero, i.e., no recovered water satisfies the predefined standard, $c^*_{crit} = 0.1$, within the wide tested range of ϕ. However, no clear pattern of β and T_i can be observed for zero RE from Figure 2 (the pattern will be explained in the next section).

3) At a small β, e.g., $\beta = 0.1$, RE increases with T_i at the same ϕ, implying a faster mass transfer rate yields a higher RE for a small immobile domain. However, such behavior is not consistent for all examined β. For example, at $\beta = 0.5$ and $\beta = 1$, the RE of $T_i = 0.1$ is greater than that of $T_i = 0.5$ and $T_i = 1$, indicating that the RE is not a monotonic function of T_i.

4) At a large T_i, e.g., $T_i = 10$, RE decreases with β, implying a larger immobile domain yields a lower RE for a fast mass transfer rate coefficient. At low T_i s except those cases with zero RE, RE also decreases with β. However, at different low T_i s, the cases of zero RE do not show a consistent pattern.

4.1.1 Zero and non-zero RE

Understanding the pattern of cases with zero RE is an essential problem for ASR design because it identifies specific conditions inappropriate for ASR. According to the zero-gradient boundary condition at the well during the extraction phase, the concentration of extracted water is identical to the concentrations at adjacent locations. $RE = 0$ implies that after the storage phase the concentration at such adjacent locations are greater than c^*_{crit} so that no fresh water can be extracted. Consider such an adjacent

point, R_0^+ , with an infinitesimally small distance to the well boundary. During the injection phase, we assume that the concentration at this point will quickly change to zero as a result of fresh water flushing at a large flow rate. Thus, the immobile concentration history at this point during the injection phase is governed by the following equation:

$$\frac{\partial c_{im}^*\left(R_0^+\right)}{\partial \tau} = -c_{im}^* \quad (17)$$

which yields

$$c_{im}^*\left(R_0^+\right) = \exp(-\tau) \quad (18)$$

and the initial condition for the subsequent storage phase is:

$$\begin{aligned} c_{m0}^* &= 0 \\ c_{im}^* &= \exp(-T_i) \end{aligned} \quad (19)$$

Substituting Eqs. (initial storage m) and (initial storage im) into (cm storage) yields the concentration at the end of the storage phase:

$$c_m^*\left(R_0^+, T_i + T_s\right) = \frac{\beta}{1+\beta}\exp(-T_i)\left\{1-\exp\left[-(1+\beta)T_s\right]\right\} \quad (20)$$

Thus, for a non-zero RE, the ASR system must satisfy

$$\frac{\beta}{1+\beta}\exp(-T_i)\left\{1-\exp\left[-(1+\beta)T_s\right]\right\} < c_{crit}^* \quad (21)$$

This is a simple relationship that can be applied to evaluate the applicability for a single ASR cycle. For the proposed case, $T_i = T_s$ and $c_{crit}^* = 0.1$, we have:

$$c_m^*\left(R_0^+, T_i + T_s\right) = \frac{\beta}{1+\beta}\exp(-T_i)\left\{1-\exp\left[-(1+\beta)T_i\right]\right\} < 0.1 \quad (22)$$

Figure 3 shows the contourlines of $c_m^*\left(T_s\right)$ as a function of β and T_i . The area contained by the thick contourline of 0.1 indicates the regions of β and T_i that will yield zero RE. All simulated cases in Figure 2 are shown by "+". There is no exception that all the cases with zero RE fall into the area contained by 0.1 contourline and all the cases with non-zero RE are located outside of this area. Thus, the simple inequality (inequatity) provides an efficient approach for determining the likelihood of single ASR cycle being successful. Furthermore, inequality (inequatity) gives operational guidance for ASR systems: (1) inequality (inequatity) does not involve the well pumping rate, indicating that increasing the well pumping rate is not an effective way for improving the RE within a single ASR cycle at aquifers falling into the zero-RE area

shown in Figure 3; and (2) there are two ways to convert a zero-RE case to a non-zero RE case by increasing the injection period, which yields a longer mass transfer duration to deplete contaminant in the immobile domain, and by decreasing the storage period, which yields a shorter mass transfer duration for the high concentration in the immobile domain entering the low-concentration mobile domain. Essentially, these approaches are to move the points vertically upward from inside the zero-RE area in Figure 3. In addition, if the concentration at the end of the injection phase is greater than c^*_{crit} , decreasing the storage period is not effective. Finally, Figure 3 also shows that a lower c^*_{crit} yields a larger zero-RE area. An aquifer with a fast mass transfer rate coefficient, i.e., a larger T_i , or a small immobile domain, i.e., a small β , is generally appropriate for ASR. Thus, for aquifers without mass transfer or with equilibrium (i.e., instantaneous) mass transfer, we can always have a positive RE.

4.1.2 Effects of mass transfer parameters

Given the same ASR operational strategies, i.e., constant well flow rate q and phase durations (t_i, t_s and t_e), the RE is controlled by the mass transfer parameters, including capacity ratio β and mass transfer timescale τ_{im} , and the dispersivity α_L . According to the dimensionless groups, the effect of dispersivity is opposite to the well flow rate: a larger dispersivity yields a lower RE because more fresh water is contaminated due to enhanced mixing. In the following, we consider constant ASR operational parameters and dispersivity and examine the transferability of an ASR strategy to aquifers with different mass transfer parameters by varying β and T_i (Note T_i is controlled by τ_{im} for a constant t_i).

With the same flow rate and dispersivity, the RE is ultimately controlled by the mobile concentration at the adjacent points to the well boundary at the end of the storage phase, described by Eq. (equation mobile). That is, a lower $c^*_m(T_s)$ yields a higher RE and a higher $c^*_m(T_s)$ a lower RE. Taking derivatives of Eq. (cm*Ts) with respect to β and T_i (We assume $T_i = T_s$), we have:

$$\frac{\partial c^*_m\left(R_0^+, T_i + T_s\right)}{\partial \beta} = \frac{1}{(1+\beta)^2}\exp(-T_i)\left\{1-\exp\left[-(1+\beta)T_i\right]\right\} + \frac{\beta T_i}{1+\beta}\exp(-T_i)\exp\left[-(1+\beta)T_i\right] > 0 \quad (23)$$

$$\frac{\partial c^*_m\left(R_0^+, T_i + T_s\right)}{\partial T_i} = \frac{\beta}{1+\beta}\left\{(2+\beta)\exp\left[-(2+\beta)T_i\right] - \exp(-T_i)\right\} \quad (24)$$

Thus, for a constant mass transfer timescale, $c^*_m\left(R_0^+, T_i + T_s\right)$ always increases with β ,

resulting in a decreasing RE as shown by Figure 2. For a constant β, let $\frac{\partial c_m^*\left(R_0^+, T_s\right)}{\partial T_i} = 0$. We obtain a critical T_i,

$$T_{crit} = \frac{\ln(2+\beta)}{1+\beta} \quad (25)$$

and

$$\begin{aligned} &\frac{\partial c_m^*\left(R_0^+, T_i + T_s\right)}{\partial T_i} > 0, \ \textbf{if } T_i < T_{crit} \\ &\frac{\partial c_m^*\left(R_0^+, T_i + T_s\right)}{\partial T_i} < 0, \ \textbf{if } T_i > T_{crit} \end{aligned} \quad (26)$$

Thus, the changing pattern of $c_m^*\left(R_0^+, T_i + T_s\right)$ with the mass transfer timescale or mass transfer rate coefficient is non-monotonic.

Figure 4 shows that T_{crit} decreases with β and the concentration gradient non-monotonically changes with T_i. Figure 4a identifies the specific cases shown in Figure 2. For $\beta = 0.5$, $T_{crit} = 0.61$. Thus, Figure 2 shows a decrease of RE from $T_i = 10$ to $T_i = 1$ (negative concentration gradient in Figure 4b) and then an increase to $T_i = 0.1$ (positive concentration gradient in Figure 4b). In fact, this non-monotonic behavior always occurs in the presence of mass transfer. Consider two limiting cases: one with an extremely high T_i and the other nearly 0. The high T_i case represents a small mass transfer timescale or a very large mass transfer rate coefficient. Thus, the rate-limited mass transfer process becomes equilibrium and the transport problem may be described by an advection-disperion equation with a retardation factor. On the other hand, the low T_i case implies a large mass transfer timescale or a very small mass transfer rate coefficient. In such cases, mass transfer may be neglected and the transport problem may be simplified into an advection-dispersion equation. Both limiting cases will yield high RE and T_{crit} is the turning point between them.

Figure 5 shows the concentration profiles for the cases with $\beta = 0.5$ and different T_i at the same well flow rate and pumping durations. Here we do not terminate the recovery phase when the concentration is greater than the criterion in order to show the concentration profiles during a complete cycle. During the injection phase, the immobile domain serves as a contaminant source for all cases. However, immobile concentrations drop significantly for $T_i = 10$ due to fast mass transfer and remain high levels for $T_i = 0.1$ due to slow mass transfer. During the storage phase, the mobile concentration rebounds as a result of mass transfer from the immobile domain with higher concentrations. By the end of the storage phase, mobile and immobile

concentrations reach equilibrium for $T_i = 10$, while there remain small and significant concentration differences for $T_i = 1$ and $T_i = 0.1$, respectively · As a result of the equilibrium concentrations, the immobile domain always serves as a sink during the recovery phase for $T_i = 10$, which has positive impact on the RE. For $T_i = 1$, the immobile domain initially acts as a contaminant source and then as a sink after the plume front in the mobile domain passes. By contrast, the immobile domain mostly serves as a contaminant source near the pumping well for $T_i = 0.1$. However, such negative impact on the RE may not be significant because of slow mass transfer rates. That is, the overall effect on the RE is an integral result of both immobile domain functions and mass transfer rates. With the increase of T_i , the immobile domain transforms from a contaminant source to a sink, but the increased mass transfer rate may enhance the negative impact from the function as a contaminant source more than the positive impact from the function as a contaminant sink. The critical value of T_{crit} reflects a turning point when the immobile domain functions and mass transfer rate reach a certain balanced state.

Inequalities (ineuqal more) and (ineuqal less) also provide very useful operational guidance for ASR systems at sites where there is flexibility in injection times. At a site with $T_i > T_{crit}$, increasing the injection duration always improves the RE. However, if $T_i < T_{crit}$, one may need to increase the injection duration significantly in order to achieve an improved RE. A slight increase may even result in a lower RE. Furthermore, Eq. (Tcrit) yields the range $(0, \ln 2)$ for T_{crit} , which implies that if the injection duration satisfies $t_i > \ln 2\tau_{im}$ (or $t_i > 0.6931\tau_{im}$), increasing pumping duration is an effective approach for improving RE. $\ln 2\tau_{im}$ is known as the half life of mass transfer, i.e., the time period for the concentration to decay to one half of its initial value by assuming first-order decay. Thus, increasing pumping period is effective when the period is greater than the half life of mass transfer.

4.2 Multiple ASR Cycles

Figure 6 shows a typical concentration history at the pumping well during multiple ASR cycles for specified parameters. For injection phases, the concentration remains zero as a result of freshwater flushing. During the first three ASR cycles, no water can be recovered because at the end of the storage phase the concentration is greater than the predefined standard due to mass transfer from the immobile domain. Thus, recovery phases during the first three cycles actually function as storage phases. From the fourth cycle, the mobile concentration drops below the standard at the end of the storage phase so that fresh water can be extracted from the pumping well until the concentration rises to the standard. The withdrawal period during the recovery phase increases with the ASR cycle, representing that the RE increases with the ASR cycle. The immobile domain functions as a contaminant source at the early ASR cycles, and gradually transforms into a contaminant sink during the recovery phase. In general, the RE of an ASR system improves with ASR cycles and a zero-RE ASR system for a single

cycle may eventually develop into an ASR system with a positive RE because multiple ASR cycles essentially increase the injection duration and total injected fresh water. Here, we are particularly interested in how many ASR cycles are necessary for such a transformation.

To determine the number of needed ASR cycles for a system to transform from a zero RE to a non-zero RE, we still focus on the adjacent points to the well boundary. Because no water can be extracted for an ASR system with a zero RE, the actual storage duration is actually the sum of the designed storage phase and the recovery phase. By the end of such a cycle, the mobile and immobile concentrations are:

$$\begin{aligned} c^*_{m,n-1}\left(R_0^+, T_i+T_s+T_e\right) &= c^*_{im0,n-1}\exp\left(-T_i\right)\frac{\beta}{1+\beta}\left\{1-\exp\left[-\left(1+\beta\right)\left(T_s+T_e\right)\right]\right\} \\ c^*_{im,n-1}\left(R_0^+, T_i+T_s+T_e\right) &= c^*_{im0,n-1}\exp\left(-T_i\right)\frac{1}{1+\beta}\left\{\beta+\exp\left[-\left(1+\beta\right)\left(T_s+T_e\right)\right]\right\} \end{aligned} \quad (27)$$

where $c^*_{m,n-1}$ and $c^*_{im,n-1}$ are the mobile and immobile concentrations during the $(n-1)$ th ASR cycle, and $c^*_{im0,n-1}$ is the initial immobile concentration of the n th cycle. Thus, at the end of the storage phase of the n th cycle, we have:

$$\begin{aligned} c^*_{m,n}\left(R_0^+, T_i+T_s\right) = &\frac{\beta}{1+\beta}\exp\left(-T_i\right)\left\{1-\exp\left[-\left(1+\beta\right)T_s\right]\right\} \\ &\left\{\exp\left(-T_i\right)\frac{1}{1+\beta}\left\{\beta+\exp\left[-\left(1+\beta\right)\left(T_s+T_e\right)\right]\right\}\right\}^{n-1} \end{aligned} \quad (28)$$

A non-zero RE for the n th cycle requires:

$$c^*_{m,n}\left(R_0^+, T_i+T_s\right) < c^*_{crit} \quad (29)$$

By assuming $T_i = T_s = T_e$, we have:

$$c^*_{m,n}\left(R_0^+, T_i+T_s\right) = \frac{\beta}{1+\beta}\exp\left(-T_i\right)\left\{1-\exp\left[-\left(1+\beta\right)T_i\right]\right\}\left\{\exp\left(-T_i\right)\frac{1}{1+\beta}\left\{\beta+\exp\left[-2\left(1+\beta\right)T_i\right]\right\}\right\}^{n-1} < c^*_{crit} \quad (30)$$

which yields

$$n > 1+\left\{-T_i+\ln\left[\frac{1}{1+\beta}\left\{\beta+\exp\left[-2\left(1+\beta\right)T_i\right]\right\}\right]\right\}^{-1}\ln\left\{\frac{1+\beta}{\beta}\frac{\exp\left(T_i\right)}{1-\exp\left[-\left(1+\beta\right)T_i\right]}c^*_{crit}\right\} \quad (31)$$

Figure 7 shows the areas with zero RE and non-zero RE delineated by the contourlines of the mobile concentration at the end of the storage phase of the n th cycle.

The subplot of cycle 1 is identical to Figure 3. With the increase of ASR cycles, the area with zero RE, i.e., the area contained by the contourline of 0.1 becomes smaller and more tested cases, "+" symbols, fall outside of the area. At cycle 7, all the tested cases, except the one with $\beta = 10$ and $T_i = 0.1$, should have non-zero RE at a large pumping rate. In addition, the area with zero RE shrinks with ASR cycles, but the shape of the contourlines remains similar, indicating that the effects of mass transfer and operational parameters on multiple ASR cycles may be similar to those identified in the single ASR cycle.

Actually, taking derivatives of Eq. (multiple C) with respect to n, β, and T_i, respectively, we can also obtain $\frac{\partial c^*_{m,n}\left(R_0^+, T_i+T_s\right)}{\partial n} < 0$ for $n \geq 2$, $\frac{\partial c^*_{m,n}\left(R_0^+, T_i+T_s\right)}{\partial \beta} > 0$, and a critical value, $T_{crit}(n, \beta)$, by setting $\frac{\partial c^*_{m,n}\left(R_0^+, T_i+T_s\right)}{\partial T_i} = 0$. Thus, the RE improves with ASR cycles, decreases with capacity ratio, and exhibits non-monotonic behavior in terms of mass transfer timescale and the injection duration. Figure 8 shows that the critical timescale decreases with ASR cycle and all cases with different β approach a low value of 0.0405 according to our numerical solution. In addition, T_{crit} is a monotonic, decreasing function of β at the first cycle, a non-monotonic function at intermediate cycles, and a monotonic, increasing function at late cycles.

Figure 9 shows the contoured areas for the required cycles to achieve a non-zero RE. For $\beta \leq 1$ or $T_i > 1$, all the tested cases should expect a non-zero RE within two ASR cycles. For a large β and a small T_i, e.g., $\beta = 5$ and $T_i = 0.1$, more ASR cycles are required. In particular, the case with $\beta = 10$ and $T_i = 0.1$ requires more than 10 cycles.

Figure 10 shows the numerically-simulated RE for $\beta = 5$ at a constant ϕ. For large mass transfer rate coefficients, i.e., $T_i = 5$ and 10, the first ASR cycle has a non-zero RE. For $T_i = 1,\ 0.5,$ and 0.1, it requires 2, 4, and 7 ASR cycles, respectively. The result is consistent with that shown by Figures 6, 7 and 9.

The above analyses delineate between zero RE and non-zero RE and determine the number of ASR cycles required to sufficiently "flush" the subsurface and move from zero RE to non-zero RE. However, in practial ASR applications, a low RE of, say, 5% may be considered effectively a failure despite being non-zero. Thus, the number of ASR cycles determined here may serve as an indicator for broad comparisons between hydrogeological and operational combinations (i.e. those that are likely to be fairly quickly flushed versus those which are likely to require many flushing cycles), and may not be taken as a strict predictor of how many cycles/years before an operation becomes viable.

5 Summary and Conclusion

ASR is an effective strategy for sustainable management of water resources, but its efficiency may be limited by kinetic mass transfer caused by contaminant sorption and dual-domain behavior of subsurface media. A numerical model is developed for simulating ASR performance by combining the convergent and divergent dispersion models with a first-order mass transfer model. More importantly, by analyzing the concentration history at the pumping well, simple relationships between mass transfer parameters and ASR operational parameters are derived for understanding ASR performance and improving its efficiency. Several practical and useful contour figures are generated based on such relationships for delineating the ranges of mass transfer parameters and the necessary ASR cycles that may yield effective and efficient ASR performance. The developed numerical model and analyzed results provide very useful and practical guidance for determining a potential ASR site with mass transfer limitations and optimizing ASR operations. The main conclusions that can drawn from the analysis are as follows:

1) Increasing well pumping rates may yield higher RE for a single ASR cycle, but usually does not transform an ASR system from zero RE to non-zero RE.

2) RE decreases with the mass transfer capacity ratio, i.e., a large immobile domain or sorption capacity often undermines the ASR efficiency.

3) The effect of mass transfer rate coefficients and the injection period on the ASR efficiency is non-monotonic. A critical value, T_{crit} , may be defined for both single and multiple ASR cases. When the injection period is greater than such a critical value, increasing injection period results in a higher RE. Contrarily, when the injection period is less than the critical value, increasing the injection period may even yield a lower RE.

4) ASR efficiency improves with multiple ASR cycles and the required cycles for a zero-RE ASR in a single cycle to transform into a non-zero RE is derived as a function of mass transfer parameters and the durations of injection, storage and recovery phases.

5) The immobile domain may function as a contaminant source or sink or both during the recovery phase. In aquifers with large capacity ratio and slow mass transfer, the immobile domain may serve as a long-term contaminant source that causes negative impacts on ASR efficiency. By contrast, in aquifers with small capacity ratio and fast mass transfer, concentrations in the mobile and immobile domain may quickly reach equilibrium at the end of the storage phase so that the immobile domain mostly serves as a contaminant sink, which improves the RE. With the increase of ASR cycles, the immobile domain will eventually transform from a contaminant source to a sink.

Our analyses and results are based on the transport model with both a mobile and an immobile domain with adjustable mass transfer parameters, which may represent an aquifer with high and low permeability zones and mass transfer between these zones. As stated in the introduction and conceptual model, many other mechanisms may significantly influence the ASR performance, such as density effects and regional flow.

Further modeling work is required to study the combined effects of these mechanisms and rate-limited mass transfer in more realistic geological settings.

Acknowledgement

This research was sponsored by the National Institutes of Water Resources (NIWR) and U.S. Geological Survey (USGS) under project ID 2007GA165G. We thank three anomenous reviewers for their constructive comments which significantly improve the manuscript quality.

References

Almulla, A., A. Hamad, and M. Gadalla (2005), Aquifer storage and recovery (ASR): a strategic cost-effective facility to balance water production and demand for Sharjah, *Desalination, 174*, 193-204.

Bear, J. (1979), Hydraulics of Groundwater. New York: McGraw-Hill.

Becker, M.W., and R.J. Charbeneau (2000), First-passage-time transfer functions for groundwater tracer tests conducted in radially convergent flow, *J. Contam. Hydrol., 40*, 299-310.

Chen, C.-S. (1985), Analytical and approximate solutions to radial dispersion from an injection well to a geological unit with simultaneous diffusion into adjacent strata, *Water Resour. Res., 21*, 1069-1076.

Chen, C.-S. (1986), Solutions for radionuclide transport from an injection well into a single fracture in a porous formation, *Water Resour. Res., 22*, 508-518.

Chen, C.-S. (1987), Analytical solutions for radial dispersion with Cauchy boundary at injection well, *Water Resour. Res., 23*, 1217-1224.

Chen, C.-S., and G.D. Woodside (1988), Analytical solution for aquifer decontamination by pumping, *Water Resour. Res., 24*, 1329-1338.

Coats, K.H., and B.D. Smith (1964), Dead-end pore volume and dispersion in porous media, *Soc. Pet. Eng. J., 4*, 73--81.

Culkin, S.L., K. Singha, and F.D. Day-Lewis (2008), Implications of rate-limited mass transfer for aquifer storage and recovery, *Ground Water, 46*, 591--605.

Eastwood, J.C., and P.J. Stanfield (2001), Key success factors in an ASR scheme, *Q. J. Eng. Geol. Hydrogeol., 34*, 399-409.

Goltz, M.N., and M.E. Oxley (1991), Analytical modeling of aquifer decontamination by pumping when transport is affected by rate-limited sorption, *Water Resour. Res., 27*, 547-556.

Harvey, C.F., R. Haggerty, and S.M. Gorelick (1994), Aquifer remediation: a method for estimating mass transfer rate coefficients and evaluation of pulsed pumping, *Water Resour. Res.*, *30*, 1979--1991.

Huang, J., J.A. Christ, and M.N. Goltz (2010), Analytical solutions for efficient interpretation of single-well push-pull tracer tests, *Water Resour. Res.*, *46*, W08538.

Huang, J., and M.N. Goltz (2006), Analytical solutions for solute transport in a spherically symmetric divergent flow field, *Trans. Porous Media*, *63*, 305-321.

Kumar, A., and O.K. Kimbler (1970), Effect of dispersion, gravitational segregation, and formation stratification on the recovery of freshwater stored in saline aquifers, *Water Resour. Res.*, *6*, 1689--1700.

Kimbler, O.K., R.G. Kazmann, and W.R. Whitehead (1975), Cyclic Storage of Fresh Water in Saline Aquifers. Louisiana State University, Baton Rouge, LA.

Lowry, C. (2004), Assessment of aquifer storage recovery: defining hydraulic controls on recovery efficiency at three representative sites in Wisconsin. M.S. thesis, Department of Geology and Geophysics, University of Wisconsin at Madison, Madison, Wisconsin.

Langevin, C.D. (2008), Modeling axisymmetric flow and transport, *Ground Water*, *46*, 579--590.

Lowry, C.S., and M.P. Anderson (2006), An assessment of aquifer storage recovery using ground water flow models, *Ground Water*, *44*, 661--667.

Lu, C.H., P.K. Kitanidis, and J. Luo (2009), Effects of kinetic mass transfer and transient flow conditions on widening mixing zones in coastal aquifers, *Water Resour. Res.*, *45*, W12402, doi:10.1029/2008WR007643.

Maliva, R.G., W.X. Guo, and T.M. Missimer (2006), Aquifer storage and recovery: recent hydrogeological advances and system performance, *Water Environ. Res.*, *78*, 2428-2435.

Merritt, M.L. (1986), Recovering fresh water stored in saline limestone aquifers. *Ground Water*, *24*, 516--529.

Moench, A.F. (1995), Convergent radial dispersion in a double-porosity aquifer with fracture skin: Analytical solution and application to a field experiment in fractured chalk, *Water Resour. Res.*, *31*, 1823-1835.

Moench, A.F. (1989), Convergent radial dispersion: A Laplace transform solution for aquifer tracer testing, *Water Resour. Res.*, *25*, 439-447.

Moulder, E.A. (1970), Freshwater bubbles: a possibility for using saline aquifers to store water. *Water Resour. Res.*, *6*, 1528--1531.

Novakowski, K.S. (1992), The analysis of tracer experiments conducted in divergent radial flow fields, *Water Resour. Res.*, *28*, 3215-3225.

Pyne, R.D.C. (2005), Aquifer Storage and Recovery Issues and Concepts, St. Johns River Water Management District Special Publication SJ2005-SP12; St. Johns River Water Management District: Jacksonville, Florida.

Shammas, M.I. (2008), The effectiveness of artificial recharge in combating seawater intrusion in Salalah coastal aquifer, Oman. *Environ. Geol.*, *55*, 191-204.

Sheng, Z. (2005), An aquifer storage and recovery system with reclaimed wastewater to preserve native groundwater resources in El Paso, Texas, *J. Environ. Manage.*, 75, 367-377.

Vandenbohede, A., E. Van Houtte, and L. Lebbe (2008), Study of the feasibility of an aquifer storage and recovery system in a deep aquifer in Belgium, *Hydrolog. Sci. J.*, *53*, 844-856.

van Genuchten, M.T., and P.J. Wierenga (1976), Mass-transfer studies in sorbing porous-media: 1. Analytical solution, *Soil Sci. Soc. Am. J.*, *40*, 473--480.

Ward, J.D., C.T. Simmons, and P.J. Dillon (2007), A theoretical analysis of mixed convection in aquifer storage and recovery: How important are density effects? *J. Hydrol.*, *343*, 169--186.

Ward, J.D., C.T. Simmons, and P.J. Dillon (2008), Variable-density modelling of multiple-cycle aquifer storage and recovery (ASR): importance of anisotropy and layered heterogeneity in brackish aquifers, *J. Hydrol.*, *356*, 93--105.

Ward, J.D., C.T. Simmons, P.J. Dillon PJ, and P. Pavelic (2009), Integrated assessment of lateral flow, density effects and dispersion in aquifer storage and recovery, *J. Hydrol.*, *370*, 83--99.

Figure 1

Schematic conceptual model of an ASR system with a fully-penetrating well in a confined aquifer in an axisymmetric coordinate system. The right panel is the concentration along the radial direction.

Figure 2

Recovery efficiency (RE) for a single ASR cycle at various mass transfer parameters and pumping operational parameters.

Figure 3

Concentration in the mobile domain after the storage phase for a single ASR cycle. Contour lines represent predefined concentration criteria. + indicates the numerical case with a zero RE and "*" indiates the case with a non-zero RE.

Figure 4

Critical timescale at different capacity ratio and sensitivity of concentration at the pumping well to the dimensionless timescale.

Figure 5

Concentration profiles during a single ASR cycle at different mass transfer timescale or injection duration.

Figure 6

Concentration history at the pumping well for multiple ASR cycles.

Figure 7

Evolution of zero-RE cases with ASR cycles as a function of mass transfer parameters.

Figure 8

Critical timescale at multiple ASR cycles.

Figure 9

Required number of ASR cycles for achieving a non-zero RE.

Figure 10

RE improvement with ASR cycles for $\beta = 5$ and $\phi = 1 \times 10^5$.

Figure 1

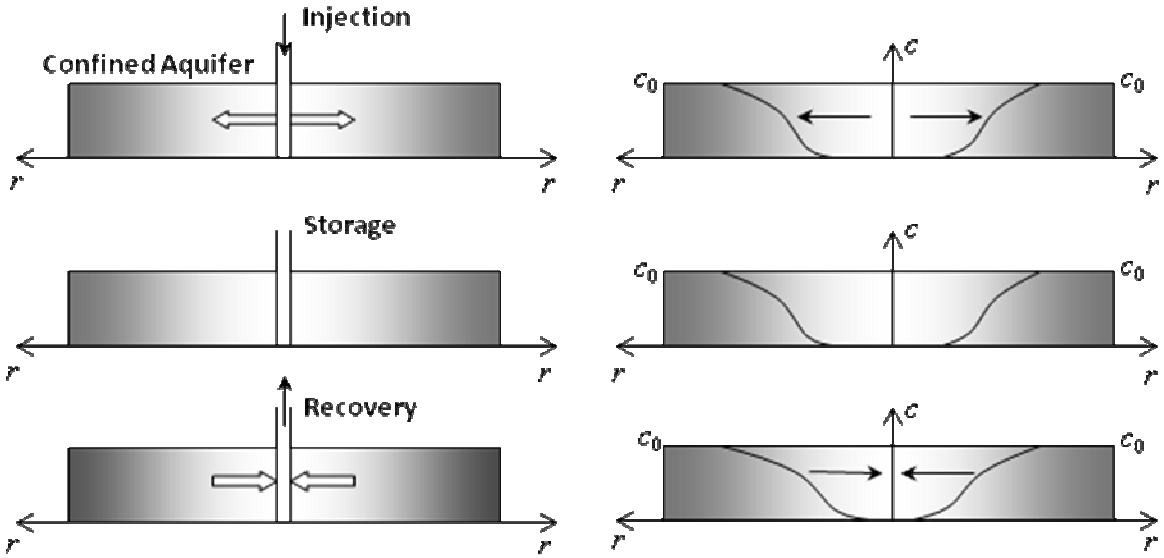
Injection
Confined Aquifer
r
r
Storage
r
r
Recovery
r
r
c
c_0
c_0
r
r
c
c_0
c_0
r
r
c
c_0
c_0
r
r

Figure 2

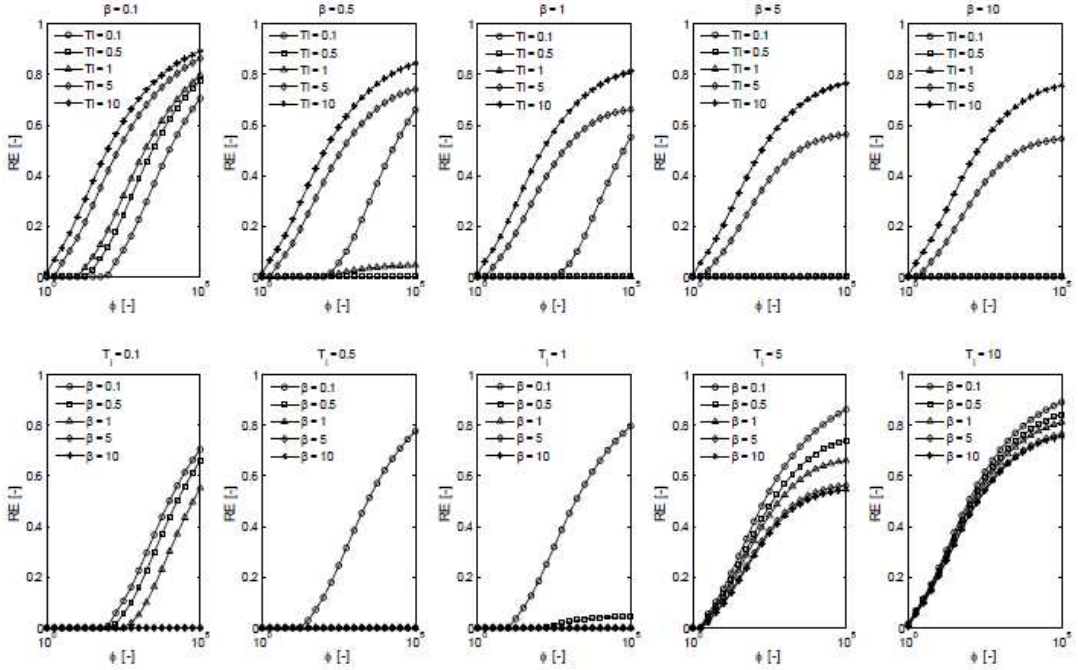
β = 0.1
β = 0.5
β = 1
β = 5
β = 10
Ti = 0.1
Ti = 0.5
Ti = 1
Ti = 5
Ti = 10
RE [-]
ϕ [-]
Ti = 0.1
Ti = 0.5
Ti = 1
Ti = 5
Ti = 10
β = 0.1
β = 0.5
β = 1
β = 5
β = 10

Figure 3

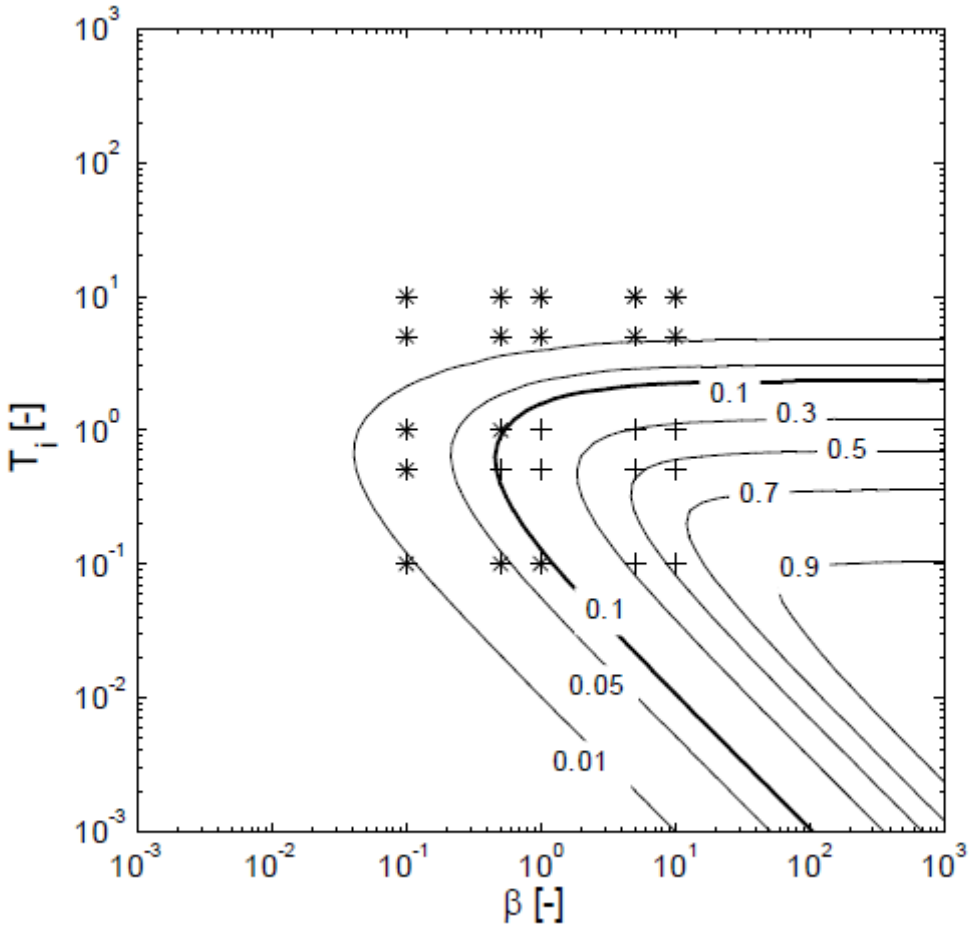
10^3
10^2
10^1
10^0
10^{-1}
10^{-2}
10^{-3}
T_i [-]
10^{-3}
10^{-2}
10^{-1}
10^0
10^1
10^2
10^3
β [-]
0.1
0.3
0.5
0.7
0.9
0.1
0.05
0.01

Figure 4

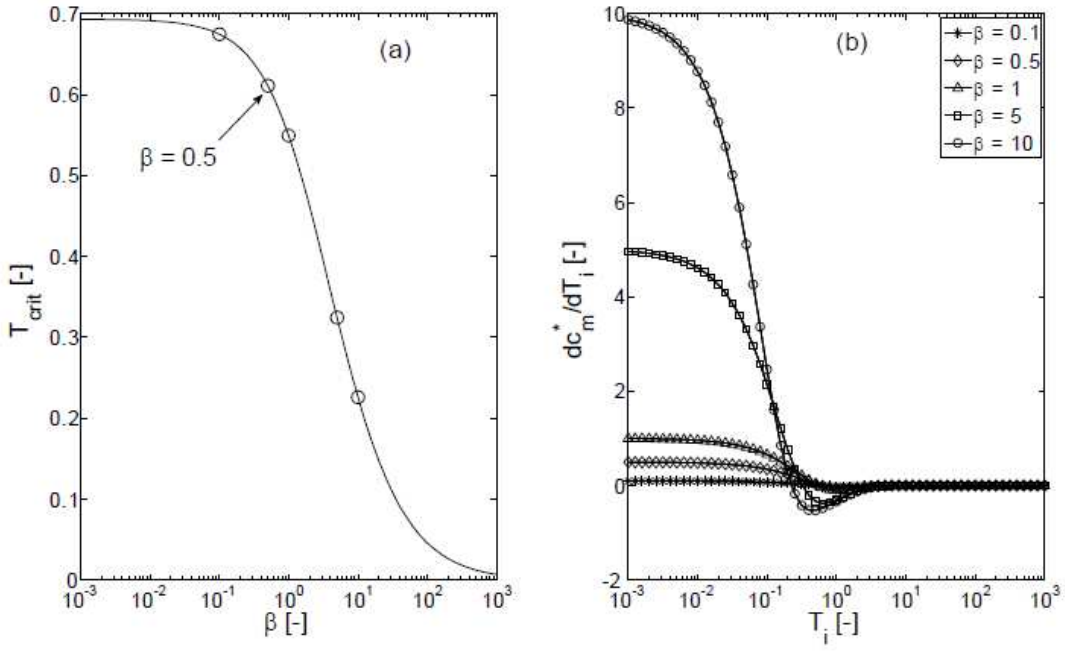

Figure 5

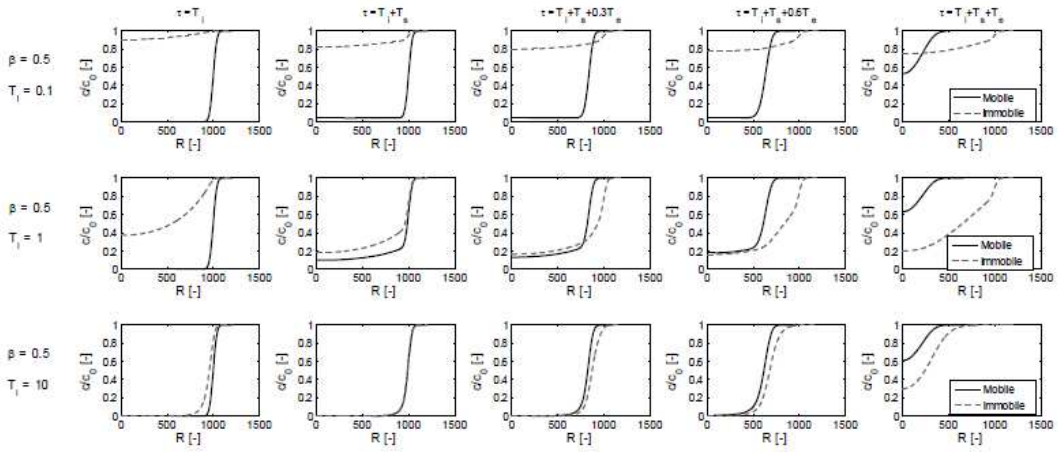
β = 0.5
T_l = 0.1
β = 0.5
T_l = 1
β = 0.5
T_l = 10
τ = T_l
τ = T_l+T_s
τ = T_l+T_s+0.3T_e
τ = T_l+T_s+0.6T_e
τ = T_l+T_s+T_e
c/c_0 [-]
R [-]
Mobile
Immobile

Figure 6

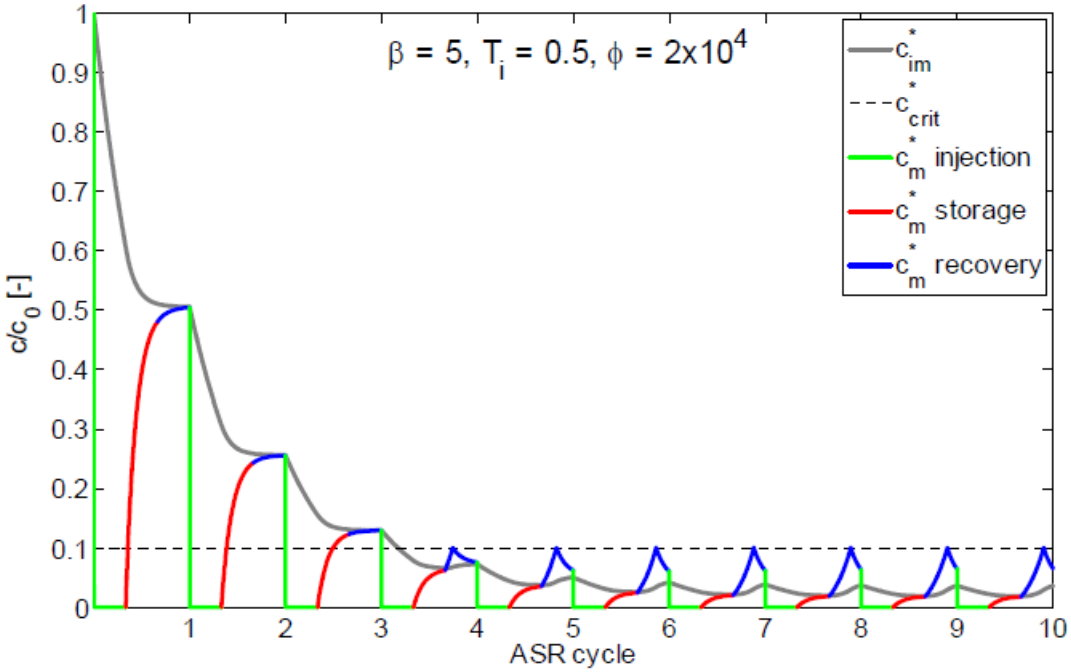
β = 5, T_i = 0.5, ϕ = 2x10^4
c*_im
c*_crit
c*_m injection
c*_m storage
c*_m recovery
c/c_0 [-]
ASR cycle
0
0.1
0.2
0.3
0.4
0.5
0.6
0.7
0.8
0.9
1
1
2
3
4
5
6
7
8
9
10

Figure 7

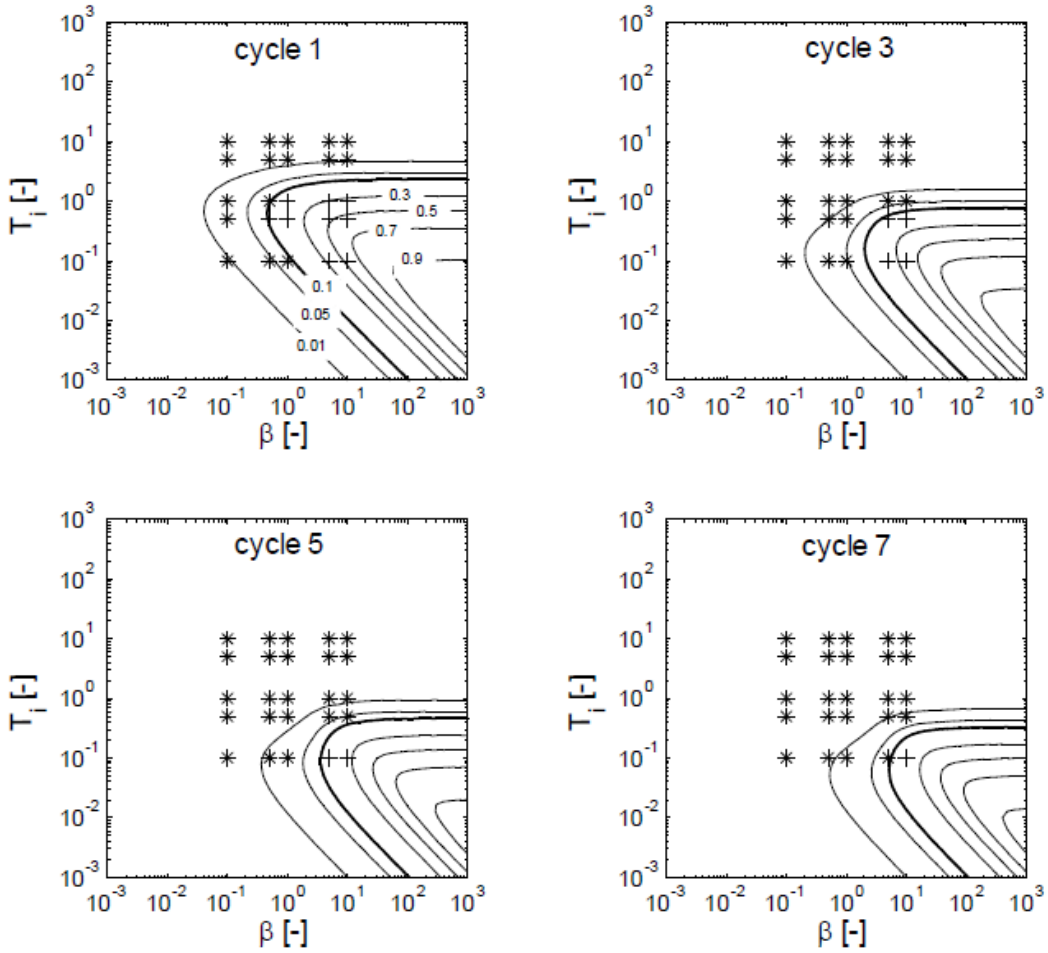

Figure 8

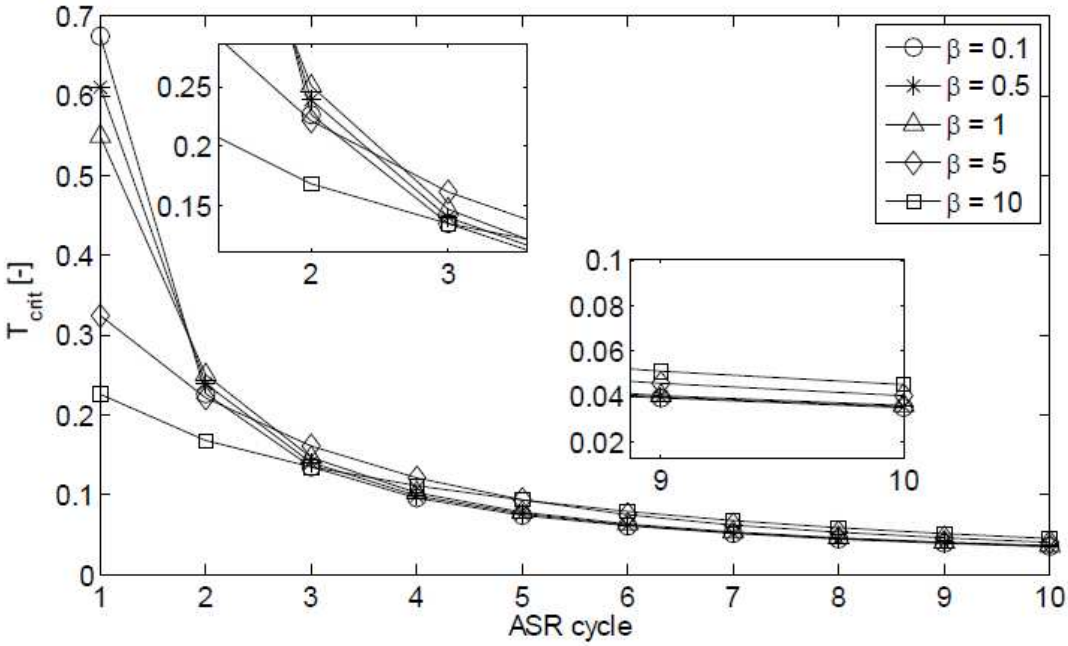
β = 0.1
β = 0.5
β = 1
β = 5
β = 10
T cnt [-]
ASR cycle
0.7
0.6
0.5
0.4
0.3
0.2
0.1
0
1
2
3
4
5
6
7
8
9
10
0.25
0.2
0.15
2
3
0.1
0.08
0.06
0.04
0.02
9
10

Figure 9

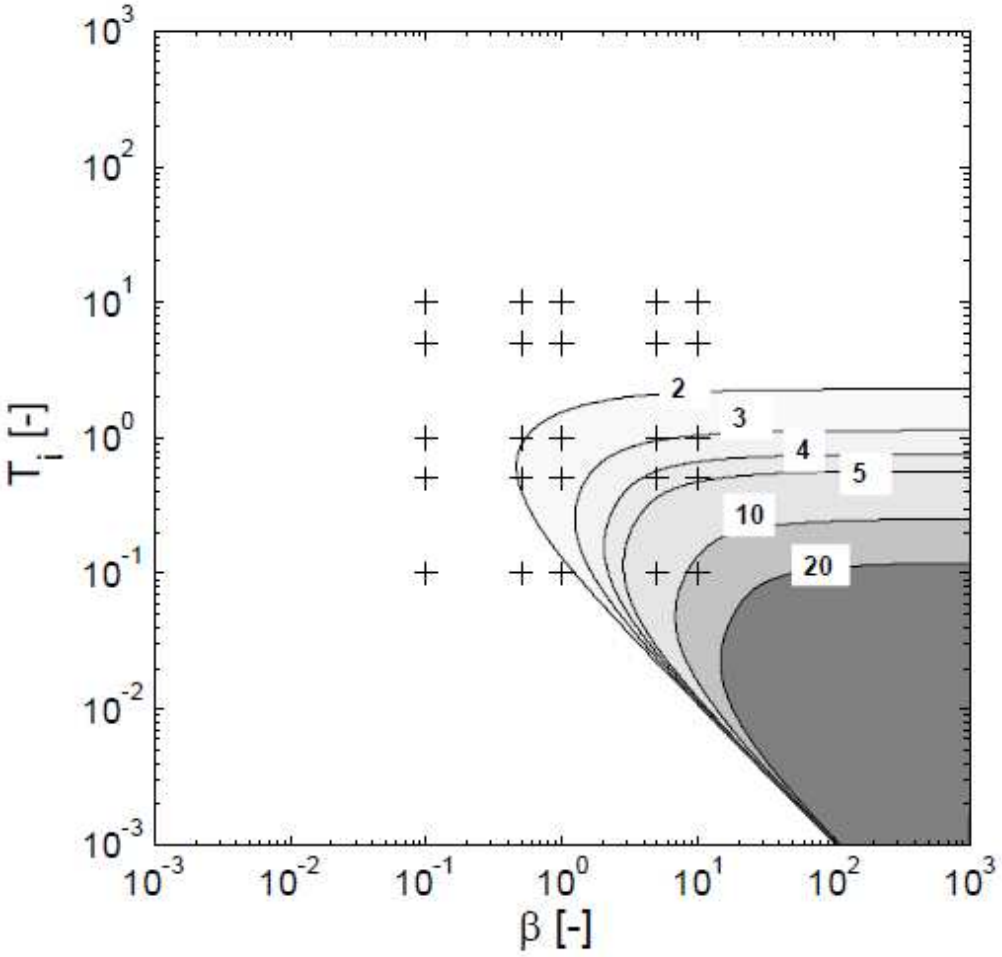
10^3
10^2
10^1
10^0
10^{-1}
10^{-2}
10^{-3}
T_i [-]
10^{-3}
10^{-2}
10^{-1}
10^0
10^1
10^2
10^3
β [-]
2
3
4
5
10
20

Figure 10

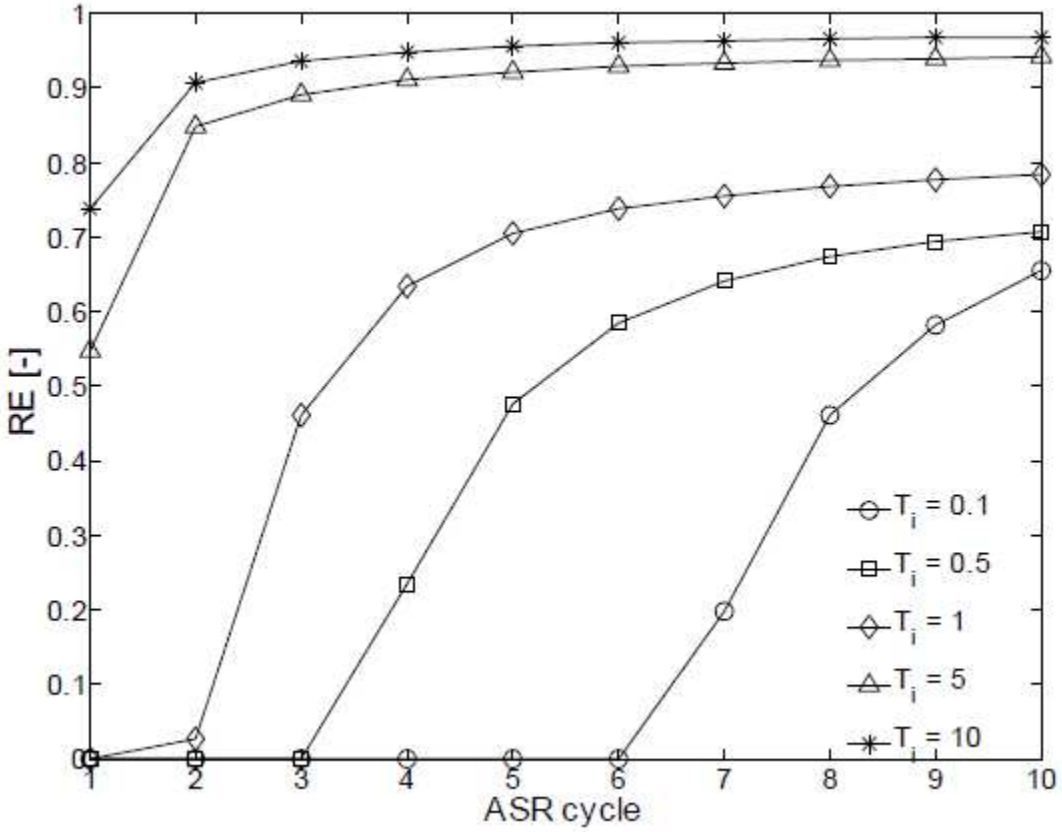

Chap. 2

Dynamics of freshwater-seawater mixing zone development in dual-domain formations

Abstract

The dynamic response of freshwater-seawater mixing zones to seasonal freshwater level fluctuations and the presence of kinetic mass transfer between mobile and immobile domains has been analyzed using numerical models. Mixing zone enhancement is mainly controlled by the unsynchronized behavior of concentration distributions in the mobile and immobile domain. Such behavior is maximized at the aquifer bottom when the retention time scale in the immobile domain is comparable to the period of freshwater level fluctuations, resulting in a thicker mixing zone. Kinetic mass transfer may alter the time tag between periodic freshwater level fluctuations and the movement of the mixing zone, causing the expansion and contraction of the mixing zone. That is, the effect of mixing enhancement by kinetic mass transfer may be nonuniform in the mixing zone, and the mixing zone thickness may vary significantly within a period. By contrast, large dispersion coefficients may create thicker mixing zones, but may not cause such unsynchronized behavior and alter the time lags of different concentration contour lines, i.e., the mixing enhancement is rather uniform in the mixing zone. The dynamics of mixing zone development is sensitive to the flow velocity, which is influenced by the hydraulic conductivity, amplitude of the freshwater level fluctuations, and the capacity ratio of kinetic mass transfer.

1 Introduction

The mixing zone developed at the freshwater-seawater interface is one of the most important features in complex coastal hydrogeologic systems [*Cooper et al.*, 1964]. Across the mixing zone, the salt concentration and fluid density vary between those of freshwater and seawater. The density gradient within the mixing zone causes the rise of diluted saltwater, overlaying seawater, and results in flow circulation as the seawater moves towards the mixing zone to replace the diluted saltwater. Understanding the dynamics of mixing-zone development under various hydrogeologic conditions is essential for designing effective management strategies of groundwater resources and implementing sustainable stewardship of coastal and offshore environments.

The present research aims to numerically investigate the dynamic process of mixing-zone development in a dual-domain subsurface medium. Our previous study has found that kinetic mass transfer between relatively mobile fluids and fluids in stagnant pores combined with periodic movement of the mixing zone may significantly enhance mixing and result in a much thicker mixing zone, shown in Figure 1 [*Lu et al.*, 2009]. Kinetic mass transfer occurs in almost all fractured and porous media over various scales ranging from pore scale to field scale, and has significant implications on coastal

groundwater management. For example, the aquifer storage and recovery (ASR) strategy may have a low freshwater recovery ratio in a dual-domain coastal aquifer due to the mobilization of solutes initially residing in immobile domains [*Eastwood and Stanfield*, 2001; *Culkin et al.*, 2008]. Prior to our finding, thick mixing zones were usually characterized by large dispersion coefficients or assuming highly heterogeneous hydraulic conductivity fields, both of which may not be realistic [*Dagan*, 2003]. In addition, the recharge and tidal fluctuations may only slightly increase the thickness of the mixing zone in the absence of kinetic mass transfer [*Lu et al.*, 2009]. In this note, we conduct numerical experiments to further illustrate the dynamic process of mixing-zone enhancement for a periodically moving mixing zone in the presence of kinetic mass transfer. Specifically, the major questions that have been considered during this work are: how does the distribution of a mixing zone vary in response to variations of hydrogeologic conditions and how are such variations different from those by assuming large dispersion coefficients?

2 Numerical Method

A typical two-dimensional domain (see Figure 1) is set up to represent a cross-shore transect of an unconfined coastal aquifer with a length of 200m, a thickness of 35m, and a beach slope of 0.1, similar to previously reported numerical experiments [*Michael et al.*, 2005; *Robinson et al.*, 2006, 2007; *Lu et al.*, 2009]. For this domain, a base model is first built by defining the following hydrogeologic conditions. The aquifer is isotropic and homogeneous with both mobile and immobile porosities being 0.2. The value of the hydraulic conductivity K is 30m/d. The longitudinal and transverse dispersivity are 0.5m and 0.05m, respectively. Seasonal freshwater level fluctuations are imposed at the landward boundary by defining a triangular, periodic hydraulic head variation with the amplitude A=1m and the period T=360d. The use of the triangular function instead of a sinusoid function is to minimize the pressure periods required to reproduce the periodic function [*Zhang et al.*, 2001; *Brovelli et al.*, 2007]. The first-order mass transfer rate coefficient is $0.0028d^{-1}$, which implies a retention time scale in the immobile domain, defined as the reciprocal of the rate coefficient, equal to the period of freshwater fluctuations. At the seaward boundary, constant hydraulic head and salt concentration are assigned because tidal activities have a much shorter period and may hardly cause the movement of the mixing zone in a large-scale simulation [*Cartwright et al.*, 2004; *Michael et al.*, 2005]. The mean hydraulic gradient between the landward and seaward boundary is 0.005. The upper boundary in the aquifer is phreatic surface with negligible groundwater recharge, and the bottom is a no-flow boundary.

A miscible fluid model with coupled flow and transport models is applied to simulate the mixing zone development in a dual-domain coastal aquifer. Transport processes include advection, dispersion, and a first-order kinetic mass transfer between the mobile and immobile domain. Flow and transport is coupled by a linear relationship between density and concentration in the mobile domain. The density-dependent groundwater flow code SEAWAT-2000 [*Langevin et al.*, 2003] is used to simulate the groundwater flow and salt transport problem described above. The entire domain is divided into two zones: an ocean zone and an aquifer zone, which are separated by the

slanted beach. A high hydraulic conductivity (10^3m/d), an effective porosity $n_e = 1$, and a constant saltwater concentration of 35kg/m^3 are assigned to the ocean zone, and a horizontal strip of cells are added on the tope of the ocean surface to reproduce the flat surface of the ocean [*Brovelli et al.*, 2007; *Robinson et al.*, 2007]. The entire domain is discretized into a uniform grid with a cell size of 0.5m×0.5m, yielding 28000 cells in total. This grid spacing corresponds to a local Peclet number of 1.

The following numerical experiments are conducted: (1) steady-state simulations for the base model with and without mass transfer; (2) transient simulations for the base model with periodic freshwater level fluctuations; and (3) transient simulations by varying a series of parameters, including hydraulic conductivity, dispersion coefficients, amplitude of freshwater fluctuations, and mass transfer coefficients. All transient simulations start from steady-state simulations, and terminate until the salt concentration distributions reaching a dynamic equilibrium state, i.e., the computation duration is sufficiently long so that the tolerance of the maximum concentration variation is satisfied when doubling the computation periods. For simplicity, we use three normalized salt concentration contour lines, 0.1, 0.5 and 0.9, to describe the movement and distribution of the mixing zone.

3 Results and Discussion

Mixing of freshwater and seawater is enhanced primarily due to the unsynchronized behavior of concentrations in the mobile and immobile domain. Two mixing zones may be defined in a dual-domain medium: one in the mobile domain, and the other in the immobile domain. There is an overlap between these two mixing zones, but they do not exactly coincide. The non-equilibrium concentrations in the mobile and immobile domain create the driving force for mass transfer and enhance mixing.

Figure 2 illustrates this process within one period by analyzing the concentration profiles at three points, (70, 0), (90, 0), and (110, 0), all of which are located at the aquifer bottom (Figure 1), where the mixing enhancement is the most significant. At the beginning of the period, non-equilibrium concentrations in the mobile and immobile domains drive mass transfer from the immobile domain to the mobile domain, which result in slowly increasing mobile concentrations and slowly decreasing immobile concentrations. With the decrease of the freshwater level, significant landward movement of the mixing zone causes a fast increasing concentration in the mobile domain, which results in a fast increasing concentration in the immobile domain due to enhanced mass transfer driving forces. Maximum concentrations in the mobile domain occur in the second quarter. After that, the mobile concentration gradually decreases as a result of mass transfer, while the immobile concentration keeps rising until these two become equal. When the hydraulic gradient is reversed as a result of the rise of the freshwater level, seaward movement of the mixing zone causes significant dilution and a fast decreasing mobile concentration. The immobile concentration then decreases due to the reversed mass transfer process. The point at (110, 0), the closest point to the seaward boundary, has the longest period for salt mass transferred from the mobile domain to the immobile domain because the influence by seawater intrusion is more significant than that by freshwater dilution. Contrarily, the point at (70, 0) has the shortest period of mass

transfer from the mobile domain to the immobile domain because it is easier to be diluted by the freshwater with the movement of the mixing zone.

Figure 3 illustrates the impacts of hydrogeologic conditions on the dynamics of the mixing zone development by the temporal and spatial distributions of three concentration contour lines, 0.1, 0.5 and 0.9.

Panel A shows the base model results: (1) the movement of different contour lines in response to freshwater fluctuations is unsynchronized due to kinetic mass transfer, resulting in significantly varying moving ranges for different contour lines, by a factor of 4; and (2) a time lag exists between freshwater level fluctuations and the movement of the mixing zone.

Panel B shows that the mixing zone in the case with larger dispersivities (B2) is thicker than that with smaller dispersivities (B1) in the absence of kinetic mass transfer. However, the enhanced thickness of the mixing zone is nearly uniform within a period for both cases without mass transfer. This indicates synchronized behavior for different contour lines in response to freshwater fluctuations, resulting in similar moving ranges for different contour lines. In specific, the 0.5 contour line remains almost at the middle of the mixing zone for the cases without mass transfer, but approaches the 0.1 contour line when the mixing zone expands and the 0.9 contour line when the mixing zone shrinks for the case with mass transfer. Because the freshwater level drops from the mean level at the beginning of a period, one may expect that the maximum landward movement of the mixing zone occurs at the end of the second quarter when the freshwater level rises to the mean level from the lowest level, which implies a three-month time lag between the freshwater level variation and the mixing zone movement. With the consideration of mass transfer, this time lag becomes shorter than a quarter, i.e., the maximum landward movement of the mixing zone occurs within the second quarter. *Michael et al.* [2005] identified a time lag between the seasonal freshwater level fluctuations and the submarine groundwater discharge rate in the absence of mass transfer. Our analysis indicates that the kinetic mass transfer may alter such time lags. In addition, the cases without mass transfer show almost synchronized time lags for different contour lines, while the case with mass transfer shows significant discrepancies in time lags for different concentration contour lines: the 0.9 contour line has the shortest time lag while the 0.1 contour line the longest, resulting in the expansion of the mixing zone. Likewise, similar time lag behavior and movement discrepancies of contour lines are found in the fourth quarter for the seaward movement of the mixing zone, resulting in the contraction of the mixing zone.

Panel C in Figure 3 shows the mixing zone distributions for different hydraulic conductivities: 10 m/d, 30 m/d (base model), and 50 m/d. It is shown that higher hydraulic conductivity causes larger maximum and smaller minimum mixing zone thickness and more unsynchronized responses of various concentration contour lines. Mixing enhanced by mass transfer causes more significantly non-equilibrium concentrations between the mobile and immobile domain for faster flow due to enhanced time scale discrepancies between mass transfer and advection. In addition, higher hydraulic conductivities lead to larger landward and seaward movement. The impact of

the amplitude of freshwater level fluctuation is similar to that of the hydraulic conductivity because variations of the amplitude essentially change the hydraulic gradient and the flow velocity. Furthermore, given a constant total porosity, altering capacity ratio, the ratio between the immobile and mobile porosity, yields different effective mobile porosities and different flow velocities. Thus, the impact of the capacity ratio is also similar to that of hydraulic conductivity and amplitude of freshwater fluctuations.

Panel D in Figure 3 shows the impacts of the first-order mass transfer coefficient. The mass transfer rate coefficient controls how quickly mass is exchanged between the mobile and immobile domain. Our previous study found that when the retention time scale and the period of freshwater level fluctuations become comparable, the mixing-zone thickness is maximized [*Lu et al.*, 2009]. Three time scale ratios are considered: 0.01, 1(base model) and 100. It is shown that narrower mixing zones are developed for the ratios 0.01 and 100, compared with the ratio 1, and their unsynchronized time-lag behavior of the contour lines is similar to the case without kinetic mass transfer. Actually, mass transfer models with very small and large mass transfer rate coefficients may be simplified to a classical advective-dispersive transport problem. For a small time scale ratio, i.e., the mass transfer is approximately equilibrium, the transport equation may be simplified by including a retardation factor. Thus, D1 also shows smaller displacements of the landward and seaward movement of the mixing zone. By contrast, for a large time scale ratio, i.e., the mass transfer is slow, the mass transfer between the mobile and immobile domains may be negligible and the entire system behaves approximately like a single-domain system with the effective porosity approaching the mobile porosity. As a consequence, the decreased porosity effectively speeds up the flow, resulting in a larger moving range of the mixing zone (see D2).

4 Conclusion

Our numerical experiments show that mixing enhancement in a dual-domain coastal aquifer is mainly controlled by the unsynchronized behavior of concentration distributions in the mobile and immobile domain. Such behavior is maximized at the aquifer bottom when the retention time scale in the immobile domain is comparable to the period of freshwater level fluctuations, resulting in nonuniform moving ranges of different concentration contour lines, nonuniform mixing enhancement in the mixing zone, and significantly varying mixing zone thickness during a period. A time lag exists between the freshwater fluctuations and the movement of the mixing zone. This time tag may be altered by kinetic mass transfer. By contrast, large dispersion coefficients may create thicker mixing zones, but may not cause the unsynchronized behavior and alter the time lags of different concentration contour lines, i.e., the mixing enhancement is rather uniform in the mixing zone. The dynamics of mixing zone development is sensitive to the flow velocity, which is influenced by the hydraulic conductivity, amplitude of the freshwater level fluctuations, and the capacity ratio of mass transfer. These findings provide useful insights for understanding the mechanisms responsible for thick mixing zones and identifying key transport processes in coastal aquifers. Field data collection and analysis is underway for verifying these numerical results.

Acknowledgements

This research was sponsored by the National Institutes of Water Resources (NIWR) and U.S. Geological Survey (USGS) under project ID 2007GA165G.

Reference

Brovelli, A., X. Mao, D.A. Barry (2007), Numerical modeling of tidal influence on density-dependent contaminant transport, *Water Resour. Res.*, *43*, W10426, doi:10.1029/2006WR005173.

Cartwright, N., L. Li, and P. Nielsen (2004), Response of the salt-freshwater interface in a coastal aquifer to a wave-induced groundwater pulse: field observations and modeling, *Adv. Water Res.*, *27*, 297-303.

Cooper, H.H., F.A. Kohout, H.R. Henry, and R.E. Glover (1964), Sea water in coastal aquifers, U.S. Geological Water-Supply Paper, 1613-C.

Culkin, S.L., K. Singha, and F.D. Day-Lewis (2008), Implications of rate-limited mass transfer for aquifer storage and recovery, *Ground Water*, *46*, 591-605.

Dagan, G. (2006), Transverse mixing at freshwater saltwater interfaces: An unresolved issue, First International Joint Salt Water Intrusion Conference - Tutorials, Cagliari, Italy.

Eastwood, J.C., and P.J. Stanfield (2001), Key success factors in an ASR scheme, *Q. J. Eng. Geol. Hydrogeol.*, *34*, 399-409.

Langevin, C.D., W.B. Shoemaker, W. Guo (2003), Modflow-2000, The U.S. Geological Survey modular ground-water flow model Documentation of the Seawat-2000 version with the variable density flow process (VDF) and the integrated MT3DMS transport process (IMT), U.S. Geol. Surv. Open File Rep., 03-426.

Lu, C., P.K. Kitanidis, and J. Luo (2009), Effects of kinetic mass transfer and transient flow conditions on widening mixing zones in coastal aquifers, *Water Resour. Res.*, *45*, W12402, doi:10.1029/2008WR007643.

Michael, H.A., A.E. Mulligan, and C.F. Harvey (2005), Seasonal oscillations in water exchange between aquifers and the coastal ocean, *Nature*, *436*, 1145-1148.

Robinson, C., B. Gibbes, and L. Li (2006), Driving mechanisms for groundwater flow and salt transport in a subterranean estuary, *Geophys. Res. Lett.*, *33*, L03402, doi:10.1029/2005GL025247.

Robinson, C., L. Li, and H. Prommer (2007), Tide-induced recirculation across the aquifer-ocean interface, *Water Resour. Res.*, *43*, W07428, doi:10.1029/2006WR005679.

Zhang, Q., R.E. Volker, and D.A. Lockington (2001), Influence of seaward boundary condition on contaminant transport in unconfined coastal aquifer, *J. Contam. Hydrol.*, *49*, 201 -- 215.

Figure Caption

Figure 1

A numerical simulation of freshwater-seawater mixing zone in an unconfined aquifer. (A) steady-state normalized concentration distribution in the absence of kinetic mass transfer; and (B) normalized concentration distribution of a transient simulation with kinetic mass transfer at the time event when the freshwater boundary (left boundary) equals the mean freshwater head. The thick black lines represent the coastal beach with a slope of 0.1. The mixing zones are characterized by three concentration contour lines normalized by the seawater salt concentration: 0.1, 0.5, and 0.9. The stars in (B) represent three observation points at the aquifer bottom.

Figure 2

Temporal profiles of concentrations in the mobile and immobile domain at three observation points: (70,0), (90,0), and (110,0) for the case with kinetic mass transfer and periodic freshwater fluctuations.

Figure 3

The dynamics of mixing zone development influenced by hydrogeologic conditions, including dispersion, hydraulic conductivity, and mass transfer rate coefficient. Temporal and spatial evolution of the mixing zone distribution is characterized by three normalized concentration contour lines at the aquifer bottom (left y-axis) corresponding to periodic freshwater fluctuations (right y-axis). Panel A is the base model with defined parameters: hydraulic conductivity 30m/d, first-order mass transfer rate coefficient $0.0028d^{-1}$, which corresponds to a unitary time scale ratio between the retention in the immobile domain and the period of freshwater fluctuations, and longitudinal and transverse dispersivities 0.5m and 0.05m, respectively. Panel B shows the impact of dispersion, in which B1 is the base model without kinetic mass transfer and B2 is the base model with larger dispersivities (2.5m and 0.25m) and without kinetic mass transfer. Panel C shows the impact of hydraulic conductivity, in which C1 is the base model with hydraulic conductivity 10m/d and C2 50m/d. Panel D shows the impact of mass transfer rate coefficient, in which D1 has a time scale ratio of 0.01 and D.

Figure 1

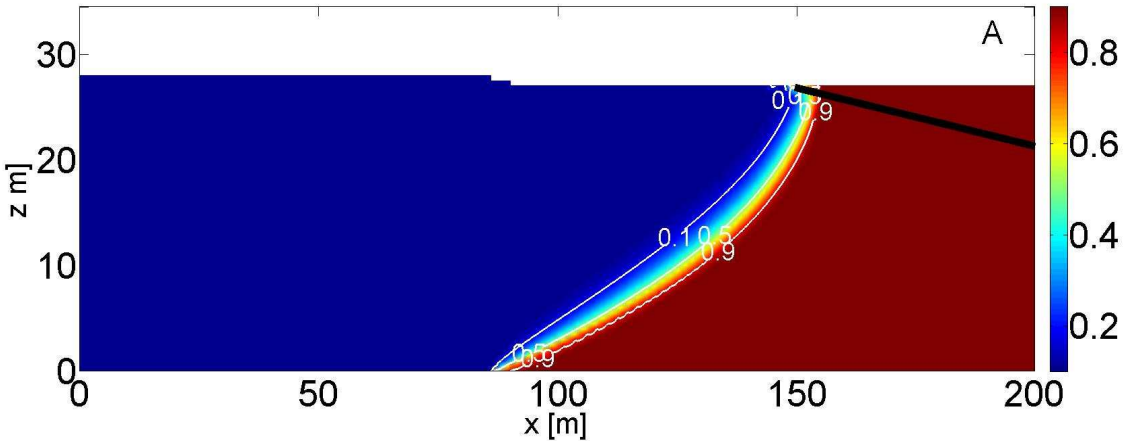

Figure 2

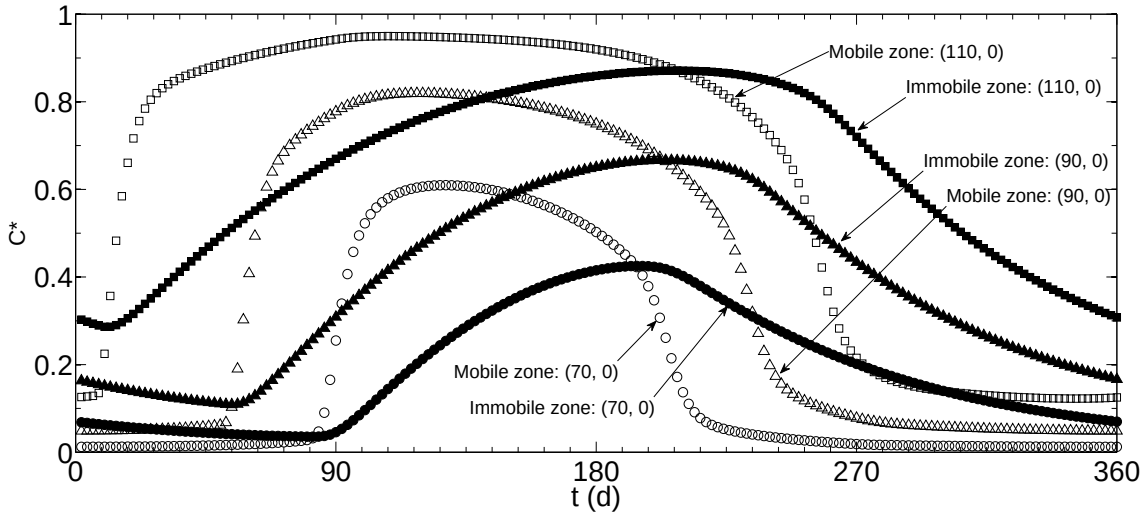
Mobile zone: (110, 0)
Immobile zone: (110, 0)
Immobile zone: (90, 0)
Mobile zone: (90, 0)
Mobile zone: (70, 0)
Immobile zone: (70, 0)
C*
t (d)
0
0.2
0.4
0.6
0.8
1
0
90
180
270
360

Figure 3

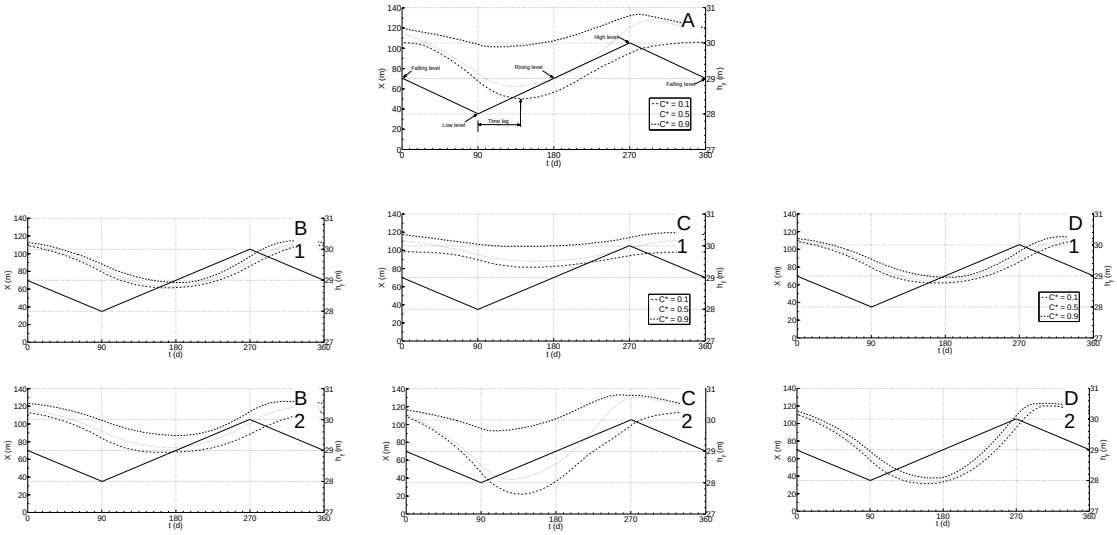
A
B 1
C 1
D 1
B 2
C 2
D 2
High level
Rising level
Falling level
Low level
Time lag
C* = 0.1
C* = 0.5
C* = 0.9
X (m)
t (d)

Chap. 3

Solute transport in transient divergent flow

Abstract

Efficient approaches are developed to analytically evaluate solute transport in a horizontal, radially divergent flow field with a time-dependent well injection rate and input concentration. By working on the cumulative injected flow domain, the transient-flow problem can be transformed into a steady-state flow problem. Linear convolution can then be applied on the cumulative injected flow domain to evaluate the solution for time-dependent input concentrations. Solutions on the regular time domain can be conveniently obtained by mapping the solution on the cumulative injected flow domain to the time domain.

1 Introduction

Significant contributions have been made to evaluate analytical solutions to the problem of advection and dispersion in a homogeneous aquifer due to well injection or extraction in a horizontal, radially divergent or convergent flow field [e.g., *Ogata*, 1958; *Tang and Babu*, 1979; *Moench and Ogata*, 1981; *Chen*, 1985, 1986, 1987; *Hsieh*, 1986; *Chen and Woodside*, 1988; *Moench*, 1989, 1995; *Goltz and Oxley*, 1991; *Huang and Goltz*, 2006; *Huang et al.*, 2010]. Such solutions have important applications in groundwater practice whenever well pumping is involved, such as tracer tests in convergent and divergent radial flow fields [e.g., *Novakowski*, 1992; *Moench*, 1995; *Becker and Charbeneau*, 2000], decontamination by pumping with rate-limited sorption or mass transfer [e.g., *Goltz and Oxley*, 1991; *Harvey et al.*, 1994], and single-well push-pull tracer tests [*Huang et al.*, 2010], etc. One major assumption for these analytical solutions is that the radial flow field is steady state, i.e., the velocity field is a spatial function of the distance to the pumping well, but does not vary temporally. In this note, we present efficient approaches to analytically evaluate solute transport in transient, divergent flow fields with a time-dependent well injection rate and input concentration.

2 Numerical Model

Consider a recharge well that fully penetrates a homogeneous, confined aquifer of uniform thickness and infinite lateral extent. The transport problem can be described by a one-dimensional radially advective-dispersive equation as the following by neglecting molecular diffusion [e.g., *Hoopes and Harleman*, 1967; *Hsieh*, 1986]:

$$\theta \frac{\partial c}{\partial t} = -\theta v \frac{\partial c}{\partial r} + \frac{1}{r} \frac{\partial}{\partial r} \left(\theta r \alpha_L |v| \frac{\partial c}{\partial r} \right), \quad r > r_w \quad (1)$$

where t [T] is the time; r [L] is the radial distance from the well center; r_w [L]

is the well radius; c [M/L^3] is the dissolved solute concentration; θ [$-$] is the porosity; α_L [L] is the longitudinal dispersivity; v [L/T] is the pore fluid velocity; and $|v|$ represents the absolute magnitude of v .

When the well injection rate is constant, the velocity field is only a spatial function of r ,

$$v(r)=\frac{q}{2\pi\theta r},\quad r>r_w \quad (2)$$

where q [L^2/T] is the specific injection rate, defined as the flow recharge rate per unit length of aquifer thickness. The initial condition is:

$$c(r,t=0)=0 \quad (3)$$

and the boundary condition with a constant injection concentration is:

$$c(r\to\infty,t)=0,\quad c(r=r_w,t)=c_0 \quad (4)$$

For a time-dependent well pumping rate $q(t)$, we assume that the velocity field varies with the well pumping rate and the velocity field is a function of both r and t , i.e.,

$$v(r,t)=\frac{q(t)}{2\pi\theta r},\quad r>r_w \quad (5)$$

and for a time-dependent input concentration, the boundary condition is:

$$c(r\to\infty,t)=0,\quad c(r=r_w,t)=c_0(t) \quad (6)$$

Eq. (2) neglects the transition period between two well pumping rates and assumes a steady-state velocity for each pumping rate. *Harvey et al.* [1994] showed that velocities approach steady state rapidly (exponentially decay with the increase of time and radial distance) for changing pumping rates. For a sand aquifer, velocities may take only minutes to couple of days to reach 99% of steady state for a scale up to 100 meters. Thus, the model setup is appropriate for a discrete pumping profile with a long pumping period for each pumping rate.

3 Analytical Solutions

3.1 Steady-state flow with a constant input concentration

For the sake of completeness, we first summarize the analytical solution in a steady-state flow field with a constant input concentration, which will also be used later to evaluate the solution in a transient flow field. We denote c_s as the solution in a steady-state flow field. By introducing the following dimensionless groups:

$$c_s^* = \frac{c_s}{c_0}, R = \frac{r}{\alpha_L}, R_0 = \frac{r_w}{\alpha_L}, \tau = \frac{qt}{2\pi\theta\alpha_L^2} \quad (7)$$

Eq. (1) can be transformed into:

$$\frac{\partial c_s^*}{\partial \tau} = \frac{1}{R}\left(-\frac{\partial c_s^*}{\partial R} + \frac{\partial^2 c_s^*}{\partial R^2} \right) \quad (8)$$

The analytical solution on the Laplace domain is given by [*Moench and Ogata*, 1981]:

$$\overline{c_s^*}(R, p) = \frac{1}{p}\exp\left(\frac{R - R_w}{2} \right)\frac{\mathbf{Ai}(Y)}{\mathbf{Ai}(Y_w)} \quad (9)$$

where p is the Laplace coordinate, Ai (z) is an Airy function, and

$$\begin{aligned} Y &= \frac{4Rp + 1}{4p^{2/3}} \\ Y_w &= \frac{4R_w p + 1}{4p^{2/3}} \end{aligned} \quad (10)$$

The time-domain solution can be evaluated numerically by inverse Laplace algorithms [e.g., *de Hoog et al.*, 1982] or analytically by [*Moench and Ogata*, 1981]:

$$c_s^*(R, \tau) = 1 - \int_0^\infty F(\upsilon)\, d\upsilon \quad (11)$$

where

$$F(\upsilon) = \frac{2\exp\left[-\upsilon^2\tau + (R - R_w)/2 \right]}{\pi\upsilon}\frac{\mathbf{Ai}(y)\mathbf{Bi}(y_w) - \mathbf{Ai}(y_w)\mathbf{Bi}(y)}{[\mathbf{Ai}(y_w)]^2 + [\mathbf{Bi}(y_w)]^2} \quad (12)$$

$$y = \frac{1 - 4R\upsilon^2}{4\upsilon^{4/3}} \quad (13)$$

$$y_w = \frac{1 - 4R_w\upsilon^2}{4\upsilon^{4/3}} \quad (14)$$

3.2 Steady-state flow with a time-dependent input concentration

For a steady-state divergent flow field with a time-dependent injection history at the pumping well, $c_0(t)$, the solution can be conveniently evaluated by linear convolution:

$$c(R,\tau)=\int_0^{\tau} c_0(\tau')\,g(\tau-\tau')\,d\tau' \quad (15)$$

where g is known as the transfer function or impulse response function corresponding to a unit impulse input function at the pumping well. g can be evaluated by taking inverse Laplace transform of:

$$\bar{g}(R,p)=\exp\left(\frac{R-R_w}{2}\right)\frac{\mathbf{Ai}(Y)}{\mathbf{Ai}(Y_w)} \quad (16)$$

or by taking the first derivative of Eq. (steady solution) with respect to τ :

$$g(R,\tau)=\int_0^{\infty} \upsilon^2 F(\upsilon)\,d\upsilon \quad (17)$$

Because there is a scaling factor between t and τ according to the definition of dimensionless groups, g on the time domain is given by:

$$g(r,t)=\frac{q}{2\pi\theta\alpha_L^2}\,g(R,\tau) \quad (18)$$

3.3 Transient flow with a constant input concentration

To evaluate solute transport in a transient radial flow field, we may discretize the time-dependent function, $q(t)$, into a number of small intervals, $q(t_0), q(t_1),\ldots$, and assume a steady-state flow field within each time interval $t_{n-1}\le t<t_n$. The solution within the first time interval, $0=t_0\le t<t_1$, is given by Eq. (steady solution). For all subsequent time intervals, the transport problem can be described by Eq. (pumping) with a steady-state velocity field but with a non-zero initial condition. Laplace transform of such a problem leads to an inhomogeneous differential equation, which may be solved by the Green's function approach [e.g., *Chen and Woodside*, 1988]. This method is computationally complicated and its accuracy significantly relies on the discretization of the transient pumping rate q .

We notice that Eq. (steady solution) is a general solution on the transformed time domain τ for a steady-state flow field with an arbitrary well pumping rate. For the solution on the regular time domain t , one only needs to scale τ according to the definition of dimensionless parameters, i.e.,

$$c^*(r,t)=c_s^*\left(\frac{r}{\alpha_L},\frac{qt}{2\pi\theta\alpha_L^2}\right) \quad (19)$$

We define:

$$Q(t) = qt \quad (20)$$

which represents the cumulative amount of injected flow. Eq. (c trans) can then be written as:

$$c^*(r,t) = c_s^*\left(\frac{r}{\alpha_L}, \frac{Q(t)}{2\pi\theta\alpha_L^2}\right) \quad (21)$$

For any two different steady-state flow fields with well flow rates, q_1 and q_2, we have:

$$c_{s1}^*(r,Q;q_1) = c_{s2}^*(r,Q;q_2) \quad (22)$$

which implies that the concentration distribution is independent of specific flow rate q given a constant total injected flow Q.

Eq. (22) leads to an efficient approach to transform a transient pumping history $q(t)$ to a constant pumping rate by working on the Q domain instead of the regular time domain t. Consider a simple $q(t)$ with a two-step injection: $q_1(0 \le t < t_1)$ and $q_2(t_1 \le t < t_2)$. At the end of the first pumping period, the concentration is given by:

$$c^*(r,t_1;q_1) = c_s^*(r,Q_1;q_1) = c_s^*(r,Q_1;q_2) \quad (23)$$

where Q_1 is the total injected flow amount during the first injection period, i.e., $Q_1 = q_1 t_1$. Eq. (cts) implies that the initial concentration for the second period may be considered as a result of the pumping rate q_2 for a total injected flow of Q_1. Thus, the transient flow field created by a two-step injection can be transformed into a steady-state flow field with a constant injection rate. The solution at t_2 can then be conveniently evaluated by:

$$c^*(r,t_2;q_2) = c_s^*(r,Q_1+Q_2;q_2) \quad (24)$$

Eq. (22) can be generalized to an arbitrarily discretized pumping history, $q_1(t_1), q_2(t_2), \ldots, q_n(t_n)$:

$$c^*(r,t_i;q_i) = c_s^*\left(r, \sum_{j=1}^{i} Q_j; q_i\right) = c_s^*\left(r, \sum_{j=1}^{i} Q_j; q'\right) \quad (24)$$

where q' represents an arbitrary, constant specific flow rate.

Similarly, for a continuous pumping function, we have:

$$c^*(r,t;q(t)) = c_s^*\left(r, \int_0^t q dt; q'\right) \quad (25)$$

Essentially, Eqs. (discrete) and (continuous) evaluate the solution on the domain of the cumulative injection flow volume, Q, instead of the time domain. On the Q domain, Eq. (cQ) may be considered as the solution for a unit step injection flow rate, i.e., on the Q domain, the transient flow can be transformed into steady-state flow. To obtain the time-domain solution, one only needs to map the solution to the time domain according to the relation between t and $Q(t)$. The general procedure to analytically evaluate the concentration solution in a transient divergent flow field with a constant injection concentration can be summarized as follows:

- Calculate the analytical solution for a steady-state flow field $c^*(R,\tau)$;
- Transform $c^*(R,\tau)$ into $c^*(r,Q)$ according to the definition of dimensionless groups, i.e., $r = \alpha_L R$ and $Q = 2\pi\theta\alpha_L^2\tau$;
- Evaluate the cumulative pumping function $Q(t) = \int_0^t q dt$;
- Map $c^*(r,Q)$ onto the time domain, $c^*(r,t)$.

3.4 Transient flow with a time-dependent input concentration

For both a time-dependent well flow rate, $q(t)$, and input concentration, $c_0(t)$, we may discretize the functions into $q(t_0), q(t_1), \ldots$ and $c_0(t_0), c_0(t_1), \ldots$. Consider the simple case with the first two steps: $q_1(0 \le t < t_1), c_1(0 \le t < t_1)$ and $q_2(t_1 \le t < t_2), c_2(t_1 \le t < t_2)$. Following the procedure describe in the previous section, the solution at t_1 is given by:

$$c(r,t_1;q_1,c_1) = c_s(r,Q_1;q_1,c_1) = c_s(r,Q_1;q_2,c_1) \quad (26)$$

That is, the initial solution for the second period can be regarded as a result of the pumping rate q_2 for a total injected flow Q_1 at a constant input concentration c_1. Thus, for the second period, the problem becomes a steady-state flow with a time-dependent input history at the pumping well, which can be solved by linear convolution,

$$c(r,t_2;q_2,c_2) = g(r,Q_1+Q_2)c_1 + g(r,Q_1)c_2 \quad (27)$$

where the transfer function $g(r,Q)$ is given by

$$g(r,Q)=\frac{g(r,t)}{2\pi\theta\alpha_L^2}$$ 928)

The general solution on the Q domain is given by:

$$c(r,Q;q(t),c_0(t))=\int_0^Q g(r,Q')c_0(Q-Q')dQ' \quad (29)$$

where the input concentration is written as a function of Q instead of t. Thus, the procedure to analytically evaluate solute transport in a transient divergent flow field with a time-dependent input concentration can be summarized as follows:

- Calculate the transfer function $g(r,t)$ in a steady-state flow field;
- Transform $g(r,t)$ into $g(r,Q)$ according to the definition of dimensionless groups;
- Evaluate the cumulative pumping function $Q(t)=\int_0^t qdt$;
- Transform the input concentration history $c_0(t)$ into $c_0(Q)$;
- Evaluate the linear convolution, Eq. (conv);
- Map $c(r,Q)$ onto the time domain, $c(r,t)$.

4 Case Study

In this section, we present a synthetic case to validate the developed algorithms describe in the previous section. Consider a discrete functions for $q(t)$:

$$q(t)=\begin{cases}10\,m^2/d, & 0\le t<20d\\ 8\,m^2/d, & 20d\le t<30d\\ 5\,m^2/d, & 30d\le t<40d\\ 2\,m^2/d, & 40d\le t<50d\\ 10\,m^2/d, & t\ge 50\end{cases} \quad (30)$$

Associated with the well flow rate, we consider a input history:

$$c_0^*(t)=\begin{cases}1, & 0\le t<10d\\ 0.5, & 10d\le t<20d\\ 0.2, & 20d\le t<40d\\ 1, & 40d\le t<50d\\ 0, & t\ge 50\end{cases} \quad (31)$$

Other parameters include: $rw = 0.5m$, $\alpha_L = 1m$, and $\theta = 0.3$.

Figure 1 shows the well flow rate history (Figure 1a) and the input concentration history (Figure 1b). Figure 1c shows the cumulative injected flow, Q . Figure 1d shows the input concentration as a function of Q by mapping $c_0^*(t)$ onto the Q domain.

Figure 2 compares analytical solutions using the developed methods with numerical solutions evaluated using the Matlab built-in *ode* solver. The cases compared include: (a) steady-state flow for a constant well injection rate, $q = 10m^2/d$, and a constant input concentration, $c_0 = 1$, throughout the pumping history; (b) steady-state flow, $q = 10m^2/d$, and the time-dependent input concentration history described by Eq. (c0t); (c) transient flow created by the time-dependent pumping history, Eq. (qt), and a constant input concentration, $c_0 = 1$; and (d) transient flow with the time-dependent input concentration history. The developed analytical solutions and numerical solutions match very well for all cases.

5 Conclusion

We develop efficient approaches to analytically evaluate solute transport in transient divergent flow fields created by time-dependent pumping. By working on the cumulative injected flow domain, Q , instead of the time domain, the transient flow problem can be transformed into a steady-state flow problem. Thus, by directly mapping the analytical solution in a steady-state flow field according to the relation between the cumulative injected flow and time, one can conveniently evaluate the solution in transient-flow fields. For time-dependent input concentrations, linear convolution can be applied on the Q domain and the solution on the time domain can be obtained by direct mapping.

The developed approaches can be conveniently extended to uniform flow fields in homogeneous aquifers if diffusion is negligible. For example, in a two-dimensional homogeneous aquifer, the transport equation may be written as:

$$\theta \frac{\partial c}{\partial t} = -q(t)\frac{\partial c}{\partial x} + \alpha_L q(t)\frac{\partial^2 c}{\partial x^2} + \alpha_T q(t)\frac{\partial^2 c}{\partial y^2} \quad (32)$$

where the time-dependent Darcy's velocity $q(t)$ is along the x direction and α_T is the transverse dispersivity. Both longitudinal and transverse dispersion are only linearly dependent on the magnitude of velocity. *Carlier* [2008] proposed to analytically evaluate such a problem by time transformation for a discretized $q(t)$. Using our developed approaches, the transient problem becomes a steady-state flow problem on the qt domain. Thus, the concentration for an arbitrary function of q and input concentration can be conveniently evaluated.

Acknowledgement

This research was sponsored by the National Institutes of Water Resources (NIWR) and U.S. Geological Survey (USGS) under project ID 2007GA165G.

References

Becker, M.W., and R.J. Charbeneau (2000), First-passage-time transfer functions for groundwater tracer tests conducted in radially convergent flow, *J. Contam. Hydrol., 40*, 299-310.

Carlier, E. (2008), Analytical solutions of the advection-dispersion equation for transient groundwater flow. A numerical validation, *Hydrol. Process., 22*, 3500-3506.

Chen, C.-S. (1985), Analytical and approximate solutions to radial dispersion from an injection well to a geological unit with simultaneous diffusion into adjacent strata, *Water Resour. Res., 21*, 1069-1076.

Chen, C.-S. (1986), Solutions for radionuclide transport from an injection well into a single fracture in a porous formation, *Water Resour. Res., 22*, 508-518.

Chen, C.-S. (1987), Analytical solutions for radial dispersion with Cauchy boundary at injection well, *Water Resour. Res., 23*, 1217-1224.

Chen, C.-S., and G.D. Woodside (1988), Analytical solution for aquifer decontamination by pumping, *Water Resour. Res., 24*, 1329-1338.

de Hoog, F. R., J. H. Knight, and A. N. Stokes (1982), An improved method for numerical inversion of Laplace transforms, *SIAM J. Sci. Stat. Comput., 3*, 357-366.

Goltz, M.N., and M.E. Oxley (1991), Analytical modeling of aquifer decontamination by pumping when transport is affected by rate-limited sorption, *Water Resour. Res., 27*, 547-556.

Harvey, C.F., R. Haggerty, and S.M. Gorelick (1994), Aquifer remediation: a method for estimating mass transfer rate coefficients and evaluation of pulsed pumping, *Water Resour. Res., 30*, 1979--1991.

Hoopes, J. A., and D. R. F. Harleman (1967), Dispersion in radial flow from a recharge well, *J. Geophys. Res., 72*, 3595-3607.

Hsieh, P. A. (1986), A new formula for the analytical solution of the radial dispersion problem, *Water Resour. Res., 22*, 1597-1605.

Huang, J., J.A. Christ, and M.N. Goltz (2010), Analytical solutions for efficient interpretation of single-well push-pull tracer tests, *Water Resour. Res., 46*, W08538.

Huang, J., and M.N. Goltz (2006), Analytical solutions for solute transport in a

spherically symmetric divergent flow field, *Trans. Porous Media*, *63*, 305-321.

Moench, A.F. (1995), Convergent radial dispersion in a double-porosity aquifer with fracture skin: Analytical solution and application to a field experiment in fractured chalk, *Water Resour. Res.*, *31*, 1823-1835.

Moench, A.F. (1989), Convergent radial dispersion: A Laplace transform solution for aquifer tracer testing, *Water Resour. Res.*, *25*, 439-447.

Moench, A, F., and A. Ogata (1981), A numerical inversion of the Laplace transform solution to radial dispersion in a porous medium, *Water Resour. Res.*, *17*, 250-252.

Novakowski, K.S. (1992), The analysis of tracer experiments conducted in divergent radial flow fields, *Water Resour. Res.*, *28*, 3215-3225.

Tang, D. H., and D. K. Babu (1979), Analytical solution of a velocity dependent dispersion problem, *Water Resour. Res.*, *15*, 1471-1478.

Figure 1

Numerical case for testing developed algorithms for analytically evaluating solute transport in transient divergent flow with time-dependent input concentrations. (a) well flow rate; (b) input concentration; (c) cumulative injected flow; and (d) input concentration as a function of cumulative injected flow.

Figure 2

Comparison of analytical solutions with numerical solutions. (a) steady-state flow and a constant input concentration; (b) steady-state flow and time-dependent input concentrations; (c) transient flow and a constant concentration input; and (d) transient flow and time-dependent input concentrations.

Figure 1

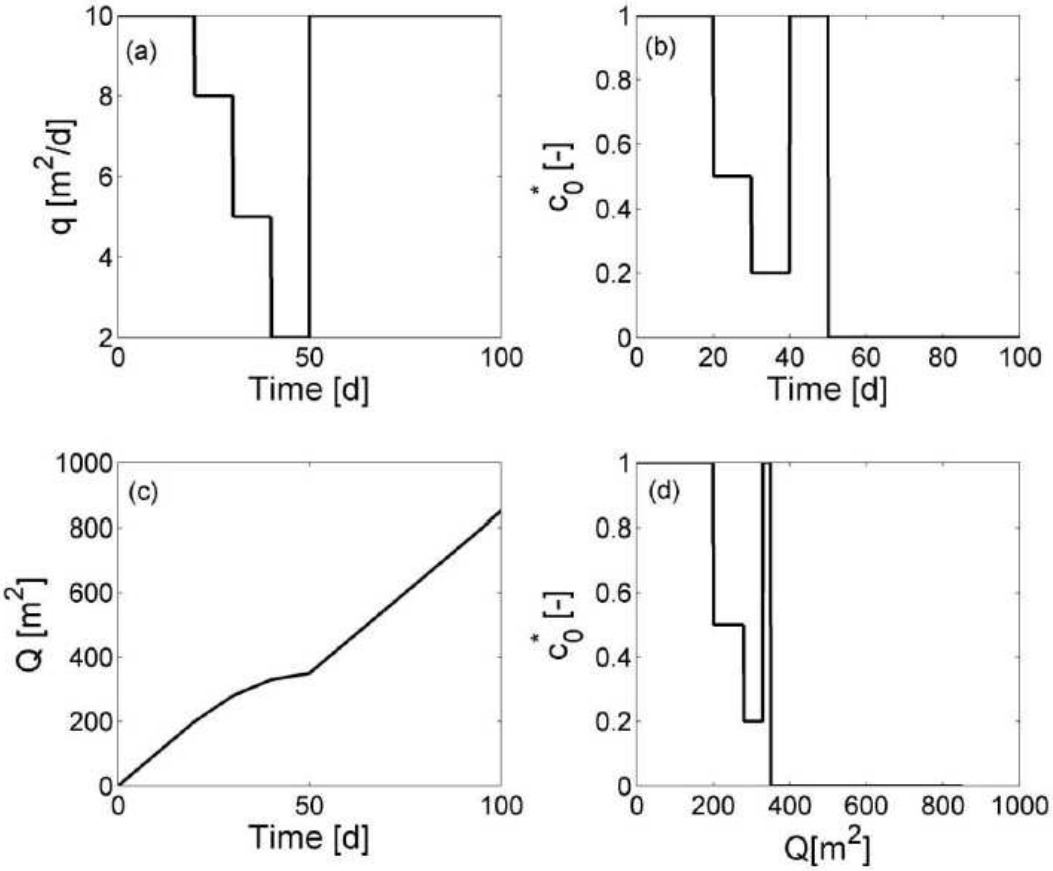

Figure 2

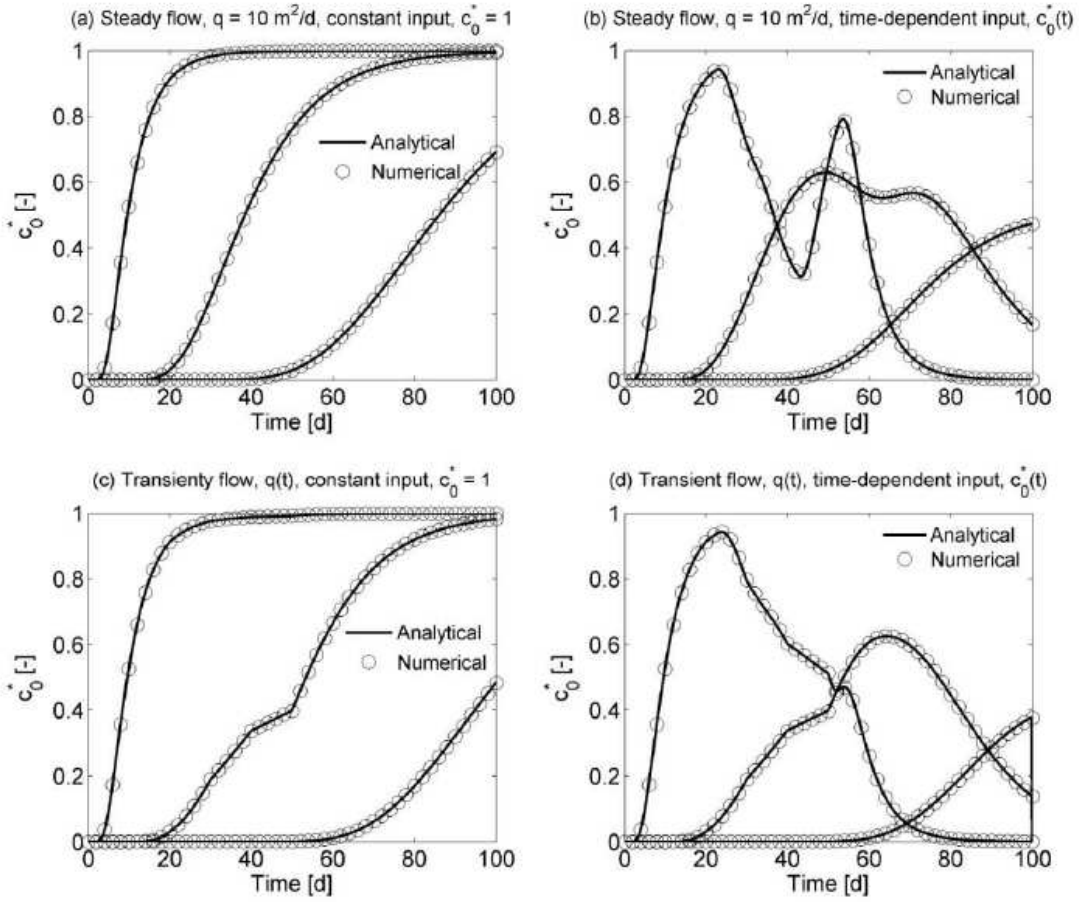
(a) Steady flow, q = 10 m²/d, constant input, c₀* = 1
(b) Steady flow, q = 10 m²/d, time-dependent input, c₀*(t)
(c) Transienty flow, q(t), constant input, c₀* = 1
(d) Transient flow, q(t), time-dependent input, c₀*(t)
Analytical
Numerical
c₀* [-]
Time [d]
0
0.2
0.4
0.6
0.8
1
0
20
40
60
80
100

Assessing impacts of hemlock demise on a southern Appalachian stream using aquatic macroinvertebrates

Basic Information

Title:	Assessing impacts of hemlock demise on a southern Appalachian stream using aquatic macroinvertebrates
Project Number:	2010GA233B
Start Date:	3/1/2010
End Date:	2/28/2011
Funding Source:	104B
Congressional District:	10
Research Category:	Biological Sciences
Focus Category:	Ecology, Acid Deposition, Conservation
Descriptors:	
Principal Investigators:	Darold Paul Batzer

Publication

1. Pitt, D.B. and Batzer, D.P. 2011. Woody Debris as a Resource for Aquatic Macroinvertebrates in Stream and River Habitats of the Southeastern United States: A Review. Proceeding of the 2011 Georgia Water Resources Conference

Title: **Assessing impacts of hemlock demise on a southern Appalachian stream using aquatic macroinvertebrates**

Author: **Darold P. Batzer, Professor of Entomology, University of Georgia, Athens**

Period of Performance: **March 1, 2010 to February 28, 2011.**

Executive Summary

The recent invasion by the hemlock woolly adelgid and the resultant demise of hemlock trees could affect Georgia mountain streams. A loss of riparian shading, altering temperature and light regimes of streams, might negatively affect biota. Streams adjacent to hemlocks treated with imidacloprid to prevent tree death might be negatively affected by the pesticide applications. Once the hemlock trees die, a massive influx of woody debris into streams might occur and have long term consequences for stream ecology. For this project, I used aquatic macroinvertebrates as response organisms, and have developed the following three hypotheses regarding the impacts of hemlock demise on stream ecology: 1) Loss of shading from hemlock demise will have negligible impacts on aquatic invertebrates because other plants already provide much of the natural canopy over channels. 2) Imidacloprid treatments to save riparian hemlocks in high priority area, if properly applied, will not adversely affect stream invertebrates. 3) A future large influx of woody debris from dead hemlocks into stream channels will significantly alter invertebrate community composition in terms of both abundance and biomass. Hypotheses were tested experimentally in Billingsley Creek in the southern Appalachians of Georgia from October 2009 through April 2011. Data thus far supported Hypotheses 1 and 2, but not Hypothesis 3. At least at this stream, the invasion of the hemlock woolly adelgid may not have profound implications for the ecology of aquatic macroinvertebrates. However, analyses are not complete. For Hypothesis 3 regarding impacts of wood addition only a single collection has been assessed, and then only partially. Impacts might not become evident in samples until the wood was present for a longer period of time.

List of Figures

PROJECT SCOPE AND OBJECTIVES

The hemlock woolly adelgid (*Adelgus tsugae*) was first observed in the eastern US in Virginia during the 1950s, and has since spread south into the southern Appalachians, including Georgia. It is causing extensive mortality of eastern hemlock trees (*Tsuga canadensis*), which typically die within a few years after infestation (Cheah et al. 2004). The extreme susceptibility of eastern hemlock has led to real concerns that the tree species could go extinct in Georgia, except where protected by human intervention. Currently the only effective control method is inoculation of the trees with imidacloprid insecticide (Cowles 2009). Because hemlock is such an important component of the riparian forest along many streams, numerous concerns have developed about consequences for the streams' ecology (Snyder et al. 2002).

The invasion by the hemlock woolly adelgid and the resultant demise of the trees could affect Georgia mountain streams in three main ways: 1) the death of hemlocks could reduce riparian shading, alter temperature and light regimes of streams, and negatively affect biota; 2)

streams adjacent to hemlocks treated with imidacloprid might be negatively affected by the insecticide applications; and 3) once the hemlock trees die, a massive influx of woody debris into streams might occur and have long term consequences for stream ecology.

For most, loss of shading and insecticide treatments associated with hemlock infestation by adelgid would seem the most logical issues of concern. However, I predict that the most dramatic ecological change in streams from the demise of hemlocks will be the large influx of woody debris, and the impacts from loss of shading and insecticide treatments on streams probably will be negligible.

REVIEW OF PAST RELEVANT WORK

Woody debris provides food and habitat for invertebrates, provides refugia for fish, and influences flow, substrate and nutrient dynamics (O'Connor 1991, Wallace et al. 1995, Eggert and Wallace 2007). Numerous experimental studies have demonstrated the ecosystem values of woody debris to streams (Wallace et al. 1995, Lester et al. 2007, Entrekin et al. 2009), with the major concern of past studies being the consequences of a lack of this resource. However, the demise of hemlock will pose a new concern that has rarely been addressed. What are the ecological effects of an excess of woody debris? In headwater streams of the Pacific Northwest, my colleagues and I (Haggerty et al. 2004, Jackson et al. 2007) demonstrated that an excessive influx of woody debris from logging operations had unexpected consequences to stream invertebrates, with the fauna of slash inundated streams becoming even more shredder and collector-gatherer dominated than is typical. It is likely that ecological conditions in Appalachian streams will be altered in reaches where large amounts of hemlock wood are deposited, and this impact could persist for decades. Wallace et al. (2001) found that streams of the southern Appalachians are still being significantly affected by the influx of wood from the demise of the American Chestnut almost 80 years ago. Although the impact of dead hemlock wood might not occur for several years, as trees die and decay, conducting an experiment now might permit us to predict consequences. For this project, an article was published (Pitt and Batzer 2011) that reviewed the importance of woody debris to aquatic macroinvertebrates in stream of the Southeastern US, and that paper is available at http://www.gawrc.org/2011paper_pdfs/4.2.3Pitt.pdf.

The primary reason I suspect that loss of riparian shading will not be a major impact of hemlock demise is that most streams in the Georgia Appalachians have a very diverse riparian forest. Independent of hemlock, most small order streams are frequently bordered by a dense *Rhododendron* and shrub riparian zone that provides intense shading. The overstory forest of streams of all sizes is typically composed of a mixed hardwood/pine forest (of which hemlock is only a part) that provides additional shade. Even if hemlock death reduces shading, reduction will probably only be temporary because canopy gaps will be filled by other trees or shrubs. Hemlock shading might perhaps be more important in winter after deciduous trees drop their leaves, but even then, shading from evergreen *Rhododendron* will probably still dominate in most cases. Loss of shading will probably only be important to those few stream reaches bordered by very dense mono-typic stands of hemlock which also lack a *Rhododendron* sub-canopy.

Imidacloprid, as a broad spectrum insecticide, clearly has the potential to impact the ecology of aquatic habitats by harming invertebrates (Stoughton et al. 2008, Tisler et al. 2009). However, I predict that properly administered imidacloprid treatments to control hemlock woolly adelgid near Appalachian streams will probably be of negligible importance to stream ecology.

Operational procedures have already been developed to minimize risk of treatments to streams (Cowles 2009). In addition, the risk to streams in Georgia has already been addressed to some extent. The potential demise of hemlock in Georgia led the US Forest Service to establish refugia areas where stands of hemlocks are being treated with imidacloprid with the goal of saving some reproductive trees. (Their hope is that more effective adelgid control methods might emerge in the future, e.g., biological control, and these trees might serve as seed stock for hemlock reestablishment.) The treatments have turned out to be very effective at saving some tree stands (USFS, personal communication). Because personnel at the US Forest Service anticipated concerns about the impacts of insecticide treatments on stream ecosystems, they have already commissioned assessment studies. Results (USFS, unpublished), thus far, indicate that aquatic invertebrates, the stream organism mostly likely to be affected by the insecticide, do not exhibit detectable treatment effects, and samplings of stream water indicate that levels of the insecticide are very low in treated areas. The insecticide is applied to the soil around the trees, and the insecticide is believed to bind to soil organic matter, minimizing lateral spread (Cowles 2009). Operationally, care is taken to avoid treating trees in very close proximity to stream channels.

For this project, I used aquatic macroinvertebrates as response organisms, and have developed the following three hypotheses regarding the impacts of hemlock demise on stream ecology:

1) Loss of shading from hemlock demise will have negligible impacts on aquatic invertebrates because other plants already provide much of the natural canopy over channels.
2) Imidacloprid treatments to save riparian hemlocks in high priority area, if properly applied, will not adversely affect stream invertebrates.
3) A future large influx of woody debris from dead hemlocks into stream channels will significantly alter invertebrate community composition in terms of both abundance and biomass.

METHODS

Study Site

The US Forest Service has designated several hemlock stands in Chattahoochee National Forest to be protected from hemlock woolly adelgid using imidacloprid treatments. One of these sites, Billingsley Creek, a third-order tributary of Holcomb Creek in the Chattooga River watershed in northeast Georgia, had attributes especially conducive to my proposed studies. The site has an intact stand of hemlock trees straddling about a 200 m reach of the stream, which should persist indefinitely because of imidacloprid treatments. A re-occurring problem with studies of invasive species is maintaining a reference standard in similar but uninvaded habitat; the existence of this treated stand eliminated that problem for my work. Although this stand was protected, extensive similar reaches of stream exist both above and below the protected area where the hemlocks were dead or dying. Thus, similar stream habitat existed in Billingsley Creek with and without living hemlocks. Finally, previous studies on aquatic invertebrates in the "treated" reach of Billingsley Creek failed to detect any negative impacts of the insecticide treatments when compared to a non-treated reference elsewhere (US Forest Service, J. Hanula), and the two-year data set on invertebrates collected in that study was fully available for my use.

Contrasting the upstream and downstream areas with the middle treated reach of Billingsley Creek provided an opportunity to re-confirm that stream biota are not being impacted by imidacloprid insecticide treatments. Additionally, because vibrant hemlock trees existed in the treated area, while hemlock upstream and downstream were dying or dead, the Billingsley Creek site also offered a unique opportunity to assess impacts of the death of hemlock trees on

stream ecology. As mentioned, I hypothesize that neither imidacloprid treatment nor simply the death of hemlock trees will be a significant influence on stream ecology. However, the Billingsley Creek system offered me an opportunity to re-consider those impacts, under the auspices of an experimental study designed primarily to assess potential impacts of a future influx of hemlock wood.

Study Design and Sampling

In October 2009, I randomly selected 9 plots, each ~2 m long, from the set of gravel, cobble riffles in the 200 m portion of Billingsley Creek adjacent to the treated hemlock trees. (The only other common habitats in the creek were sandy runs, with only occasional depositional pools or bedrock outcrops.) I also randomly selected 6 similar gravel/cobble plots in a portion of the stream about 250 to 400 meters downstream from the treated reach, and another 6 plots in an area about 50 to 200 meters upstream from the treated areas (Figure 1). A 250 m buffer was maintained between treated reach and the downstream sites to minimize impacts of pesticide-carry downstream. Thus, I had 9 plots with riparian hemlock trees kept alive by insecticide applications, and 12 plots where the hemlock trees were dead and no insecticide treatments were being applied. Each plot location was entered into a GPS unit so they could be revisited.

I used aquatic macroinvertebrate communities as my indicator of stream ecological condition. There is a rich tradition of using aquatic macroinvertebrates as a measure of biotic integrity of streams (see Rosenberg et al. 2008), including the southern Appalachians (but I do not review that literature here). As mentioned, I had access from the US Forest Service to two years of invertebrate data (2006-2008) from the center reach of Billingsley Creek collected with a Surber sampler. In October 2009, I again sampled the aquatic invertebrates in that reach in each of 9 plots, plus in my 12 plots located upstream (6) or downstream (6). However, instead of a Surber sampler, I opted to use a T-sampler because that device was more practical to use in subsequent studies where large amount of woody debris were present (see below). A T-sampler (Merritt et al. 2008) is essentially a small version of a Surber or Hess sampler, where sediments, gravel, and cobble are agitated within a 15 cm wide tube and then transferred into a side net. The shallow depths (<15 cm) in gravel/cobble riffles of Billingsley Creek permitted the use of this device. Because of the relatively small size of the core, I collected four T-samples per plot and pooled the material into single samples. I collected samples in October 2009, April 2010, July 2010, October 2010, and April 2011. On each invertebrate sampling visit, depths, rates of flows, temperature, electrical conductivity, and pH of the water were also assessed.

I also sampled invertebrates from wood. For this effort I tethered 25 cm sections of dead hemlock wood (10 cm diameter) into each of the 21 plots in December 2009, and retrieve them the next June, 2010. New pieces were tethered in June of 2010 and were retrieved in December 2010, and an additional sample will be collected in June 2011. Invertebrates colonizing the wood were extracted in the laboratory. Also in December (after leaf fall) and June (at full canopy closure), light levels were measured using a light meter and canopy covers were measured using a spherical densiometer. Benthic organic matter was measured in July using a core sampler in each of the 21 plots.

Figure 1. Map of research site indicating treated area with intact hemlock, and locations of sample plots.

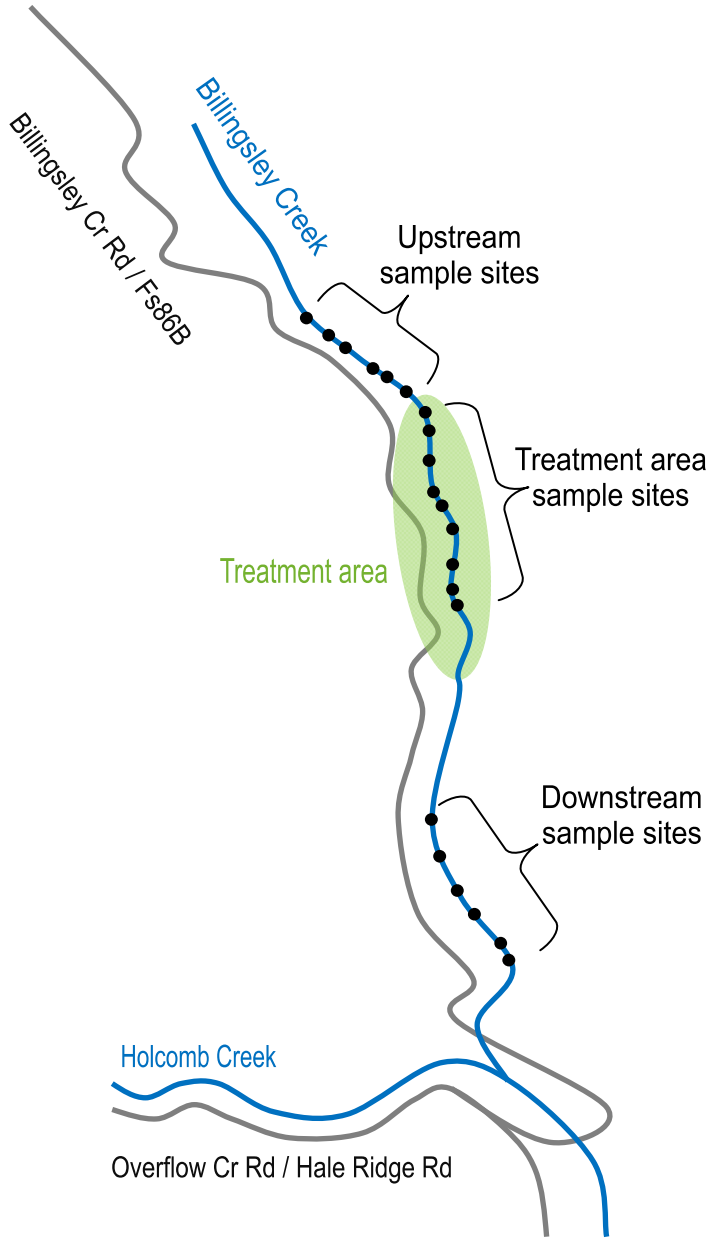

After the July 2010 samples were collected, I initiated the woody debris aspects of the study. Over the previous spring, I quantified the amount and volume of woody debris that is naturally occurring in the Billingsley Creek channel using the methods of Wallace and Benke (1984), including individually sampling each of the 21 2-m long plots. A preliminary survey of the creek indicates that existing wood was not accumulating in any particular sub-habitat, and was now only common near sources of dead fall. I cut a supply of dead hemlock wood (adelgid-killed) from standing trees in the vicinity of Billingsley Creek (but not from my study reaches proper) and transported it to the site. I amassed 11 sets of assorted-sized pieces of dead stem wood that approximated 10 times the ambient level of wood in a 2-m reach of the stream. This

order of magnitude increase in the amount of wood was designed to approximate the increase from future influxes of hemlock wood, but specific levels were not possible to predict with any precision. I then randomly select 3 plots from each of the upstream and downstream study reaches (6 of the 12 total), and 5 of the 9 plots in the middle reach, and with the help of the US Forest Service, added the allotted wood to each designated plot. Using metal rods and wire (as in Wallace et al. 1995), if necessary, the wood was anchored into plots. Flow in Billingsley Creek was not sufficient to dislodge large wood, but wood sets were checked after every flood event and replenished or anchored more securely if necessary. After wood was introduced I had 3 plots with wood and 3 plots without in both the downstream and upstream reaches, and 5 plots with wood and 4 without wood in the central reach (see Figure 1).

After wood was added, all sampling efforts resume on the schedule indicated above. The small size of the T-sampler permitted efficient sampling of benthos even in congested wood addition plots (unlike a conventional Surber sampler), hence its choice for this study. Invertebrates were not sampled directly from the large pieces if wood that were introduced (as they were only present in 11 of 21 plots), but instead wood-associated organisms were monitored on the 25 cm X 10 cm pieces of dead hemlock wood tethered into each of the 21 plots.

Analyses

Macroinvertebrates were identified to genus (if possible), enumerated, measured to length, and biomass calculated using published mass-length regressions (Benke et al. 1999). Organic matter in core samples was measured by drying and ashing samples, and calculating AFDM of the cores.

This project was designed primarily to address potential impacts of excessive wood additions, with the impacts of loss of shading and imidacloprid treatments as secondary concerns. To assess shading and imidacloprid impacts the design was pseudoreplicated, although having upstream and downstream plots added interpretative power. However, my hypotheses stated that neither shading nor imidacloprid should have any affect, so a lack of statistical significance was anticipated. If these hypotheses were borne out by my analyses, pseudoreplication was less of a problem (if reaches are very similar, it is unlikely that adding "true" replicates would result in differences emerging). With negative effects being anticipated, I was most concerned with Type II error (saying there is no difference when in fact there is), and therefore used a relaxed alpha of 0.10, rather than 0.05.

For the wood addition aspects of the study, the unit of interest was the plot rather than the reach, and thus for that factor the design was not pseudoreplicated (although extrapolating results to other streams would have to be conducted with caution). If stream reach effects were unexpectedly significant (regardless of mechanism), I was still able to address impacts of wood additions using stream reach as a blocking effect.

Univariate responses (total macroinvertebrate abundance or biomass, taxon specific abundance or biomass, benthic organic matter biomass, water quality attributes) were contrasted between treatments (with or without wood, with or without live hemlocks, with or without insecticide) using ANOVA. Multivariate ANOSIM analyses, coupled with Non-Metric Multidimensional Scaling Ordination to provide a visual perspective, was used to assess differences in macroinvertebrate community composition among treatments (using both Bray-curtis and Euclidean distances measures).

CONCLUSIONS AND RECOMMENDATIONS

Data collected through October 2010 has been fully processed and provides some preliminary conclusions on my hypotheses:

Abundance and biomass invertebrate data analyzed with ANOSIM from October 2009, April 2010, and July 2010, prior to any wood additions, and October 2010, after additons, indicated that some differences among the three study reaches existed, but these patterns did not suggest a response to imidacloprid treats or loss of hemlock trees. Instead differences simply suggest a natural continuum along the stream (Table 1), where communities only tended to differ between the upper and lower reaches. The central Treated reach was never unique from both the up-stream and downstream reaches.

Table 1. Differences in macroinvertebrate densities and biomass among Downstream (D), central Treatment (T), and Upstream (U) reaches as assessed using ANOSIM, evaluated with Bray-Curtis (top) and Euclidean (bottom) distance measures. Shaded cells indicate a significant difference ($\alpha = 0.1$) for the specific comparison. Biomass data for October 2010 are still being processed.

Bray-Curtis

Sample	Abundance			Biomass		
	D vs. U	D vs. T	U vs. T	D vs. U	D vs. T	U vs. T
Overall	0.155	0.904	0.431	0.224	0.814	0.908
Oct 2009	0.006	0.113	0.281	0.004	0.159	0.117
Apr 2010	0.532	0.727	0.819	0.173	0.489	0.961
Jul 2010	0.069	0.771	0.365	0.123	0.944	0.738
Oct 2010	0.540	0.858	0.828			

Euclidean

Sample	Abundance			Biomass		
	D vs. U	D vs. T	U vs. T	D vs. U	D vs. T	U vs. T
Overall	0.177	0.293	0.134	0.152	0.267	0.951
Oct 2009	0.024	0.031	0.398	0.019	0.155	0.721
Apr 2010	0.589	0.857	0.691	0.290	0.398	0.994
Jul 2010	0.067	0.317	0.092	0.156	0.769	0.738
Oct 2010	0.450	0.872	0.654			

Black = significant difference

Data collected using a densiometer at full canopy cover in Jul 2010 indicated natural changes along the gradient of the stream as well (percent cover: upstream 57.7%, treatment 68.4%, downstream 84.8%). While there was a significant difference in canopy cover between the upstream and downstream reaches ($\alpha = 0.1$, $p = 0.066$), the treatment reach was not unique, but instead simply intermediary to upstream and downstream reaches.

Thus preliminary findings support the hypotheses that:

1) Loss of shading from hemlock demise had negligible impacts on aquatic macroinvertebrates because other plants already provide much of the natural canopy over channels; and

2) Imidacloprid treatments to save riparian hemlocks in a high priority area, if properly applied, does not adversely affect stream macroinvertebrates.

In terms of the potential impacts of wood debris, I only have data from October 2010 T-samples processed and analyzed. April 2011 samples were collected and are now being processed. In October 2010, no significant differences in invertebrate community composition was detected between sites with or without wood additions (ANOSIM; Bray-Curtis: $p = 0.372$; Euclidean: $p = 0.559$). Thus, at this early stage of the study, findings do not support the hypothesis that:

3) A future large influx of woody debris from dead hemlocks into stream channels will significantly alter the invertebrate community composition in terms of abundance and biomass.

Additional samplings for 2011 will further assess all hypotheses.

References Cited

Benke AC, Huryn AD, Smock LA, Wallace JB. 1999. Length-mass relationships for freshwater macroinverebrates in North America with particular reference to the southeastern United States. Journal of the North American Benthological Society 18:308-343.

Cheah CASJ, Montgomery ME, Salom SM, Parker B, Costa S, Skinner M. 2004. In Onken B, ReardonR (eds.) Biological Control of Hemlock Woolly Adelgid. USDA Forest Service pp.1-22.

Cowles RS. 2009. Optimizing dosage and preventing leaching of imidacloprid for management of hemlock woolly adelgid. Forest Ecology and Management 257:1026-1033.

Eggert SL, Wallace JB. 2007. Wood biofilm as a food resource for stream detritivores. Limnology and Oceanography 52:1239-1245.

Entrekin SA, Tank JL, Rosi-Marshall EJ, Houllein TJ, Lamberti GA. 2009. Response of secondary production by macroinvertebrates to large wood addition in three Michigan streams. Freshwater Biology 54:1741-1758.

Haggerty SM, Batzer DP, Jackson CR. 2004. Macroinvertebrate response to logging in coastal headwater streams of Washington, USA. Canadian Journal of Fisheries and Aquatic Science 61:529-537.

Jackson, C. R., D. P. Batzer, S. S. Cross, S. M. Haggerty, and C A. Sturm. 2007. Headwater streams and timber harvest: channel, macroinvertebrate, and amphibian response and recovery. Forest Science 53:356-370.

Lester RE, Wright W, Jones-Lennon M. 2007. Does adding wood to agricultural streams enhance biodiversity? An experimental approach. Marine and Freshwater Research 58:687-698.

Merritt, R. W., K. W. Cummins, V. H. Resh, and D. P. Batzer. 2008. Sampling aquatic insects: collection devices, statistical considerations, and rearing procedures for aquatic insects. Chapter 3 *in* R. W. Merritt, K. W. Cummins, and M. O. Berg (eds.). An Introduction to the Aquatic Insects of North America, 4th edition. Kendall/Hunt, Dubuque, IA.

O'Connor NA. 191. The effects of habitat complexity on the macroinvertebrates colonising wood substrates in a lowland stream. Oecologia 85:504-512.

Pitt, D. B. and D. P. Batzer. 2011. Woody debris as a resource for aquatic macroinvertebrates in stream and river habitats of the Southeastern United States: A review. Proceedings of the 2011 Georgia Water Resources Conference.

Rosenberg DM, Resh VH, and King RS. 2008. Use of aquatic insects in biomonitoring. In Merritt RW, Cummins KW, and Berg MB (eds.) An Introduction to the Aquatic Insects of North America, 4th ed, Kendall/Hunt, Dubuque, IA.

Snyder CD, Young JA, Lemarie DP, Smith DR. 2002. Influence of eastern hemlock (*Tsuga canadensis*) forests on aquatic invertebrate assemblages in headwater streams. Canadian journal of Fisheries and Aquatic Sciences 59:262-275.

Stoughton SJ, Liber K, Culp J, Cessna A. 2008. Acute and chronic toxicity of imidacloprid to the aqautuc invertegrates *Chironomus tentans* and *Hyalella azteca* under constant- and pulse-exposure conditions. Archives of Environmental Contamination and Toxicology 54:662-673.

Tisler T, Jemec A, Mozetic B, Trebse P. 2009. Hazard identification of imidacloprid to aquatic environment. Chemosphere 76:907-914.

Wallace JB, Benke AC. 1984. Quantification of wood habitat in subtroopical coastal plain streams. Canadian Journal of Fisheries and Aquatic Sciences 41:1643-1652.

Wallace JB, Webster JR, Eggert SL, et al. 2001. Large woody debris in a headwater stream: Long-term legacies of forest disturbance. International Review of Hydrobiology 86: 501-513.

Wallace JB, Webster JR, Myer JL. 1995. Influence of log additions on physical and biotic characteristics of a mountain stream. Canadian Journal of Fisheries and Aquatic Sciences 52:2120-2137.

Assessment of endocrine disruption in fish and estrogenic potency of waters in Georgia

Basic Information

Title:	Assessment of endocrine disruption in fish and estrogenic potency of waters in Georgia
Project Number:	2010GA234B
Start Date:	3/1/2010
End Date:	2/28/2011
Funding Source:	104B
Congressional District:	GA-010
Research Category:	Biological Sciences
Focus Category:	Surface Water, Acid Deposition, Water Quality
Descriptors:	
Principal Investigators:	Robert Bringolf, Cecil A. Jennings

Publications

There are no publications.

Assessment of Endocrine Disruption in Fish and Estrogenic Potency of Waters in Georgia

Annual Report for the Period:
March 1, 2010 through February 28, 2011

Submitted to:

Georgia Water Resources Institute

By

Robert B. Bringolf, Ph.D.
University of Georgia
Warnell School of Forestry & Natural Resources
Athens, GA 30602-2152
Tel: 706-542-1477
Fax: 706-542-8356
E-mail: rbringolf@warnell.uga.edu

And

Cecil Jennings, Ph.D.
Unit Leader
USGS Georgia Cooperative Fish & Wildlife Research Unit
Warnell School of Forestry & Natural Resources
Athens, GA 30602-2152
Tel: 706-542-4837
Fax: 706-542-8356
E-mail: jennings@uga.edu

Submitted May 16, 2011

Executive summary

The overall goal of this project was to provide information on the incidence of intersex bass and estrogenic potency of waters across the state of Georgia. Specific objectives of this project were to (1) assess intersex condition in fish collected from rivers and lakes across Georgia; (2) determine estrogenic potency (a measure of the estrogens and estrogen-like substances) of surface waters near municipal effluent discharges, which are commonly associated with intersex fish; (3) compare the sensitivity of in vivo and in vitro assays to detect estrogens in river water.

This project has supported one Ph.D. student, Kristen Kellock, in the UGA Interdisciplinary Toxicology Program. Kristen received the Best Student Presentation Award at the 2011 Georgia Water Resources Conference held in Athens, GA, April 11-13, 2011. Kristen published her findings in the Conference Proceedings (Kellock and Bringolf 2011).

After one year of sampling we have confirmed that intersex is prevalent in some water bodies across the state and that intersex is not confined to rivers that receive wastewater effluent. Of the 147 male bass collected in 2010, 42.9% were intersex (contained eggs in testes). Of the male fish collected from impoundments, 51.8% were intersex whereas 12.1% of males from rivers were intersex. Most strikingly, intersex rates were >66% in all male bass collected from impoundments with a surface area of 20 acres or less (N=5). Additional sampling from Georgia rivers and impoundments is critical to fully elucidate the extent and factors influencing the occurrence of intersex fish in the state.

The yeast-based assay (BL-YES assay) used to measure total estrogenic potency in water samples was initially unsuccessful. Despite thorough troubleshooting and considerable time and effort, the bioluminescent yeast strain did not respond to estrogens in a consistent and predictable manner. Therefore, we obtained a different strain of transgenic yeast (YES assay) and, following optimization, we are presently analyzing water samples collected from each of the rivers and lakes with the YES assay to determine estrogen activity in these waters.

To determine if water temperature influences the effects of early-life estrogen exposure, we performed a preliminary lab study with newly-hatched fathead minnows that were exposed to an estrogen at various temperatures. Interestingly, no intersex was evident by 75 days post hatch (dph) which suggests that the E2 exposure did not induce intersex, or the fish 'recovered' from the intersex condition by 75 dph. There was high mortality in the 35^{o}C treatment but all fish at 30^{o}C appeared healthy and grew better than those exposed to 25^{o}C for 15 d early in life. Although all fish were cultured at the different temperatures for just 15 days prior to transfer to 25^{o}C for grow out, all fish (regardless of E2 exposure) raised at 30^{o}C for 15 days were significantly less responsive to the second estrogen exposure than those raised at 25^{o}C early in

life. This suggests that a permanent effect occurred in the fish exposed to 30^{o}C that resulted in estrogen insensitivity later in life. This study must be repeated and requires further investigation before the full implication of temperature effects on estrogen sensitivity can be understood.

Overall, this research has greatly advanced the understanding of the distribution and severity of the intersex condition in bass in Georgia and has discovered substantial, unexpected and novel trends in the waters where intersex occurs most frequently. Additional investigation is warranted to understand the primary factors involved in development of intersex gonads, to elucidate the relative sensitivity of bass compared to other fishes, and to determine potential population-level effects of the condition.

Introduction

Reports of intersex fish in water bodies around the world (including Georgia) have stimulated widespread concern about the effects that chemicals are having in the environment. Intersex is a term used to describe the presence of both male and female characteristics in individual fish, most commonly presence of oocytes (eggs) in testicular tissue, a pathological condition that is not routinely observed in most fish species (Hecker et al. 2006). The intersex condition has often been associated with a hormonally active component of municipal wastewater effluent discharge and has been induced in laboratory studies where fish were exposed to natural and synthetic hormones (Jobling et al. 2002), which are routinely measured in treated municipal wastewater effluent. The intersex condition has individual- as well as population-level implications; intersex male fish have been shown to have altered sperm production and reproductive success compared to non-intersex male fish (Jobling et al. 2002). These findings generate numerous questions about the ecological implications of intersex fish and fuel widespread concerns about the role of chemicals in well-documented trends in reproductive abnormalities in human health as well (Colborn et al. 1994). Understanding the extent and distribution of intersex fish in the environment and the chemicals that are known to induce this condition is a critical first step toward developing a management strategy.

In a widely-publicized recent scientific article, Hinck et al. 2009 reported that intersex largemouth bass (*Micropterus salmoides*) were found in rivers across the US. Intersex bass were more common (up to 91%) in Southeastern US rivers than in other sampled areas of the country. The Chattahoochee, Flint and Savannah Rivers in Georgia were included in the sampling, and of the five sites sampled in these rivers, the incidence of intersex in bass ranged from 30–50%. The fish all appeared to be male but had oocytes in their testes. Causes for the intersex condition are currently unknown and in this study the authors did not analyze water samples for the presence of estrogens or other hormones that have previously been associated with this condition. Sample sites were not associated with wastewater effluent or particular contaminants but were stratified by land use (urban, agricultural, etc.). Other indicators of reproductive system abnormalities were not assessed. Additional sampling is required to fully understand the extent of the distribution of intersex fish in Georgia and the underlying causes for this condition. Our objectives are to: (1) assess intersex condition in fish collected from rivers and lakes across Georgia; (2) determine estrogenic potency (a measure of the estrogens and estrogen-like substances) of surface waters; and (3) compare the sensitivity of in vivo and in vitro assays to detect estrogens in river water.

Methods

RIVER SAMPLING. Black bass sampling was conducted from April – June 2010. Fish were collected by boat electroshocking and/or hook and line from the North Oconee River, Broad River, Ocmulgee River, and Savannah Rivers in Georgia. The target was to collect 15 adult (age 1+) male fish at each site but this was not reached in all samples (Table 1). Fish from all rivers except the Broad R. were collected within 1 km of a municipal wastewater effluent outfall. The fish were kept alive in an aerated live well until sufficient numbers were obtained. Fish were anesthetized by buffered MS-222 overdose, weighed and measured. Gonads from each fish were examined macroscopically for confirmation of gender. Gonads were dissected from each fish, weighed and preserved in 10% buffered formalin for histological preparation by the Fish Pathology Laboratory at the University of Georgia College of Veterinary Medicine Diagnostic Lab. We determined the incidence and severity of intersex based on presence of oocytes in the testes of apparent (macroscopic) male fish. Severity of intersex was rated with criteria described previously (Blazer et al. 2007) for smallmouth bass by scoring each fish on a scale of 0 (no intersex) to 4 (multiple clusters of more than 5 closely associated oocytes in the testes). A mean index of severity was calculated for fish from each river.

IMPOUNDMENT SAMPLING. Black bass were collected (also in April – June 2010) by boat electroshocking from eleven impoundments across Georgia. Ten to 15 adult bass adult (age 1+) were obtained from each lake. The fish were kept alive in an aerated live well until sufficient numbers were obtained. Fish were anesthetized by buffered MS-222 overdose, weighed and measured. Gonads were dissected from the fish, weighed and preserved in 10% buffered formalin for histological analysis. Rates of intersex from the lakes were compared to the intersex rate in males from rivers receiving high volume municipal wastewater effluent. Severity of intersex was rated with criteria described previously for river fish. A mean index of severity was calculated for fish from each impoundment.

ESTROGENIC POTENCY. River water samples (2 L) were collected from at least 1 km upstream and less than 1 km downstream of point source effluent discharges. Lake water samples were collected as close to the center of the lake as possible. The water samples were filtered to remove suspended solids and extracted on a C-18 solid phase extraction column. The column was eluted with 3 x 1 ml methanol and extracts were stored at 4^{o}C until analysis. Total estrogenic activity will be determined by the yeast estrogen screen (YES) assay, an in vitro assay with yeast (*Saccharomyces cerevisiae*) cells that have been transfected with the human estrogen receptor and an enzyme reporter gene. Estrogenic compounds in water samples bind the receptors and stimulate production of an enzyme, the activity of which can be measured

with a colorimeter. The YES assay has been previously validated for rapid, sensitive detection of estrogenic compounds in water samples (Routledge and Sumpter 1996).

TEMPERATURE EFFECTS ON INTERSEX. We performed a preliminary lab study with newly-hatched fathead minnows that were exposed to an estrogen early in life at various temperatures. Larval fathead minnows were exposed to 10 or 100 ng/L of 17-β estradiol (E2) at different temperatures (25, 30, 35 ^{o}C) from day 0 to 15 days post-hatch (dph). Three replicates of 600-ml glass beakers with 500 ml of dechlorinated tap water and 20 larval fish were used for each treatment. Water was renewed (90%) daily. Prior to renewal, water samples (n=3) were collected for confirmation of estradiol exposure concentrations. Following estradiol exposure, all fish were transferred to 19 L aquaria with clean, dechlorinated tap water at 25^{o}C and cultured to 75 dph. Fish were fed flake food and live A*rtemia* nauplii daily to satiation. At 75 dph, all fish were challenged with an exposure of 100 ng/L of E2. At 82 dph, fish were euthanized, weighed, measured, gonads were dissected out and the carcass was homogenized and frozen at -80^{o}C. The gonads were fixed in 10% buffered formalin and processed for sectioning and H&E stain. Gonads were staged (development) and evaluated for incidence and severity of intersex. Fish homogenates were assayed for vitellogenin, the egg yolk protein precursor, which is induced by exposure to estrogens.

Table 1. Intersex black bass collected in 2010 from Georgia rivers and impoundments.

Water Body Type	Site	GA County	Surface Area (ac)	Male Bass	Intersex	% Intersex Males
Impoundment	Hatchery Pond	Ben Hill	3.2	22	18	81.8
Impoundment	Private pond 1	Wilkes	7	5	5	100
Impoundment	Lake Paradise	Barrien	17	6	4	66.7
Impoundment	Private pond	Hancock	18	15	12	80
Impoundment	Private pond 2	Wilkes	20	17	14	82.4
Impoundment	Dodge Co. PFA	Dodge	104	4	2	50
Impoundment	Antitoch East	Floyd	202	5	0	0
Impoundment	Lake Blackshear	Lee	8,600	9	0	0
Impoundment	Walter George	Clay	11,184	14	3	21.4
Impoundment	Lake Oconee	Greene	19,050	8	1	12.5
Impoundment	Lake Seminole	Seminole	37,000	9	0	0
River	North Oconee	Clarke	n/a	5	3	60
River	Broad River	Elbert	n/a	12	0	0
River	Ocmulgee River	Bibb	n/a	8	0	0
River	Savannah River	Richmond	n/a	8	1	12.5

Results and Discussion

Preliminary results suggest that intersex is prevalent in some water bodies across Georgia and that intersex is not confined to rivers that receive wastewater effluent (Table 1). Of the total 147 male bass collected in 2010, 42.9% were intersex. Of the male fish collected from impoundments, 51.8% were intersex whereas 12.1% of males from rivers were intersex. Among fish from rivers, bass from the North Oconee River (downstream of wastewater effluent) had the highest incidence of intersex at 60%, but the sample size from the river was low. The only other river with intersex fish was the Savannah, with just one of eight males with intersex. Interestingly, the highest rate of intersex was found in small impoundments, particularly those less than 200 surface acres. Surface area was a good predictor of intersex rate, accounting for 78% of the variability in incidence of intersex among fish from impoundments (Figure 1). We had expected to see the highest rates of intersex in fish collected from rivers; however, our results suggest that black bass from small ponds (<200 acres) are highly susceptible to the intersex condition. Factors affecting intersex in small ponds are not known at this time but are likely different from those in river that receive wastewater effluent containing estrogens and other hormone-mimicing compounds. Some of the factors that differ among the various impoundments include: 1) small ponds sampled in this study generally had dense, overcrowded, bass populations as opposed to the larger impoundments which had much lower bass densities; 2) small ponds were generally more eutrophic than larger bodies of water; and 3) water temperature was greater in ponds than in other waters. These factors have led us to a number of hypotheses regarding factors that may be involved in intersex. Clearly, additional studies will be necessary to determine the factors that lead to development of intersex in bass and other fishes. Detailed chemical and environmental analyses as well as targeted lab testing may help further elucidate the causes of intersex fish in the state.

Severity of intersex did not differ (T-test, p=0.899) between rivers (2.0 ± 1.5) and impoundments (2.0 ± 1.5). Additionally, severity of intersex was variable among impoundments and was not correlated with surface area of the impoundment (Figure 2). Intersex incidence and severity do not appear to be interrelated as impoundments with low incidence often had high severity.

We are presently analyzing water samples collected from each of the rivers and lakes with the YES assay to determine estrogen activity in these waters. The YES data from 2010 will be informative; however, temporal sampling is required because estrogen levels may not be stable throughout the year and annual patterns (i.e., year to year) are unknown. We hypothesized that the highest estrogen concentrations would be found in water samples from areas with greater incidence of intersex fish; however, high concentrations of estrogens seem unlikely in

lake samples because few of the lakes we sampled receive effluent or had homes or other facilities located nearby.

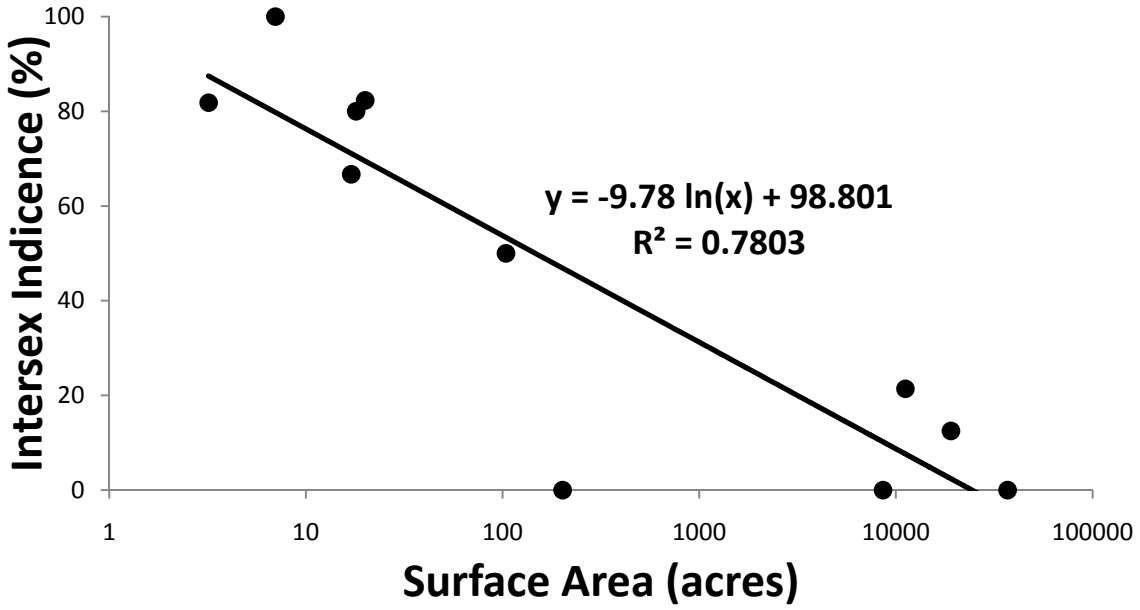

Figure 1. Relationship between incidence of intersex in bass and surface area of impoundments where fish were collected across Georgia.

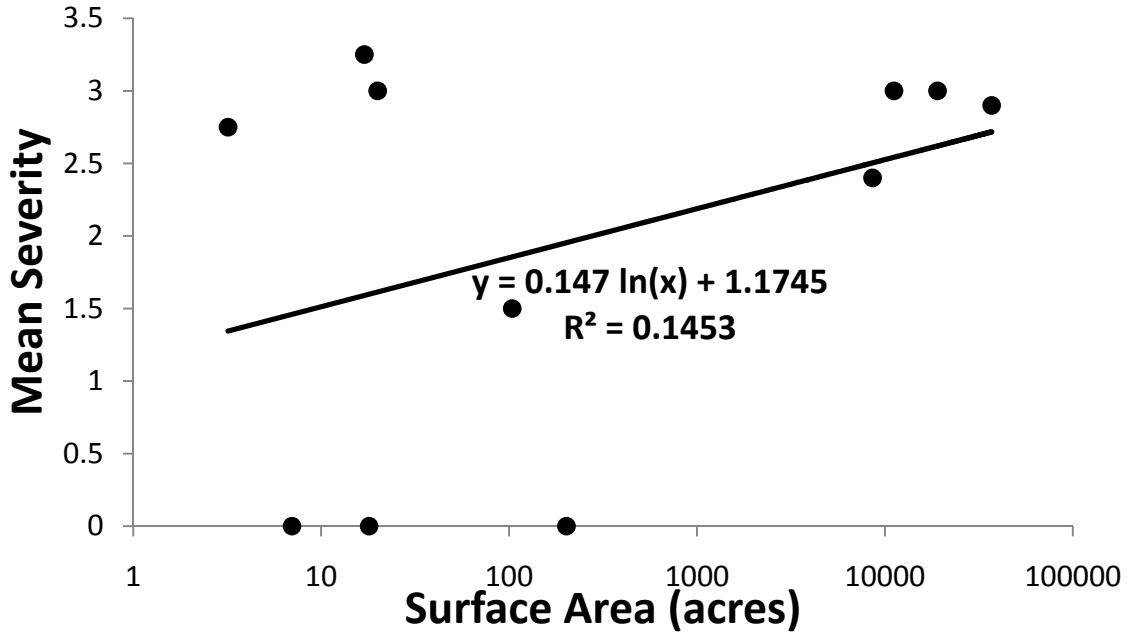

Figure 2. Relationship between severity of intersex and surface area of impoundments were fish were collected across Georgia.

In the lab study, all of the fish exposed to 35^{o}C died by the end of the 15-day exposure. All fish cultured at 25 and 30^{o}C survived. Sex ratio ranged from 50% males to 72% males and did not differ among any of the temperatures or estradiol treatments (ANOVA, Tukey's Test, N=3, df=5, p=0.899). Measured concentrations of estradiol were 84-210% of target concentrations and no estradiol was detected in the controls. Males and females cultured at 30^{o}C early in life, regardless of estrogen exposure, were generally in later stages of gonadal development by 82 dph. Early life estradiol exposure stimulated gonad development in both males and females. Early life exposure to estradiol did not significantly alter sensitivity to estrogen exposure (i.e. vitellogenin induction) later in life, at 75 dph (Figure 3); however, fish cultured at 30^{o}C early in life were much less sensitive to estradiol (less vitellogenin induction) at 75 dph than those that were cultured at 25^{o}C throughout life (Figure 3). The same trends existed for males (Figure 4).

We expected skewed sex ratios in favor of females but this did not occur. Because exposure concentrations were verified, we conclude that the exposure concentrations or duration were insufficient to induce alteration of sex ratio. Based on published literature, we expected to se intersex and this did not occur either. We conclude that one of two things occurred, either 1) fish developed intersex then 'recovered' once placed in clean water for 60 days, or 2) intersex did not develop during the test period. Previous studies have used a similar exposure period and estradiol concentrations to induce intersex, but those investigators cultured the fish in clean water for at least 150 days. The possibility exists that intersex does not manifest until the fish become reproductively mature. Further study is warranted to fully understand the effects of temperature and early life estrogen exposure on reproductive health.

Conclusions. This study will provide the first investigation of estrogens in Georgia's surface waters and intersex fish in many of Georgia's rivers and lakes. The results are crucial for understanding the spatial and temporal distribution of estrogens in surface waters. Intersex is currently thought to be an abnormal condition for bass, but little research on the background incidence of intersex has been reported. Comparison of intersex in fish from rivers and lakes will allow insight into the 'normal' background incidence of intersex in basses and provide additional evidence to determine if the condition is indeed linked to estrogens in the water. Our preliminary results suggest that intersex rates are high in some bass populations, including those in lakes, but the factors influencing intersex are currently poorly understood. Results of our sampling suggest that intersex is not confined to fish in Georgia rivers but occurs in lake populations as well. Additional sampling is required to elucidate the incidence and severity of intersex in Georgia fish and to determine potential causes of the condition.

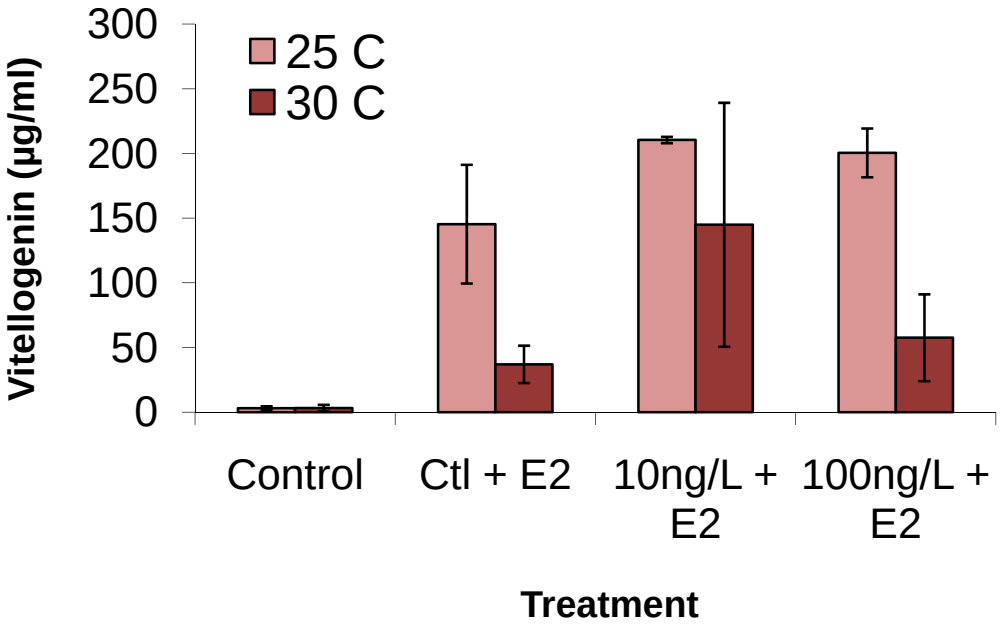

Figure 3. Effects of early life exposure to estradiol at two temperatures (25 or 30°C) during days 0 to 15 dph. Fish were cultured in clean water at 25°C from 15 dph to 75 dph then exposed to estradiol until 82 dph. Different letters indicate significant differences ($p<0.05$) among treatments within a temperature (ANOVA, Tukey's, N=3).

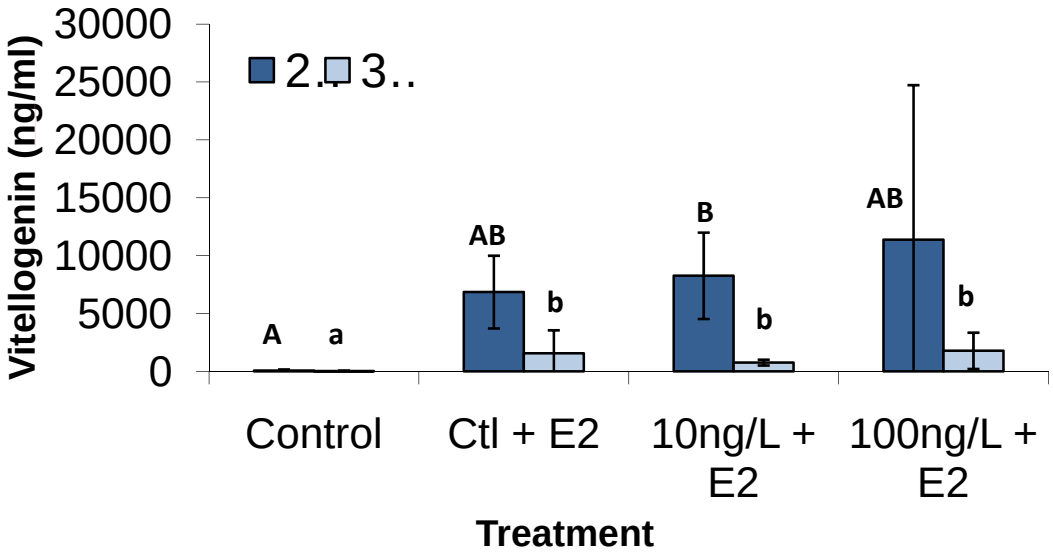

Figure 4. Effects of early life exposure to estradiol at two temperatures (25 or 30°C) during days 0 to 15 dph. Fish were cultured in clean water at 25°C from 15 dph to 75 dph then exposed to estradiol until 82 dph. Different letters indicate significant differences ($p<0.05$) among treatments within a temperature (ANOVA, Tukey's, N=3).

REFERENCES

Blazer, V. 2007. Intersex (testicular oocytes) in smallmouth bass from the Potomac River and selected nearby drainages. Journal of Aquatic Animal Health 19:242-253.

Colborn, T., F. vom Saal, and A. Soto. 1994. Developmental effects of endocrine-disrupting chemicals in wildlife and humans. Environmental Impact Assessment Review 14:469-489.

Hecker, M., M. Murphy, K. Coady, D. Villeneuve, P. Jones, J. Carr, K. Solomon, E. Smith, G. Van Der Kraak, and T. Gross. 2006. Terminology of gonadal anomalies in fish and amphibians resulting from chemical exposures. Reviews of Environmental Contamination and Toxicology 187:103-131.

Hinck, J.E., V.S. Blazer, C. Schmitt, D. Papoulias, and D. Tillitt. 2009. Widespread occurrence of intersex in black basses (Micropterus spp.) from US rivers, 1995–2004. Aquatic Toxicology 95: 60-70.

Jobling, S., S. Coey, J. Whitmore, D. Kime, K. Van Look, B. McAllister, N. Beresford, A. Henshaw, G. Brighty, and C. Tyler. 2002. Wild intersex roach (Rutilus rutilus) have reduced fertility. Biology of Reproduction 67:515-524.

Routledge, E.J. and J.P. Sumpter. 1996. Estrogenic activity of surfactants and some of their degradation products assessed using a recombinant yeast screen. Environmental Toxicology and Chemistry 15:241-248.

Temporal and micro-site variation in flow characteristics in estuarine habitats

Basic Information

Title:	Temporal and micro-site variation in flow characteristics in estuarine habitats
Project Number:	2010GA238B
Start Date:	3/1/2010
End Date:	2/28/2011
Funding Source:	104B
Congressional District:	5th
Research Category:	Biological Sciences
Focus Category:	Ecology, Solute Transport, None
Descriptors:	
Principal Investigators:	Donald R. Webster, Marc Weissburg

Publications

1. Berry, W.A., Webster, D.R., Wilson, M.L. Ferner, M.C., Smee, D.L., and Weissburg, M.J., 2011, "Characterization of Turbulent Hydrodynamics in the Intertidal Zone of a Small Estuary with Respect to Predator-Prey Chemical Signaling, submitted to Environment Fluid Mechanics.
2. Wilson, M.L., Webster, D.R., and Weissburg, M.J. "site and Tide-Specific Variation in the Hydrodynamic Landscape Relative to Odor-Mediated Predators in Salt Marsh System" in preparation for Wilson's Ph.D thesis defense (chapter 5) on 06/03/11. The manuscript will be polished subsequently into a journal submission.
3. Wilson, M.L., Webster, D.R., and Weissburg, M.J., "Tide and Wind Effects on the Fluctuating Flow Parameters in Shallow Intertidal Salt Marsh Habitats" in preparation for Wilson's Ph.D. thesis defense (Chapter 6) on 06/03/11. The manuscript will be polished subsequently into a journal submission.

Final Report

Temporal and micro-site variation in flow characteristics in estuarine habitats

Donald R. Webster
School of Civil and Environmental Engineering
Georgia Institute of Technology
Atlanta, GA 30332-0355

Marc Weissburg
School of Biology
Georgia Institute of Technology
Atlanta, GA 30332-0230

Summary of Activities and Accomplishments:
The goal of this project is to provide comprehensive and detailed information about flow dynamics in the intertidal region of an estuary on the Georgia coast. Coupled with our current and ongoing work on olfactory predators, knowledge about the variability and range of flow environments allows us to make predictions concerning which aspects of fluid flow may impact predator behavior. Our measurements address a series of questions regarding flow properties in the intertidal zone: (1) What are the temporal trends in flow characteristics at both small (over one tidal cycle) and large (over 3 months) scales? (2) Are flow characteristics correlated with any other concurrent physical parameters unique to the estuary system such as tidal range or wind speed? (3) At what temporal scales do study sites need to be examined in order to fully characterize those turbulent flow parameters that may impact biological interactions? (4) At what spatial scales do micro-sites differ in their turbulent flow characteristics – that is, what is the variability in a single region within an estuary? And (5) What sampling regimes need to be used in order to fully characterize those flow parameters that could impact interspecific interactions (i.e. How long should the instrumentation be deployed? How many different micro-sites should be sampled within each study area?)?

As planned, during Summer 2010 we deployed 6 acoustic Doppler velocimeters (ADVs) in Wassaw Sound and tributaries. Measurements were performed at four sites and data for Spring, Neap, and Normal tide types were collected at each site for 48 hour periods. We also deployed two ADV probes at the Priest Landing site continuously for a three month period. To analyze and interpret the data, we have developed a new method for separating the wave and turbulent components of the velocity fluctuations. Three manuscripts have been prepared and are presented here to report the details of the activities and accomplishments:

W.A. Berry, D.R. Webster, M.L. Wilson, M.C. Ferner, D.L. Smee, and M.J. Weissburg. "Characterization of Turbulent Hydrodynamics in the Intertidal Zone of a Small Estuary with Respect to Predator-Prey Chemical Signaling," submitted to *Environmental Fluid Mechanics* (Feb 2011).

M. L. Wilson, D.R. Webster, and M.J. Weissburg. "Site- and Tide-Specific Variation in the Hydrodynamic Landscape Relative to Odor-Mediated Predators in Salt Marsh System," in preparation for Wilson's Ph.D. thesis defense (Chapter 5) on 6/3/11. The manuscript will be polished subsequently into a journal submission.

M. L. Wilson, D.R. Webster, and M.J. Weissburg. "Tide and Wind Effects on the Fluctuating Flow Parameters in Shallow Intertidal Salt Marsh Habitats," in preparation for Wilson's Ph.D. thesis defense (Chapter 6) on 6/3/11. The manuscript will be polished subsequently into a journal submission.

The project was also highlighted on the NortekUSA website:
http://www.nortekusa.com/usa/news/nortek-vectors-used-to-study-odor-mediated-interactions

Miranda Wilson (Ph.D. student) was supported on the project.

Characterization of Turbulent Hydrodynamics in the Intertidal Zone of a Small Estuary with Respect to Predator-Prey Chemical Signaling

W.A. Berry[1], D.R. Webster[1,5], M.L. Wilson[2], M.C. Ferner[3], D.L. Smee[4], and M.J. Weissburg[2]

[1] *School of Civil & Environmental Engineering, Georgia Institute of Technology, Atlanta, GA 30332-0355*

[2] *School of Biology, Georgia Institute of Technology, Atlanta, GA 30332-0230*

[3] *San Francisco Bay National Estuarine Research Reserve, San Francisco State University, Tiburon, CA 94920*

[4] *Department of Life Sciences, Texas A&M University, Corpus Christi, Texas 78412*

[5] Corresponding author, email: dwebster@ce.gatech.edu, phone: 404-894-6704, fax: 404-385-1131

Keywords:

turbulence, estuary, acoustic Doppler velocimetry (ADV), ecology, chemical signaling

Abstract

This study quantifies naturally occurring differences in the hydrodynamic environment in a variety of field sites in Wassaw Sound and associated tributaries (near Savannah, GA, USA). Previously, these sites were used to study predator-prey interactions, and the current study provides a more in-depth characterization of the flow and turbulence characteristics. Velocity time records were recorded using acoustic Doppler velocimeter (ADV) probes at six sites on four days, with a total of 11 data sets. Each set spans one complete tidal cycle and consists of periodically-collected 5-minute bursts of data. These data were subjected to differential-estimate phase filtering in order to identify erroneous velocity measurements. Additionally, the wave component was separated from the turbulent kinetic energy (TKE) and Reynolds shear stress measurements via spectral analysis combined with the coherence function between the simultaneously collected velocity and pressure records. The wave component was in the range of 15 to 56% for the TKE and 13 to 44% for the Reynolds shear stress. Burst-averaged velocity statistics, TKE, Reynolds shear stress, and turbulence intensity (TI) are presented for each data set. Because multiple sites were monitored over multiple days, variation was examined both spatially and temporally. Large variability in turbulent characteristics was observed at different sites on the same day as well as at the same site over different days. The high level of variability in the flow and turbulence characteristics provides insights into the complex, chemosensory-mediated predator-prey interactions that have been observed in the Wassaw Sound ecosystem.

1. Introduction

Ecological processes in aquatic systems, such as predation, reproduction, and benthic settling, are often chemically-mediated, and resultantly, these processes are strongly influenced by flow and chemical transport characteristics (reviewed in Zimmer and Butman 2000, Weissburg et al. 2002, Webster and Weissburg 2009). In the context of benthic predation, the transport of chemical cues in (typically) turbulent flow is particularly important to define when attempting to understand and explain organism behavior and predator-prey interactions. In both laboratory and field studies, turbulence manipulation experiments have shown that the influence of increased flow and mixing on perceptive abilities is species-specific for both the predator and prey organisms (Weissburg and Zimmer-Faust 1993, Finelli et al. 2000, Powers and Kittinger 2002, Smee et al. 2008, Ferner et al. 2009). For instance, slower moving predators (i.e., knobbed whelks) can forage effectively at large flow and mixing rates that produce more dispersed chemical signals, whereas highly mobile predators (i.e., blue crabs) function best at smaller flow and mixing rates that result in less dispersed chemical plumes (Powers and Kittinger 2002, Ferner and Weissburg 2005, Jackson et al. 2007). Further, prey, such as bivalves, alter their behavior depending on the hydrodynamic conditions (Smee and Weissburg 2006), in some cases apparently manipulating the excurrent flow conditions to (presumably) alter the downstream odorant landscape (Delavan and Webster 2011).

The current study seeks to identify naturally occurring differences in the flow and turbulence characteristics at a variety of field sites near the Skidaway Institute of Oceanography on the coast of Georgia, USA. These sites have been used recently to examine predator-prey interactions in the field (e.g., Smee and Weissburg 2006, Smee et al. 2008, Ferner et al. 2009, Smee et al. 2010). An understanding of the turbulent environment in these sites serves to illuminate some of the factors mediating the transmission of chemical signals, which in turn play a role in the predator-prey interactions among local organisms that shape ecological processes. Relatively few studies have quantitatively examined the flow and turbulence characteristics in the intertidal zone of small estuaries. In contrast to a controlled laboratory setting, significant difficulties and challenges arise in the collection of field data. Complex bed morphologies, unsteady flows, and irregular disturbances such as changing atmospheric conditions, upstream inputs, and anthropogenic or organismal interference can all yield modified flow characteristics.

The spatial and temporal variability of studies in a natural environment presents additional challenges to quantifying the connection between effects and observations in predator-prey interactions. Similarly, understanding the extent of temporal and spatial variation is helpful for identifying regions that are characterized by similar flow patterns. Such areas often serve to make observations or perform ecological experiments to understand the role of environmental forcing on ecological interactions.

1.1 Background

In a tidally-driven river, the mean velocity lags slightly behind the water level (Kawanisi and Yokosi 1994, Trevethan et al. 2008). Trevethan et al. (2008) and Trevethan and Chanson (2009) observed flood tide velocities that exceed those of ebb tide, suggesting a net upstream flux. In contrast, Shiono and West (1987) and Voulgaris and Meyers (2004) observed larger velocities in the ebb tide compared to flood tide, and Verney et al. (2006) observed both conditions depending on the measurement location and other factors. Hence, the tidal flow asymmetry appears to depend on local conditions.

Turbulent properties exhibit great spatial variability (Trevethan and Chanson 2009). Relative turbulence intensities are large when compared to similar results from larger estuaries, indicating increased turbulent activity due to greater friction and bed roughness impacts in shallow water (Trevethan and Chanson 2009). Salinity measurements indicate that vertical stratification found in ebb tides can reduce the ratio of Reynolds stress to turbulence intensity, whereas flood tides can be considered well mixed and have larger ratios (Kawanisi and Yokosi 1994). Near-bed fluctuations behave similarly to bed-generated turbulence found in laboratory settings and generate a well-mixed zone near the bed during flood tides (Shiono and West 1987). In contrast, shear-generated turbulent behavior is observed during ebb tides (Shiono and West 1987). These studies illuminate some important turbulent characteristics of small estuaries, and Trevethan and Chanson (2009) call for further study from a hydrodynamics standpoint, as there can be significant variability both among and within these small estuaries.

1.2. Objectives

The objective of the current study is to quantify the flow and turbulence characteristics in the intertidal zone at six sites on the coast of Georgia, USA. The data consist of time records of velocity for a period of one tidal cycle. Data were collected simultaneously at three or four sites, facilitating spatial comparisons. Data were collected at the same site for a series of days, facilitating a temporal comparison. A primary objective of the data analysis is to separate the wave and turbulence components of the fluctuating velocity. We also discuss how the flow and turbulence characteristics provide insight to chemical cue transport and success of knobbed whelk and blue crab predators at these sites.

2. Materials and Methods

2.1. Data Collection

Time sequences of velocity were collected at intertidal sites located in the Skidaway, Wilmington, Herb, and Moon Rivers as well as at Dead Man's Hammock and House Creek in May 2007 (see Figure 1). The sites exhibit extended periods of tidally-driven unidirectional flow. The sites are bordered by marsh grass, *Spartina alterniflora*, have average salinity in the range 20-28 ppt, experience a tidal range of 2 to 3 m, and receive small levels of freshwater inflow (Smee et al. 2010). Substrates primarily consist of fine-grained sand and mud. The sites were generally located 10 to 20 meters from oyster, *Crassostrea virginica*, reefs. Exceptions were the Skidaway River and Wilmington River sites, which were located at larger distances due to the minimal oyster reefs presence.

Acoustic Doppler velocimeters (ADVs) (NortekUSA Vector) were placed simultaneously at up to four sites for data collection. ADVs recorded three components of velocity, signal-to-noise ratio, correlation coefficient for each sensor, and pressure. ADVs were mounted such that the x-direction was roughly parallel to the mean flow direction, and the direction upwards from the bed corresponds to positive z-component velocity. Data were collected at 16 Hz for 5 minute bursts with 10 minute intervals between bursts. The ADV sampling volume center was located approximately 0.18 m above the substrate and at the mean lower-low water (MLLW) contour. The probe placement is consistent with our goal to quantify the flow and turbulence

characteristics at locations that predators (blue crabs and knobbed whelks) inhabit. During data processing, the *x*- and *y*-direction velocity components were rotated to maximize the magnitude of the *x*-direction velocity within each burst. Additional rotation was performed to ensure that the rotated *x*-direction velocity component is positive for flood tide and negative for ebb tide. ADVs were deployed for a minimum of one tidal cycle. See Table 1 for more information about the individual data sets. The DMH (side) data set collected on 5/16/07 was obtained using a side-mounted ADV.

2.2. Data Analysis

Regarding notation, overbar notation is used to indicate averaging within a burst of data. The $\langle\ \rangle$ notation indicates ensemble averaging over the sequence of burst-averaged values covering one tidal cycle (i.e., the average for one tidal cycle).

2.2.1. Basic Filtering of Data

Velocity data were first evaluated by computing the mean values of the three correlation coefficients (provided for each sample in the ADV data) for each burst. The entire burst was discarded if the mean value of any correlation coefficient was below 70%. Typically, poor correlation coefficient values corresponded to bursts collected while the probe was exposed to the atmosphere at low tides. Additionally, any burst with a string of 500 consecutive points (31.25 seconds out of 5 minutes total) having a mean correlation coefficient below 70% was also excluded, to account for bursts with partial probe exposure.

2.2.2. Phase Filtering

Erroneous “spikes” occur in ADV data due to aliasing of the Doppler signal, resulting in erroneous data that still may possess good correlation coefficient and signal-to-noise ratio. Individual velocity measurement filtering was composed of two components: spike detection and spike replacement. For spike detection, individual velocity measurements are assumed to behave as *n* independent, identically distributed, standard, normal random variables (Goring and Nikora

2002). Data points were flagged when the first and second order differencing estimates indicate that a non-physical spike has occurred based on the universal threshold for normal random variables (Goring and Nikora 2002). Table 1 reports the percentage of samples flagged for each set, which was below 3% for all cases. For spike replacement, erroneous velocity samples were replaced by a polynomial best fit at the velocity component level. A third-order polynomial fit was used, employing 12 points on either side of the identified spike, with an expanded range used in the presence of nearby spikes.

2.2.3. Removal of Wave Energy

Turbulent measurements are more difficult to accurately obtain in aquatic systems in the presence of waves. Grant et al. (1984) identified the potential for wave fluctuations contributing to apparent turbulent fluctuations, which can occur if sensors are improperly aligned with the principal axes of the flow or if there is sloping bed geometry (also see Trowbridge 1998). The apparent wave contribution to turbulent quantities can result in inaccurate calculations that either over- or underestimate parameters due to wave fluctuations that should not be considered turbulent because of their low frequency periodicity.

This study uses the coherence of the velocity and pressure measurements to identify and remove wave contributions to the Reynolds shear stress and turbulent kinetic energy (TKE), two quantities that provide important information about the turbulent environment at each site. The study also assesses the importance of wave influence at each site.

Instantaneous velocity samples are decomposed into the following convention:

$$u = \overline{u} + \tilde{u} + u' \quad (1)$$

where $\overline{u}$ is the mean component, $\tilde{u}$ is the wave-induced component, and u' is the turbulent fluctuation. Computing the Reynolds shear stress through Reynolds averaging of the velocity components yields:

$$\frac{\tau}{\rho} = \overline{\tilde{u}\tilde{w}} + \overline{\tilde{u}w'} + \overline{u'\tilde{w}} + \overline{u'w'} \quad (2)$$

Ideally, the first three terms of Equation (2) can be neglected. However, instrument uncertainty or sloping bed geometry yields $\overline{\tilde{u}\tilde{w}} \neq 0$, which artificially inflates the estimate of the Reynolds shear stress (Trowbridge 1998).

The objective of the analysis procedure described below is to estimate the normal and shear Reynolds stress components based on the time record of a single probe. The method is described in detail for the Reynolds shear stress and the normal stresses are calculated in an analogous manner (and subsequently combined to report the TKE). Rising or falling trends (typically due to the tide) in the velocity and pressure (5 minute) time records are removed by performing a linear trend removal (Bendat and Piersol 2010). The mean value is also subtracted from the records, thus the notation below implies that the mean component of each record is zero. Following the method of Benilov and Filyushkin (1970), the coherence function is calculated for the u velocity component and the pressure, *p*, as a function of frequency:

$$\gamma^2(\omega) = \frac{S_{up}(\omega) S_{up}^*(\omega)}{S_{uu}(\omega) S_{pp}(\omega)} \qquad (3)$$

where S_{up} is the cross-spectral density (CSD) of *u* and *p*, S_{uu} and S_{pp} are the respective power spectral density (PSD) functions, ω is frequency, and * indicates the complex conjugate.

Assuming that the coherent signal between the pressure and velocity measurement is due to waves, the power spectral density (PSD) for the turbulence portion of the signal is obtained by:

$$S_{u'u'}(\omega) = \left[1 - \gamma^2(\omega)\right] S_{uu}(\omega) \qquad (4)$$

The magnitude of the turbulent velocity fluctuation, $\left|U_j'\right|$, is then calculated based on the power spectral density for each discrete frequency via:

$$S_{u'u'j} = \frac{1}{d\omega}\left|U_j'\right|^2 \qquad (5)$$

where the subscript *j* indicates the discrete frequency value, and the capital case notation indicates that the velocity is represented in the frequency domain compared to the lower case notation corresponding to the time domain. The procedure is repeated based on the coherence

between the w velocity component and the pressure to yield $\left|W_j'\right|$. In this manner, the magnitude of each velocity component is adjusted by the coherence of the respective velocity component with the pressure signal.

The phase of the velocity components must be incorporated with the adjusted velocity fluctuation magnitude to calculate the Reynolds shear stress. The Fourier coefficients of the respective velocity components can be expressed in phasor notation:

$$U_j = \left|U_j\right| e^{i\angle U_j}, \quad W_j = \left|W_j\right| e^{i\angle W_j} \tag{6}$$

with the phase of each defined as:

$$\angle U_j = \arctan\left[\frac{\mathrm{Im}\left(U_j\right)}{\mathrm{Re}\left(U_j\right)}\right], \quad \angle W_j = \arctan\left[\frac{\mathrm{Im}\left(W_j\right)}{\mathrm{Re}\left(W_j\right)}\right] \tag{7}$$

The CSD can then be expressed as:

$$U_j^* W_j = \left|U_j\right|\left|W_j\right| e^{i\left(\angle W_j - \angle U_j\right)} = \left|U_j\right|\left|W_j\right|\left(\cos\left(\angle W_j - \angle U_j\right) - i\sin\left(\angle W_j - \angle U_j\right)\right) \tag{8}$$

The imaginary part of the CSD may be neglected in the summation over the two-sided spectral domain. Hence, the Reynolds shear stress is given by:

$$\overline{u'w'} = \sum_j U_j'^* W_j' = \sum_j \left|U_j'\right|\left|W_j'\right| \cos\left(\angle W_j - \angle U_j\right) \tag{9}$$

where $\left|U_j'\right|$ and $\left|W_j'\right|$ are calculated via Equation (5) and $\angle U_j$ and $\angle W_j$ are calculated via Equation (7). As a final step, the wave portion of the covariance is calculated by difference:

$$\overline{\tilde{u}\tilde{w}} = \overline{uw} - \overline{u'w'} \tag{10}$$

As mentioned above, the normal Reynolds stresses are calculated in an analogous manner, although the calculation is more streamlined since the phase difference in Equation (9) is zero for the normal stresses. Summing the three normal stresses yields the TKE:

$$TKE = \frac{1}{2}\left(\overline{u'u'} + \overline{v'v'} + \overline{w'w'}\right) \tag{11}$$

Turbulence intensity (TI) is calculated by normalizing the TKE via the mean velocities:

$$TI = 100 \times \frac{\sqrt{2TKE}}{\sqrt{\overline{u}^2 + \overline{v}^2 + \overline{w}^2}} \quad (12)$$

3. Results

3.1. Wave Removal

The results of the wave removal procedure can be seen in Table 2. The wave contribution to TKE or Reynolds shear stress was in the range of 13 to 30% of the total measured value for the majority of data sets. For the DMHside16 and DHM16 data sets, however, the wave contribution to TKE and Reynolds shear stress accounted for a larger fraction of the measured value (28 – 56%). The Dead Man's Hammock measurement site is more directly exposed to Wassaw Sound and the Atlantic Ocean (Figure 1) suggesting larger wave exposure, which is in accordance with visual observations. The greater propensity for wave action at this site is consistent with the larger contribution of wave motion relative to the other locations.

3.2. Flow Measurements on 5/14/07

This section presents example burst-averaged records collected on 5/14/07. Burst-averaged quantities for each set are computed for the first full tidal cycle, defined as a period roughly half of a day in length, in which data quality parameters indicated the probe was submerged. Two flow regimes are usually apparent in each set. The first period of the time series occurs during the flood tide, whereas the second period corresponds to the ebb tide. These examples are representative of the all of the sets, and similar results are presented for the other collection days in Berry (2009).

3.2.1. Wilmington14 Data Set

Figure 2 contains the records for the Wilmington14 data set. The burst-averaged horizontal velocity is larger in magnitude during the flood tide, with a maximum of 5.08×10^{-1} m/s at 133.71 year-days and a maximum negative value of -3.40×10^{-1} m/s at 133.93 year-days

($1.02 \times 10^{-1} \pm 3.23 \times 10^{-1}$ m/s [mean ± standard deviation], note the mean value does not match the mean of the absolute value of velocity reported in Table 3). The burst-averaged vertical velocity is positive for the flood tide and changes sign following high tide around 133.83 year-days. The within burst variability is large for the vertical velocity as indicated by the size of the error bars. Both TKE and Reynolds shear stress have maximum absolute values during the flood tide around 133.75 year-days. A local maximum for TKE and the magnitude of the Reynolds shear stress is also observed during the ebb tide around 133.93 year-days.

3.2.2. Skidaway14 Data Set

Figure 3 contains the records for the Skidaway14 data set. The burst-averaged values of horizontal velocity ($0.31 \times 10^{-1} \pm 1.45 \times 10^{-1}$ m/s [mean ± standard deviation]) exhibit unusual "lull periods". For instance, $\bar{u}$ for the Skidaway14 set is close to zero around 133.73 year-days, during which time the $\bar{u}$ velocity in the Wilmington14 data set (Figure 2) is at a maximum value (characteristic of a flood tide). A similar phenomenon is observed around 133.93 year-days. This observation is explained by the fact that the Skidaway River site has tidal influence from both Wassaw Sound and Ossabaw Sound (located to the South of the map in Figure 1). Under certain conditions the tidal flows may collide at the Skidaway River site and create an apparent "lull period", as we observe in this example. The burst-averaged vertical velocity ($-5.18 \times 10^{-3} \pm 5.82 \times 10^{-3}$ m/s [mean ± standard deviation]) is small throughout the record. TKE for the Skidaway14 set peaks from 133.80 to 133.87 year-days, which corresponds to an elevated period of $\bar{u}$ velocity in the set. Another period with elevated TKE is observed around 134.02 year-days, which again corresponds to a period of large magnitude for $\bar{u}$. The periods of minimum TKE value around 133.73 and 133.93 year-days correspond roughly with the "lull periods". The burst-averaged value of the Reynolds shear stress is small and varies minimally during the record.

3.2.3. Moon14 Data Set

Figure 4 contains the records for the Moon14 data set. The record exhibits a flood-ebb tidal cycle of burst-averaged horizontal velocity ($-0.26 \times 10^{-1} \pm 2.94 \times 10^{-1}$ m/s [mean ± standard

deviation]), with high tide occurring around 133.84 year-days. The values of burst-averaged horizontal velocity are positive for the flood tide (maximum of 3.77×10^{-1} m/s at 133.71 year-days) and negative for the ebb tide (maximum negative value of -4.65×10^{-1} m/s at 133.92 year-days). The burst-averaged vertical velocity values are positive for the flood tide with a maximum of 2.58×10^{-2} m/s at 133.71 year-days (matching the time of maximum $\bar{u}$ velocity) and negative for the ebb tide with a maximum negative value of -2.34×10^{-2} m/s at 133.87 year-days. TKE is largest during the ebb tide around 133.93 year-days, concurrent with the maximum negative value of $\bar{u}$. The magnitude of the Reynolds shear stress also is largest during the periods of largest velocity, although the variation during the tidal cycle is small.

3.3. Set Comparisons

Characteristics for each data set are presented in Tables 3 and 4 via the ensemble average of the burst-averaged values. The $\langle|\bar{u}|\rangle$ values are in the range of 0.05 – 0.32 m/s. The absolute value of the burst-averaged horizontal velocity is reported because the relevant parameter from an ecological perspective is the magnitude of the fluid motion and the flow changes direction during the tidal cycle. The DMHside16 and DMH16 data sets stand out due to their relatively small values of $\langle|\bar{u}|\rangle$. For the data collected on different days at the same site, we expected the ensemble average of the burst-averaged values of horizontal velocity, $\langle|\bar{u}|\rangle$, to generally correlate with the tidal range (also shown in Table 3). The data from Wilmington River site follow the expected correlation, but the data from the Skidaway River and Herb River sites do not. The Skidaway14 set data may be confounded by the colliding tidal flows that create the "lull periods" in Figure 3. This comparison also may be adversely influenced by small differences in probe placement on different days at the same site. The $\langle\bar{w}\rangle$ values are negative, which indicates an ensemble-averaged downward flow, in all sets except Moon14. The magnitude is one to two orders of magnitude smaller than the horizontal velocity component. For all sets, the $\langle\bar{v}\rangle$ values are multiple orders of magnitude smaller than $\langle|\bar{u}|\rangle$ due to the data rotation (and are not shown in Table 3).

TKE is largest for the Wilmington14 (3.03×10^{-3} m^2/s^2) and House16 (2.62×10^{-3} m^2/s^2) sets (Table 4). Of these two sets, the Wilmington14 set (Figure 2) shows the largest tidal variability. The Wilmington14 set also has the largest deviation from the ensemble average and largest within-burst variability for the vertical velocity. TKE is smallest for the Skidaway14 and DMH16 sets (0.48×10^{-3} m^2/s^2 and 0.49×10^{-3} m^2/s^2, respectively). The DMH16 set has the largest TI (60.5%), but it has one of the smaller TKE values. Conversely, while the House16 set has among the largest TKE, the TI (22.5%) is much smaller than that of the DMH16 set. The variation of the absolute value of burst-averaged Reynolds shear stresses among the sets generally followed the pattern for the TKE. As with the horizontal burst-averaged velocity, the ensemble average of the absolute value of the Reynolds shear stress is reported due to the sign change during the tidal cycle.

Tidal influences within the estuary are indicated by observations that turbulent characteristics often reach maximum absolute values during the flood or ebb tides, and sites generally were less energetic near high and low tide when the flow rate is at a minimum. However, some sets (Skidaway14, for example) did not show a clear tidal response, further illustrating the spatial and temporal variability observed in the study. Similar variability in turbulence parameters has been seen in another study in a small estuary by Trevethan and Chanson (2009), where variability was primarily attributed to small water depths, among other factors.

3.3.1. Spatial Comparison

Comparison of the three sets collected on 5/14/2007 is presented in Figure 5. Similar comparisons for the other collection days are presented in Berry (2009). Of the 5/14/2007 sets, the Wilmington14 set exhibits the most tidal influence, as $\overline{u}$, $\overline{w}$, TKE, and Reynolds shear stress vary in direct correspondence with the flood and ebb tides (Figure 2). The variation of *w* in the Wilmington14 set both within-burst and among burst-averaged values is the largest of any set collected on any day (Figure 2). The large mean velocities of the Wilmington14 set ($\langle|\overline{u}|\rangle$ of 3.19×10^{-1} m/s, for example) result in a TI value that is among the smallest of all sets. The mean absolute value of the burst-averaged Reynolds shear stress is largest for the Wilmington14 set (

$\left\langle \left| \overline{u'w'} \right| \right\rangle$ = 49.0 × 10^{-5} m^2/s^2). The Moon14 set reveals tidal behavior in the records of $\bar{u}$ and $\bar{w}$, but tidal response in TKE and Reynolds shear stress is predominately seen in the ebb tide, if at all (Figure 4). The mean of the burst-averaged values of $|\bar{u}|$, TKE, and Reynolds shear stress for the Skidaway14 set are smaller than the corresponding quantities for the data collected at other sites (Figure 5). This is also observed in the data collected on 5/19/07 (Tables 3 and 4). Of particular note are the "lull periods"' that occur around 133.73 and 133.93 year-days (see Figure 3). These are periods in which the other sets exhibit maximum values of the measured quantities, but the Skidaway14 mean velocity and turbulence values are depressed and exhibit small within-burst variability in *u* and *w* (see Figure 3). Due to the small mean velocity, the turbulence intensity has the largest set mean value for the Skidaway14 set among the sets on 5/14/2007 (Figure 5). Among these sets, $\left\langle |\bar{u}| \right\rangle$, TKE, and $\left\langle \left| \overline{u'w'} \right| \right\rangle$ vary in lockstep (i.e., a large value of $\left\langle |\bar{u}| \right\rangle$ also indicates a large value of TKE and $\left\langle \left| \overline{u'w'} \right| \right\rangle$), whereas TI follows a converse trend (Figure 5). These relationships also are evident in the data collected on 5/16/07, whereas the relationships among the sets on 5/19/07 are not as clear due to the similar values of $\left\langle |\bar{u}| \right\rangle$ (Table 3).

3.3.2. Temporal Comparison

Data were collected at the Skidaway River site on 5/14/2007, 5/19/2007, and 5/20/2007. Comparison of the ensemble average of the burst-averaged values is provided in Figure 6 for the three days. Variation is observed among the sets collected on different days at the same site, likely due to different tidal height, wind, and other conditions including slightly different probe placement. The unusual $\bar{u}$ velocity "lull periods" exhibited in the Skidaway14 data set (Figure 3) were not seen in the Skidaway19 or Skidaway20 data sets (records not shown here). On both occasions (5/14/2007 and 5/19/2007) when other sites were concurrently monitored, the ensemble averaged TKE value for the Skidaway River sets was substantially smaller than that for the other sites (see Table 4). In contrast, the mean value of TKE for the Skidaway20 set is larger

and similar to that measured at other sites on different days. The same trend is not exhibited for $\overline{u}$, $\overline{w}$, or Reynolds shear stress.

3.3.3. Overall Comparison

As shown in Figure 7, there is an apparent direct relationship between $\langle|\overline{u}|\rangle$ and $\langle TKE\rangle$ and between $\langle|\overline{u}|\rangle$ and $\langle|\overline{u'w'}|\rangle$. Figure 7 suggests possible direct relationships, and a linear regression yields statistically significant trend lines, as shown. Turbulence intensity ($\langle TI\rangle$), in contrast, decreases with increasing $\langle|\overline{u}|\rangle$, which is expected since the mean velocity appears in the denominator of the definition of TI. Further, there is an apparent direct relationship between the turbulence quantities, $\langle|\overline{u'w'}|\rangle$ and $\langle TKE\rangle$, with a statistically significant trend line revealed by linear regression (Figure 7). Thus, although it is difficult to see trends in the site-to-site comparisons for simultaneous records and in the within sites comparison among different days, there appears to be a universal connection between the horizontal velocity magnitude and the turbulence quantities.

4. Discussion

4.1. Phase Filtering

This study serves to illustrate the importance of rigorous consideration of data quality when using data collected from ADV probes. Whereas no more than 3% of individual velocity measurements were flagged as spikes (Table 1), these points are exclusively extreme values. The data identified as spikes were found to alter the burst-averaged values of TKE because the extreme values disproportionately contribute to elevated TKE measurements due to their relatively large magnitudes. These findings are consistent with prior observations regarding the importance of advanced data filtering when working with ADV data (see Goring and Nikora 2002 and Chanson et al. 2008).

4.2. Wave Removal

The separation of wave energy in this study addresses the magnitude of the wave contribution to the apparent TKE and Reynolds shear stress measurement at the study sites and serves to demonstrate the importance of considering wave contributions in studies where waves may be present. Despite prior observations of relatively small surface wave activity (Ferner et al. 2009), the current data demonstrate substantial (i.e., greater than 15%) wave contributions to both TKE and Reynolds shear stress in some regions within the Wassaw Sound ecosystem (see Table 2). Wave-related fluctuations accounted for as much as 56% of the measured TKE (DMH16 set) and as much as 44% of the measure Reynolds shear stress (also DMH16 set) in the ensemble averaged data, and the minimum wave contribution was 15% and 13%, respectively, for TKE and Reynolds shear stress. It is therefore clearly important to address the wave contribution when characterizing field sites in order to gain a better understanding of the sources of velocity fluctuations within the system. This is particularly true in shallow habitats, where wind waves may have a larger impact, and in small estuarine systems, where minimal prior work has been done to describe the turbulent characteristics.

We also extensively tested the wave-turbulence decomposition method described by Bricker and Monismith (2007). The method consists of identifying the frequency range corresponding to wave motion in the PSD and calculating the wave component via the difference between the PSD and a linear fit of the PSD data at higher and lower frequencies. The difference is used to estimate the velocity component associated with the wave motion, $\left|\tilde{U}_j\right|$, which is then used to calculate $\overline{\tilde{u}\tilde{w}}$ via an equation analogous to Equation (9). We found that this method struggled to faithfully separate the wave component for data from our shallow water environment. Consistently, Bricker et al. (2005) reported that, near the water surface, the Bricker and Monismith (2007) method yielded Reynolds stress results that were an order of magnitude different (smaller) than the results from other decomposition methods. For the current data, we found that the frequency range corresponding to wave motion changed among burst sets, which required manual tuning of the range. The algorithm output is sensitive to the identified range, which adds subjectivity to the analysis. Further, we observed that the CSD, in certain sets, contained a band of frequencies with large positive values and a second band with large negative values. These bands effectively balance to yield a comparatively smaller value of

$\overline{uw}$. The effect of modifying a particular band of frequencies during this analysis is to disrupt the balance and yield values of $\overline{\tilde{u}\tilde{w}}$ (and $\overline{u'w'}$) that are two or even three orders of magnitude greater than the measured value, $\overline{uw}$. Overall, the Bricker and Monismith (2007) method yielded results for TKE that were generally consistent with the results of the analysis based on the method described in the Discussion section. Specifically, the percentage of TKE due to wave component was in the range of 12 to 57% for the Bricker and Monismith (2007) method (reported in Berry 2009) in comparison to the range of 15 to 56% shown in Table 2. In contrast, the Bricker and Monismith (2007) analysis frequently yielded results for the Reynolds shear stress that are difficult to physically reconcile due to $\overline{u'w'}$ switching sign compared to $\overline{uw}$ and $\overline{u'w'}$ being orders of magnitude greater than $\overline{uw}$ (Berry 2009). We decided not to employ the method of Bricker and Monismith (2007) for our data analyses given the less subjective and more reliable nature of the method described in the Discussion section.

4.3. Set Comparisons

Because data were collected from multiple sites simultaneously, it is possible to compare the turbulent characteristics under the same large-scale environmental conditions. For the sets collected on 5/14/2007 (Wilmington14, Skidaway14, and Moon14), there is great variability. Tidal influence is seen in the Wilmington14 and Moon14 sets, whereas the Skidaway14 site exhibited less tidal influence, likely due to colliding tidal flows, and yielded smaller magnitudes and smaller variability for $\overline{u}$, $\overline{w}$, TKE, and Reynolds shear stress. The findings illustrate the importance of factors that act on scales smaller than the primary tidal forcing within the estuary. Whereas sites monitored simultaneously were subjected to identical estuary-scale tidal behavior, significant differences in turbulent characteristics were observed. Local bed geometry, local vegetation, biogenic structure (bivalve reefs, for example), and flow influx from tributaries or subsurface sources are all factors that could alter turbulent properties at the cross-site scales monitored in this experiment (e.g., Finelli 2000, Dade et al. 2001, van Duren et al. 2006, Widdows et al. 2008, Folkard and Gascoigne 2009, Jamieson et al. 2010).

The relatively short periods of observation reported herein provide only a limited characterization of the flow and turbulence. The variation among sets collected on different days

at the same site also demonstrates the temporal variability of flow and turbulence characteristics. The data suggest that to adequately quantify the flow characteristics at a site and to assess the variability in these characteristics, data should be collected over a period exceeding several days in order to capture temporal variation, in particular spring/neap and seasonal variation.

Despite the noted spatial and temporal variability, Figure 7 suggests a linear relationship among $\langle|\bar{u}|\rangle$, $\langle TKE\rangle$, and $\langle|\overline{u'w'}|\rangle$ across all sets. Potentially, this is a useful observation since in ecological studies it is not always practical or possible to fully characterize the turbulence characteristics. Hence, a measure of one quantity may provide, with a suitable calibration, additional insight to the hydrodynamic conditions.

4.4. Ecological Consequences

A number of previous laboratory studies have examined how hydrodynamic regime affects odor-mediated benthic foraging, and it is instructive to compare the flow conditions employed in those studies to the field conditions reported here. Zimmer and Zimmer (2008) explain the importance of correctly reproducing field environmental conditions in laboratory experiments in order for the laboratory results to have ecological significance. Laboratory studies that report flow and turbulence quantities generally employ conditions within the range of parameters shown in Figure 7 (e.g., Weissburg and Zimmer-Faust 1993, Moore and Grills 1999, Ferner and Weissburg 2005, Jackson et al. 2007). Rahman and Webster (2005), for instance, report a mean channel velocity of 0.05 m/s, TKE values in the range of 0.05×10^{-3} to 0.1×10^{-3} m^2/s^2, and $\overline{u'w'}$ in the range of 1×10^{-5} to 3×10^{-5} m^2/s^2. Although these data are consistent with the conditions summarized in Figure 7, the lab conditions are clearly to the lower end of the range for mean flow and turbulence. Laboratory experiments predominately report mean velocities of less than 0.1 m/s (exceptions include Weissburg and Zimmer-Faust 1993 [maximum channel velocity of 0.144 m/s], Ferner and Weissburg 2005 [0.15 m/s], and Smee and Weissburg 2006 [0.11 m/s]). Employing conditions at the lower end of the field range is not surprising since the studies are often performed in low velocity flumes under highly-controlled conditions (for experimental repeatability). Many of these studies are geared towards examining basic mechanisms of odor-mediated foraging and therefore use conditions permissive of

behavioral response. The turbulence quantities also appear to be smaller in the laboratory flows, presumably due to the controlled conditions compared to the field. Flume environments do not replicate all of the mechanisms by which turbulence is generated in field conditions and use uniform substrate conditions and topography. However, some studies use different substrate types (e.g. Weissburg and Zimmer-Faust 1993, Jackson et al. 2007) or other roughness elements (Ferner and Weissburg 2005) to enhance turbulence in specific velocity conditions. It is also important to note that the laboratory studies do not include the effects of waves, which the current study indicates is a potentially substantial contribution to the fluid motion and hence chemical transport. It may be possible to reproduce a wider range of flow and turbulence conditions in controlled field trials of benthic foraging. Finelli et al. (1999, 2000), for instance, report a wide range of flow and turbulence conditions that span ranges similar to that reported in Figure 7.

The overall findings of the study suggest that TKE, Reynolds shear stress, and TI vary substantially within the Wassaw Sound ecosystem, both spatially and temporally. Spatial and temporal variability demand extensive sampling, particularly in time, to make reliable generalizations about hydrodynamic differences between regions or even adjacent sites in this estuary. Previous observations indicate that knobbed whelk predation is dominant at the Dead Man's Hammock and House Creek sites, whereas blue crab predation dominates at the Skidaway River, Wilmington River, Herb River, and Moon River sites (Ferner et al. 2009 and Smee et al. 2010). One potential explanation is that these patterns reflect, at least partially, the chemosensory foraging strategies of each species. Knobbed whelks appear much more proficient at foraging in conditions that are detrimental to blue crab foraging and hence, may select or be confined to more turbulent environments where they enjoy an advantage (Ferner et al. 2009). Our data are not inconsistent with this notion; some of the largest TKE and TI values come from sites where knobbed whelks are the dominant predator (e.g. Dead Man’s Hammock and House Creek). However, the data in the current study do not reveal common mean flow, TKE, TI, and Reynolds stress characteristics at these grouped sites, and the lack of consistent simultaneous sampling across these sites hinders more accurate comparisons. Although prior studies have suggested TI (see Robson et al. 1999, Smee et al. 2008, Ferner et al. 2009) and root-mean-square of velocity fluctuations (see Smee and Weissburg 2006, Smee et al. 2010) to be

useful parameters for gauging the impacts of turbulent flow on ecological processes, other characteristics should be considered. The Reynolds shear stress, for instance, is a critical component in defining the boundary layer where benthic predator and prey organisms are found, hence this appears to be a relevant parameter to define the physical environment. As revealed by our analysis, several parameters are correlated and statistical regressions explain 60 to 80% of the variance. It is possible that a small number of variables may be sufficient to characterize the environment, and/or that simple velocity measures may provide a rough guide to turbulence statistics. It is important to note, however, that mean velocity and turbulence seem to exert independent effects on chemosensory foraging in blue crabs (Smee et al. 2010). Further, it is important to realize that organism behavioral reaction may be dependent on (rare) large instantaneous fluctuations rather than average values (e.g., Crimaldi et al. 2002). Additional work is needed to determine whether correlations we observe are robust in other environments and if other parameters that are important from a flow characterization standpoint also are ecologically significant.

4.5. Future Directions

The ease of use and robust features of ADV probes likely means they will continue to be commonly used for collecting point velocity time records in the field. It is therefore important to continue to improve methods for addressing data quality and analysis accuracy. The phase filtration method and wave component separation technique used in this study are essential aspects in quantitative description of the flow and turbulence characteristics in tidal channels of relatively small estuaries. The wave separation technique presented is particularly necessary for isolating the component of the velocity fluctuations that is truly associated with turbulence. The mean flow and turbulence data presented in this study provide important information about the environment that aquatic organisms experience in this habitat. The significant temporal variability suggests long term flow records are required to characterize turbulent properties, and that across site comparisons are most accurate when these locations are sampled simultaneously. The high degree of spatial variability means spatial sampling at different scales will be necessary to adequately identify regions where flow properties are roughly similar. This is an important consideration for ecological studies attempting to address biological-physical linkages, such as

the role of the flow environment in modulating chemosensory foraging. Proper characterization and interpretation of near-bed turbulence data are also important for many other processes such as sediment resuspension and transport, particle flux to suspension feeders, porewater flushing, and nutrient uptake by benthic algae (e.g., Boudreau and Jørgensen 2001). The observed variability, both spatial and temporal, suggests that we need significantly more data in order to reasonably assess conditions among habitat sites and changes at daily, monthly and seasonal scales.

Acknowledgements The authors thank the National Science Foundation for financial support under grant OCE-0424673 to M.J.W. and D.R.W. and for NSF IGERT fellowships awarded to W.A.B. and M.L.W. National Science Foundation grants OCE-0648433 and OCE-0821215 to D.L.S. also supported this work. Further support was provided by the U.S. Dept. of Interior/Geological Survey via the State Water Resources Research Program. The authors additionally thank Dr. Kevin Haas for helpful discussion.

References

Bendat JS, Piersol AG (2010) Random data: Analysis and measurement procedures. 4th Edition. John Wiley and Sons, Hoboken, N.J.

Benilov AY, Filyushkin BN (1970) Application of methods of linear filtration to an analysis of fluctuations in the surface layer of the sea. Izv Atmospheric and Ocean Physics 6:810-819

Berry WA (2009) A hydrodynamic characterization of tidal ecosystems with respect to predation. M.S. thesis, Georgia Institute of Technology, USA, 114 pp

Boudreau BP, Jørgensen, BB (eds) (2001) The benthic boundary layer: Transport processes and biogeochemistry. Oxford University Press, New York

Bricker JD, Inagaki S, Monismith SG (2005) Bed drag coefficient variability under wind waves in a tidal estuary. Journal of Hydraulic Engineering 131:497-508

Bricker JD, Monismith SG (2007) Spectral wave-turbulence decomposition. Journal of Atmospheric and Oceanic Technology 24:1479-1487

Chanson H, Trevethan M, Aoki S (2008) Acoustic Doppler velocimetry (ADV) in small estuary: Field experience and signal post-processing. Flow Measurement and Instrumentation 19:307-313

Crimaldi JP, Thompson JK, Rosman JH, Lowe RJ, Koseff JR (2002) Hydrodynamics of larval settlement: The influence of turbulent stress events at potential recruitment sites. Limnology and Oceanography 47:1137-1151

Dade WB, Hogg AJ, Boudreau BP (2001) Physics of flow above the sediment-water interface. In: BP Boudreau and BB Jørgensen (eds) The benthic boundary layer: Transport processes and biogeochemistry. Oxford University Press, New York, pp. 4-43

Delavan SK, Webster DR (2011) Unsteadiness of bivalve clam jet flow according to environmental conditions. Aquatic Biology, in review

Folkard AM, Gascoigne JC (2009) Hydrodynamics of discontinuous mussel beds: Laboratory flume simulations. Journal of Sea Research 62:250-257

Ferner MC, Weissburg MJ (2005) Slow-moving predatory gastropods track prey odors in fast and turbulent flow. Journal of Experimental Biology 208:809-819

Ferner MC, Smee DL, Weissburg MJ (2009) Habitat complexity alters lethal and non-lethal olfactory interactions between predators and prey. Marine Ecology Progress Series 374:13-22

Finelli CM (2000) Velocity and concentration distributions in turbulent odor plumes in the presence of vegetation mimics: A flume study. Marine Ecology Progress Series 207:297-309

Finelli CM, Pentcheff ND, Zimmer-Faust RK, Wethey DS (1999) Odor transport in turbulent flows: Constraints on animal navigation. Limnology and Oceanography 44:1056-1071

Finelli CM, Pentcheff ND, Zimmer RK, Wethey DS (2000) Physical constraints on ecological processes: A field test of odor-mediated foraging. Ecology 81:784-797

Goring DG, Nikora VI (2002) Despiking acoustic Doppler velocimeter data. Journal of Hydraulic Engineering 128:117-126

Grant WD, Williams AJ, Glenn SM (1984) Bottom stress estimates and their prediction on the northern California continental shelf during CODE-1: The importance of wave-current interaction. Journal of Physical Oceanography 14:506-527

Jackson JL, Webster DR, Rahman S, Weissburg MJ (2007) Bed roughness effects on boundary-layer turbulence and consequences for odor tracking behavior of blue crabs (*Callinectes sapidus*). Limnology and Oceanography 52:1883-1897

Jamieson EC, Post G, Rennie CD (2010) Spatial variability of three-dimensional Reynolds stresses in a developing channel bend. Earth Surface Processes and Landforms 35:1029-1043

Kawanisi K, Yokosi S (1994) Mean and turbulence characteristics in a tidal river. Estuarine, Coastal and Shelf Science 38:447-469

Moore PA, Grills JL (1999) Chemical orientation to food by the crayfish *Orconectes rusticus*: influence of hydrodynamics. Animal Behaviour 58:953-963

Powers SP, Kittinger JN (2002) Hydrodynamic mediation of predator-prey interactions: differential patterns of prey susceptibility and predator success explained by variation in water flow. Journal of Experimental Marine Biology and Ecology 273:171-187

Rahman S, Webster DR (2005) The effect of bed roughness on scalar fluctuations in turbulent boundary layers. Experiments in Fluids 38:372-384

Robson BJ, Chester ET, Davis JA (1999) Manipulating the intensity of near-bed turbulence in rivers: Effects on benthic invertebrates. Freshwater Biology 42:645-653

Shiono K, West JR (1987) Turbulent perturbations of velocity in the Conwy Estuary. Estuarine, Coastal and Shelf Science 25:533-553

Smee DL, Weissburg MJ (2006) Clamming up: Environmental forces diminish the perceptive ability of bivalve prey. Ecology 87:1587-1598

Smee DL, Ferner MC, Weissburg MJ (2008) Alteration of sensory abilities regulates the spatial scale of nonlethal predator effects. Oecologia 156:399-409

Smee DL, Ferner MC, Weissburg MJ (2010) Hydrodynamic sensory stressors produce nonlinear predation patterns. Ecology 91:1391-1400

Trevethan M, Chanson H (2009) Turbulent mixing in a small estuary: Detailed measurements. Estuarine, Coastal and Shelf Science 81:191-200

Trevethan M, Chanson H, Brown R (2008) Turbulent measurements in a small subtropical estuary with semidiurnal tides. Journal of Hydraulic Engineering 134:1665-1670

Trowbridge JH (1998) On a technique for measurement of turbulent shear stress in the presence of surface waves. Journal of Atmospheric and Oceanic Technology 15:290-298

van Duren LA, Herman PMJ, Sandee AJJ, Heip CHR (2006) Effects of mussel filtering activity on boundary layer structure. Journal of Sea Research 55:3-14

Verney R, Brun-Cottan JC, Lafite R, Deloffre J, Taylor JA (2006) Tidally-induced shear stress variability above intertidal mudflats in the macrotidal Seine estuary. Estuaries and Coasts 29: 653-664

Voulgaris G, Meyers ST (2004) Temporal variability of hydrodynamics, sediment concentration and sediment settling velocity in a tidal creek. Continental Shelf Research 24:1659-1683

Webster DR, Weissburg MJ (2009) The hydrodynamics of chemical cues among aquatic organisms. Annual Review of Fluid Mechanics 41:73-90

Weissburg MJ, Ferner MC, Pisut DP, Smee DL (2002) Ecological consequences of chemically mediated prey perception. Journal of Chemical Ecology 28:1953-1970

Weissburg MJ, Zimmer-Faust RK (1993) Life and death in moving fluids: Hydrodynamic effects on chemosensory-mediated predation. Ecology 74:1428-1443

Widdows J, Pope ND, Brinsley MD (2008) Effect of *Spartina anglica* stems on near-bed hydrodynamics, sediment erodability and morphological changes on an intertidal mudflat. Marine Ecology Progress Series 362:45-57

Zimmer RK, Butman CA (2000) Chemical signaling processes in the marine environment. Biological Bulletin 198:168-187

Zimmer RK, Zimmer CA (2008) Dynamic scaling in chemical ecology. Journal of Chemical Ecology 34:822-836

Table 1. Summary of ADV data collection information for each data set. The last column reports the mean percentage of samples flagged by the phase filtration method and replaced by the polynomial fitting method described in the text.

Site	Data Set Name	Start Time	Mean % Flagged
Wilmington River	Wilmington14	5/14/2007 12:03:00	0.9
Skidaway River	Skidaway14	5/14/2007 12:05:00	2.4
Moon River	Moon14	5/14/2007 12:09:00	1.9
DMH (side)	DMHside16	5/16/2007 14:00:00	2.7
Herb River	Herb16	5/16/2007 14:00:00	2.1
DMH	DMH16	5/16/2007 14:00:00	2.3
House Creek	House16	5/16/2007 14:00:00	1.8
Herb River	Herb19	5/19/2007 19:00:00	2.4
Skidaway River	Skidaway19	5/19/2007 19:00:00	1.9
Wilmington River	Wilmington19	5/19/2007 19:00:00	2.4
Skidaway River	Skidaway20	5/20/2007 19:00:00	1.9

Table 2. Comparison of TKE and Reynolds shear stress before and after wave component removal. PF indicates result based on phase-filtered fluctuations, and WR indicates the value calculated after wave component removal. Note that the percentage due to wave component is calculated for each burst, then the ensemble is averaged to yield the reported value, hence the value does not correspond to the percentage of the ensemble-averaged values reported in the other columns.

Set Name	$\langle$TKE$\rangle$ PF $\times 10^{-3}$ (m^2/s^2)	$\langle$TKE$\rangle$ WR $\times 10^{-3}$ (m^2/s^2)	$\left\langle \begin{matrix}\%\text{ Due to Wave} \\ \text{Component}\end{matrix} \right\rangle$	$\langle \overline{u'w'} \rangle$ PF $\times 10^{-5}$ (m^2/s^2)	$\langle \overline{u'w'} \rangle$ WR $\times 10^{-5}$ (m^2/s^2)	$\left\langle \begin{matrix}\%\text{ Due to Wave} \\ \text{Component}\end{matrix} \right\rangle$
5/14/2007						
Wilmington14	3.62	3.03	17	40.2	33.6	17
Skidaway14	0.60	0.48	18	0.23	0.23	33
Moon14	1.50	1.21	17	4.18	3.04	26
5/16/2007						
DHMside16	1.90	1.06	47	6.25	4.28	28
Herb16	1.69	1.32	21	-1.22	-1.69	18
DMH16	1.12	0.49	56	1.55	0.46	44
House16	3.21	2.62	18	7.93	6.19	19
5/19/2007						
Herb19	1.38	1.17	15	4.56	3.31	17
Skidaway19	0.88	0.74	15	-5.16	-4.44	23
Wilmington19	1.34	1.13	16	17.1	14.35	13
5/20/2007						
Skidaway20	1.42	1.09	18	2.44	1.39	13

Table 3. Tidal range, set length, and set mean velocity data. The mean and standard deviation are computed based on the ensemble of burst-averaged values over the sequence covering one tidal cycle. The v component of velocity is near zero due to the data rotation described in Section 2.1.

Set Name	Tidal range (m)	Length (days)	$\lvert\overline{u}\rvert$ (m/s) $\times 10^{-1}$		$\overline{w}$ (m/s) $\times 10^{-3}$	
			mean	std dev	mean	std dev
5/14/2007						
Wilmington14	2.92	0.43	3.19	1.02	-9.54	36.6
Skidaway14		0.40	1.19	0.87	-5.18	5.82
Moon14		0.40	2.65	1.24	5.99	13.9
5/16/2007						
DHMside16	3.11	0.36	0.84	0.45	-4.26	5.15
Herb16		0.39	1.78	1.34	-13.8	5.80
DMH16		0.39	0.53	0.32	-3.47	1.64
House16		0.32	2.15	0.85	-16.9	5.28
5/19/2007						
Herb19	2.62	0.45	1.91	0.91	-9.96	4.17
Skidaway19		0.45	1.77	1.02	-5.89	3.38
Wilmington19		0.44	1.62	1.11	-12.4	9.39
5/20/2007						
Skidaway20	2.34	0.48	1.59	0.85	-9.44	10.3

Table 4. Set TKE, Turbulence Intensity (TI), and Reynolds shear stresses data. The mean and standard deviation are computed based on the ensemble of burst-averaged values over the sequence covering one tidal cycle.

Set Name	TKE (m^2/s^2) $\times 10^{-3}$		TI (%)		$\left\|\overline{u'w'}\right\|$ (m^2/s^2) $\times 10^{-5}$	
	mean	std dev	mean	std dev	mean	std dev
5/14/2007						
Wilmington14	3.03	1.35	14.0	1.9	49.0	41.9
Skidaway14	0.48	0.34	24.6	26.1	3.24	4.06
Moon14	1.21	0.68	13.3	13.0	13.4	8.75
5/16/2007						
DHMside16	1.06	1.55	40.4	29.9	8.26	7.20
Herb16	1.32	0.87	20.4	8.4	21.8	15.5
DMH16	0.49	0.35	60.5	86.5	3.02	2.78
House16	2.62	0.64	22.5	10.9	23.0	12.5
5/19/2007						
Herb19	1.17	0.46	31.1	62.7	13.7	7.54
Skidaway19	0.74	0.64	13.4	5.8	9.82	10.1
Wilmington19	1.13	0.49	34.0	33.2	18.1	13.9
5/20/2007						
Skidaway20	1.09	0.74	23.4	27.1	9.22	9.22

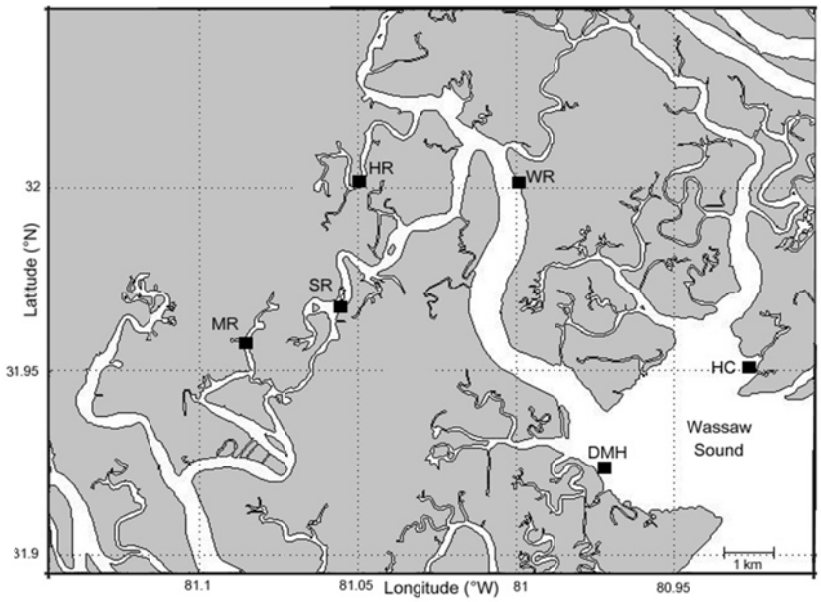

Figure 1. Map of field site locations. ADV measurements were taken at Herb River (HR), Wilmington River (WR), Skidaway River (SR), Moon River (MR), House Creek (HC) and Dead Man's Hammock (DMH).

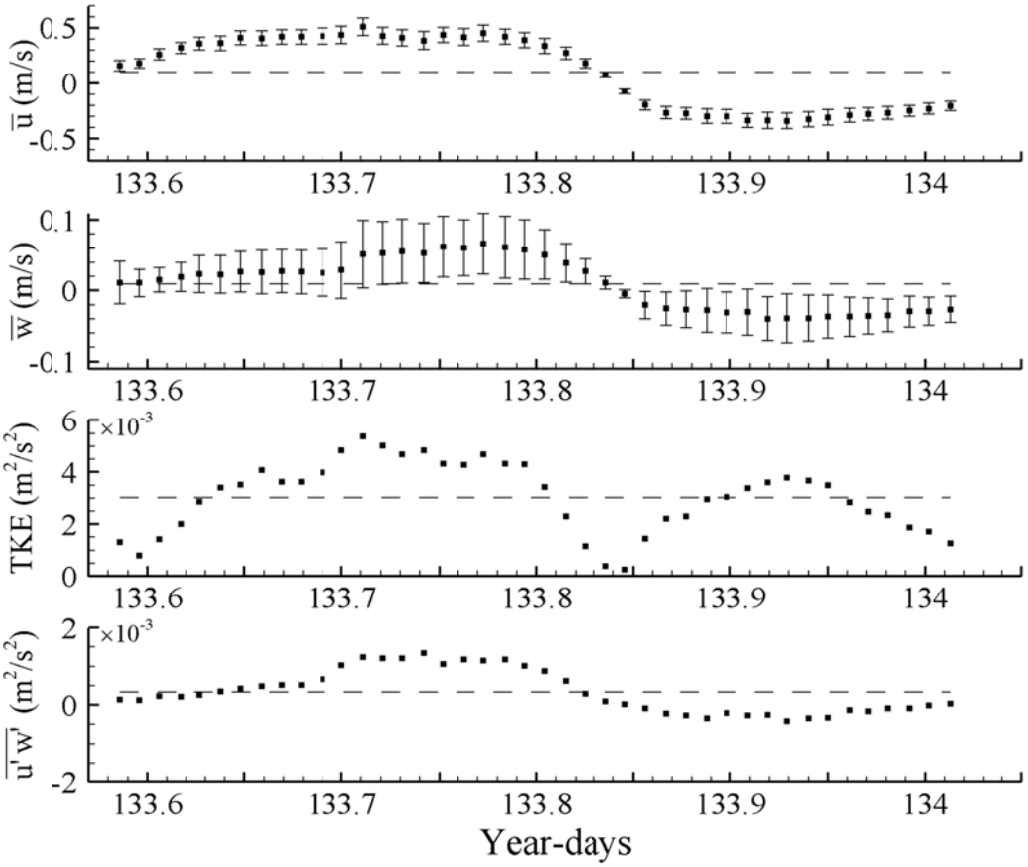

Figure 2. Burst-averaged records for Wilmington14 data set. The dashed line indicates the mean of the burst-averaged values. The error bars correspond to standard deviation of the variation within the burst.

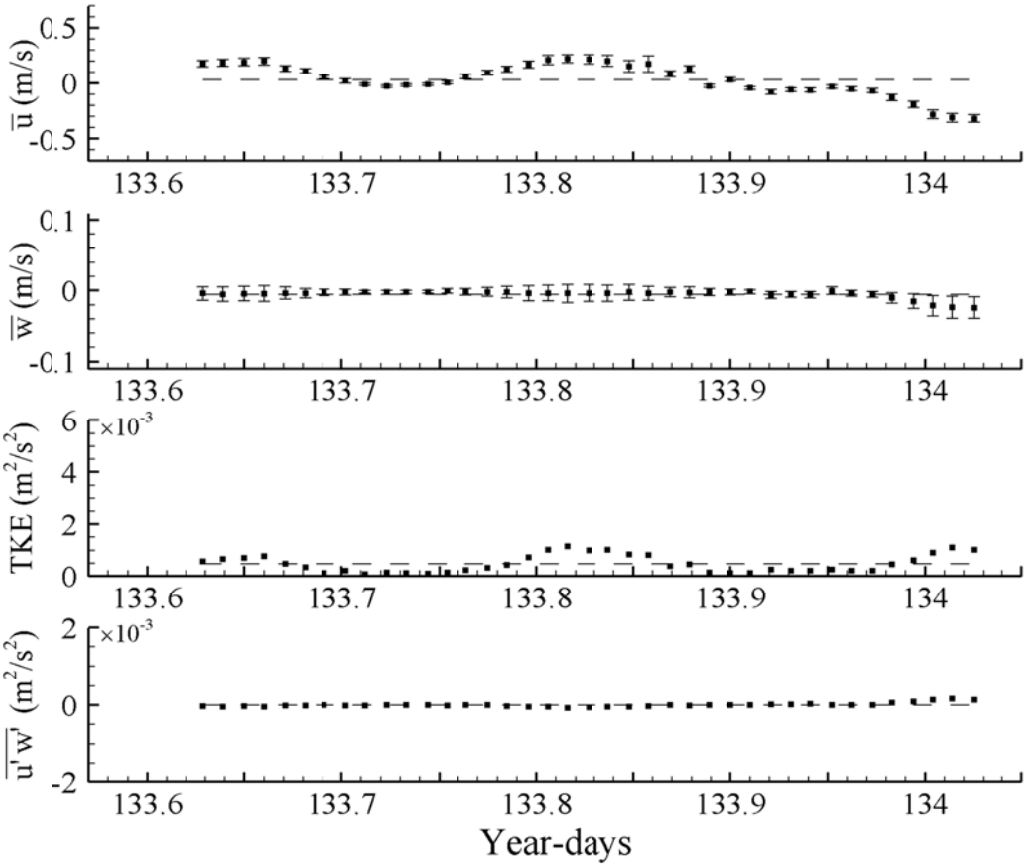

Figure 3. Burst-averaged records for Skidaway14 data set. The dashed line indicates the mean of the burst-averaged values. The error bars correspond to standard deviation of the variation within the burst.

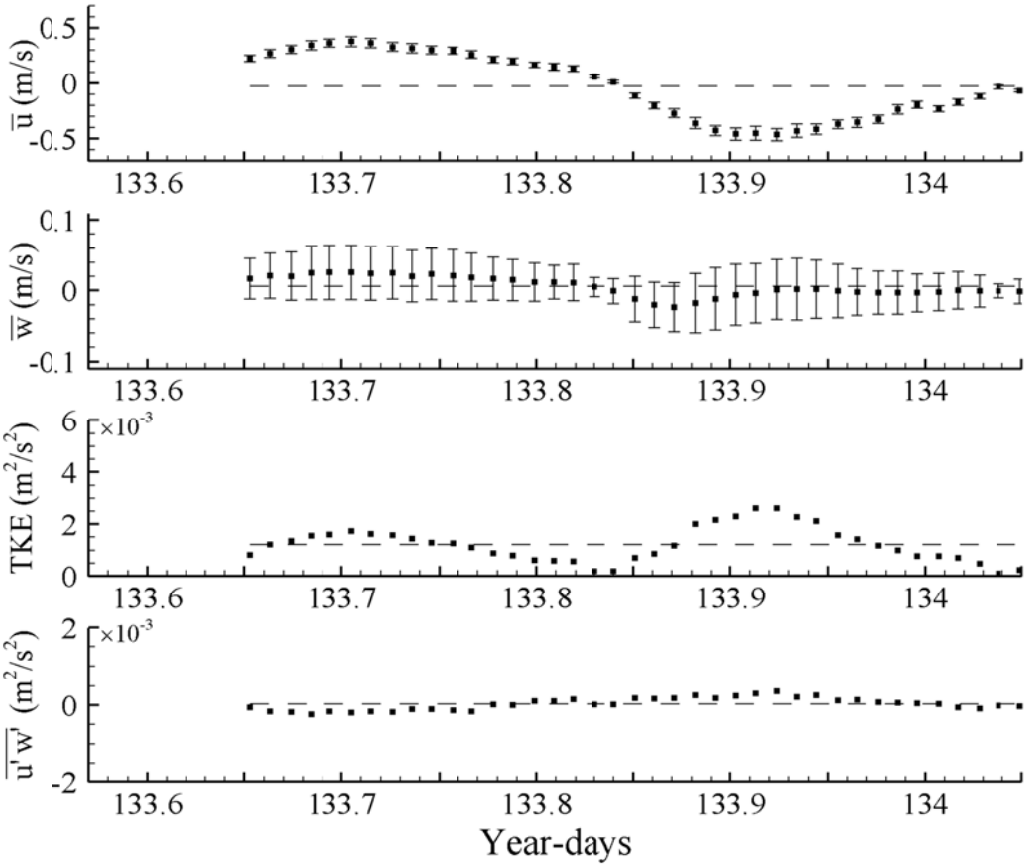

Figure 4. Burst-averaged records for Moon14 data set. The dashed line indicates the mean of the burst-averaged values. The error bars correspond to standard deviation of the variation within the burst.

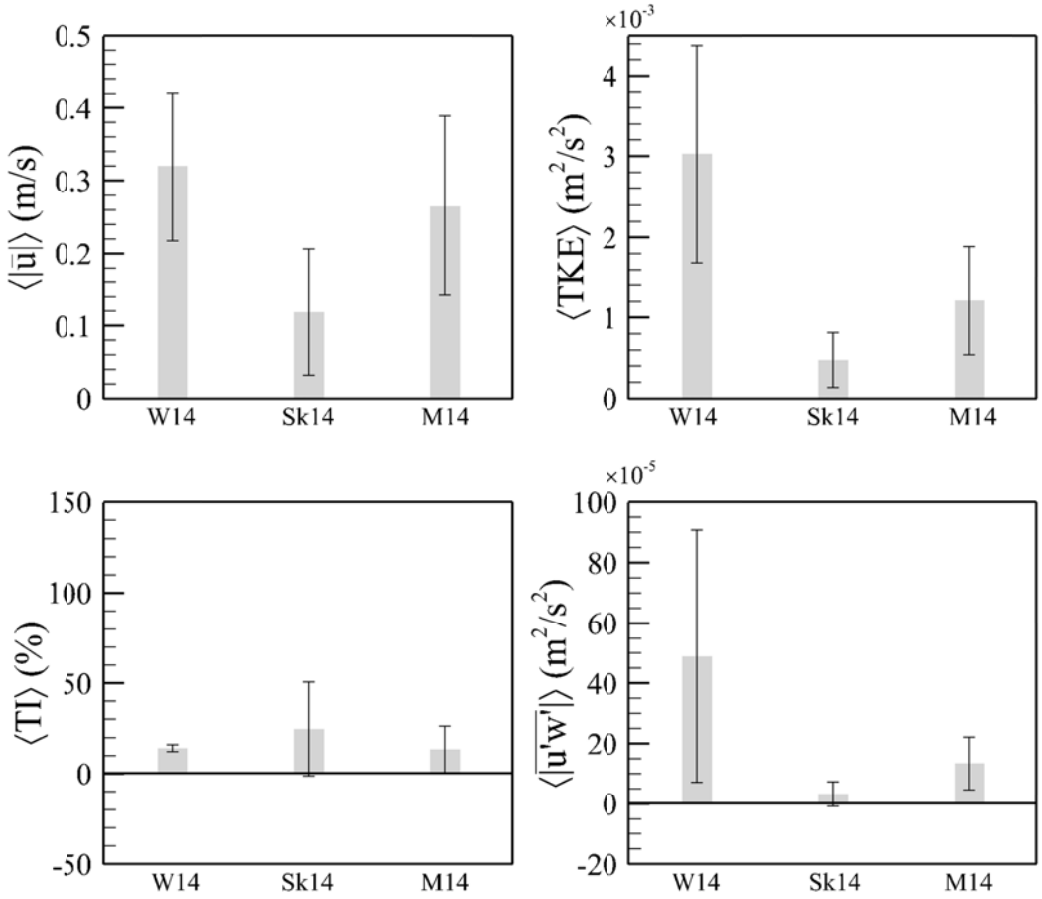

Figure 5. Comparison of the set mean values of the absolute value of the horizontal velocity $\left\langle |\overline{u}| \right\rangle$, turbulent kinetic energy $\left\langle TKE \right\rangle$, turbulence intensity *TI*, and absolute value of the Reynolds shear stress $\left\langle \left| \overline{u'w'} \right| \right\rangle$ for all sites where data were collected on 5/14/07. The error bars correspond to the standard deviation of the variation among the burst-averaged values over a sequence covering one tidal cycle. W14 indicates Wilmington14, Sk14 indicates Skidaway14, and M14 indicates Moon14.

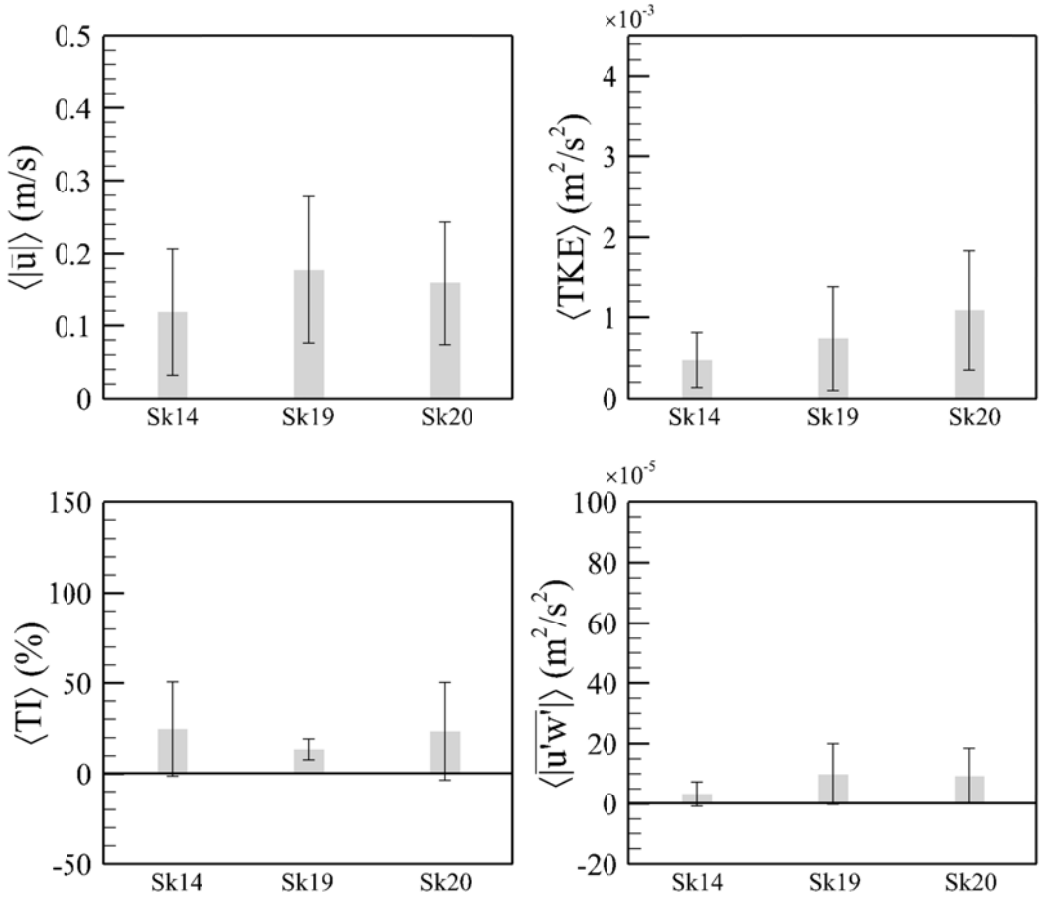

Figure 6. Comparison of the set mean values of the absolute value of the horizontal velocity $\left\langle |\overline{u}| \right\rangle$, turbulent kinetic energy $\left\langle TKE \right\rangle$, turbulence intensity *TI*, and absolute value of the Reynolds shear stress $\left\langle \left| \overline{u'w'} \right| \right\rangle$ for all sets collected at the Skidaway River site. The error bars correspond to the standard deviation of the variation among the burst-averaged values over a sequence covering one tidal cycle. Sk14 indicates Skidaway14, Sk19 indicates Skidaway19, and Sk20 indicates Skidaway20.

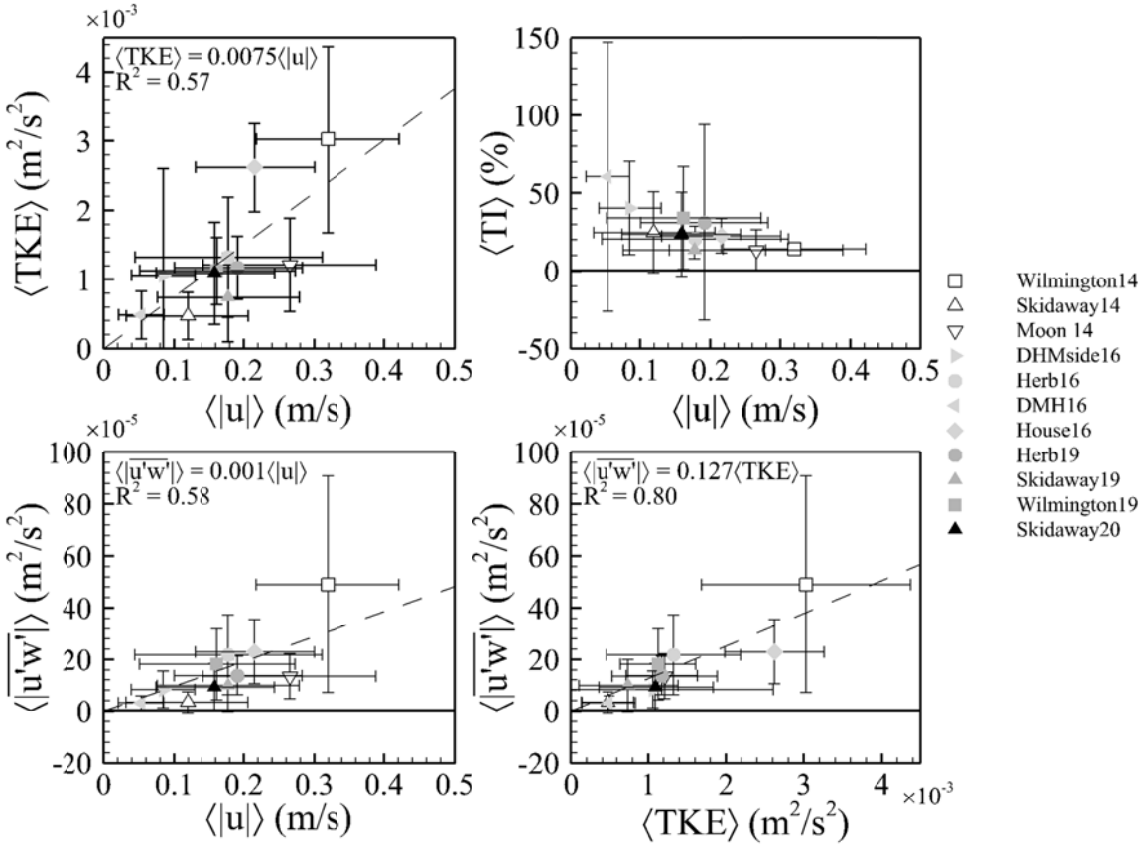

Figure 7. Relationship among the ensemble average of the burst-averaged values of absolute value of the horizontal velocity $\left\langle \left|\overline{u}\right| \right\rangle$, turbulent kinetic energy $\left\langle TKE \right\rangle$, turbulence intensity $\left\langle TI \right\rangle$, and absolute value of the Reynolds shear stress $\left\langle \left|\overline{u'w'}\right| \right\rangle$ for all sets. The symbols denote the set mean values and the error bars correspond to the standard deviation of the variation among the burst-averaged values. The dashed lines show the trend lines, as indicated.

Site- and tide-specific variation in the hydrodynamic landscape relative to odor-mediated predators in salt marsh systems

Miranda L. Wilson[1], Donald R. Webster[2], and Marc J. Weissburg[1]

[1]School of Biology, Georgia Institute of Technology

[2]School of Civil and Environmental Engineering, Georgia Institute of Technology

1 Introduction

Many physical processes in estuarine systems, such as the transportation of sediment, toxins, and wastewater runoff, are influenced by the turbulent characteristics of the water flow (Chanson et al. 2005). Flow and turbulence also mediate a variety of ecological interactions. For instance, flow and turbulence have been shown to mediate the distribution and intensity of larval settlement (Pawlik and Butman 1993, Abelson and Denny 1997), contribute to the erosion or smothering of infaunal communities (Miller et al. 2002), and impact odor-mediated predator-prey interactions (reviewed in Weissburg 2000, Webster and Weissburg 2009).

Odor-mediated predator-prey interactions are important in estuarine environments where suspended sediment and algal blooms increase the turbidity of water and prevent visual cues from being used to locate prey. The ability of predators to extract information from chemical cues entrained in flows mediates their ability to successfully locate prey individuals and hence affects prey populations. Variation in flow velocity, turbulence intensity, and Reynolds stresses affect predator tracking abilities in laboratory flume studies (Weissburg and Zimmer-Faust 1993, Jackson et al. 2007) and translate into changes in predatory success in the field (Zimmer-Faust et al. 1995, Finelli et al. 2000, Smee et al.

2010). The magnitude and effects of flow characteristics on predators, and subsequently prey populations, is predator-specific and directly related to their sensory capabilities and foraging modalities. For example, blue crabs (*Callinectes sapidus*) in the lab show decreased tracking success in swift flows (Weissburg and Zimmer-Faust 1993), and flows with large turbulence intensity (Jackson et al. 2007). The decrease in tracking success leads to reduced predation rates on infaunal bivalve populations in the field (Smee et al. 2008, Smee et al. 2010). It is hypothesized that the blue crabs' quick movement, consisting of cross-stream comparisons of chemical cues in conjunction with upstream movement in response to concentrated odor filaments, reduces their ability to gather adequate information from prey plumes in highly turbulent flows where odors are diluted, homogenized and spread out from the plume centerline fairly quickly. Knobbed whelks (*Busycon carica*), in contrast, show increased predation success in the field when roughness elements are placed around prey patches (Ferner et al. 2009) and in faster flow velocities (Powers and Kittinger 2002). Their slow movement may help them time-average information contained in dilute prey odor plumes and enhance foraging efficiency in turbulent environments.

The ability of predators to locate food can affect the abundance and distribution of prey populations, which is important in estuary systems along the East coast where blue crabs (Hines et al. 1990) and whelks (Carriker 1951) are two significant predators on infaunal bivalve populations. Predation rates by these two predators may likely be context-specific (both spatially and temporally) because local flow conditions may be dependent on site and bulk flow characteristics (Smee et al. 2010). By combining information about the fluid environment with corresponding biological behavior, informed hypotheses can be formulated as to the spatial and temporal patterns in predation success,

and by extension, a better understanding of the ability of predators to control and shape prey populations can be created.

Thus far, information about flow characteristics in near-bed estuarine habitats has been sparse; relegated to short sampling time periods, irrelevant locations above the substrate, arbitrarily-selected sampling time periods, and limited study sites (but see Smee et al. 2008, Ferner et al. 2009, Smee et al. 2010, and Berry et al. 2011). Hence, information about turbulent flows experienced by benthic foragers is largely unknown, preventing adequate development of hypotheses as to how physical parameters may impact interspecific interactions over temporal and spatial scales that are relevant to odor-mediated predator and prey populations.

A relatively few studies have examined turbulent flow characteristics in the near-bed habitats of small-channel estuaries, or explore how processes like tidal forcing, wind generation of currents, and turbulence interact to affect large-scale estuarine dynamics as well as sediment entrainment and deposition processes (Kawanisi and Yokosi 1994, Bell et al. 1997, Collins et al. 1998, Le Hir et al. 2000, Voulgaris and Meyers 2004). Although these studies were not motivated to address ecological issues, they can be used to identify those processes and flow characteristics that may be important in estuarine dynamics. Bell et al. [1997] showed that mean velocity was correlated with tidal strength; with spring tides showing larger magnitude velocity flows (although see Trevethan et al. 2008 for contrasting tidal patterns). Although these studies provide essential information as to the variation and causes of turbulent flow characteristics, information about temporal and spatial variation in turbulent flow characteristics (especially over long time-periods, in multiple sites, and in areas where concurrent information about predation is known) is lacking.

In order to understand how turbulent flows impact odor-mediated predation, we

must assess the flow environments in which these predator-prey interactions occur at relevant spatial and temporal scales. Specifically, we must explore the spatial variation in flow environments (at multiple scales) that may result in spatially-explicit impacts on odor-mediated predator prey interactions and their corresponding effects on prey populations. To do this we measured velocity time series at multiple locations within four sites across an intertidal estuary system. We also obtained measurements across and within multiple sites corresponding to variation in tidal forcing (neap tide, normal tide, and spring tide). Based on previous studies of intertidal estuary turbulent properties, we predict that tidal forcing will have a large effect on mean flow properties, with stronger forcing (spring tide) resulting in larger velocities and increased turbulence. We also predict that the values of turbulent flow parameters will vary within and between sites, although the extent to which these variations impact odor-mediated interactions should be greater between sites than within sites. We deployed multiple acoustic Doppler velocimeters (ADVs) over a three month survey period in Wassaw Sound, Georgia, USA to explore these hypotheses.

2 Methods

2.1 Data Collection

Time series of three-dimensional flow velocity were obtained during June-August 2010 at four sites in Wassaw Sound, GA and its surrounding tributaries including; Dead Man's Hammock (DMH), across from Priest Landing (APL), the Skidaway Narrows (SN), and Priest Landing (PL) (comparison site; Figure 1). These sites are characterized by semi-diurnal tidally-driven flow with tidal ranges of 2-3 m. All sites are exposed to largely unidirectional flows during both ebb and flood tides. All sites have substrates consisting of

a mix of mud and fine sand, are bordered by marsh grass (*Spartina alterniflora*) or oyster reefs (*Crassostrea virginica*), and range in salinity from 20-28 ppt (Smee et al. 2010).

Four acoustic Doppler velocimeters (ADVs; NortekUSA Vector) were simultaneously placed within each site, with each site measured over different dates during the sampling period. Instruments were placed 1 m, 5 m, and 10 m from a reference instrument within each site. Concurrent to measurements taken within each site, two ADVs were placed 1 m apart at the Priest Landing comparison site. All instruments were placed parallel to the water line at the mean low tide level. The sampling volume for each instrument was approximately 0.10 m above the substrate. This experimental protocol was repeated for each of the three other sites (not the PL comparison site) and for each of three tidal types (spring tide (SP), neap tide (NP), and normal tide (NL)). This facilitated within-site and between-site spatial comparisons of flows in the context of large scale changes in tidal forcing. To examine patterns of flow at larger within-site spatial scales, within-site comparisons were also made for the Priest Landing comparison site during three tidal types using six ADVs located at 1 m, 5 m, 10 m, 15 m, and 20 m from a reference instrument.

All ADVs recorded three components of velocity, pressure, signal-to-noise ratios, and correlation coefficients over 4 consecutive complete tidal cycles (from low tide to subsequent low tide) for each tidal type deployment. Instruments were placed in the field such that the x-velocity was predominately the along-stream component and the direction upwards from the substrate was represented by a positive z-velocity. During data analysis, the x- and y-direction velocity components were rotated to maximize the magnitude of the x-velocity component and to ensure that the x-velocity was positive for flood tide and negative for ebb tide. Data were collected continuously at 16 Hz during 5 minute bursts, which were separated by 10 minutes.

2.2 Data Analysis

2.2.1 Data Filtering

Bursts were discarded if the mean correlation coefficient calculated was less than 70 %. Bursts also were discarded if they contained more than 500 consecutive points with a mean correlation coefficient less than 70 %. These two conditions occurred as a result of probe exposure to the atmosphere during low tides and resulted in removal of an average of 10 bursts for each tidal cycle data set.

2.2.2 Phase Filtering

"Spikes" commonly occur in ADV data because of aliasing of the Doppler signal, which results in erroneous data that still show good signal-to-noise ratios and correlation coefficients. To detect spikes we used the phase filtering method of Goring and Nikora [2002], which uses the first and second order differencing estimates to reveal non-physical spikes based on the universal threshold. Erroneous spikes were removed and replaced using a third-order polynomial fit including 12 points on either side of the spike, with an extended range in the presence of other nearby spikes (Goring and Nikora 2002).

2.2.3 Removal of Wave Energy

The presence of wind waves in shallow water estuaries can result in apparent wave motion contributions to turbulence parameters. Fluctuations from waves can also contribute to the turbulence signature when sensors are aligned improperly with the principal axis or when there is sloping bed geometry (Grant et al. 1984, Trowbridge 1998). The apparent contribution of wave motion to turbulent parameters should not be

considered turbulence because of their low frequency ranges. Instantaneous velocity is decomposed into the mean component $\overline{u}$, the wave motion component $\tilde{u}$, and the turbulent fluctuation component u' according to:

$$u = \overline{u} + \tilde{u} + u' \tag{1}$$

We used the coherence between the velocity and pressure measurements to identify and remove the wave portion of the kinetic energy and the Reynolds shear stress using methodology developed by Berry et al. [2011]. The following is a brief description of the calculations involved in separating the wave component of the Reynolds shear stress. An analogous method is used for the normal stresses in order to separate the wave component of TKE (see Berry et al. [2011] for a more thorough description of all calculations).

Trends due to a rising or falling tide were first removed from the velocity and pressure time series (each 5 minute burst) using a linear trend removal (Bendat and Piersol 2010). The mean value was then subtracted to obtain the fluctuating component of velocity and pressure. The notation employed below implies that the mean component is therefore zero. Following the methodology of Benilov and Filyushkin [1970], we calculated the coherence function for the u component of velocity and pressure (p), as a function of frequency:

$$\gamma^2(\omega) = \frac{S_{up}(\omega)S^*_{up}(\omega)}{S_{uu}(\omega)S_{pp}(\omega)} \tag{2}$$

where S_{up} is the cross-spectral density (CSD) of u and p, S_{uu} and S_{pp} are power spectral density (PSD) functions, ω is frequency, and * represents the complex conjugate.

Assuming that the coherence between velocity and pressure is due to wave influence,

we then calculated the PSD for the turbulent portion of the signal by:

$$S_{u'u'}(\omega) = [1 - \gamma^2(\omega)]S_{uu}(\omega) \tag{3}$$

and used it to calculate the magnitude of the turbulent velocity fluctuation $|U'_j|$ as a function of discrete frequency (denoted with index j) via:

$$S_{u'u'j} = \frac{1}{d\omega}|U'_j|^2 \tag{4}$$

These steps were then repeated for the w component of velocity and pressure such that the magnitude of the turbulent velocity fluctuations for both the u and w velocity components were adjusted using the coherence of the respective velocity components with the pressure signal.

To calculate the Reynolds shear stress we then incorporated the phase of each velocity component with the magnitude of the turbulent velocity fluctuation. We can express the velocity components using phasor notation of the Fourier coefficients:

$$U_j = |U_j|e^{i\angle U_j} \text{ and } W_j = |W_j|e^{i\angle W_j} \tag{5}$$

with the phases defined by:

$$\angle U_j = arctan\left[\frac{Im(U_j)}{Re(U_j)}\right] \text{ and } \angle W_j = arctan\left[\frac{Im(W_j)}{Re(W_j)}\right] \tag{6}$$

Using this, the CSD can be expressed as:

$$U_j^* W_j = |U_j||W_j| e^{j(\angle W_j - \angle U_j)} = |U_j||W_j|(\cos(\angle W_j - \angle U_j) - i\sin(\angle W_j - \angle U_j)) \tag{7}$$

Neglecting the imaginary part of the CSD, the Reynolds shear stress can be calculated using:

$$\overline{u'w'} = \sum_j U_j'^* W_j' = \sum_j |U_j'||W_j'|\cos(\angle W_j - \angle U_j) \tag{8}$$

where $|U_j'|$ and $|W_j'|$ are calculated from Equation (4) and $\angle U_j$ and $\angle W_j$ are calculated from Equation (6). The wave portion of the Reynolds shear stress then is calculated by subtracting the turbulent velocity fluctuation from the total covariance:

$$\overline{\tilde{u}\tilde{w}} = \overline{uw} - \overline{u'w'} \tag{9}$$

We used this methodology to calculate the wave contribution to TKE and Reynolds shear stress for all bursts in each data set except the first two and last two bursts of each tidal cycle for data sets collected at Priest Landing. The two downward facing fixed stem ADVs at the Priest Landing site were mounted such that they were able to record velocity data while the pressure sensor was not immersed at the beginning and end of each tidal cycle, preventing the calculation of coherence between velocity and pressure for these bursts.

2.2.4 Calculation of Turbulent Parameters

Mean turbulence characteristics were calculated for each burst. Turbulence parameters calculated are as follows:

$$Turbulent\ Kinetic\ Energy\ (TKE) = 0.5(\overline{(u')^2} + \overline{(v')^2} + \overline{(w')^2}) \tag{10}$$

$$Reynolds\ Shear\ Stress = \overline{u'w'} \tag{11}$$

$$Turbulence\ Intensity\ (TI) = \frac{\sqrt{\overline{(u')^2} + \overline{(v')^2} + \overline{(w')^2}}}{\sqrt{\overline{u}^2 + \overline{v}^2 + \overline{w}^2}} * 100 \tag{12}$$

2.2.5 Statistical Analysis

To examine the spatial variability within sites, we performed a series of correlations between turbulence data from each ADV probe and the corresponding reference instrument within each site. Distance comparisons for the DMH, SN, and APL sites were 0×1 m, 0×5 m, and 0×10 m, and distance comparisons for the PL site were 0×1 m, 0×5 m, 0×10 m, 0×15 m, and 0×20 m, where zero represents the reference instrument. Burst-averaged data from four measured tidal cycles (approximately 140 bursts) was used to calculate correlation coefficients. Pearson correlations were used to calculate correlation coefficients for the burst-averaged absolute value of the u-component of velocity, and Spearman rank correlations were used for all other flow parameters (TKE, $|\overline{u'w'}|$, TI) because we were unable to achieve normality via transformation.

To determine correlation strengths between turbulent flow parameters at each site (DMH, APL, and SN) and the PL comparison site, we again utilized a series of Pearson and Spearman rank correlation analyses for each turbulent flow parameter and each tidal

type. Data used for between-site correlations were for time series taken simultaneously at PL and each individual site (approximately 135 bursts).

To determine the influence of site and tidal forcing (and any interactions) on mean turbulent flow parameters, we utilized a two-way analysis of variance (ANOVA), which is fairly robust to issues of non-normality (Zar 1999). Because we were unable to achieve normality via transformation for most of our turbulent parameters (TKE, TI, and $|\overline{u'w'}|$), we also utilized non-parametric Kruskal-Wallis tests to confirm significance of one-way comparisons. This was done for each flow parameter separately using burst-averaged data from the entire deployment period described above (approximately 140 bursts).

Regression analysis also was used to determine the relationship between values of $|\overline{u}|$, TKE, and $|\overline{u'w'}|$ using the ensemble-averaged values calculated for each site by tidal type combination for comparison.

3 Results

3.1 Flow Time Series and Comparison Within Sites

Similar values of $\overline{u}$, TKE and $\overline{u'w'}$ were obtained from the four simultaneously deployed instruments within a site (Figure 2 shows example data from the APL-NP data set). Similar patterns were seen for set comparisons within all sites. Overall, there is greater variation between instruments for values of TKE and $\overline{u'w'}$ than values of $\overline{u}$ and greater variation between instruments during ebb tide, regardless of the turbulent flow parameter. These patterns hold for the entire four tidal cycle sampling period (Figure 3).

3.2 Correlation within and between Sites

Correlation coefficients for within-site comparisons of all turbulent flow parameters were large and significantly different from zero for all distance comparisons and at the DMH, SN, and APL sites (Table 1, see Figure 4 for an example of correlations within the PL site). Correlation coefficients tended to decrease with separation distance, but statistics were not used to determine significant differences between correlation coefficients within each site. Comparisons of multiple correlation coefficients greater than 0.9 are discouraged because the z-transformation needed to normalize and stabilize the variance of the underlying correlation coefficient distribution is not reliable for coefficients greater than 0.9 (Zar 1999). Correlation coefficients ranged from 0.99 for $|\overline{u}|$ to 0.18 for $|\overline{u'w'}|$ (Table 1). For the DMH, SN, and APL sites, correlation coefficients for $|\overline{u}|$ were generally the highest and correlation coefficients for $|\overline{u'w'}|$ were generally the lowest, with the correlation coefficients for the other two turbulent flow parameters (TKE and TI) falling in between.

Correlation coefficients for within-site comparisons at PL also were large and significantly different from zero (Table 2). Correlation coefficients at PL ranged from 0.99 for $|\overline{u}|$ to 0.25 for TI, with generally the highest correlation coefficients for $|\overline{u}|$ and the lowest for $|\overline{u'w'}|$. Average correlation coefficients for PL (including all tidal types) showed a general decrease with distance for all flow parameters except TI, which were relatively similar for all distance comparisons.

Correlation coefficients for within-site comparisons at the PL, DMH, SN, and APL sites were similar for all flow parameters except for TI. Data at the PL site showed smaller correlation coefficients for TI for all distance comparisons when compared to the other three sites. Average correlation coefficients for all turbulent flow parameters (except TI)

for the PL 0×20 m and DMH, SN, and APL 0×10 m distance comparisons were similar and large, indicating that flow parameters are still highly correlated at 20 m separation distance. We did not see any clear effects of tidal type on correlation coefficients for any site.

For between-site comparisons we found larger correlation coefficients for all turbulent parameters for sites that are located closer to each other (Table 3 and Figure 1), but we did not see a clear effect of tidal type on correlation strength. The largest correlation coefficient was seen for the neap tide comparison of $|\overline{u}|$ between data for the APL and PL site (0.77), and the smallest was for the normal tide comparison of data for the SN and PL sites for both $|\overline{u}|$ and TI with a value of 0.02. As seen for within-site correlation coefficients (Table 1), comparisons of $|\overline{u}|$ between sites generally resulted in larger correlation coefficients than for other turbulence parameters. Negative correlations were seen for many between-site comparisons, possibly resulting from local bed topography (DMH is bordered by extensive mudflats) or in the case of SN, tidal influence from the adjacent Obassaw Sound (Figure 1).

As expected, correlation coefficients are generally larger for within-site comparisons than between-site comparisons (largest within-site correlation coefficient = 0.99; largest between-site correlation coefficient = 0.77).

3.3 Site and Tide Comparisons

We found a significant effect of site ($F_{3,1537} = 72.08, P < 0.001$), tidal type ($F_{2,1537} = 38.62, P < 0.001$), and interaction between site and tidal type ($F_{6,1537} = 2.88, P = 0.008$) on $|\overline{u}|$ (Figure 5). Kruskal-Wallis tests confirmed significance of one-way interactions (site: $H = 190.64, d.f. = 3, P < 0.001$, tide: $H = 44.31, d.f. = 2, P < 0.001$). Data at the DMH site showed the smallest $|\overline{u}|$ for all tidal

types which may be related to the extensive mudflats located near the sampling site. $|\overline{u}|$ generally increased from neap tide to normal tide, with spring tide showing larger velocities than either other tidal type. The lone exception was data at the SN site where neap tide and normal tide show no apparent differences in velocity. Patterns of $|\overline{u}|$ confirm that increases in tidal forcing, with spring tide having a larger tidal range than neap tide, correspond to increases in flow velocity.

TKE was significantly affected by site ($F_{3,1537} = 17.71, P < 0.001$) and tidal type ($F_{2,1537} = 20.97, P < 0.001$), but there was not a significant interaction between site and tidal type ($F_{6,1537} =, P = 0.153$) (Figure 6). One-way analyses confirmed significant effects of site and tide (site: $H = 154.48, d.f. = 3, P < 0.001$ tide: $H = 58.24, d.f. = 2, P < 0.001$). Data for APL and PL sites had greater TKE than data for the DMH and SN sites (almost two times greater for some sites). All sites had greater TKE during spring tide than during either neap or normal tides (Figure 6).

Turbulence intensity (TI) was significantly affected by site ($F_{3,1537} = 63.52, P < 0.001$) and tidal type ($F_{2,1537} = 3.19, P = 0.041$) (Figure 7), with DMH having greater TI than the other three sites. On average, there was lower turbulence intensity during spring tide than other tidal types, the result of large u velocities during spring tide (See Equation 12 and Figure 5). One-way analyses confirmed significance of site and tidal type (site: $H = 455.46, d.f. = 3, P < 0.001$ tide: $H = 7.67, d.f. = 2, P = 0.022$). There also was a significant interaction between site and tidal type ($F_{6,1537} = 3.52, P = 0.002$). At the PL and APL sites, the data reveal greater TI during neap and spring tides, but the data at the SN site show greater turbulence intensity during normal tide. Turbulence intensity at the DMH site was greater during neap and normal tides than spring tide.

There also was a significant effect of site ($F_{3,1433} = 10.02, P < 0.001$) and tide ($F_{2,1433} = 8.38, P < 0.001$) on Reynolds shear stress (Figure 8), with greater Reynolds shear stress at the APL site than the other three sites and greater Reynolds shear stress during normal tides (although this seems to be driven by large Reynolds shear stress for the APL site only). Kruskal-Wallis tests confirm significance of one-way analyses (site: $H = 51.85, d.f. = 3, P < 0.001$, tide: $H = 20.48, d.f. = 2, P < 0.001$). There also was a significant interaction between site and tidal type ($F_{6,1433} = 9.761, P < 0.001$), with APL showing greater Reynolds shears tress during normal tide as opposed to the other three sites that show smaller Reynolds shear stress during normal tide.

Regressions between ensemble-averaged values of $|\overline{u}|$ and TKE ($F_{1,10} = 1.957$, $P = 0.19$), $|\overline{u}|$ and $|\overline{u'w'}|$ ($F_{1,10} = 3.78$, $P = 0.08$), and TKE and $|\overline{u'w'}|$ ($F_{1,10} = 4.09$, $P = 0.07$) for all site by tidal type combinations were marginally non-significant (Figure 9). Values of $|\overline{u}|$ were only able to explain 14 % of the variance in values of TKE and 27 % of the variance in values of $|\overline{u'w'}|$. Values of TKE explained 21 % of the variance in values of $|\overline{u'w'}|$. Relationships between values of turbulent flow parameters within sites are more similar to each other than relationships between values of turbulent flow parameters within each tidal type (i.e. values of turbulent flow parameters group together by site and not tidal type; Figure 9).

4 Discussion

Results from our within- and between-site comparisons of turbulent flow dynamics indicate that there is significant predictive ability (based on correlation strengths) within sites using limited instrument locations. However, the predictive ability between sites

seems to be dependent on site separation distance, where differences in channel topography may be greater than within sites. This indicates that characterization of flow environments needs to be done for each site where experiments occur, but may not need to be obtained for multiple locations within sites (at least up to 20 m separation distance). There also are significant differences in mean values of flow parameters between sites and for different strengths of tidal forcing. There were significant interaction effects between sites and tidal types, indicating that tidal forcing may operate in a site-dependent manner to influence turbulent flow. This prevents large-scale generalizations concerning the influence of site and tidal forcing on turbulent flow parameters and suggests that observations need to be conducted within sites during different tidal forcing strengths to understand the variability in turbulent flow that organisms may be exposed to in natural environments. Differences in mean values, ranges, and maximum values of flow parameters may have important effects on odor-mediated interactions, potentially creating site-specific impacts on predator foraging efficiency and, subsequently, prey population densities and distributions.

4.1 Variation of Flow within Sites

Our study indicates that values of within-site turbulent flow parameters are very similar for simultaneously deployed instruments (Figure 2) and are well correlated up to 20 m distant, regardless of tidal type (Tables 1 and 2). This suggests that large scale tidal forcing may overwhelm small differences in substrate or local topography within sites that could affect turbulent flow parameters. Still, we do see generally smaller correlation coefficients for turbulent flow parameters that are more dependent on small-scale substrate differences or bed topography (TKE and $\overline{u'w'}$) than those that are dependent on large-scale tidal forcing (Table 1). There are few studies that have measured turbulent flow

properties at multiple locations within a single site, although to our knowledge none have taken simultaneous measurements. Both Chanson et al. [2005] and Collins et al. [1998] measured flow at multiple locations within single sites during subsequent sampling periods (separated by up to a month), possibly confounding differences between microsites and differences in large scale flow patterns. Simultaneous sampling within our sites confirms that measurements of turbulent flow parameters from one instrument can be highly predictive of turbulent flow parameters up to 20 m distant and that this predictive ability is not dependent on tidal type. Larger-scale comparisons (20 m plus) need to be made to confirm the ability of single-location measurements to predict values of turbulent flow parameters at larger distances within sites. We do not see a break-point in the relationship between distance and correlation coefficients with distance, suggesting correlations will continue to decline with much the same slope observed from 0 to 20 m. In the absence of other studies, it is impossible to determine whether the patterns we observe characterize other estuaries as well.

The area defined as a single site also varies drastically among studies. Sites range in separation distance from approximately 200 m (Chanson et al. 2005) to multiple kilometers (Collins et al. 1998). Studies examining turbulent flow parameters at multiple within-site locations have done so at separation distances of approximately 80 m (Chanson et al. 2005) to 200 m (Collins et al. 1998). Our data suggest that these larger separation distances may comprise sites that exhibit substantial differences in flow properties. For ecological applications of flow monitoring, we suggest that the scale of sampling within-sites should be relevant to the ecology of the focal organism (sensu Levin 1992). Odor-mediated predators in our study system are highly varied in their mobility, with blue crabs moving at greater than 3 cm/s (Weissburg and Zimmer-Faust 1994) and knobbed whelks moving

at 0.15 cm/s (calculated from Ferner and Weissburg 2005). Blue crab movement in the field has been reported as slower than in the laboratory at approximately 20 m/hr (0.5 cm/s) (Hines et al. 1995). The scale of our survey seems ecologically-relevant, as both predator species would spend ample time in our survey area.

4.2 Variation of Flow between Sites

The strength of between-site correlations for turbulent flow parameters seems dependent on the distance between sites, but not on tidal type (Table 3). Sites that are closer in proximity may be subject to more similar large-scale tidal forcing processes than those farther apart. There were also site- and tide-specific impacts on all mean turbulent flow parameters, indicating that flow impacts on odor-mediated interactions may be highly context-specific.

Other studies comparing multiple intertidal sites within Wassaw Sound, GA (Smee et al. 2010, Berry et al. 2011) have shown site-specific differences in mean turbulent flow parameters. Both $|\overline{u}|$ and TKE at DMH and SN in our study are similar to those measured by Berry et al. [2011] for the DMH16 and Skidaway14/19/20 sets, but $|\overline{u'w'}|$ for these two sites is an order of magnitude larger in our data set than reported in Berry et al. [2011]. This may be due to differences in the respective wave contributions for the two data sets (See *Chapter 6*), substrate properties due to erosion or sedimentation in the four years between sampling, or distance of the sampling volume from the bed. Velocities reported by Smee et al. [2010] for the Skidaway River (our SN site) are approximately 20% larger than our measured velocities, which can be accounted for by differences in our data filtration processes and sampling volume height.

Relationship trends between values of average turbulent flow parameters measured at

each site and for each tidal type match those described in Berry et al. [2011] (Figure 9). Values from our study represent only the lower values of those measured in Berry et al. [2011], which may account for the different numerical relationships between the variables within the two studies and the marginal non-significance in our study. The relationships between values of average turbulent flow parameters measured in our study seem to group together based on site rather than tidal type, indicating that variation between sites drives the overall relationship between turbulent flow parameters (Figure 9). Berry et al. [2011] utilized more sites characterized by greater variability in bulk flow, exposure to Wassaw Sound, and sediment composition than our study, possibly accounting for differences in the linear relationships and significance of relationships between turbulent flow parameters in our two studies.

Differences in turbulent parameters between sites could have large spatial impacts on odor-mediated interspecific interactions throughout estuary systems. Using information about predator foraging efficiency under different flow regimes in combination with our observed vales of turbulent flow parameters (Figures 5, 6, 8) we can make predictions about temporal and spatial patterns of predation in the field. When turbulent properties such as $|\overline{u}|$ and TKE follow similar patterns in relation to tidal type or site, similar predictions of predation rates in the field would be made based on each turbulent flow parameter. Predators such as blue crabs, seem to be more sensitive to changes in turbulence than velocity in the laboratory (Jackson et al. 2007), suggesting that if patterns in $|\overline{u}|$ and TKE differ based on site or tidal type it could result in different predictions being made as to the impacts of these two turbulent flow parameters on predation efficiency. For example, higher $|\overline{u}|$ and TKE during spring tide both suggest a reduction in foraging efficiency by blue crabs during spring tide relative to neap and normal tides, but high values of $|\overline{u}|$ and low

values of TKE at the SN site suggest opposing influences on blue crab foraging efficiency. Field assessments of blue crab predation rates also need to be made to confirm site and tidal forcing predictions, as there have not been any large-scale experiments comparing predation rates or bivalve prey densities (Walker and Tenore 1984) in our specific sites (although see Smee et al. [2010] for predation rates at other sites in Wassaw Sound, GA).

4.3 Variation in Flow as a Function of Tidal Forcing

Some studies have shown that the influence of tidal forcing on turbulent flow parameters at different sites is dependent on the balance between freshwater and marine inputs (Chanson et al. 2005, Chanson et al. 2008). This effect did not seem to be a factor in our study, as all of our sites are distant from freshwater inflow (Figure 1). Differences in turbulent flow characteristics between sites can be due to channel topography (Collins et al. 1998), substrate characteristics (Shiono and West 1987), tidal lag, or variation in tidal forcing (Le Hir et al. 2000). Other studies support our findings that u-velocity (Figure 5) (Trevethan et al. 2008, Le Hir et al. 2000, Trevethan and Chanson 2009, Bell et al. 1997) and TKE (Figure 6) (Trevethan and Chanson 2009) are greater during spring tide than neap tide. Trevethan et al. [2008] also recorded 2 to 4 times more variability in values of u-velocity during spring tides than during neap tides, which we confirmed for our DMH, APL, and PL sites, but not at our SN site (Figure 5).

There was a 3 to 4 cm/s increase in $|\overline{u}|$ between neap and spring tides in data for all our sites (Figure 5). In laboratory studies, a 2.8 cm/s increase in flow velocity (from 1 cm/s to 3.8 cm/s) resulted in a 50% reduction in predation success by blue crabs (Weissburg and Zimmer-Faust 1993). Increases in turbulence (due to increased bed roughness) also resulted in an approximately 50% reduction in blue crab foraging success (Jackson et al. 2007).

Independent of other processes, differences in turbulent flow parameters between neap and spring tide could result in significant differences in blue crab predation rates in the field, although additional field surveys and experimentation are needed to confirm this.

4.4 Summary

Based on large within-site correlation coefficients, we suggest that a limited number of sampling locations are necessary to accurately predict variation in turbulent flow parameters that an organism may encounter over distances of 10 to 20 m. Based on distant-dependent correlation strength between sites, we suggest that additional between-site comparisons be made to determine the distance at which predictive capabilities are maintained. Differences in turbulent flow parameters between sites and during different tidal types suggest that odor-mediated interactions should vary both spatially and temporally within the estuary system. This could have important consequences for predator-prey population dynamics via the creation of flow-mediated refuges from predation (as suggested by Smee and Weissburg [2006] and Smee et al. [2010]) and vary based on the dominant predator species.

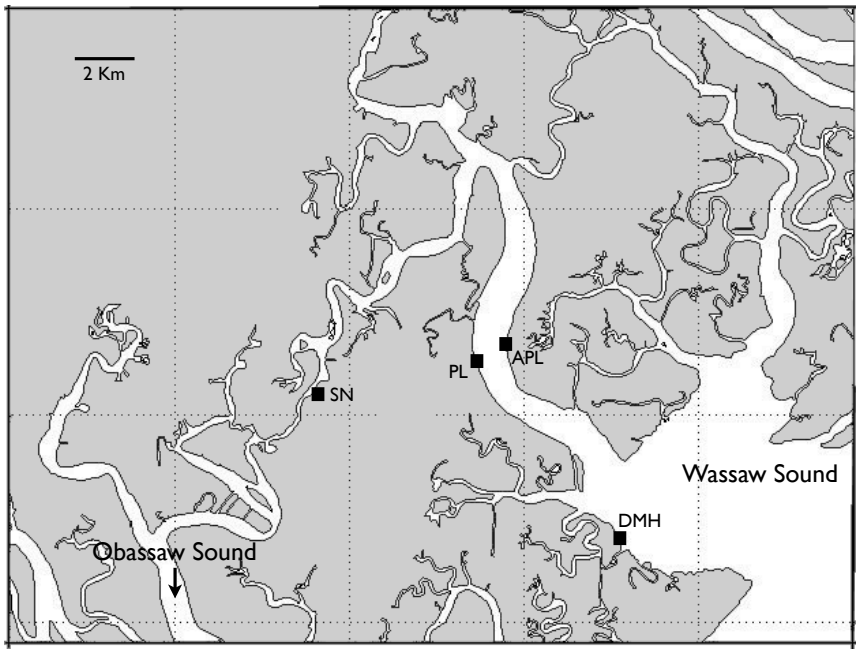

Figure 1: Map of Wassaw Sound, Georgia where instruments were deployed June-August 2010. DMH = Dead Man's Hammock, PL = Priest Landing, APL = Across from Priest Landing, SN = Skidaway Narrows.

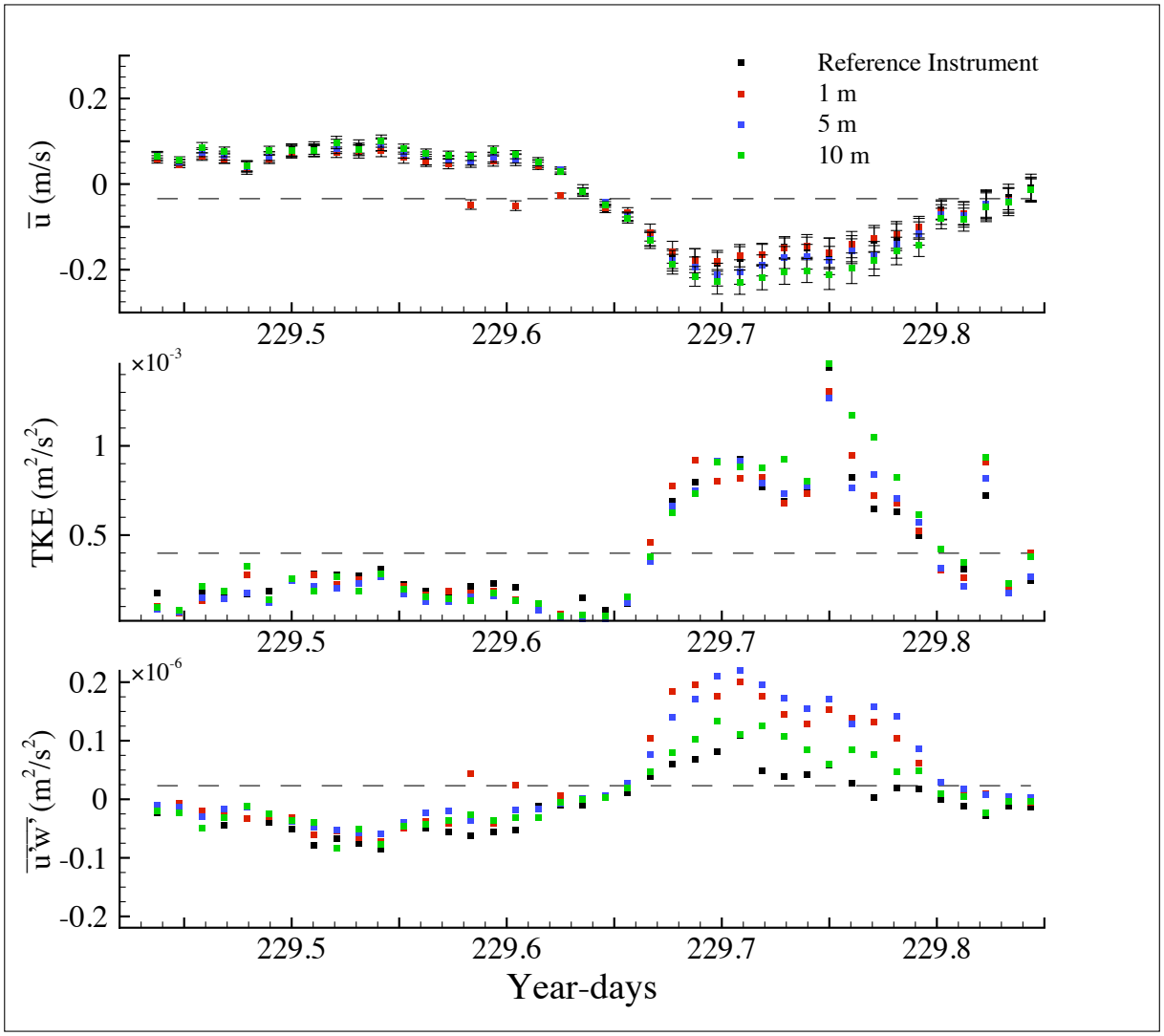

Figure 2: Time-series of flow parameters ($\overline{u}$ [top], TKE [middle], and $\overline{u'w'}$ [bottom]) from four simultaneously deployed ADVs within the APL site during neap tide for one tidal cycle. Error bars represent one standard deviation. Dashed lines represent the mean value for all instruments combined. Differently colored symbols represent the four instruments: Reference instrument = black, 1 m = red, 5 m = blue, and 10 m = green.

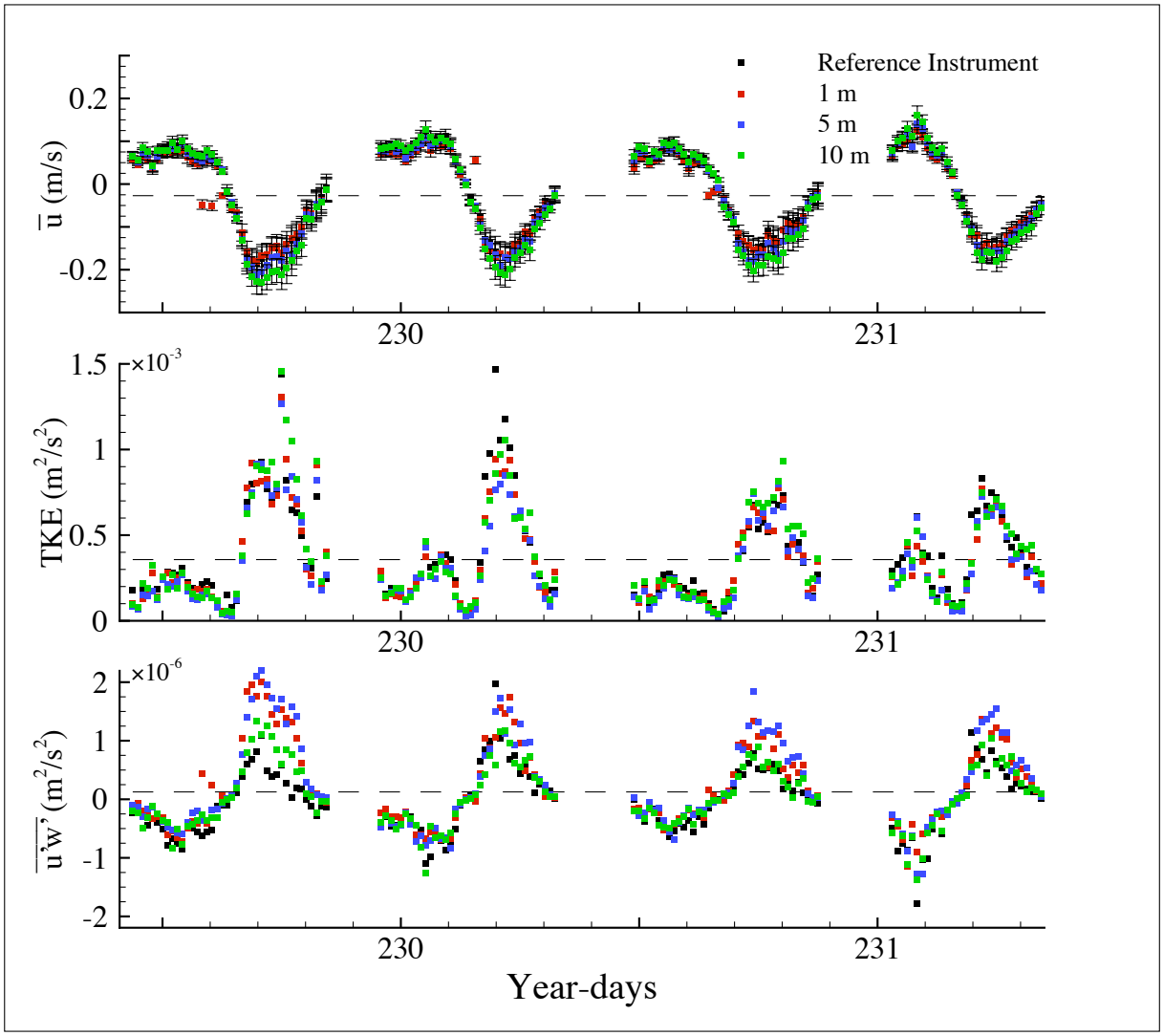

Figure 3: Time-series of flow parameters ($\overline{u}$ [top], TKE [middle], and $\overline{u'w'}$ [bottom]) from four simultaneously deployed ADVs within the APL site during neap tide for four tidal cycle. Error bars represent one standard deviation. Dashed lines represent the mean value for all instruments combined. Differently colored symbols represent the four instruments: Reference instrument = black, 1 m = red, 5 m = blue, and 10 m = green.

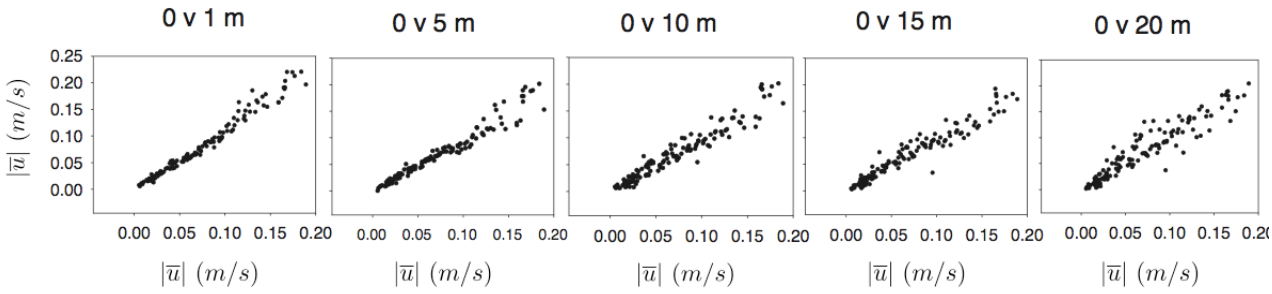

Figure 4: Within-site correlations of the absolute value of burst averaged u-velocity at Priest Landing site during normal tide. Correlation coefficients are shown for comparisons between each instrument and the reference instrument that was simultaneously deployed. Data included in the correlation calculation consisted of 128 bursts collected over 4 tidal cycles.

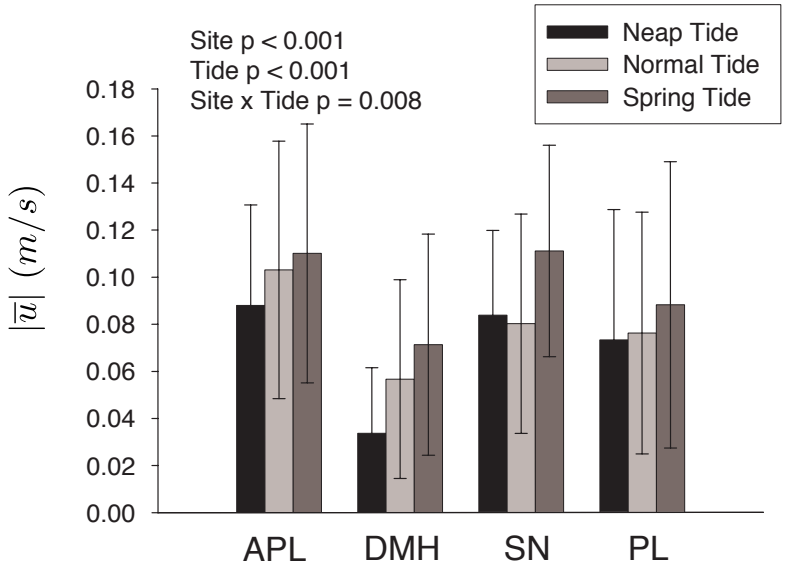

Figure 5: Ensemble average of the absolute value of burst-averaged values of u-velocity (m/s). Error bars represent one standard deviation. For the number of bursts included in calculating ensemble averages see Tables 1 and 2. APL = Across from Priest Landing, DMH = Dead Man's Hammock, SN = Skidaway Narrows, and PL = Priest Landing. Statistical significance was determined using a two-way ANOVA.

Site	Tidal Type	No. Bursts	$\lvert\overline{u}\rvert$			TKE		
			0×1 m	0×5 m	0×10 m	0×1 m	0×5 m	0×10 m
SN	Normal	141	0.99	0.95	0.88	0.90	0.80	0.82
SN	Neap	173	0.99	0.97	0.92	0.86	0.84	0.85
SN	Spring	126	0.99	0.96	0.91	0.97	0.93	0.88
APL	Normal	149	0.91	0.99	0.97	0.99	0.94	0.94
APL	Neap	145	0.99	0.98	0.97	0.96	0.97	0.95
APL	Spring	137	0.94	0.92	0.91	0.77	0.76	0.76
DMH	Neap	129		0.92	0.94		0.84	0.88
DMH	Spring	143	0.98	0.96	0.95	0.95	0.96	0.95
All	All		0.97 ± 0.03	0.96 ± 0.03	0.93 ± 0.03	0.91 ± 0.08	0.88 ± 0.08	0.88 ± 0.07

Site	Tidal Type	No. Bursts	TI			$\overline{u'w'}$		
			0×1 m	0×5 m	0×10 m	0×1 m	0×5 m	0×10 m
SN	Normal	141	0.93	0.83	0.77	0.81	0.73	0.80
SN	Neap	173	0.88	0.78	0.70	0.86	0.61	0.72
SN	Spring	126	0.85	0.78	0.71	0.70	0.81	0.74
APL	Normal	149	0.87	0.85	0.72	0.94	0.93	0.92
APL	Neap	145	0.78	0.76	0.84	0.72	0.68	0.79
APL	Spring	137	0.49	0.37	0.45	0.54	0.83	0.54
DMH	Neap	129		0.85	0.87		0.20	0.18
DMH	Spring	143	0.95	0.95	0.94	0.44	0.63	0.50
All	All		0.82 ± 0.16	0.77 ± 0.17	0.75 ± 0.15	0.72 ± 0.18	0.68 ± 0.22	0.65 ± 0.23

Table 1: Correlation coefficients for comparisons of spatially-separated simultaneous data (0×1 m, 0×5 m, and 0×10 m) within each tidal type and site for each turbulent parameter ($\lvert\overline{u}\rvert$, TKE, TI, and $\overline{u'w'}$). "No. Bursts" indicates the number of bursts that were compared to calculate the correlation coefficients. Sites are named using the following convention; SN = Skidaway Narrows, APL = Across from Priest Landing, DMH = Dead Man's Hammock. All correlation coefficients are significantly different from zero.

Site	Tidal Type	No. Bursts	$\lvert\overline{u}\rvert$					TI				
			0×1 m	0×5 m	0×10 m	0×15 m	0×20 m	0×1 m	0×5 m	0×10 m	0×15 m	0×20 m
PL	Normal	128	0.99	0.98	0.97	0.96	0.88	0.48	0.79	0.49	0.61	0.51
PL	Neap	134	0.99	0.83	0.95	0.92	0.88	0.81	0.65	0.89	0.88	0.78
PL	Spring	136	0.99	0.99	0.97	0.92	0.88	0.31	0.52	0.42	0.40	0.25
PL	All		0.99	0.93 ± 0.09	0.96 ± 0.01	0.93 ± 0.02	0.53 ± 0.25	0.88	0.65 ± 0.14	0.6 ± 0.25	0.63 ± 0.24	0.51 ± 0.27

Site	Tidal Type	No. Bursts	TKE					$\overline{u'w'}$				
			0×1 m	0×5 m	0×10 m	0×15 m	0×20 m	0×1 m	0×5 m	0×10 m	0×15 m	0×20 m
PL	Normal	128	0.97	0.97	0.89	0.93	0.90	0.84	0.74	0.76	0.78	0.59
PL	Neap	134	0.94	0.89	0.90	0.88	0.87	0.74	0.70	0.43	0.29	0.59
PL	Spring	136	0.71	0.69	0.73	0.68	0.70	0.78	0.81	0.81	0.73	0.68
PL	All		0.87 ± 0.14	0.85 ± 0.14	0.84 ± 0.1	0.83 ± 0.13 for	0.82 ± 0.12	0.79 ± 0.05	0.75 ± 0.06	0.67 ± 0.21	0.6 ± 0.27	0.62 ± 0.05

Table 2: Correlation coefficients for comparisons of spatially-separated simultaneous data (0×1 m, 0×5 m, 0×10 m, 0×15 m, and 0×20 m) within each tidal type at Priest Landing (PL) and for each turbulent parameter ($\lvert\overline{u}\rvert$, TI, TKE, and $\overline{u'w'}$). "No. Bursts" indicates the number of bursts that were compared to calculate the correlation coefficients. All correlation coefficients are significantly different from zero.

Site Comparison	Tidal Type	No. Bursts	$\lvert\overline{u}\rvert$	TKE	KE_{wave}	TI	$\overline{u'w'}$	$\overline{\tilde{u}\tilde{w}}$
APL × PL	Normal	140	0.74	0.63	0.62	0.27	0.64	0.51
APL × PL	Neap	145	0.77	0.70	0.66	0.29	0.45	0.36
APL × PL	Spring	130	0.72	0.58	0.72	0.26	0.63	0.38
SN × PL	Normal	61	0.02*	-0.08*	0.17*	0.02*	-0.04*	0.10*
SN × PL	Spring	98	0.28	0.16*	0.15*	0.15*	0.08*	0.13*
DMH × PL	Normal	137	-0.41	-0.23	0.34	0.34	-0.19	0.33
DMH × PL	Spring	140	-0.36	-0.46	-0.15*	0.39	-0.31	0.15*

Table 3: Correlation coefficients for comparisons between data at each site and simultaneous data at the Priest Landing (PL) comparison site for each tidal type and for each turbulent parameter calculated ($\lvert\overline{u}\rvert$, TKE, KE_{wave}, TI, $\overline{u'w'}$, and $\overline{\tilde{u}\tilde{w}}$). "No. Bursts" indicates the number of bursts compared to calculate correlation coefficients. * indicates non-significant correlation coefficients.

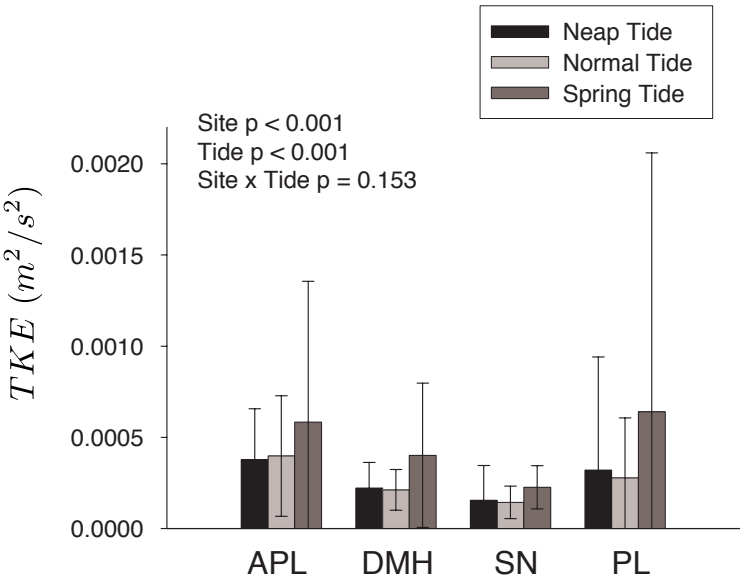

Figure 6: Ensemble average of burst-averaged values of TKE (m^2/s^2). Error bars represent one standard deviation. For the number of bursts included in calculating ensemble averages see Tables 1 and 2. APL = Across from Priest Landing, DMH = Dead Man's Hammock, SN = Skidaway Narrows, and PL = Priest Landing. Statistical significance was determined using a two-way ANOVA.

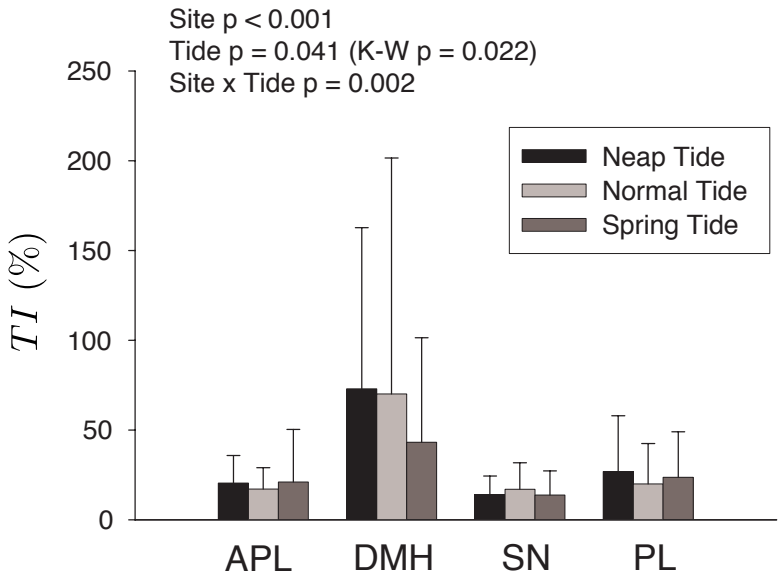

Figure 7: Ensemble average of burst-averaged values of Turbulence Intensity (TI, %). Error bars represent one standard deviation. For the number of bursts included in calculating ensemble averages see Tables 1 and 2. APL = Across from Priest Landing, DMH = Dead Man's Hammock, SN = Skidaway Narrows, and PL = Priest Landing. Statistical significance was determined using a two-way ANOVA.

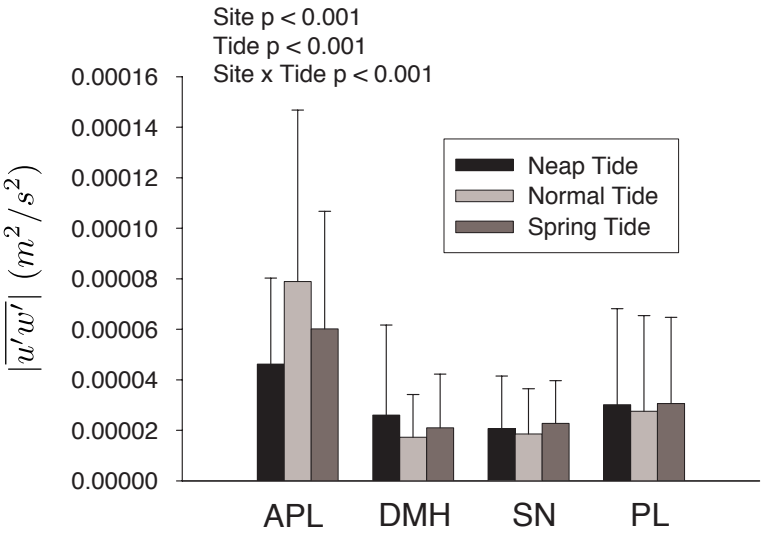

Figure 8: Ensemble average of the absolute value of the burst-averaged values of the Reynolds shear stress ($|\overline{u'w'}|$ (m^2/s^2)). Error bars represent one standard deviation. For the number of bursts included in calculating ensemble averages see Tables 1 and 2. APL = Across from Priest Landing, DMH = Dead Man's Hammock, SN = Skidaway Narrows, and PL = Priest Landing. Statistical significance was determined using a two-way ANOVA.

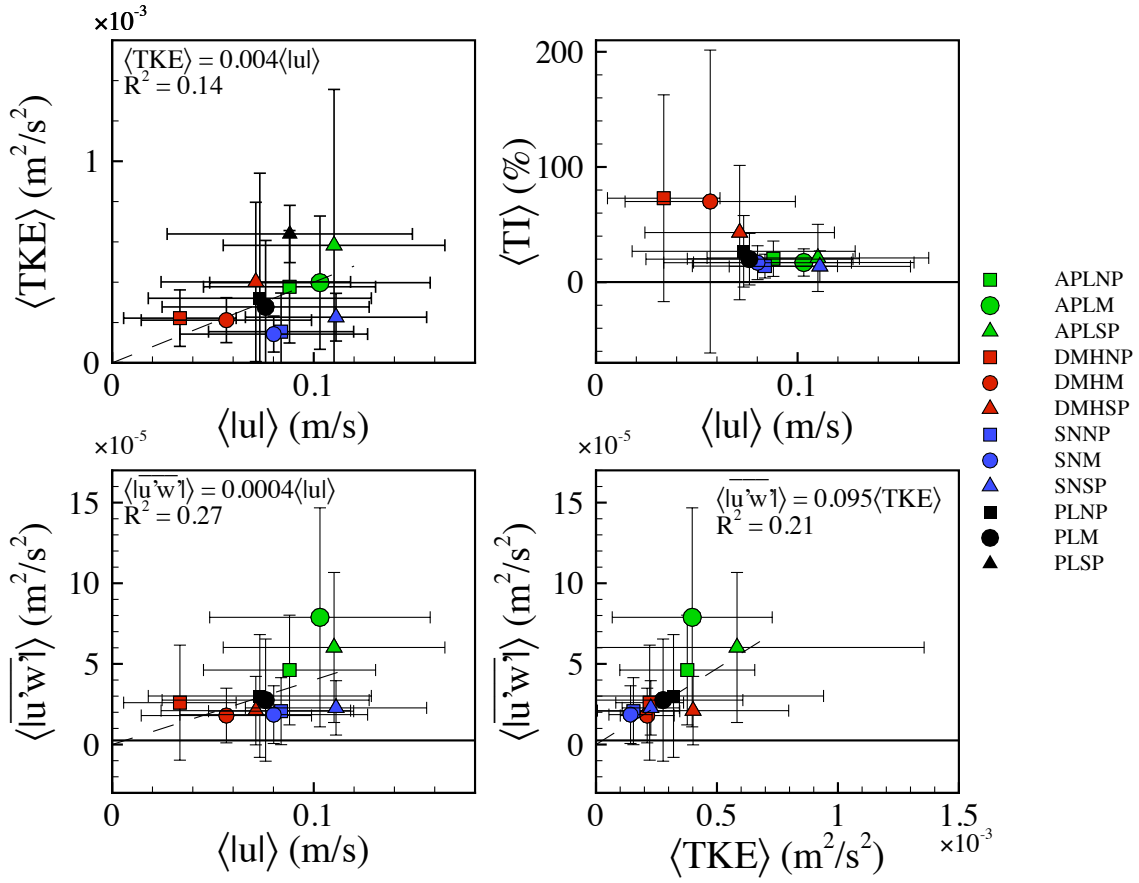

Figure 9: Relationships between values of turbulent flow parameters for emsemble averages of all sites by tidal type combinations. Data sets are named using the convention of site followed by tidal type: APL (green) = Across from Priest Landing, DMH (red) = Dead Man's Hammock, SN (blue) = Skidaway Narrows, PL (black) = Priest Landing; NP = neap tide, NL = normal tide, and SP = spring tide. Dashed lines show the line of best fit for a linear trend. Significance was determined using linear regression analysis. Brackets around each turbulent flow parameter axis label indicates the ensemble averaged (approx. 140 bursts) value. Error bars represent one standard deviation.

References

A. Abelson and M. Denny. Settlement of marine organisms in flow. *Annual Review of Ecology and Systematics*, 28:317–339, 1997.

R. G. Bell, T. M. Hume, T. J. Dophin, M. O. Green, and R. A. Walters. Characterisation of physical environmental factors on an intertidal sandflat, manukau harbour, new zealand. *Journal of Experimental Marine Biology and Ecology*, 216:11–31, 1997.

J. S. Bendat and A. G. Piersol. *Random data: Analysis and measurement procedures. 4^{th} Edition*. John Wiley and Sons, Hoboken, N. J., 2010.

A. Y. Benilov and B. N. Filyushkin. Application of methods of linear filtration to an analysis of fluctuations in the surface layer of the sea. *Izv Atmospheric and Ocean Physics*, 6:810–819, 1970.

W. A. Berry, D. R. Webster, M. L. Wilson, M. C. Ferner, D. L. Smee, and M. J. Weissburg. Characterization of turbulent hydrodynamics in the intertidal zone of a small estuary with respect to predator-prey chemical signaling. 2011.

M. Carriker. Observations on the penetration of tightly closing bivalves by *Busycon* and other predators. *Ecology*, 32:73–83, 1951.

H. Chanson, R. Brown, J. Ferris, I. Ramsay, and K. Warburton. Preliminary measurements of turbulence and environmental parameters in a sub-tropical estuary of eastern australia. *Environmental Fluid Mechanics*, 5:553–575, 2005.

H. Chanson, M. Trevethan, and S. Aoki. Acoustic doppler velocimetry (adv) in small

estuary: Field experience and signal post-processing. *Flow Measurement and Instrumentation*, 19:307–313, 2008.

M. B. Collins, Z. Ke, and S. Gao. Tidally-induced flow structure over intertidal flats. *Estuarine, Coastal and Shelf Science*, 46:233–250, 1998.

M. Ferner and M. J. Weissburg. Slow-moving predatory gastropods track prey odors in fast and turbulent flow. *Journal of Experimental Biology*, 208:809–819, 2005.

M. C. Ferner, D. L. Smee, and M. J. Weissburg. Habitat complexity alters lethal and non-lethal olfactory interactions between predators and prey. *Marine Ecology Progress Series*, 374:13–22, 2009.

C. Finelli, N. D. Pentcheff, R. K. Zimmer, and D. S. Wethey. Physical constraints on ecological processes: A field test of odor-mediated foraging. *Ecology*, 81:784–797, 2000.

D. G. Goring and V. I. Nikora. Despiking acoustic doppler velocimeter data. *Journal of Hydraulic Engineering*, 128:117–126, 2002.

W. D. Grant, III A. J. Williams, and S. M. Glenn. Bottom stress estimates and their prediction on the northern california continental shelf during code-1: The importance of wave-current interaction. *Journal of Physical Oceanography*, 14:506–527, 1984.

A. Hines, A. M. Haddon, and L. E. Wierchert. Guild structure and foraging impact of blue crabs and epibenthic fish in a subestuary of chesapeake bay. *Marine Ecology Progress Series*, 67:105–126, 1990.

A. H. Hines, T. G. Wolcott, E. Gonzalez-Gurriaran, J. L. Gonzalez-Escalante, and J. Freire. Movement patterns and migrations in crabs: Telemetry of juvenile and adult

behaviour in *Callinectes sapidus* and *Maja squinado*. *Journal of the Marine Biology Association of the U. K.*, 75:27–42, 1995.

J. Jackson, D. R. Webster, S. Rahman, and M. J. Weissburg. Bed roughness effects on boundary-layer turbulence and consequence for odor-tracking behavior of blue crabs *Callinectes sapidus*. *Limnology and Oceanography*, 52:1883–1897, 2007.

K. Kawanisi and S. Yokosi. Mean and turbulence characteristics in a tidal river. *Estuarine, Coastal and Shelf Science*, 38:447–469, 1994.

P. Le Hir, W. Roberts, O. Cazaillet, M. Christie, P. Bassoullet, and C. Bacher. Characterization of intertidal flat hydrodynamics. *Continental Shelf Research*, 20: 1433–1459, 2000.

S. A. Levin. The problem of patterns and scale in ecology. *Ecology*, 73:1943–1967, 1992.

D. C. Miller, C. L. Muir, and O. A. Hauser. Detrimental effects of sedimentation on marine benthos: What can be learned from natural processes and rates. *Ecological Engineering*, 19:211–232, 2002.

J. Pawlik and C. A. Butman. Settlement of a marine tube worm as a function of current velocity: Interacting effects of hydrodynamics and behavior. *Limnology and Oceanography*, 38:1730–1740, 1993.

S. Powers and J. N. Kittinger. Hydrodynamic mediation of predator-prey interactions: Differential patterns of prey susceptibility and predator success explained by variation in water flow. *Journal of Experimental Marine Biology*, 273:171–187, 2002.

K. Shiono and J. R. West. Turbulent perturbations of velocity in the conwy estuary. *Estuarine, Coastal, and Shelf Science*, 25:533–553, 1987.

D. Smee and M. J. Weissburg. Claming up: Environmental forces diminish the perceptive ability of bivalve prey. *Ecology*, 87:1587–1598, 2006.

D. Smee, M. C. Ferner, and M. J. Weissburg. Alteration of sensory abilities regulates the spatial scale of nonlethal predator effects. *Oecologia*, 156:399–409, 2008.

D. L. Smee, M. C. Ferner, and M. J. Weissburg. Hydrodynamic sensory stressors produce nonlinear predation patterns. *Ecology*, 91:1391–1400, 2010.

M. Trevethan and H. Chanson. Turbulent mixing in a small estuary: Detailed measurements. *Estuarine, Coastal and Shelf Science*, 81:191–200, 2009.

M. Trevethan, H. Chanson, and R. Brown. Turbulent measurements in a small subtropical estuary with semidiurnal tides. *Journal of Hydraulic Engineering*, November:1665–1670, 2008.

J. H. Trowbridge. On a technique for measurement of turbulent shear stress in the presence of surface waves. *Journal of Atmospheric and Oceanic Technology*, 15:290–298, 1998.

G. Voulgaris and S. T. Meyers. Temporal variability of hydrodynamics, sediment concentration and sediment settling velocity in a tidal creek. *Continental Shelf Research*, 24:1659–1683, 2004.

R. L. Walker and K. R. Tenore. The distribution and production of the hard clam, *Mercenaria mercenaria*, in wassaw sound, georgia. *Estuaries*, 7:19–27, 1984.

D. R. Webster and M. J. Weissburg. The hydrodynamics of chemical cues among aquatic organisms. *Annual Review of Fluid Mechanics*, 41:73–90, 2009.

M. J. Weissburg. The fluid dynamical context of chemosensory behavior. *Biological Bulletin*, 198:188–202, 2000.

M. J. Weissburg and R. K. Zimmer-Faust. Life in moving fluids: Hydrodynamic effects on chemosensory-mediated predation. *Ecology*, 74:1428–1443, 1993.

M. J. Weissburg and R. K. Zimmer-Faust. Odor plumes and how blue crab use them in finding prey. *Journal of Experimental Biology*, 197:349–375, 1994.

J. H. Zar. *Biostatistical Analysis. 4^{th} Edition.* Prentice Hall, Upper Saddle River, N. J., 1999.

R. Zimmer-Faust, C. M. Finelli, N. D. Pentcheff, and D. S. Wethey. Odor plumes and animal navigation in turbulent water flow: A field study. *Biological Bulletin*, 188: 111–116, 1995.

Tide and wind effects on the fluctuating flow parameters in shallow intertidal salt marsh habitats

Miranda L. Wilson[1], Donald R. Webster[2], and Marc J. Weissburg[1]

[1]School of Biology, Georgia Institute of Technology

[2]School of Civil and Environmental Engineering, Georgia Institute of Technology

1 Introduction

The ability of predators to locate food can affect the abundance and distribution of prey populations. This is especially important in estuary systems along the East coast of the United States where blue crabs (Hines et al. 1990) and whelks (Carriker 1951) are two key odor-mediated predators on infaunal bivalve populations. Odor-mediated predators extract information from chemical cues that are transported and shaped by the flowing environment to locate resources. Their ability to do this efficiently determines their impact on prey populations in natural environments. Species-specific predation rates by these predators appear to be dependent on spatially- and temporally-specific local flow conditions, which vary with site and bulk flow characteristics (Smee et al. 2010, also see Chapter 5). By combining information about the fluid environment with corresponding biological behavior, informed hypotheses can be formulated as to the spatial and temporal patterns in predation success. By extension, we gain a better understanding of the ability of predators to control and shape prey populations.

To date, information about turbulent flow characteristics in near-bed estuarine habitats has been relegated to short sampling time periods, irrelevant locations above the substrate (i.e. not in the near-bed environments where odor-mediated predators forage),

arbitrarily-selected sampling time periods, and few study sites. A handful of recent studies have provide limited data, however (Smee et al. 2008, Ferner et al. 2009, Smee et al. 2010, and Berry et al. 2011, see Chapter 5). Some studies have investigated energy and momentum transport processes in estuaries, but have failed to adequately account for wave contributions to the fluctuating velocity (although see Shaw and Trowbridge 2001 and Bricker and Monismith 2007) or spatial and temporal differences in the wave component of fluctuating flow parameters throughout estuary systems. To our knowledge, no study of the flow environment of the intertidal zone of small-scale estuary systems has examined the wave components of fluctuating flow parameters (turbulent kinetic energy and covariance) over large spatial and temporal scales (although see Berry et al. [2011] for wave contributions during single tidal cycles). Hence, information about turbulent flows experienced by benthic foragers is largely unknown, preventing adequate development of hypotheses as to how physical parameters may impact interspecific interactions over temporal and spatial scales that are relevant to odor-mediated predator and prey populations.

Turbulence in the water column can be mediated by tidal forcing (Grant et al. 1984), the presence of whitecapping and breaking waves caused by wind forcing (Terray et al. 1996), and waves transferring energy and momentum to the water column through orbital motion (discussed in Jones and Monismith [2008]). Wave motion and tidal forcing enhance the transport of energy and momentum to the near-bed environment by increasing the thickness of the wind-affected surface layer relative to the bed stress log layer (Jones and Monismith 2008) and enhancing the dissipation rate of turbulent kinetic energy from surface layers toward the near-bed environment (Agrawal et al. 1992).

Despite the importance of flow conditions in shaping interactions between organisms,

many ecologists fail to measure water flow during field experiments or reproduce natural flow regimes in laboratory trials (Zimmer and Zimmer 2008). This prevents an understanding of how ecological interactions may vary naturally under different hydrodynamic conditions and inhibits the scope of processes used to understand patterns in data. Adequately measuring and reproducing natural hydrodynamic conditions (flow velocity and turbulence) requires expensive equipment and technological expertise that are not normally included in the typical ecologists' repertoire. It would be helpful for ecologists if adequate surrogate data that were easily collected and interpreted could be identified that would serve as a proxy for estimating flow velocity and turbulence characteristics in natural settings.

Wind speed and tidal range may be good candidates for surrogate data to make predictions about hydrodynamic environments, as these two parameters are known to have large influences on wave motion and bulk velocity characteristics, respectively. Our objective is to understand how wind and tidal forcing influence the distribution of wave and turbulent components of fluctuating flow parameters between sites and at large temporal scales to assess the predictive ability of these parameters in estimating velocity and turbulence characteristics. Information about the wave and turbulent components of the fluctuating kinetic energy and covariance also can help make predictions as to the distribution and temporal patterns of wind and tidal forcing effects on these fluctuating flow parameters and ultimately, their influence on odor-mediated predator-prey interactions. If wind speed and tidal range correlate well with the wave and turbulent components of fluctuating flow parameters, ecologists should be able to use them to supplement difficult measurements of flow when generating hypotheses and explaining patterns of interactions that are mediated by hydrodynamic processes.

We measured velocity-time series at multiple sites in Wassaw Sound, GA over a variety of different tidal forcing strengths (neap, normal, and spring tides) and naturally occurring wind speeds. We calculated the wave components of fluctuating kinetic energy and Reynolds shear stress as a function of site and tidal type. We also calculated correlation coefficients for comparisons of values of fluctuating flow parameters and wind speed or tidal range to assess their predictive capacities. Based on prior knowledge of this system (Berry 2009, Berry et al. 2011), we predict that the wave components of fluctuating kinetic energy and covariance will be greater in sites that have larger fetch (allowing generation of wind waves) and during neap tides when the transfer of energy and momentum generated from wave motion can penetrate further into the near-bed environment because of shallower water depth. We also expect to see large correlation coefficients for comparisons between tidal range and flow velocity and between wind speed and the wave component of fluctuating flow parameters (kinetic energy and covariance). We deployed multiple acoustic Doppler velocimeters (ADVs) in four sites over a three month period to assess these hypotheses.

2 Methods

2.1 Data Collection

Time-series of flow velocity were collected from June to August 2010 at four sites in Wassaw Sound, GA and its tributaries: Dead Man's Hammock (DMH), Skidaway Narrows (SN), across from Priest Landing (APL), and Priest Landing (PL) (comparison site) (Figure 1). Sites are similarly characterized by semi-diurnal tidal flow with ranges of 2 to 3 m. All sites are exposed to largely unidirectional flows during ebb and flood tides. Sites all

contain substrates of mud and fine sand, are bordered by marsh grass (*Spartina alterniflora*) or oyster reefs (*Crassostrea virginica*), and range in salinity from 20 to 28 ppt (Smee et al. 2010).

Four acoustic Doppler velocimeters (ADVs) (NortekUSA Vector) were simultaneously placed within each site, with each site measured over different dates during the sampling period. Instruments were placed 1 m, 5 m, and 10 m from a reference instrument within each site. Concurrent to measurements taken within each site, two ADVs were placed 1 m apart at the Priest Landing comparison site. Flow velocity at the Priest Landing comparison site was also recorded for an additional 35 days, independent of the other three sites. All instruments were placed parallel to the water line at the mean low tide level. The sampling volume of each instrument was approximately 0.10 m above the substrate. This experimental deployment was repeated for each of the four sites and for each of three tidal types (spring tide [SP], neap tide [NP], and normal tide [NL]).

All ADVs recorded three components of velocity, pressure, signal-to-noise ratios, and correlation coefficients over 4 consecutive complete tidal cycles (from low tide to subsequent low tide) for each tidal type deployment. Instruments were placed in the field such that the x-velocity was predominately the along-stream component and the direction upwards from the substrate was represented by a positive z-velocity. During data analysis, the x- and y-velocity components were rotated to maximize the magnitude of the x-velocity component and to ensure that the x-velocity was positive for flood tide and negative for ebb tide. Data were collected continuously at 16 Hz during 5 minute bursts, which were separated by 10 minutes.

Tidal ranges were obtained during the sampling period for Romerly Marsh Creek (Figure 1) from published tables (http://www.tidesandcurrents.noaa.gov). Tidal ranges

from only one location were used because published data from Romerly Marsh Creek are highly similar to other sites in Wassaw Sound and its tributaries. Average and maximum wind speeds were obtained from the Skidaway Institute of Oceanography weather station (Figure 1) at 5 minute intervals (corresponding to the 5 minute bursts of recorded water velocity time-series).

2.2 Data Analysis

2.2.1 Data Filtering

ADV data were filtered to remove erroneous samples by discarding individual bursts if the mean correlation coefficient calculated was less than 70 % and if bursts contained more than 500 consecutive points whose mean correlation coefficients were less than 70%. We also filtered out erroneous data that manifested as "spikes" because of aliasing of the Doppler signal. We used the phase filtering method of Goring and Nikora [2002] to identify, remove and replace spikes throughout our data set (see Chapter 5 for more detailed information about data filtering).

2.2.2 Identification of the Wave Component of Fluctuating Flow Parameters

The presence of wind waves in shallow water estuaries results in wave motion contributions to fluctuating flow parameters. Fluctuations from waves also can contribute to the turbulence signature when sensors are aligned improperly with the principal axis or when there is sloping bed geometry (Grant et al. 1984, Trowbridge 1998). The contribution of wave motion to fluctuating flow parameters should not be considered turbulence because of their low frequency ranges, periodicity, and orbital motion.

We used the coherence between the velocity and pressure measurements (as seen in Benilov and Filyushkin [1970]) to identify and separate the wave component of the fluctuating kinetic energy and the covariance using the methodology developed by Berry et al. [2011]. Fluctuations in the velocity components due to wave motions are coherent to simultaneously measured fluctuations in the water surface level (recorded as pressure in our data; Benilov and Filyushkin 1970). Correspondingly, the component of the fluctuating velocity that is not coherent with the fluctuating pressure can be attributed to turbulence. The following is a brief description of the calculations involved in separating the wave component of the covariance (and analogously the variance of each velocity component to separate the wave component of the fluctuating kinetic energy). See Chapter 5 and Berry et al. [2011] for a more thorough description of the calculations.

Instantaneous velocity can be decomposed into the mean component $\overline{u}$, the wave motion component $\tilde{u}$, and the turbulent fluctuation component u':

$$u = \overline{u} + \tilde{u} + u' \tag{1}$$

Trends due to rising or falling tides were first removed from the velocity and pressure time series (each 5 minute burst) using a linear trend removal (Bendat and Piersol 2010), and the mean was subtracted to obtain the fluctuating component of velocity and pressure. The notation employed below imples that the mean component is therefore zero. The coherence function for the u component of velocity and pressure (p) was then calculated as a function of frequency (following the methodology of Benilov and Filyushkin [1970]):

$$\gamma^2(\omega) = \frac{S_{up}(\omega)S^*_{up}(\omega)}{S_{uu}(\omega)S_{pp}(\omega)} \tag{2}$$

where S_{up} is the cross-spectral density (CSD) of u and p, S_{uu} and S_{pp} are power spectral density (PSD) functions, ω is frequency, and $*$ represents the complex conjugate.

The PSD for the turbulent portion of the signal was then calculated (assuming that the coherence between velocity and pressure is due to wave influence) using:

$$S_{u'u'}(\omega) = [1 - \gamma^2(\omega)]S_{uu}(\omega) \tag{3}$$

which was then used to calculate the magnitude of the turbulent velocity fluctuation $|U'_j|$ as a function of discrete frequency (denoted with index j) via:

$$S_{u'u'j} = \frac{1}{d\omega}|U'_j|^2 \tag{4}$$

The above calculations were repeated for the w component of velocity and pressure. The Reynolds shear stress was then calculated by incorporating the phases of each velocity component with the magnitude of the turbulent velocity fluctuation. Velocity components can be expressed using phasor notation of the Fourier coefficient according to:

$$U_j = |U_j|e^{i\angle U_j} \text{ and } W_j = |W_j|e^{i\angle W_j} \tag{5}$$

where the phases are defined by:

$$\angle U_j = arctan\left[\frac{Im(U_j)}{Re(U_j)}\right] \text{ and } \angle W_j = arctan\left[\frac{Im(W_j)}{Re(W_j)}\right] \tag{6}$$

Using this the CSD can be expressed as:

$$U_j^* W_j = |U_j||W_j| e^{j(\angle W_j - \angle U_j)} = |U_j||W_j|(\cos(\angle W_j - \angle U_j) - i\sin(\angle W_j - \angle U_j)) \quad (7)$$

and the Reynolds shear stress can be calculated using:

$$\overline{u'w'} = \sum_j U_j'^* W_j' = \sum_j |U_j'||W_j'| \cos(\angle W_j - \angle U_j) \quad (8)$$

where $|U_j'|$ and $|W_j'|$ are calculated from Equation (4) and $\angle U_j$ and $\angle W_j$ are calculated from Equation (6).

We used this methodology to calculate the wave component of the fluctuating kinetic energy and covariance (KE_{wave} and $|\overline{\tilde{u}\tilde{w}}|$, respectively) for all bursts in each data set except the first two and last two bursts of each tidal cycle for data sets collected at the Priest Landing comparison site. Two downward facing, fixed stem ADVs at the Priest Landing site were mounted such that they were able to record velocity data while the pressure sensor was not immersed at the beginning and end of each tidal cycle, which prevented the calculation of coherence between velocity and pressure for these bursts.

Mean fluctuating characteristics also were calculated for each burst. Turbulence parameters calculated are as follows:

$$Total\ Fluctuating\ KE = 0.5(\overline{u - \overline{u}^2} + \overline{v - \overline{v}^2} + \overline{w - \overline{w}^2}) \quad (9)$$

$$TKE = 0.5(\overline{(u')^2} + \overline{(v')^2} + \overline{(w')^2}) \quad (10)$$

$$KE_{wave} = Fluctuating\ KE - TKE \tag{11}$$

$$Total\ Fluctuating\ Covariance = \overline{u - \overline{u}w - \overline{w}} \tag{12}$$

$$Reynolds\ Shear\ Stress = \overline{u'w'} \tag{13}$$

$$\overline{\tilde{u}\tilde{w}} = \overline{u - \overline{u}w - \overline{w}} - \overline{u'w'} \tag{14}$$

$$Turbulence\ Intensity\ (TI) = \frac{\sqrt{\overline{(u')^2} + \overline{(v')^2} + \overline{(w')^2}}}{\sqrt{\overline{u}^2 + \overline{v}^2 + \overline{w}^2}} * 100 \tag{15}$$

We also calculated the percent contribution of the respective wave contributions to total fluctuating KE and total fluctuating covariance.

2.2.3 Statistical Analysis

To determine the influence of site and tidal type (neap, normal, and spring tide; and any interactions) on values of wave components of fluctuating flow parameters (KE_{wave} and $|\overline{\tilde{u}\tilde{w}}|$) and their percent contribution to the total, we utilized a two-way analysis of variance (ANOVA), which is fairly robust to issues of non-normality (Zar 1999), with site and tidal type as factors. We also utilized non-parametric Kruskal-Wallis tests to confirm significance of one-way comparisons because we were unable to achieve normality via transformation for our fluctuating flow parameters. This was done for each fluctuating flow parameter separately (KE_{wave}, $|\overline{\tilde{u}\tilde{w}}|$, % KE_{wave}, and % $|\overline{\tilde{u}\tilde{w}}|$) using burst-averaged data from the reference instrument at each site and for each deployment period described above (approximately 140 bursts).

We calculated correlation coefficients for comparisons between maximum wind speed and values of fluctuating flow parameters ($|\overline{u}|$, TKE, KE_{wave}, $|\overline{u'w'}|$, and $|\overline{\tilde{u}\tilde{w}}|$) to examine

the relationship between wind speed and values of fluctuating flow parameters by using a non-parametric Spearman correlation for each site separately, including all tidal types. We used burst-averaged data from each site-specific reference instrument to calculate correlation coefficients (approximately 140 bursts). A Spearman correlation also was used to determine if site-specific relationships were similar to comparisons using data from all four sites.

The relationship between wind speed and values of fluctuating flow parameters as a function of sampling duration was further elucidated using long term time-series data from Priest Landing. We assessed comparisons between wind speed (average and maximum) and values of fluctuating flow parameters ($|\overline{u}|$, TKE, KE_{wave}, $|\overline{u'w'}|$, $|\overline{\tilde{u}\tilde{w}}|$, and TI) by calculating correlation coefficients (Spearman correlation) using tidal-cycle-averaged data for each variable. The number of tidal cycles used to calculate correlation coefficients ranged from 4 to 79. Data from individual tidal cycles was sequenced randomly to achieve the desired number of tidal cycles for calculation.

We also assessed comparisons between tidal range and values of fluctuating flow parameters at Priest Landing ($|\overline{u}|$, TKE, KE_{wave}, $|\overline{u'w'}|$, $|\overline{\tilde{u}\tilde{w}}|$, and TI) by calculating correlation coefficients (Spearman correlation). We utilized tidal-cycle-averaged data for all fluctuating flow parameters, with the range of tidal cycles used to calculate correlation coefficients. Again, the number of tidal cycles used to calculate correlation coefficients ranged from 4 to 79 and the sequence was random. Tidal range was calculated by taking the difference between the height above mean low water for the high tide and the average of the height above mean low water for the previous and subsequent low tides using published records (see above).

We also investigated the impact of tidal type and flow direction (flood and ebb) on

values of turbulent flow parameters ($|\overline{u}|$, TKE, and $|\overline{u'w'}|$), because there seemed to be intrinsic asymmetries in values of fluctuating flow parameters between flood and ebb tides. The effect of tidal type and flow direction on values of fluctuating flow parameters was determined using a two-way ANOVA with tidal type and tide direction as factors. Ensemble-averaged values corresponding to flood and ebb tide from the PL site were used for the analysis.

3 Results

3.1 Velocity Data Associated with Wave Motions

There was a significant effect of site ($F_{3,1474} = 67.79, P < 0.001$; Figure 2) on KE_{wave}, with the greatest values of KE_{wave} at the DMH site and the smallest at the SN site. There also was a significant effect of tidal type ($F_{2,1474} = 9.25, P < 0.001$) and interaction between site and tidal type ($F_{6,1474} = 11.37, P < 0.001$), with greater values of KE_{wave} during neap and spring tide at all sites except for the PL site which had the greatest values of KE_{wave} during neap tide only (Figure 2). Non-parametric Kruskal-Wallis tests (site: $H = 745.72$, $df = 3$, $P < 0.001$; tide: $H = 28.58$, $df = 2$, $P < 0.001$) confirmed significance of one-way interactions. The percent wave contribution to total fluctuating KE showed similar patterns to the dimensional values of KE_{wave}. There was a significant effect of site ($F_{3,1474} = 588.38, P < 0.001$) and tidal type ($F_{2,1474} = 16.03, P < 0.001$) on the percent wave contribution to total fluctuating KE (Figure 2). The wave contribution to total fluctuating KE was greatest for the DMH site and smallest for the SN site. Overall, the greatest wave contribution to total fluctuating KE was during neap tide, but there was a significant interaction between site and tidal type ($F_{6,1474} = 10.67, P < 0.001$). Both the

APL and DMH sites had greater wave contributions to total fluctuating KE during neap and spring tide, but the PL site had the smallest contributions during spring tide and there were negligible differences in wave contributions to total fluctuating KE between tidal types at the SN site (Figure 2). Non-parametric Kruskal-Wallis tests (site: $H = 785.66$, $df = 3$, $P < 0.001$; tide: $H = 6.58$, $df = 2$, $P = 0.037$) again confirmed significance of one-way analyses.

Values of $|\overline{\tilde{u}\tilde{w}}|$ showed similar patterns to KE_{wave} based on site and tidal type relationships: there was a significant effect of site ($F_{3,1367} = 98.94, P = 0.001$) and tidal type ($F_{2,1367} = 37.36, P < 0.001$) on values of $|\overline{\tilde{u}\tilde{w}}|$ (Figure 3). There also was a significant interaction between site and tidal type ($F_{6,1367} = 79.90, P < 0.001$). Non-parametric Kruskal-Wallis tests (site: $H = 287.69$, $df = 3$, $P < 0.001$; tide: $H = 8.55$, $df = 2$, $P = 0.017$) confirmed significance of one-way analyses. The SN site had the smallest values of $|\overline{\tilde{u}\tilde{w}}|$, and values of $|\overline{\tilde{u}\tilde{w}}|$ were greater during neap and spring tide at all sites except at the APL site where $|\overline{\tilde{u}\tilde{w}}|$ was greater during the normal tide (Figure 3). The percent wave contribution to total fluctuating covariance also had similar patterns to the wave contribution to total fluctuating KE based on site and tidal type. There was a significant effect of site ($F_{3,1367} = 86.08, P < 0.001$) on the wave contribution to total fluctuating covariance with the greatest percentage of wave contribution at the DMH site (Figure 3). Significance of this one-way interaction was confirmed using a Kruskal-Wallis test ($H = 227.08$, $df = 3$, $P < 0.001$). There also was a significant effect of tide ($F_{2,1367} = 3.52, P < 0.03$) on the percent wave contribution to total fluctuating covariance based on a two-way ANOVA, but this was not confirmed using a one-way non-parametric Kruskal-Wallis test ($H = 2.00$, $df = 2$, $P = 0.367$). There was no significant site by tidal type interaction ($F_{6,1367} = 1.21, P = 0.297$) on the percent wave contribution to total

fluctuating covariance.

3.2 Correlation of Wind Speed and Fluctuating Flow Parameters

There were significant correlations between burst-averaged values of fluctuating flow parameters and maximum wind speed, but significance was site and parameter specific. Comparisons between values of fluctuating flow parameters and average wind speed resulted in similar relationships between correlation coefficients to those calculated using maximum wind speed, although a lower number of correlation coefficients were statistically significant when using average wind speed for comparisons. Therefore, we chose to report results only for comparisons using maximum wind speed. There were significant correlations between values of TKE, KE_{wave}, and $|\overline{\tilde{u}\tilde{w}}|$ with maximum wind speed at the APL site (Table 1). There were similar patterns of significant correlations at the DMH site as at the APL site, with the exception of the correlation between $|\overline{\tilde{u}\tilde{w}}|$ and maximum wind speed, which was not significant. There were no significant correlations between values of any fluctuating flow parameter and maximum wind speed at the PL site, although the correlation coefficient for the comparison between KE_{wave} and maximum wind speed was only marginally insignificant. There were significant correlations between all fluctuating flow parameters (except KE_{wave}) and maximum wind speed at the SN site, but as maximum wind speed increased, values of the fluctuating flow parameters decreased (i.e. correlation coefficients were negative). This relationship cannot be explained by errors in the raw or filtered data. There was a significant correlation for the comparison of KE_{wave} with maximum wind speed (Table 1) when data from all sites were combined (APL, DMH, SN, and PL).

Long-term time-series indicate a close relationship between values of fluctuating flow

parameters and maximum wind speed at the PL site (Figure 4). To quantify the apparent relationship, the correlation coefficient was calculated as a function of the number of tidal cycles. Correlations between wind speed (maximum and average) and $|\overline{\tilde{u}\tilde{w}}|$ at the PL site were significantly different from zero for correlations using sample sizes greater than 9 tidal cycles (Figure 5). More than 43 and 55 tidal cycles were needed to achieve correlation coefficients significantly different from zero for correlations between KE_{wave} and maximum and average wind speed, respectively. Values of $|\overline{u'w'}|$ and TI were never significantly correlated with maximum or average wind speed. Marginally significant correlations between $|\overline{u}|$ and maximum or average wind speed were seen only for comparisons using data from more than 55 tidal cycles (Figure 5).

3.3 Correlation of Tidal Range and Fluctuating Flow Parameters

Long-term time-series at Priest Landing indicate the tight relationship between values of fluctuating flow parameters and tidal range (Figure 6). Correlations between $|\overline{u}|$, TKE, and $|\overline{\tilde{u}\tilde{w}}|$ and tidal range at the Priest Landing site were all significantly different from zero using data from more than 4 tidal cycles (Figure 5). Correlations between $|\overline{u'w'}|$ and tidal range were significantly different from zero using data from more than 9 tidal cycles. Correlations between KE_{wave} and tidal range were marginally significant using data from more than 37 tidal cycles. Values of TI were never significantly correlated with tidal range.

Values of $|\overline{u}|$ were greater during spring tides and during ebb tides (Figure 7). There was a significant effect of flood versus ebb tide on values of the $|\overline{u}|$ component at the PL site ($F_{1,18} = 123.36, P < 0.001$), and a marginally insignificant effect of tidal type ($F_{2,18} = 3.20, P = 0.065$). There was not a significant interaction between tidal type and flood/ebb tide status on values of $|\overline{u}|$ ($F_{2,18} = 0.15, P = 0.86$). There was a significant effect

of tidal type on TKE ($F_{2,18} = 3.59, P = 0.049$), with greater values of TKE during spring tides (Figure 7). There also was a significant effect of flood/ebb tide status on TKE ($F_{1,18} = 6.24, P = 0.022$), but no significant interaction between tidal type and flood/ebb tide status ($F_{2,18} = 1.78, P = 0.19$). Values of $|\overline{u'w'}|$ were greater during ebb tides than during flood tides (Figure 7). There was a significant effect of flood/ebb tide status on values of $|\overline{u'w'}|$ ($F_{1,18} = 113.23, P < 0.001$), but no significant effects of tidal type ($F_{2,18} = 0.20, P = 0.82$) or tidal type by flood/ebb tide status interaction on $|\overline{u'w'}|$ ($F_{2,18} =, P = 0.42$). Similar asymmetries were observed in the values of fluctuating flow parameters for all other sites, with greater values during the ebb portion of the tide compared to the flood portion.

4 Discussion

4.1 Context-Specificity of Wave Components of Fluctuating Flow Parameters

Wave contributions to total fluctuating KE and total fluctuating covariance in our study agree well with previous data reported by Berry et al. [2011] for the same estuary system. The magnitude of wave components of fluctuating turbulent parameters seems site dependent for data from both studies. Wave contributions to total fluctuating KE at our SN site and the Skidaway River site of Berry et al. [2011] were $17 - 19\%$ and $15 - 18\%$, respectively. At our DMH site and the DMH16 site of Berry et al. [2011], wave contributions to total fluctuating KE were $59 - 72\%$ and 56%, respectively. Another study in the same estuary system (Ferner et al. 2009), estimated the contribution of wave activity

to values of fluctuating flow parameters as small, although these results may be accounted for by the relatively simple calculation of wave contributions using the root mean square of wave amplitude as compared to the spectral-based method employed in the current study. Studies focusing on wave contributions to fluctuating flow parameters primarily focus on decomposition techniques (Bricker and Monismith 2007, Trowbridge 1998, Shaw and Trowbridge 2001) and lack discussion of the distribution of wave contributions to values of turbulent flow parameters in different locations or systems, hence preventing comparisons with our study. In the shallow intertidal environments that are of interest in the current study, it is essential to account for wave contributions to values of fluctuating flow parameters to fully assess the turbulent environment that odor-mediated predator may be exposed to while foraging.

Unlike the study of Berry et al. [2011], which compared the wave contribution to values of total fluctuating KE and total fluctuating covariance in a variety of sites in Wassaw Sound, GA using data from one tidal cycle, we were able to collect information about wave contributions to fluctuating flow parameters at a variety of sites over longer periods (4 tidal cycles) of different tidal types (neap, normal, and spring tides). Spatially-explicit patterns of the wave contributions to the fluctuating flow parameters (Figures 2 and 3) suggest that wave contributions may be mediated by the area available for the generation of wind waves (i.e., the fetch). For example, the DMH site, which is exposed to Wassaw Sound and has a fetch that ranges from approximately 5 km to 20 km depending on wind direction (Figure 1), has the largest measured value of KE_{wave} and $|\overline{\tilde{u}\tilde{w}}|$ (Figures 2 and 3). The SN site, in comparison, has the smallest values of KE_{wave} and $|\overline{\tilde{u}\tilde{w}}|$ as well as the smallest fetch (< 1 km), regardless of wind direction. Prevailing wind orientation (202.5° for our study; 204° from Powell and Rinard [1998]; with 0° indicating

winds from due north [Figure 1]) supports the idea of greater wave generation at the APL site, but greater exposure to Wassaw Sound may contribute to the influence of waves at the DMH site (Figure 1). Waves generally slow down and steepen in shallow environments which allows more transfer of energy from wind to wave motion (Holthuijsen 2007), suggesting that the DMH site also may have a greater influence of wave motion on fluctuating flow parameters because of the extensive mudflats that border the site. Data from Berry et al. [2011] support these patterns of wave influence as a function of exposure to Wassaw Sound, but additional sites with significant exposure need to be assessed for comparison.

Differences between sites in the wave contribution to the fluctuating flow parameters may have significant effects on odor-mediated foraging that could not be predicted from examining the turbulent portion of fluctuating flow parameters only. For example, based on values of KE_{wave} (Figure 2), blue crabs would have reduced foraging efficiency and success in the more turbulent environments at the DMH site than the other three sites, but based on values of TKE (See Chapter 5), blue crabs would have reduced foraging at the APL and PL sites relative to the DMH and SN sites. Combining values of KE_{wave} and TKE indicate that the DMH site has greater total fluctuating kinetic energy than the other three sites, suggesting that blue crabs may have reduced foraging in the DMH site relative to the other three sites. Whelk foraging success is less affected by turbulence than blue crabs (Powers and Kittinger 2002, Ferner and Weissburg 2005), suggesting that their dominance at the DMH site (Ferner et al. 2009) may be related to their maintenance of foraging success relative to blue crabs. The wave component of fluctuating kinetic energy represents a larger portion of the total fluctuating kinetic energy at the DMH site than at the SN site (Figure 2), possibly making this site less attractive to foraging blue crabs and

more attractive to whelks. Correlations between maximum wind speed and values of wave components of fluctuating flow parameters at different sites over 4 tidal cycles (Table 1) support site-specific influences of the wave contributions to values of total fluctuating flow parameters. Thus far, no experiments have been done to explicitly connect wave characteristics with plume dispersion and subsequent impacts on chemically-mediated predator-prey interactions. Additional studies are needed to describe wave impacts on odor plume dispersion to better predict predatory behaviors under conditions of wave motion.

Significant differences in the wave components of fluctuating flow parameters, generally and as a function of tidal type, indicate that large-scale tidal forcing may influence the transfer of energy and momentum to the near-bed environment (Figures 2 and 3). The magnitude of wind impacts to near-bed environments will increase as water depth decreases (Agrawal et al. 1992, Terray et al. 1996, Holthuijsen 2007, Jones and Monismith 2008), suggesting that greater wave contributions to values of total fluctuating KE during neap tide (Figure 2) may be attributed to water-depth-specific patterns of TKE. Patterns of wave contributions to values of fluctuating flow parameters also suggest greater contributions during spring tides. This may be associated with increases in Reynolds shear stress throughout the water column, which would increase the size of the wave-affected surface layer and increase momentum flux to the near-bed environment (Jones and Monismith 2008).

The larger the contribution of the wave component to total fluctuating flow parameters, the greater influence any patterns in tidal type dependence will have on values of total fluctuating flow parameters. Specific patterns of mean values of total fluctuating flow parameters based on tidal type will be dependent on corresponding patterns in the wave and turbulent components of total fluctuating flow parameters. Values of total

fluctuating flow parameters suggest that foraging efficiency and success of odor-mediated predators will vary over a roughly weekly time scale (the scale at which tidal types change). It also suggests that care should be taken when designing sampling schema for ecological experiments; taking into account possible variation in predation rates concurrent to changes in tidal type.

Tidal asymmetries are a common component of flow patterns in small-scale estuaries, but the relationship between values of turbulent flow parameters during flood and ebb tide are not dependent on large-scale tidal forcing in our system (neap, normal, and spring tides) (Figure 7). Asymmetries in the $|\overline{u}|$ velocity component, TKE and $|\overline{u'w'}|$ that favor ebb tides (Chanson et al. 2005, Collins et al. 1998) are usually associated with freshwater input, whereas asymmetries that favor flood tide result from local channel topography that acts to slow down tidal propagation (Le Hir et al. 2000). Our sites have very little freshwater input (Walker and Tenore 1984) despite very large asymmetries in $|\overline{u}|$ favoring ebb tide. Although there are differences in $|\overline{u}|$ and TKE based on tidal type, there were no changes in the strength and direction of the flood/ebb asymmetry (although this has been seen in other estuary systems [Trevethan et al. 2008]). The asymmetry of $|\overline{u}|$ between flood and ebb tide in our system is comparable to that for laboratory experiments challenging blue crabs to locate prey odors under different hydrodynamic conditions (Weissburg and Zimmer-Faust 1993). Weissburg and Zimmer-Faust [1993] observed that an increase in flow velocity by 10.6 cm/s (from 3.8 cm/s to 14.4 cm/s), which closely mirrors differences in our study between $|\overline{u}|$ during flood and ebb tides (Figure 7), resulted in a roughly 50% decrease in foraging success (from 22% to 10% success). To our knowledge, no studies have examined differences in predatory success between ebb and flood tidal periods in the field.

4.2 Ability to Predict Fluctuating Flow Parameters

Ecologists often have limited or no ability to make detailed flow and turbulence measurements of the environments used in their field studies. Hence, it is useful to make connections between surrogate information, such as tidal range and wind speed, and mean and fluctuating flow parameters. If robust correlations can be identified for the intertidal zone, then surrogate data will provide insightful characterization of the flow environment when detailed assessment is impossible or impractical.

There are site-dependent differences in the predictive capacity of maximum wind speed to estimate values of fluctuating flow parameters (Table 1). Wind speed is directly related to the formation of whitecapping waves (Jones and Monismith 2008), which increases orbital motion in the water column and helps transfer energy and momentum to near-bed environments. The relationship between maximum wind speed and values of fluctuating flow parameters is not related to the distance between each site and the location where wind speed was measured (Figure 1). The wind speeds recorded during our observation period were relatively small compared to others examining the relationship between wind speed and fluctuating flow parameters (our study = 0 to 8 m/s, Jones and Monismith [2008] = 0 to 15 m/s, Bricker et al. [2005] = 0 to 12 m/s), which decreases the range of our comparisons and the power needed to detect a significant relationship.

Wind speed (both maximum and average) and tidal range are correlated to values of fluctuating flow parameters at the Priest Landing Site, but the amount of data needed (tidal cycles) to achieve significant predictive ability varies as a function of specific fluctuating flow parameter. Wind speed is significantly correlated with $|\overline{\widetilde{u}\widetilde{w}}|$ when more than 9 tidal cycles are used to calculate correlation coefficients, but KE_{wave} is significantly

correlated with maximum wind speed only when more than 43 tidal cycles are used. The majority of fluctuating flow parameters ($|\overline{u}|$, TKE, $|\overline{u'w'}|$, and $|\overline{\tilde{u}\tilde{w}}|$) are significantly correlated with tidal range using data from more than 4 tidal cycles. Values of fluctuating flow parameters track more closely with those of tidal range than wind speed (compare Figures 4 and 6), thus we suggest that tidal range is a better predicator than wind speed for values of fluctuating flow parameters.

The predictive capacity of tidal range and wind speed to values of fluctuating flow parameters, should only be used at temporal scales similar to those of the ecological experimentation. Most ecological experiments occur over short time scales (e.g. 48 hrs in Smee and Weissburg 2006, see Chapter 1; although see Ferner et al. 2009 for experiments on the scale of 28 days) where correlations between wind speed or tidal range and values of fluctuating flow parameters are not significant. Tidal range seems to be a good predictor of a wide range of fluctuating flow parameters ($|\overline{u}|$, TKE, $|\overline{u'w'}|$, and $|\overline{\tilde{u}\tilde{w}}|$) at time scales greater than 4 complete tidal cycles, whereas wind speed seems to be a good predictor of $|\overline{\tilde{u}\tilde{w}}|$ and KE_{wave} at time scales greater than 9 and 43 complete tidal cycles, respectively.

4.3 Summary Comments

Fluctuating flow parameters have the capacity to influence ecological interactions in intertidal near-bed habitats in salt marsh systems, making characterization of the hydrodynamic environment essential in understanding the processes mediating interactions. The predictive capacity of both tidal range and wind speed can give some insight to the mean and fluctuating flow parameters organisms are exposed to, but we suggest that these relationships only be utilized if the temporal scale of ecological experimentation matches that of significant correlations between wind speed or tidal range and fluctuating flow

parameters. We also caution that the influence of wind speed on values of fluctuating flow parameters can vary between sites at small temporal scales, suggesting that the outcome of ecological interactions may be site-specific. Additional site-specific information about wind speed, tidal range, and values of fluctuating flow parameters needs to be assessed to determine relationships between these parameters for longer temporal scales throughout estuary systems.

5 Figures

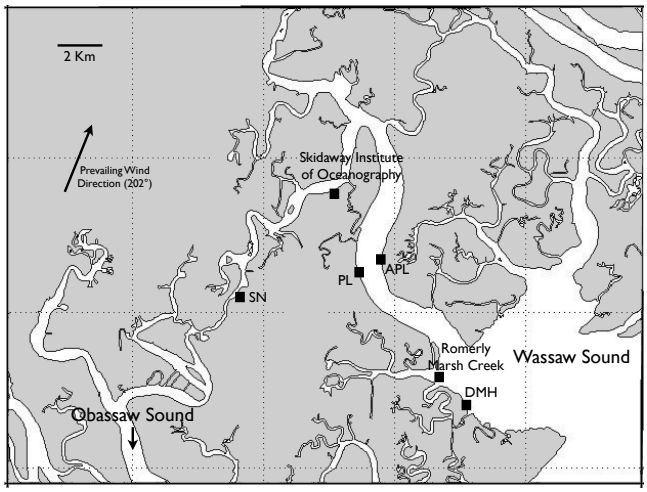

Figure 1: Map of Wassaw Sound, Georgia where instruments were deployed June-August 2010. DMH = Dead Man's Hammock, PL = Priest Landing, APL = Across from Priest Landing, SN = Skidaway Narrows. Also shown are the locations of the Skidaway Institute of Oceanography (site of wind speed measurement) and Romerly Marsh Creek (site of tidal range data).

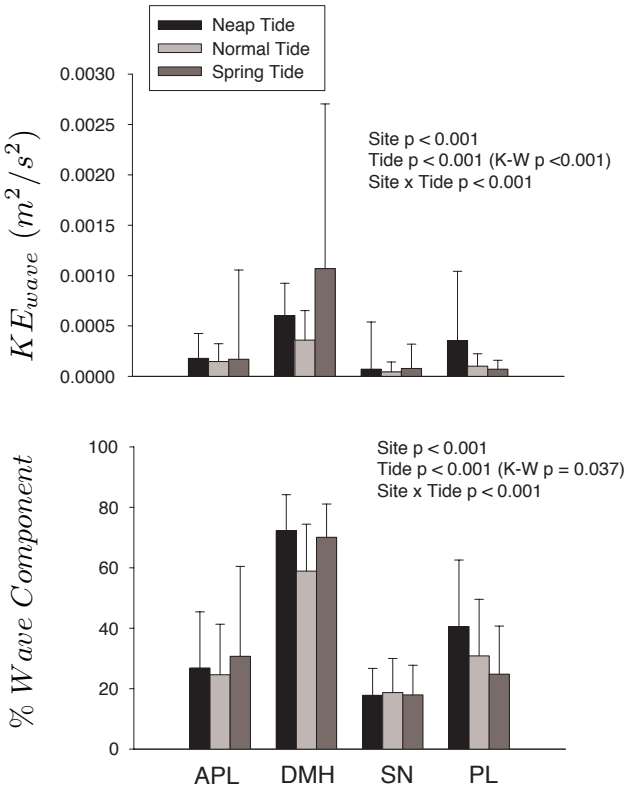

Figure 2: Ensemble average of burst-averaged values of KE_{wave} $(m^2/s^2$; top) and percentage of the total fluctuating kinetic energy attributable to the wave component (bottom). Error bars represent one standard deviation. The number of bursts included was: 149, 145, and 137 (APL; neap tide, normal tide, spring tide, respectively); 129, 144, 143 (DMH; neap, normal, spring, respectively); 141, 173, 126 (SN; neap, normal, spring, respectively); 128, 134, 136 (PL; neap, normal, spring, respectively), where APL = Across from Priest Landing, DMH = Dead Man's Hammock, SN = Skidaway Narrows, and PL = Priest Landing. Statistical significance was determined using a two-way ANOVA, with confirmation of one-way comparisons shown using a Kruskal-Wallis test (K-W).

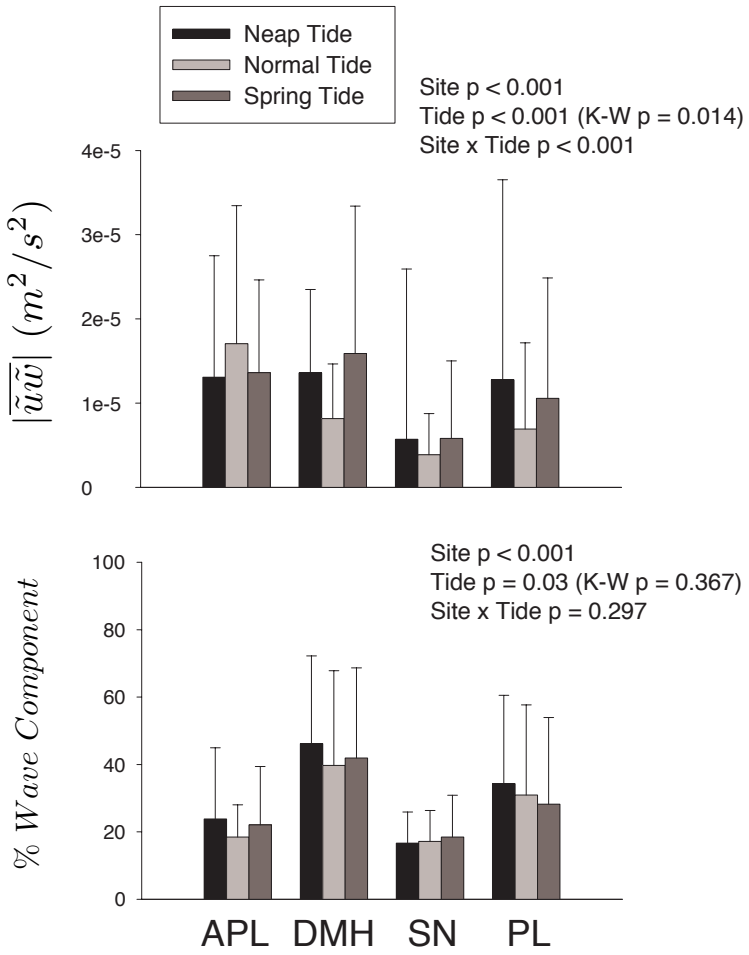

Figure 3: Ensemble average of burst-averaged values of $|\widetilde{\widetilde{u}\widetilde{w}}|$ $(m^2/s^2$; top) and the percentage of the total covariance attributable to the wave component (bottom). Error bars represent one standard deviation. The number of bursts included is the same as reported in Figure 2. APL = Across from Priest Landing, DMH = Dead Man's Hammock, SN = Skidaway Narrows, and PL = Priest Landing. Statistical significance was determined using a two-way ANOVA, with confirmation of one-way comparisons shown using a Kruskal-Wallis test (K-W).

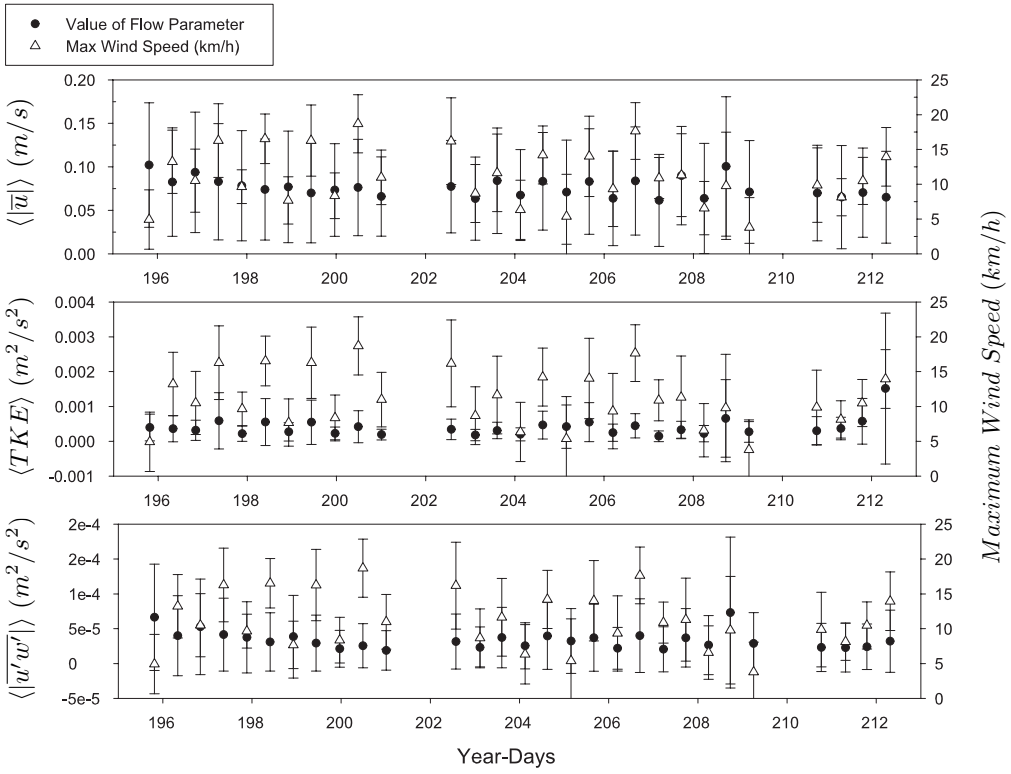

Figure 4: Long-term time-series of $\langle|\overline{u}|\rangle$ (top), $\langle TKE\rangle$ (middle), and $\langle|\overline{u'w'}|\rangle$ (bottom) at Priest Landing (filled circles). Maximum wind speed data (open triangles) are overlaid on each turbulent flow parameter to visually show the correlation. Values represent the tidal-cycle-average for all turbulent flow parameters and maximum wind speed (as denoted by angle brackets). Wind speed data were obtained from the Skidaway Institute of Oceanography weather station (see Figure 1). Error bars for turbulent flow parameters and maximum wind speed represent one standard deviation.

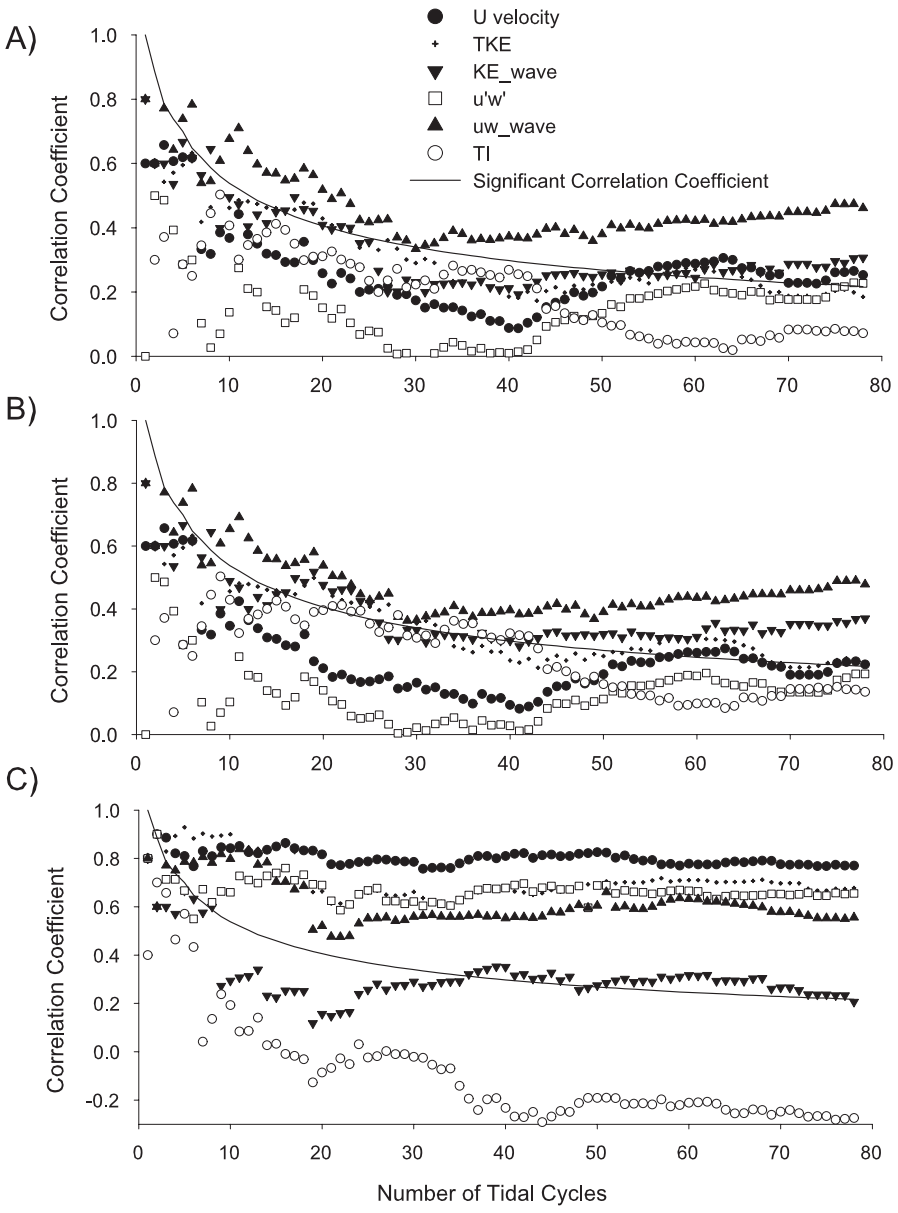

Figure 5: Correlation coefficients with (A) maximum wind speed, (B) average wind speed, and (C) tidal range as a function of the amount of data (number of tidal cycles) included in the calculation. Correlation coefficients shown for comparisons between $|\overline{u}|$ (closed circles), TKE (plus), KE_{wave} (closed inverted triangle), $|\overline{u'w'}|$ (open square), $|\widetilde{u}\widetilde{w}|$ (closed triangle), or TI (open circle). Minimum values of significant correlation coefficients are shown by the solid line. Correlation coefficients above this line are significantly different from zero.

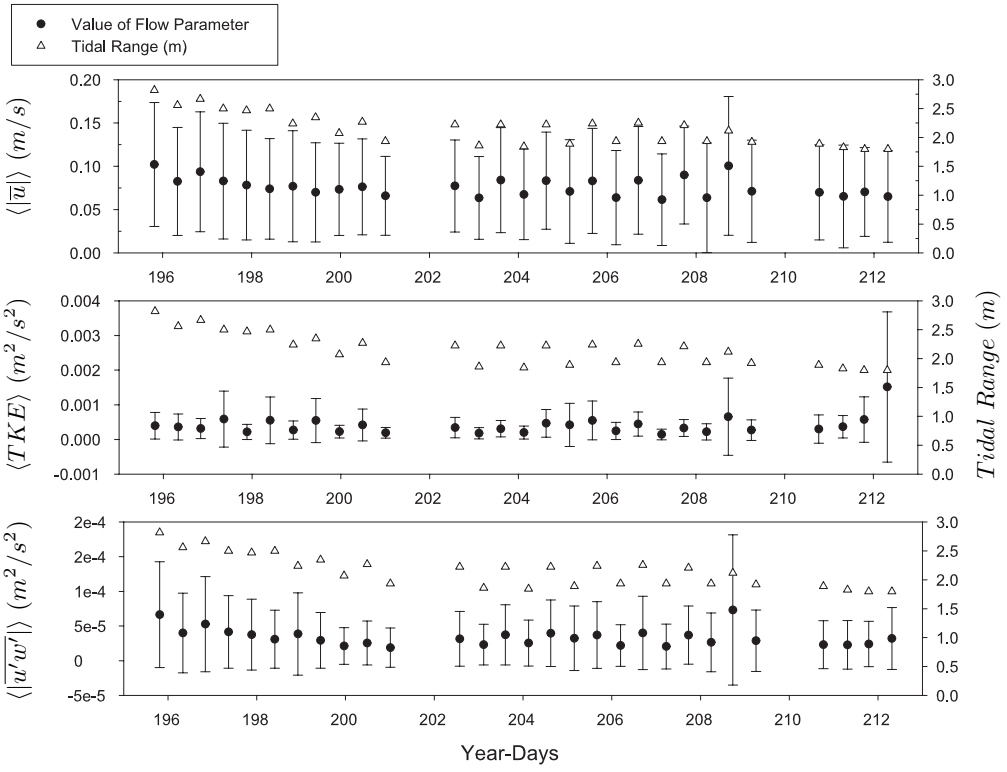

Figure 6: Long-term time-series of $\langle|\overline{u}|\rangle$ (top), $\langle TKE\rangle$ (middle), and $\langle|\overline{u'w'}|\rangle$ (bottom) at Priest Landing (filled circles). Tidal range data (open triangles) are overlaid on each turbulent flow parameter to visually show the correlation. Values represent the tidal-cycle-average for all turbulent flow parameters (as denoted with angle brackets). Tidal range was calculated as the difference between the height above mean low water for the high tide and the average of the height above mean low water for the previous and subsequent low tides. Tidal heights were obtained from published records for Romerly Marsh Creek (see Figure 1). Error bars for turbulent flow parameters represent one standard deviation.

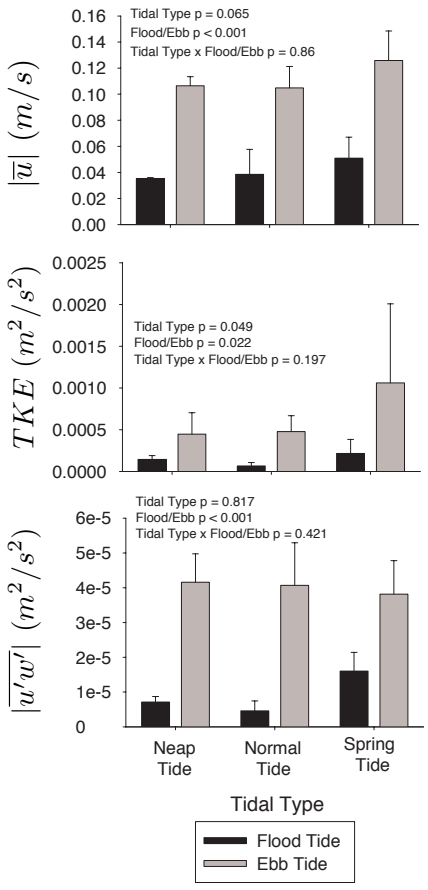

Figure 7: Effect of tidal type and ebb or flood flow on values of the turbulent flow parameters at the Priest Landing site. Values of turbulent flow parameters were calculated based on averages for flood and ebb portions of the tidal cycle ($N = 8$ for each tidal type). Error bars indicate one standard deviation. Statistical significance was determined using a two-way ANOVA.

Site	Burst. No	$\lvert\overline{u}\rvert$	TKE	KE_{wave}	$\lvert\overline{u'w'}\rvert$	$\lvert\overline{\tilde{u}\tilde{w}}\rvert$
APL	430	0.07	0.13*	0.30*	-0.03	0.15*
DMH	287	0.12	0.15*	0.12*	0.09	-0.03
PL	280	-0.02	0.01	0.10	-0.003	0.05
SN	325	-0.15*	-0.17*	-0.08	-0.14*	-0.14*
All	1322	0.03	0.03	0.08*	-0.01	-0.01

Table 1: Correlation coefficients for comparisons between maximum wind speed and values of fluctuating flow parameters. Data used for comparisons consist of burst averaged values for individual fluctuating flow parameters collected during all tidal type deployments. Wind speed data were acquired from the Skidaway Institute of Oceanography weather station. "Burst No." indicates the number of bursts that were used to calculate correlation coefficients. * indicates correlation coefficients significantly different from zero. Data sets are labeled using site names; APL = Across from Priest Landing, DMH = Dead Man's Hammock, SN = Skidaway Narrows, PL = Priest Landing.

References

Y. C. Agrawal, E. A. Terray, M. A. Donelan, P. A. Hwang, A. J. Williams III, W. M. Drennan, K. K. Kahma, and S. A. Kitaigorodskii. Enhanced dissipation of kinetic energy beneath surface waves. *Nature*, 359:219–220, 1992.

J. S. Bendat and A. G. Piersol. *Random data: Analysis and measurement procedures. 4^{th} Edition*. John Wiley and Sons, Hoboken, N. J., 2010.

A. Y. Benilov and B. N. Filyushkin. Application of methods of linear filtration to an analysis of fluctuations in the surface layer of the sea. *Izv Atmospheric and Ocean Physics*, 6:810–819, 1970.

W. A. Berry, D. R. Webster, M. L. Wilson, M. C. Ferner, D. L. Smee, and M. J. Weissburg. Characterization of turbulent hydrodynamics in the intertidal zone of a small estuary with respect to predator-prey chemical signaling. 2011.

W. A. B Berry. A hydrodynamic characterization of tidal ecosystems with respect to predation. Master's thesis, Georgia Institute of Technology, Atlanta, Georgia, 2009.

J. D. Bricker and S. G. Monismith. Spectral wave-turbulence decomposition. *Journal of Atmospheric and Oceanic Technology*, 24:1479–1487, 2007.

J. D. Bricker, S. Inagaki, S. G. Monismith, and A. M. ASCE. Bed drag coefficient variability under wind waves in a tidal estuary. *Journal of Hydraulic Engineering*, 131: 497–508, 2005.

M. Carriker. Observations on the penetration of tightly closing bivalves by *Busycon* and other predators. *Ecology*, 32:73–83, 1951.

H. Chanson, R. Brown, J. Ferris, I. Ramsay, and K. Warburton. Preliminary measurements of turbulence and environmental parameters in a sub-tropical estuary of eastern australia. *Environmental Fluid Mechanics*, 5:553–575, 2005.

M. B. Collins, Z. Ke, and S. Gao. Tidally-induced flow structure over intertidal flats. *Estuarine, Coastal and Shelf Science*, 46:233–250, 1998.

M. Ferner and M. J. Weissburg. Slow-moving predatory gastropods track prey odors in fast and turbulent flow. *Journal of Experimental Biology*, 208:809–819, 2005.

M. C. Ferner, D. L. Smee, and M. J. Weissburg. Habitat complexity alters lethal and non-lethal olfactory interactions between predators and prey. *Marine Ecology Progress Series*, 374:13–22, 2009.

D. G. Goring and V. I. Nikora. Despiking acoustic doppler velocimeter data. *Journal of Hydraulic Engineering*, 128:117–126, 2002.

W. D. Grant, III A. J. Williams, and S. M. Glenn. Bottom stress estimates and their prediction on the northern california continental shelf during code-1: The importance of wave-current interaction. *Journal of Physical Oceanography*, 14:506–527, 1984.

A. Hines, A. M. Haddon, and L. E. Wierchert. Guild structure and foraging impact of blue crabs and epibenthic fish in a subestuary of chesapeake bay. *Marine Ecology Progress Series*, 67:105–126, 1990.

L. H. Holthuijsen. *Waves in Oceanic and Coastal Waters*. Cambridge University Press, Cambridge, New York, 2007.

J. Jackson, D. R. Webster, S. Rahman, and M. J. Weissburg. Bed roughness effects on boundary-layer turbulence and consequence for odor-tracking behavior of blue crabs *Callinectes sapidus*. *Limnology and Oceanography*, 52:1883–1897, 2007.

N. L. Jones and S. G. Monismith. The influence of whitecapping waves on the vertical structure of turbulence in a shallow estuarine embayment. *Journal of Physical Oceanography*, 38:1563–1580, 2008.

P. Le Hir, W. Roberts, O. Cazaillet, M. Christie, P. Bassoullet, and C. Bacher. Characterization of intertidal flat hydrodynamics. *Continental Shelf Research*, 20: 1433–1459, 2000.

M. D. Powell and S. K. Rinard. Marine forecasting at the 1996 centennial olympic games. *Weather and Forecasting*, 13:764–782, 1998.

S. Powers and J. N. Kittinger. Hydrodynamic mediation of predator-prey interactions: Differential patterns of prey susceptibility and predator success explained by variation in water flow. *Journal of Experimental Marine Biology*, 273:171–187, 2002.

W. J. Shaw and J. H. Trowbridge. The direct estimation of near-bottom turbulent fluxes in the presence of energetic wave motions. *Journal of Atmospheric and Oceanic Technology*, 18:1540–1557, 2001.

D. Smee and M. J. Weissburg. Claming up: Environmental forces diminish the perceptive ability of bivalve prey. *Ecology*, 87:1587–1598, 2006.

D. Smee, M. C. Ferner, and M. J. Weissburg. Alteration of sensory abilities regulates the spatial scale of nonlethal predator effects. *Oecologia*, 156:399–409, 2008.

D. L. Smee, M. C. Ferner, and M. J. Weissburg. Hydrodynamic sensory stressors produce nonlinear predation patterns. *Ecology*, 91:1391–1400, 2010.

E. A. Terray, M. A. Donelan, Y. C. Agrawal, W. M. Drennan, K. K. Kahma, A. J. Williams III, P. A. Hwang, and S. A Kitaigorodskii. Estimates of kinetic energy dissipation under breaking waves. *Journal of Physical Oceanography*, 26:792–807, 1996.

M. Trevethan, H. Chanson, and R. Brown. Turbulent measurements in a small subtropical estuary with semidiurnal tides. *Journal of Hydraulic Engineering*, November:1665–1670, 2008.

J. H. Trowbridge. On a technique for measurement of turbulent shear stress in the presence of surface waves. *Journal of Atmospheric and Oceanic Technology*, 15:290–298, 1998.

R. L. Walker and K. R. Tenore. The distribution and production of the hard clam, *Mercenaria mercenaria*, in wassaw sound, georgia. *Estuaries*, 7:19–27, 1984.

M. J. Weissburg and R. K. Zimmer-Faust. Life in moving fluids: Hydrodynamic effects on chemosensory-mediated predation. *Ecology*, 74:1428–1443, 1993.

J. H. Zar. *Biostatistical Analysis. 4^{th} Edition.* Prentice Hall, Upper Saddle River, N. J., 1999.

R. Zimmer and C. A. Zimmer. Dynamic scaling in chemical ecology. *Journal of Chemical Ecology*, 34:822–836, 2008.

Administration

Basic Information

Title:	Administration
Project Number:	2010GA310B
Start Date:	3/1/2010
End Date:	2/28/2011
Funding Source:	104B
Congressional District:	5th
Research Category:	Ground-water Flow and Transport
Focus Category:	Hydrology, Surface Water, None
Descriptors:	
Principal Investigators:	Aris P. Georgakakos

Publications

1. Journal Publications 1. Georgakakos, A.P, Yao, H., Kistenmacher, M., Georgakakos, K.P., Graham, N.H., Cheng, F.-Y., Spencer, C., Shamir, E., “Value of Adaptive Water Resources Management in Northern California under Climatic Variability and Change: Reservoir Management,” J. Hydrology, in press, 2011.
2. 2. Georgakakos, K.P., Graham, N.H., Cheng, F.-Y., Spencer, C., Shamir, E., Georgakakos, A.P, Yao, H., and Kistenmacher, M., “Value of Adaptive Water Resources Management in Northern California under Climatic Variability and Change: Dynamic Hydroclimatology,” J. Hydrology, in press, 2011.
3. 3. Zhang, F. and A. P. Georgakakos, “Joint Variable Spatial Downscaling,” Climatic Change, in press, 2011.

Joint Variable Spatial Downscaling

Feng Zhang

Graduate Research Assistant
School of Civil and Environmental Engineering
Georgia Institute of Technology
790 Atlantic Drive
Atlanta, Georgia, 30332-0355

and

Aris P. Georgakakos

Professor and Principal Investigator
School of Civil and Environmental Engineering
Georgia Institute of Technology
790 Atlantic Drive
Atlanta, Georgia, 30332-0355
Aris.Georgakakos@ce.gatech.edu

May 2011

Abstract

Joint Variable Spatial Downscaling (JVSD), a new statistical technique for downscaling gridded climatic variables, is developed to generate high resolution gridded datasets for regional watershed modeling and assessments. The proposed approach differs from previous statistical downscaling methods in that multiple climatic variables are downscaled simultaneously and consistently to produce realistic climate projections. In the bias correction step, JVSD uses a differencing process to create stationary joint cumulative frequency statistics of the variables being downscaled. The functional relationship between these statistics and those of the historical observation period is subsequently used to remove GCM bias. The original variables are recovered through summation of bias corrected differenced sequences. In the spatial disaggregation step, JVSD uses a historical analogue approach, with historical analogues identified simultaneously for all atmospheric fields and over all areas of the basin under study. Analysis and comparisons are performed for 20th Century Climate in Coupled Models (20C3M), broadly available for most GCMs. The results show that the proposed downscaling method is able to reproduce the sub-grid climatic features as well as their temporal/spatial variability in the historical periods. Comparisons are also performed for precipitation and temperature with other statistical and dynamic downscaling methods over the southeastern US and show that JVSD performs favorably. The downscaled sequences are used to assess the implications of GCM scenarios for the Apalachicola-Chattahoochee-Flint river basin as part of a comprehensive climate change impact assessment.

Keywords

Statistical Downscaling, Global Circulation Model, Bias Correction, Spatial Disaggregation, Hydrologic Assessments

1. Introduction

Concerns over water resources vulnerability to climatic change are rising, and water resources planners and managers are becoming increasingly interested to quantify the implications, if any, and explore plausible mitigation and adaptation measures. This is an active research area with several past and on-going studies, including Lettenmaier and Rind, 1992; Stamm et al., 1994; Conway, 1998; Wood et al., 2004; VanRheenen et al., 2004; Tanaka et al., 2006; Maurer, 2007; Medelin-Azuara et al., 2008; Vicuna et al., 2009; K. Georgakakos et al., 2011; and A. Georgakakos et al., 2011. Among these studies, general circulation models (GCMs) are broadly used as an important tool for qualitative impact assessment. The GCMs represent (through a large system of partial differential equations) the coupled atmospheric and oceanic processes currently understood to govern the Earth's climate. Climate scenarios are generated by the numerical integration of the underlying equations over space and time. The purpose of developing such models is to obtain the range of future global climate response forced with concentrations of greenhouse gases and other constituents derived from various emissions scenarios (IPCC WGI, 2007).

At present, GCMs run on global scales at relatively low spatial resolutions (~100x100 km^2 to ~250x250 km^2). However, certain types of observational data (e.g., precipitation, ground air temperature, and wind speed) usually have much higher spatial resolution than that of GCMs. An example of GCM and observational data resolutions is shown in **Figure 1**, where the CGCM3.1 (Canadian Centre for Climate Modeling and Analysis) grid is superimposed on the observational data grid over the southeast US.

Because of their coarse spatial resolution, GCM outputs are usually inadequate to capture the spatial variability at regional or local scales necessary for hydrological applications. Kuhl et al. (1992) compared the observed river runoff of the world's largest rivers to the monthly runoff simulated by using a GCM model. They found that predicting

the runoff of high-latitude rivers directly from GCM outputs over-simplifies and ignores the lateral transfer of water between grid cells within the land phase. Xu (1999) also comments that the excess and overland flow is not well simulated by the GCMs. Another drawback of using direct GCM outputs to simulate local hydro-climate is that the regional topographic features are usually not well represented in most global climate models. Such limitation is overcome in two stages: First, downscaling procedures are used to construct climate scenarios at more application-relevant scales, capturing the sub-grid climatic variability. Second, the downscaled sequences are used to drive hydrologic watershed models which have been shown to represent sufficiently well the dynamics of runoff and other hydrologic variables.

Existing downscaling techniques can be organized into two main categories: dynamic and statistical downscaling. Fowler and Blenkinsop (2007), Wilby and Wigley (1997), and Xu (1999) thoroughly review most existing downscaling techniques of both types. The techniques most relevant to the methods developed herein are briefly discussed next.

Regarding dynamic downscaling, a regional climate model (RCM) is used to model the target region at finer scales bounded by larger GCM nodes (Miller et al., 1999; Xue et al., 2007). The results of RCMs still depend on the validity and skill of the overriding GCM. Mearns et al. (2003) outlined the advantages and disadvantages of using RCMs and provided guidance on the use of their outputs. Generally, RCMs provide high resolution climatic fields spatially and globally consistent with GCM scenarios. Although some RCMs can generate climatic fields evolving differently that the original GCM fields, they usually inherit the biases of the driving global models, and they are computationally expensive.

The North American Regional Climate Change Assessment Program (NARCCAP; Mearns et al., 2007; Mearns et al., 2009) is among the most notable dynamic downscaling research efforts and provides valuable online datasets (http://www.narccap.ucar.edu/). This

program investigates the uncertainties of regional scale projections of GCM outputs, and generates high resolution scenarios for regional climate impact assessments. NARCCAP provides a very important source of dynamically downscaled regional climatic scenarios. These simulations correspond only to SRES A2 emissions scenario, and, due to their heavy computational requirements, they are generated for selected time horizons (1971-2000; 2041-2070). It takes approximately 36 hours to complete a 30-day simulation using a RCM (e.g., MM5 or WRF) over an area of 90,000 km^2 with 30 x 30 km spatial resolution on a 2.1GHz dual core personal computer. Thus, the currently available results are not sufficient for comprehensive climate change impact assessments, but are used in this study to compare the skill of statistical versus dynamic downscaling methods. Lastly, it is unclear whether the uncertainties surrounding dynamic downscaling methods are not comparable to those of the more computationally efficient statistical downscaling methods. For example, Fowler et al. (2007) suggest that "dynamical downscaling methods provide little advantage over statistical techniques."

Statistical downscaling does not depend on GCM boundary conditions and can be used to downscale climatic variables without the full set of climatic fields at the coarse level. Statistical downscaling is based on relationships between low resolution GCM outputs and associated higher resolution observations over the same historical period. These statistical relationships are then used to infer the observations on finer grids at future times when only GCM outputs are available. Examples of statistical downscaling methods include changing factor methods (Beniston et al., 2003), regression methods (Huth, 1999), weather typing schemes (Vrac, 2007), weather generators (Wilks and Wilby, 1999), bias correction and spatial disaggregation (BCSD; Wood et al., 2004), and constructed analogues (Hidalgo et al., 2008).

Wood et al. (2004) proposed a two-step statistical downscaling method to address bias correction and spatial disaggregation (BCSD). In the first step, GCM biases are adjusted through a quantile mapping technique individually for temperature and precipitation. The spatial disaggregation step translates adjusted GCM data on climate model resolutions to a basin-relevant resolution (observational resolution) by using interpolated spatial factors. The spatial interpolation method is a modified version of inverse-distance-squared interpolation developed by Shepard (1984).

BCSD is a very efficient statistical downscaling technique for climate change assessments. At the *individual* grid level, BCSD generates a similar climatology of precipitation and temperature as the observed. However, as will be shown later in the article, the monthly BCSD fields are spatially much more homogeneous that the observed. This occurs because the same GCM data is used to interpolate several downscaled grid values. Furthermore, while the temperature shift-removing procedure enables the bias correction step without extrapolation, it also makes the assumption that future temperature distributions remain similar to those of the historical period. This, however, is not a valid assumption, as future temperature (and precipitation) distributions are not simply trend-adjusted versions of the historical distributions.

Li et al. (2010) recently proposed the equidistant cumulative distribution function matching (EDCDFm) method as an improvement to the cumulative distribution function matching (CDFm) method used as part of BCSD (bias correction step). EDCDFm explicitly considers the changes between the baseline and future distributions. It also fits the marginal CDF of precipitation and temperature with a mixed two-parameter gamma distribution and a four-parameter beta distribution respectively. By performing a synthetic experiment at a continental scale (northern Eurasia), they conclude that EDCDFm is superior to CDFm method in that it reduces the mean bias and RMSE for summer and winter, especially under

changing variability. Furthermore, EDCDFm is found to perform better than CDFm in correcting biases of extremes. However, as the original CDFm, it is based on the idea of downscaling climatic variables *individually*. This method only concerns the bias correction step and presents no new spatial downscaling experiments or data.

Hidalgo et al. (2008) and Maurer et. al. (2010) proposed and implemented the constructed analogues (CA) and the hybrid bias correction and constructed analogues (BCCA) techniques. The CA method essentially makes no bias corrections, but rather relates model-simulated variables to observed variables, using relationships established during historical periods when observations are available. These relationships are established through multiple regression analysis and are based on daily reanalysis data.Maurer and Hidalgo (2010) further investigated the application of a bias correction step before the CA process is performed and conclude that the BCCA method is consistently better than BCSD in simulating daily stream flows, especially for hydrologic extremes. The CA assumption is that the relationships between large-scale and downscaled fields derived based on historical reanalysis data will also be valid in future climates.

Overall, downscaled sequences must meet several criteria to be useful in regional water resources assessments:

- First, the downscaled sequences should be consistent with historical observations.
- Second, the downscaled sequences should capture climatic mean and variability trends.
- Third, spatial and temporal correlations and interdependencies between the atmospheric fields that largely drive hydrological processes should be represented.

- Lastly, to ensure that hydrological assessments at different temporal scales (e.g., annually, monthly, and daily) using the same downscaled products are consistent, the smoothness of these products across these time scales should be ensured.

These criteria formed the guiding principles for a new statistical downscaling method discussed next.

2. Joint Variable Spatial Downscaling (JVSD)

JVSD aims to produce high resolution gridded hydrological datasets suitable for regional watershed modeling and assessments. The method is applicable to multiple atmospheric fields, but it is presented here for precipitation and temperature, as these two variables represent the principle atmospheric forcing that drives watershed response.

JVSD conceptually follows the general approach introduced by Wood et al., 2004 (Bias Correction and Spatial Downscaling—BCSD), with several new features. First, instead of removing and replacing the variable long term trends before and after the bias correction step, JVSD uses a differencing process to create stationary time series and joint frequency distributions (for temperature and precipitation) between GCM control and future runs. Bias correction is then based on quantile-to-quantile mapping of these stationary frequency distributions. The bias corrected sequences are recovered by inverting the differenced series. For spatial disaggregation, JVSD also uses the historical analogue approach. However, historical analogues are identified *simultaneously* for all atmospheric fields being downscaled, and for all GCM cells that cover the assessment region. This feature ensures the temporal and spatial coherence of the downscaled climatic fields. Finally, a technique to expand the range of the historical analogues is implemented to handle future data values that fall outside the historical range.

JVSD is implemented as shown in **Figure 2** as a two step process: bias correction and spatial downscaling.

2.1 Bias Correction

GCM outputs contain significant biases that must be corrected before any meaningful assessment can be carried out. **Figure 3** compares the frequency distributions of GCM simulated (CGCM3.1, run1) temperature and precipitation versus observed values aggregated over the same ACF cells for the historical period 1950-1999. Biases exist not only in the mean of these distributions but throughout the distributional range, and they are uneven at different quantiles.

The JVSD bias correction process is presented using the following notation:

- TS1 and TS2: Monthly precipitation and temperature time series of GCM *future* runs on individual GCM grids:

$$TS1: \quad P\_\mathrm{GCM}_t \quad (t = 1,2,\cdots,\mathrm{NF}_{\mathrm{month}})$$

$$TS2: \quad T\_\mathrm{GCM}_t \quad (t = 1,2,\cdots,\mathrm{NF}_{\mathrm{month}})$$

  where, $\mathrm{NF}_{\mathrm{month}}$ is the length of the monthly time series.

- TS3 and TS4: Monthly precipitation and temperature time series of GCM *control* runs on individual GCM grids. GCM control runs refer to a historical time period, such as the entire 20th Century or some portion of it. In this article, the term "control runs" refers to the 20c3m (20th Century) runs.

$$TS3: \quad P\_\mathrm{CON}_t \quad (t = 1,2,\cdots,\mathrm{NC}_{\mathrm{month}})$$

$$TS4: \quad T\_\mathrm{CON}_t \quad (t = 1,2,\cdots,\mathrm{NC}_{\mathrm{month}})$$

  where, $\mathrm{NC}_{\mathrm{month}}$ is the length of the monthly time series.

- DTS5 and DTS6: Daily *observed* precipitation and temperature time series on individual observational scale grids:

$$DTS5: \quad P\_OBS_{td} \quad (td = 1,2,\cdots, NO_{day})$$

$$DTS6: \quad T\_OBS_{td} \quad (td = 1,2,\cdots, NO_{day})$$

where NO_{day} is the length of the daily observed time series.

Step 1: Upscaling

DTS5 and DTS6 are aggregated into two new monthly sequences TS5 and TS6 over the GCM spatial resolution grids.

The aggregation process first performs spatial averaging over each GCM cell and then performs temporal averaging to monthly time scales.

This process can be carried out using other spatial averaging schemes such as kriging (Drignei, 2009). The concept of spatial upscaling is illustrated in **Figure 4**.

Step 2: Differencing

Differencing aims to remove seasonalities and deterministic trends, and create stationary time series. Differencing can be applied at various lags and orders. For example, a 12-month differencing process applied to the monthly time series (*TS1*, *TS2*, *TS3*, *TS4*, *TS5*, and *TS6*) on each GCM cell can be expressed as shown below:

$$TS1': \quad SP\_GCM_t = \nabla_{12}(P\_GCM_t) \quad (t = 1,2,\cdots, NF_{month})$$

$$TS2': \quad ST\_GCM_t = \nabla_{12}(T\_GCM_t) \quad (t = 1,2,\cdots, NF_{month})$$

$$TS3': \quad SP\_CON_t = \nabla_{12}(P\_CON_t) \quad (t = 1,2,\cdots, NC_{month})$$

$$TS4': \quad ST\_CON_t = \nabla_{12}(T\_CON_t) \quad (t = 1,2,\cdots, NC_{month})$$

$$TS5': \quad SP\_OBS_t = \nabla_{12}(P\_OBS_t) \quad (t = 1,2,\cdots, NC_{month})$$

$$TS6': \qquad ST\_OBS_t = \nabla_{12}(T\_OBS_t) \quad (t = 1,2,\cdots, NC_{month})$$

where, the differencing operator ∇_D with lag D is defined as

$$\nabla_D(TS_t) = TS_t - TS_{t-D} \qquad (4)$$

For D = 12 months, the operator simply subtracts the series values one year apart (**Figure 5**). If trends persist, higher order differencing may also be used.

The effect of 12-month differencing of GCM temperature and precipitation outputs is shown on **Figure 6**. The top plots of this figure show contour lines of the joint empirical temperature-precipitation cumulative frequency curve of the control (CON) and future runs (from the Canadian GCM—CGCM3.1/ run1). Future runs are divided into the first 50-year period (FUT1) from 2000 to 2049, and the second 50-year period (FUT2) from 2050 to 2099. Thus, all sample sizes (i.e., CON, FUT1, and FUT2) are 50-year long. These plots support the following observations:

(1) The joint frequency distributions of temperature and precipitation are different in the control and future runs; and

(2) The relationship of the joint frequency distributions (of control versus future data) is appreciably different in the first versus the second 50-year period, indicating that the joint frequency distribution is non-stationary.

These differences and nonstationarities bias the results of all existing downscaling methods that are commonly based on quantile-to-quantile mapping of these or the associated marginal statistics.

On the other hand, the bottom two plots of **Figure 6** show the joint cumulative frequency distribution (of temperature and precipitation) after a 12-month differencing of the original sequences. These plots clearly show that the differenced sequences exhibit very good correspondence between control and future runs, for both future periods. Thus, the joint statistics of the 12-month differenced series are stationary and can serve as pivotal quantities

for the quantile-to-quantile bias correction process. This result and conclusion has been tested and shown to hold for all 13 GCMs available through IPCC.

To detect the possible existence of higher order nonstationarities, higher order differencing and other lags were also tested, but they did not yield any significant improvements over 12-month, single differencing.

Step 3: Joint Frequency Mapping

In keeping with the previous discussion, the bias correction process consists of *(1)* creating a differenced series of future temperature and precipitation; *(2)* finding the joint frequency of the contemporaneous differenced data values; *(3)* considering that this joint frequency is the same in the future differenced series as it is in the control differenced series; and *(4)* mapping each joint frequency point of the GCM Control distribution to a corresponding point on the joint frequency distribution of the observed differenced series (OBS). The last step is illustrated in **Figure 7**. The schematic shows two corresponding pairs of GCM and OBS joint iso-probability curves, and the nearest neighbor mapping of a GCM point to a point on the corresponding OBS iso-probability contour. The nearest neighbor is the one which minimizes the Euclidean distance between the GCM point and all points on the OBS frequency contour.

The cumulative frequency distribution functions in the above procedure are developed empirically for the observational as well as the GCM data. These empirical distributions are used in the joint frequency mapping step directly. No analytical approximations are derived for this step, although a copula type procedure (Nelsen, 1999) could be employed. Such an analytical approximation would be necessary if the ranges of these distributions are significantly different. However, the frequency distributions are derived herein for the *differenced* data, and it turns out that the extreme values are fairly commensurate. Thus, simple linear extrapolation is used occasionally to identify the bias corrected values.

The mapping of a point on the GCM joint cumulative distribution function (CDF) onto a point of the OBS joint CDF (of differenced temperature and precipitation values) can be performed in several ways, two of which are examined below. The mapping "goodness" criterion is how well the mapped GCM joint CDF corresponds to the OBS CDF. The first mapping procedure ensures that the mapped points have the same GCM and OBS CDF values, and finds the "nearest neighbors" on the T-P space. The second procedure is implemented as follows: A (T,P) point on the GCM joint CDF is associated with a joint CDF value as well as two marginal CDF values, one for temperature and a second for precipitation. The mapping is then carried out using the nearest neighbor concept in probability space. More specifically, the two points are selected to have the same joint CDF value (on the GCM and OBS CDFs) and the shortest distance between their marginal CDF values (in a Euclidian measure sense).

Figure 8 presents a comparison between the two approaches CSIRO-MK3.5 GCM (Australia). The top graph compares the OBS versus the mapped GCM joint CDFs for the first approach by displaying 9 iso-probability contour lines from 0.1 to 0.9 (in 0.1 increments). The second graph displays the same results for the second approach. The figure shows that both approaches generally represent well all CDF regions, although the second approach is somewhat more reliable. The results presented in this article use the first approach.

Step 4: Series Reconstruction

The bias corrected monthly temperature and precipitation series for each GCM cell (denoted *TS7* and *TS8*) are obtained by inverting the differencing operation on the bias corrected series:

$$TS7:\ P\_C_t = \left(\nabla_D\right)^{-1}\left(SP\_C_t\right) = SP\_C_t + SP\_C_{t-D} \quad (t = 1,2,\cdots,NF_{month}) \qquad (5a)$$

$$TS8:\ T\_C_t = \left(\bar{T}_D\right) + \left(ST\_C_t\right) = ST\_C_t + ST\_C_{t\text{-}D} \quad (t = 1,2,\cdots, NF_{month}) \qquad (5b)$$

2.2 Spatial Downscaling

The JVSD spatial downscaling component is based on matching the bias-corrected temperature and precipitation patterns with similar observed patterns (historical analogues) over the assessment region (e.g., the ACF river basin). This process has the following distinguishing features compared to existing methods:

(1) Pattern matching is performed *simultaneously* for temperature and precipitation fields;

(2) Pattern matching is performed *simultaneously* for all GCM cells that cover the region of interest (e.g., the ACF river basin), thus maintaining the climatic coherence and plausibility of the temperature and precipitation fields;

(3) Future temperature and precipitation fields that fall outside the historical range are accommodated by expanding the range of historical analogues as described in the following section.

The spatial downscaling procedure is summarized below.

Step 5: Data Range Adequacy Test

In this step, the monthly temperature and precipitation values of the relevant GCM cells are checked to determine if they fall within the historical observed range of the monthly values. If they fall within the historical range, the downscaling process continues to Step 7; otherwise, the process continues to Step 6.

Step 6: Historical Analogue Range Expansion

This step is invoked when the future GCM patterns fall outside the historical range, a case particularly relevant to a changing climate. To expand the historical analogue range, upscaling of the historical data in Step 4 is performed for periods smaller than a month, e.g., d = 15, 10, 5, or 1 days. Because these periods entail fewer days than those in a month, their

averages are expected to exhibit higher (than monthly) variability and a wider data range. This process aims to identify the largest interval *d* which generates historical analogues containing the future T and P values. The data range expansion is carried out for the calendar month to be downscaled. However, if this is not sufficient, the data range is expanded to include 15 days from the previous and 15 days from the following months, expected to exhibit a similar climatic behavior.

The process is illustrated in **Figure 9**. In the top plot, the maximum and minimum historical monthly precipitation averaged over 30, 10, 5, and 1 days are plotted in solid lines, and the corresponding standard deviations in dashed lines. In the bottom plot, the same quantities are plotted for the historical temperature. These plots show the data range expansion as the averaging interval decreases.

Step 7: Historical Analogue Matching

Next, the nearest point (OBS_P_i, OBS_T_i) in the historical sequences *TS5* and *TS6* to a particular point (GCM_P_i, GCM_T_i) in the future GCM sequences *TS7* and *TS8* is determined by minimizing the Euclidean distance:

$$R^2 = \sum_{i \in A} \alpha (OBS\_P_i - GCM\_P_i)^2 + \beta (OBS\_T_i - GCM\_T_i)^2 \quad (6)$$

where *A* is the set of cells that cover the region (basin) of interest; α and β are weighting coefficients if one wishes to emphasize matching one of the variable over the other; and *i* is the cell index on the GCM grid.

Once the nearest historical analogue point is identified, the T-P values can be spatially downscaled based on the historical T-P values over the observational cells. The downscaled temperature and precipitation sequences are denoted *TS9* and *TS10*:

$$\begin{Bmatrix} TS9 \\ TS10 \end{Bmatrix} : \begin{Bmatrix} P\_\mathrm{DS_t} \\ T\_\mathrm{DS_t} \end{Bmatrix} = Nearest\ \ Historical\ \ Ana\log ue \begin{Bmatrix} P\_OBS_j \\ T\_OBS_j \end{Bmatrix} \quad (\mathrm{t} = 1,2,\cdots,\mathrm{NF_{month}})$$

where *j* is the cell index of the observational (high resolution) grid.

Step 8: Temporal Downscaling

Daily (or other duration) temperature and precipitation sequences *DTS9* and *DTS10* can now be constructed by suitable temporal upscaling of the historical analogue fields. If the nearest historical analogue was found from the monthly historical observed fields, then, the downscaled daily sequences are directly extracted from the corresponding month. On the other hand, if the nearest historical analogue required expansion of the historical range (using the process outlined in Step 6), then, the downscaled daily sequences are constructed by assembling several nearest historical analogues the total duration of which equals one month. In the assessments carried out for the ACF river basin, data range expansion was not necessary beyond the 15 day interval.

3. Downscaling Results and Comparisons

The geographic focus of the study is the Apalachicola-Chattahoochee-Flint (ACF) river basin located in the southeast US as shown in **Figure 10**. The ACF basin begins in north Georgia (mostly within a sub-tropic region) and flows into the Gulf of Mexico, near Apalachicola, Florida. It drains an area of about 19,600 square miles. Based on its hydrological characteristics and the locations of major storage projects, the ACF basin comprises seven watersheds (sub-basins): *(1)* the Chattahoochee headwater reach extending up to and including Lake Lanier and Buford Dam; *(2)* the Chattahoochee reach from Lake Lanier up to and including West Point Lake and Dam; *(3)* the Middle Chattahoochee reach from West Point up to and including Lake Walter F. George and Dam; *(4)* the Lower Chattahoochee

reach from Lake W.F. George up to and including Lake Seminole and Jim Woodruff Lock and Dam; *(5)* the Flint headwater reach up to Montezuma; *(6)* the Flint reach from Montezuma up to Albany; and *(7)* the Flint reach from Albany to Bainbridge. **Table 1** lists the characteristics of all ACF sub-basins. More detailed descriptions of ACF basins can be found in a recent technical report (Georgakakos et al., 2010).

In this section, JVSD is evaluated by comparison with observed historical data and other statistical and dynamic downscaling methods.

3.1 Seasonal Comparison with Observed Data

The climatology maps of precipitation and temperature in the southeast US (the region where the ACF basin is located) are shown in **Figures 11** and **12**. The results presented here are from the Canadian model CGCM3.1, run1. Results from all other GCMs and scenarios can be found in the technical report by Georgakakos et al., 2010. Monthly precipitation and temperature data are aggregated by seasons (DJF, MAM, JJA, and SON) for three 50-year periods: *(1)* 01/1950 to 12/1999 using both observation data as well as data from the CMIP pilot project called 20th Century Climate in Coupled Models (20CM3); *(2)* 01/2000 to 12/2049 for the CGCM A1B scenario, and *(3)* 01/2050 to 12/2099 again for the CGCM A1B scenario. The first column is constructed from observed, high resolution data from the 1/8 degree spatial resolution dataset (Maurer et al., 2002) for the period 1950-1999. The second column shows the JVSD results with input from the coarse resolution GCM data from the 20CM3 experiments (1950-1999). The third (2000-2049) and fourth columns (2050-2099) are also generated by JVSD with input from the A1B CGCM3.1 scenario runs.

The important comparison in **Figures 11** and **12** is between the first two columns (observations versus JVSD). The figures show that JVSD results compare favorably with observed precipitation and temperature data in that they reproduce fairly well the seasonal spatial distributions and coherence. (In generating the JVSD results, the corresponding

historical month being downscaled has, of course, been *excluded* from the historical analogue data set.) Furthermore, specifically for the CGCM A1B run shown, the results in columns 3 and 4 indicate:

(1) Temperature exhibits increasing trends over the southeast and the ACF basin for all seasons; Temperature increases are more significant in the 2050 – 2099 time period. The most pronounced temperature increase appears to take place in spring and fall. The A2 scenario results (not shown) are similar but temperature increases are even greater in the second half of the 21st century. This observation holds true for most GCM scenario results and will be quantified further in a later section.

(2) Precipitation exhibits an increasing trend in winter and a mild declining trend in spring and summer.

Similar analysis (not shown) has been carried out using the BCSD method. The BCSD datasets are obtained from the Program for Climate Model Diagnosis and Intercomparison website (http://gdo-dcp.ucllnl.org/downscaled_cmip3_projections/). Generally, BCSD performs well, showing similar overall trends for seasonal temperature and precipitation as those of the observed data and JVSD. However, the following differences are noted between the two methods:

(1) The BCSD precipitation fields exhibit less spatial variability and milder changes than those of JVSD. The reasons for these differences are that (i) the BCSD downscaled values for nearby cells are calculated based on the same upscaled information (through a variant of the inverse distance weight approach) and (ii) JVSD is based on historical analogues that have been observed over the *entire* region of interest, not separately for individual cells. (More quantitative comparisons of these differences are forthcoming later in this section.)

(2) BCSD predicts that the highest temperature increases will occur during spring and fall as does JVSD. However, summer temperature increases (July and August) are higher under BCSD than under JVSD.

Furthermore, the JVSD seasonal joint temperature and precipitation CDFs were compared with their observed counterparts (Maurer et al., 2002) for each of the seven ACF sub-basins over the historical period 01/1950 - 12/1999 (control period). The results (**Figure 13**) show that JVSD represents the joint relationships fairly well over the entire frequency range, with discrepancies appearing at the extreme value regions which are characterized only by a few data points.

The performance of downscaling methods varies across seasons, stations, and indices (Fowler and Blenkinsop, 2007). Many researchers have concluded that the accuracy of statistical downscaling methods has a geographical and seasonal component (Huth, 1999). In addition, the GCM skill in simulating regional climate may vary for different locations and scales. In general, GCMs are more likely to capture the large scale climate features, and the relationships between climate variables are likely to be better simulated in locations where the topographic features are not too different from those assumed in the GCMs.

A JVSD strength is that it can represent the co-variability between temperature and precipitation. In places and seasons where there is no significant dependence between these two variables, the JVSD and BCSD bias correction procedures are equivalent. However, where such dependence exists, JVSD generates more representative downscaled fields. To demonstrate this feature, the joint distributions of temperature and precipitation for the observed as well as the BCSD and JVSD downscaled data are compared for Buford, Woodruff, and the entire ACF. **Figure 14** shows this comparison for Buford and the GFDL GCM. This figure shows that in DJF and SON, both BCSD and JVSD represent the joint temperature-precipitation relationship comparably well, although BCSD exhibits some

discrepancies in the joint distribution tails. However, in MAM and JJA, JVSD performs clearly better. The underlying reason for these performance differences is illustrated on **Figure 15** which depicts the monthly correlation coefficients between temperature and precipitation for four GCMs and the observations, BCSD downscaled data, and JVSD downscaled data (over the 1950-1999 historical period). The figure shows that in DJF and SON correlations are negligible, while in MAM and JJA correlations are significant. Thus, JVSD is more preferable than BCSD in places and seasons where temperature and precipitation exhibit strong co-variability.

Next, the seasonal coefficient of variation (CV) for each ACF watershed is computed and compared for both the observational and downscaled datasets (from JVSD as well as BCSD). The seasonal watershed CV is the spatial mean of the seasonal coefficient of variation. The seasonal CV at a particular grid cell is defined as the ratio of the standard deviation of the cell seasonal values to the mean seasonal value. Then, the watershed CV is obtained as the spatial mean of all seasonal CVs over all watershed grid cells. **Table 2** shows that the JVSD watershed CVs are more representative of the historical CVs than those of BCSD, especially for watershed precipitation. It also shows that BCSD underestimates precipitation variability within each watershed.

Lastly, the spatial inter-grid variability is compared for the same three datasets (i.e., the observations, JVSD, and BCSD). Several descriptive statistics exist to characterize the spatial patterns of gridded data including the covariance matrix (measurement of spatial dispersion), mean correlation coefficient (measurement of spatial correlation), and Ripley's K and L functions (measurements of spatial homogeneity of point data). Here, this variability is compared using the distribution of the pair-wise correlation between any two grid points within a watershed (Gissila et al., 2004). The temperature field (not shown) exhibits high grid point correlations (greater than 0.99), indicating that the monthly temperatures are highly

homogeneous within each watershed. Both JVSD and BCSD reproduce this homogeneity. However, for reasons explained below in relation to precipitation, in geographic areas where the actual temperature field exhibits significant spatial heterogeneity, BCSD would tend to over-estimate the inter-grid cross correlations.

Box-plots of these pair-wise correlation coefficients across the ACF watersheds are shown in **Figure 16**.The historical correlation distributions vary between 0.75 and 0.9. The plots show that the JVSD distributions match very closely the historical statistics, while BCSD exhibits a significant bias toward homogeneity.

Furthermore, **Figure 17** compares the spatial precipitation correlation between observations, BCSD, and JVSD for four GCMs, various grid cell distances, and months. These are correlations of the actual values of a particular cell pair over the 1950 to 1999 period and month of the year. The graphs clearly show the BCSD spatial correlation bias. For adjacent cells, the BCSD correlation is nearly 1. Even for pairs at 15 to 20 cell distances apart, the spatial correlation continues to be more than 0.9 and exhibits no distinct monthly pattern. In comparison, the spatial correlations of the observations and JVSD values have a clear monthly pattern and are consistent. As already indicated, the reason for this BCSD behavior is that the factors used to downscale nearby values are calculated based on upscaled information at the same GCM grid cells (using a general inverse distance weighting approach). This process over-estimates the spatial correlation, because the inverse distance weights for nearby cells are very similar.

While this distributional bias is not critical with respect to temperature, misrepresenting the spatial precipitation variability is more of a concern, especially if hydrologic assessments are based on distributed (or quasi-distributed) watershed models. The plots also show that the southern ACF watersheds (i.e., those that are situated below the geologic fall line that runs across Georgia) have larger inter-grid precipitation variability than

the two northern watersheds (Buford and West Point). A likely reason for this is that convective events dominate southern watershed precipitation over a longer season.

3.2 Comparison with Dynamic Downscaling Methods

In this section, JVSD and BCSD are compared with the dynamic downscaling methods used in the North American Regional Climate Change Assessment Program (NARCCAP).

High resolution climate scenarios have been produced by NARCCAP using regional climate models (RCMs). The RCMs are nested within coupled Atmospheric-Ocean GCMs for the historical period 1971-2000 and for the future period 2041-2070 (NARCCAP, 2010). Several RCM/GCM combinations have been run and some of the products are available through the ESG (Earth System Grid; http://www.earthsystemgrid.org/) data distribution center. In the comparison presented here, results from one typical RCM/GCM combination corresponding to the Canadian GCM3 run4 data (cccma_cgcm3_1 sresa2, Run 4) are selected.

As illustrated in **Figure 18**, the results from CGCM3/SRESA2/RUN4 were downscaled using JVSD, BCSD, and CRCM/CGCM3 dynamic methods. The resulting precipitation and temperature fields are aggregated over the ACF watersheds, and comparisons are made among the aggregated time series.

It is noted that the CGCM3 experiment provides boundary conditions for the CRCM run (Randel, 2007) without any bias correction. Therefore, the downscaled data inherit the original GCM biases. To account for this inconsistency, JVSD was implemented and compared with CGCM3 with and without bias correction.

To facilitate the comparison, the data values are expressed in frequency curve form (**Figures 19** and **20**). The graphs comprising these figures correspond to the ACF watersheds and include four curves corresponding to the dynamically downscaled data (blue line), BCSD downscaled data (pink line), JVSD downscaled data without bias correction (cyan line), and

JVSD downscaled data with bias correction (green line). (BCSD data without bias correction is not available.) The pair-wise statistical differences between these curves were assessed using the Kolmogorov-Smirnov test as reported in Table 3.

First, the results show that there is no significant statistical difference between dynamic downscaling (DDS) and JVSD with no bias correction. This conclusion applies for both temperature and precipitation at 0.05 and 0.01 significance. (The only exception is DDS and JVSD precipitation for the George watershed which is marginally different at the 0.05 significance level, but not at 0.01.) A plausible explanation for this interesting finding is that JVSD generates spatially coherent temperature and precipitation fields for the entire ACF, much like a dynamic downscaling scheme also does. Furthermore, temperature and precipitation over the ACF geographic region are fairly uniform.

Second, comparing JVSD with bias correction and DDS indicates that the former is significantly different from the latter for both temperature and precipitation at 0.05 and 0.01 significance levels. (Buford temperature is the only exception where the two frequency distributions cannot be assessed as different at 0.01 significance, but the test statistic is marginal.) This finding combined with the favorable JVSD(BC) comparison with observed data (in previous sections) leads to the conclusion that dynamic downscaling without some form of bias correction may not be adequate for climate change assessments. This conclusion is corroborated by Wood et al., 2004, who assess the seasonal hydrologic response in the Columbia River Basin using dynamically downscaled climate scenarios with and without bias correction.

Third, comparing BCSD and JVSD with bias correction indicates that significant precipitation differences exist for all watersheds at the 0.05 significance level, while only Buford, West Point, and Woodruff remain clearly significant at the 0.01 level. Temperature distributions, on the other hand, are not found to be statistically different at 0.05 or 0.01, with

the exception of Buford. The statistical differences between JVSD(BC) and BCSD result from the several differences between these two methods: joint variable downscaling versus marginal distribution downscaling, coherent basin-wide versus individual grid downscaling, and different handling of extreme distribution values.

4. ACF Climate Change Assessments

This section assesses the ACF precipitation and temperature change implied by the GCM scenario runs. In this regard, monthly temperature and precipitation climatologies of all 13 GCM A1B scenarios for the seven ACF sub-basins are first shown in **Figure 21**. All sub-basins show increasing temperature trends, with higher increases during spring and fall. Precipitation is projected to increase during late fall and winter and decrease during spring. March precipitation over the Buford watershed is an exception, showing a mild increase. The change direction over the first and second halves of the century is generally similar, with the second half experiencing somewhat larger changes. These observations apply also to the A2 scenarios (not shown).

The previous results provide information on mean monthly trends. Critical climate change impacts, however, are also associated with changes of other distributional statistics (e.g., extreme precipitation and temperature values). To assess such changes, **Figures 22** and **23** present monthly box plots of the historical and future precipitation and temperature scenarios (A1B and A2) for two ACF watersheds, Buford (at the ACF headwaters) and Woodruff-Bainbridge (before the river enters into Florida). In each figure, the historical box-plots are denoted "H1 through H12" while the two future scenarios are denoted "FF1 through FF12" (for the first 50 years of the 21st century) and "FS1 through FS12" (for the second 50 years). The future box-plots include data from all 13 future scenarios, while the historical box-plots include only historical data. These figures indeed show that climate change

impacts are not uniform across the months of the year. More specifically, these figures support the following observations:

(1) Buford Precipitation: **Figure 22** shows that mean precipitation increases during December through March, decreases during May through August, and remains stable in late spring (April and May) and early fall (September and October). The largest increase occurs in March, while the largest decrease occurs in July and August.

The upper quartile (UQ) of the monthly precipitation distribution increases during December through June, with the largest increase occurring in March and April (exacerbating potential flooding impacts). UQ decreases in October and November.

The lower quartile (LQ) of the monthly precipitation distribution increases in January, February, and October, and decreases in March through August. July and August register the largest such decrease, raising concerns for summer water availability.

(2) Buford Temperature: Mean monthly temperature increases in all months of the year with the most pronounced increases taking place from January through May and October through December. The largest increases, in the range 2 to 2.5 ^{o}C, are associated with the A2 climate scenarios in the second half of this century.

Likewise, the monthly upper temperature quartile increases for all months, with March and September registering the largest change (of approximately 3 ^{o}C) for the A2 scenarios and the second half of the century.

The monthly lower temperature quartile also increases for all months, with the largest increases noted in February and March (of approximately 2 ^{o}C).

Other temperature statistics of interest have also been computed (e.g., consecutive summer days with temperature higher than a certain threshold) and show similar intensifying trends. These are expected to have direct impacts on human communities, agriculture, and ecosystems, and comprise the scope of continuing assessments (Georgakakos et al., 2010).

(3) Woodruff-Bainbridge Precipitation: Unlike Buford, the Woodruff-Bainbridge watershed does not show any mean precipitation increase in spring, but it does register increases in November and December (**Figure 23**). Notable decreases occur in February, March, and July.

The monthly upper mean precipitation quartile increases for all months with the largest increase occurring in February through May. The monthly lower mean precipitation quartile shows a decreasing trend from January through August, with the most marked decline noted in June, July, and August. On the other hand, LQ is increasing in September, October, and December.

The A1B and A2 scenarios exhibit similar trends, with the latter somewhat exacerbated for the second 50-year period.

(4) Woodruff-Bainbridge Temperature: All three temperature statistics increase for all months of the year, all scenarios, and both 50-year future periods. The largest mean temperature increases occur from January through May and from October through December and are in the order of 2.5 – 3 ^{o}C. The largest UQ increases are in the order of 3 to 3.5 ^{o}C and occur from January through May and in September. Lastly, the largest LQ increase (2.5 – 3 ^{o}C) occurs in February.

Thus, the precipitation and temperature changes predicted for Woodruff-Bainbridge are similar to those of Buford, raising alarming concerns with respect to summer water availability and the impacts of a hotter climate on people, crops, and ecosystems.

5. Conclusions

This article introduces a new statistical downscaling technique, named Joint Variable Spatial Downscaling—JVSD, for the generation of high resolution gridded datasets suitable for regional watershed modeling and assessments. JVSD follows the general two-step approach

introduced by Wood et al., 2004, as part of the BCSD downscaling method, but it includes several distinguishing features including (1) joint downscaling of atmospheric fields; (2) identification of a constant pivotal quantity reducing the biases introduced by percentile-to-percentile mapping; (3) preservation of sub-grid correlations and variability; and (4) physical coherence of the downscaled sequences over the entire region of interest.

JVSD as well as all other existing statistical downscaling methods assume that the spatial pattern of finer scale precipitation and temperature within a large GCM grid and the temporal distribution of (daily) precipitation or temperature within a month will remain the same.

Comparisons with observed historical data, BCSD, and dynamic downscaling methods are favorable and demonstrate that JVSD has distinct advantages over existing methods. JVSD can also be used to post-process dynamic downscaling results to correct for remaining biases.

Application of the method to the Apalachicola-Chattahoochee-Flint (ACF) river basin (for all IPCC GCM scenarios) leads to the following conclusions:

Mean monthly temperature exhibits increasing trends over the ACF basin for all seasons and all A1B and A2 scenarios. Most significant are the A2 temperature increases in the 2050 – 2099 time periods. The most pronounced temperature increase is projected to occur in winter, spring, and fall. Temperature highs and lows also increase. In the southern ACF watersheds, mean precipitation generally exhibits a mild decline, except in late winter when it shows an increase. For the northern ACF watersheds, mean precipitation increases are noted in winter (as in the south) but also early spring. In addition to mean trends, the precipitation distribution "stretches" with higher highs and lower lows. It is notable, however, that southeast US and ACF precipitation in summer and early fall is impacted by hurricane-induced tropical storms which are not well represented in the current GCMs.

The projected changes are expected to impact human communities, agriculture, and the regional ecology. Such impacts are currently being assessed through a coupled climate-hydrology-water resources modeling framework (Georgakakos et al., 2010) to be published elsewhere. The assessment presently focuses on impacts relevant to monthly time scales. However, assessments for weekly and daily time scales are also planned.

Acknowledgments

This research was funded in part by the National Oceanic and Atmospheric Administration, Office of Global Programs, Climate Prediction Program for the Americas (CPPA; NOAA contract No. NA06OAR4310073), the Georgia Department of Natural Resources, Environmental Protection Division (Georgia EPD contract No. 761-70091), and the State Water Institute Research Program (104B) administered by USGS. The authors are grateful to all sponsors. The ideas and opinions presented herein do not necessarily reflect those of the sponsoring organizations.

References

Conway, D., (1998). "Recent Climate Variability and Future Climate Change Scenarios for Great Britain." Progress in Physical Geography 22.3: 350-74.

Drignei, D., (2009). "A Kriging Approach to the Analysis of Climate Model Experiments." Journal of Agricultural Biological and Environmental Statistics 14.1: 99-114.

Fowler, H. J., S. Blenkinsop, and C. Tebaldi, (2007). "Linking Climate Change Modelling to Impacts Studies: Recent Advances in Downscaling Techniques for Hydrological Modelling." International Journal of Climatology 27.12: 1547-78.

Georgakakos, A. P., et al., (1998). "Impacts of Climate Variability on the Operational Forecast and Management of the Upper Des Moines River Basin." Water Resources Research 34.4: 799-821.

Georgakakos, A., F. Zhang, and H. Yao, (2010). "Climate Variability and Change Assessment for the ACF River Basin, Southeast US." Georgia Water Resources Institute (GWRI) Technical Report No. GWRI/2010-TR1, Georgia Institute of Technology, Atlanta, Georgia, USA, 321 pp.

Georgakakos, A.P, Yao, H., Kistenmacher, M., Georgakakos, K.P., Graham, N.H., Cheng, F.-Y., Spencer, C., Shamir, E., (2011). "Value of Adaptive Water Resources Management in Northern California under Climatic Variability and Change: Reservoir Management," J. Hydrology (in review).

Georgakakos, K.P., Graham, N.H., Cheng, F.-Y., Spencer, C., Shamir, E., Georgakakos, A.P, Yao, H., and Kistenmacher, M., (2011). "Value of Adaptive Water Resources Management in Northern California under Climatic Variability and Change: Dynamic Hydroclimatology," J. Hydrology (in review).

Gissila, T., Black, E., Grimes, D. I. F., and Slingo, J. M., (2004). "Seasonal Forecasting of the Ethiopian Summer Rains." International Journal of Climatology 24.11: 1345-58.

Hidalgo, H. G., Dettinger, M. D., and Cayan, D. R. (2008). "Downscaling with constructed analogues: daily precipitation and temperature fields over the United States." Report No. CEC-500-2007-123, California Energy Commission, Sacramento, CA, 48 pp.

Huth, R., (1999). "Statistical Downscaling in Central Europe: Evaluation of Methods and Potential Predictors." Climate Research 13.2: 91-101.

IPCC, 2007: Climate Change (2007). "The Physical Science Basis. Contribution of Working Group I to the Fourth Assessment Report of the Intergovernmental Panel on Climate Change [Solomon, S., D. Qin, M. Manning, Z. Chen, M. Marquis, K.B. Averyt, M. Tignor and H.L. Miller (eds.)]." Cambridge University Press, Cambridge, United Kingdom and New York, NY, USA, 996 pp.

Kuhl, S. C., and J. R. Miller (1992), "Seasonal river runoff calculated from a global atmospheric model, " Water Resour. Res., 28(8), 2029–2039, doi:10.1029/92WR00917.

Lettenmaier, D. P., and D. Rind, (1992). "Hydrological Aspects of Global Climate Change - Preface." Journal of Geophysical Research-Atmospheres 97.D3: 2675-76.

Li, H., J. Sheffield, and E. F. Wood (2010), "Bias correction of monthly precipitation and temperature fields from Intergovernmental Panel on Climate Change AR4 models using equidistant quantile matching, " J. Geophys. Res., 115, D10101, doi:10.1029/2009JD012882.

Maurer, E. P., Wood, A. W., Adam, J. C., Lettenmaier, D. P., and Nijssen, B., (2002). "A Long-Term Hydrologically Based Dataset of Land Surface Fluxes and States for the Conterminous United States." Journal of Climate 15.22: 3237-51.

Maurer, E. P., (2007). "Uncertainty in Hydrologic Impacts of Climate Change in the Sierra Nevada, California, under Two Emissions Scenarios." Climatic Change 82.3-4: 309-25.

Maurer, E.P. and H.G. Hidalgo (2008) "Utility of daily vs. monthly large-scale climate data: an intercomparison of two statistical downscaling methods." Hydrology and Earth System Sciences Vol. 12, 551-563.

Maurer, E. P., Hidalgo, H. G., Das, T., Dettinger, M. D., and Cayan, D. R. (2010). "The utility of daily large-scale climate data in the assessment of climate change impacts on daily streamflow in California, " Hydrol. Earth Syst. Sci., 14, 1125-1138, doi:10.5194.

Mearns, L. O., F. Giorgi, P. Whetton, D. Pabon, M. Hulme, and M. Lal, (2003). "Guidelines for Use of Climate Scenarios Developed from Regional Climate Model Experiments." Data Distribution Center of the Intergovernmental Panel on Climate Change.

Mearns, L.O., et al., (2011). "The North American Regional Climate Change Assessment Program dataset, " National Center for Atmospheric Research Earth System Grid data portal, Boulder, CO. Data downloaded 2011-04-11.

Mearns, L. O., W. J. Gutowski, R. Jones, L.-Y. Leung, S. McGinnis, A. M. B. Nunes, and Y. Qian (2009). "A regional climate change assessment program for North America." EOS, Vol. 90, No. 36, 8 September 2009, pp. 311-312.

Medellin, A.J., Lund, J.R., and Howitt, R.E., (2007). "Water Supply Analysis for Restoring the Colorado River Delta, Mexico," J. of Water Res. Plann. and Mgt., Vol.133.

Miller, N. L., Jinwon Kim, and Robert K. HartmanJohn Farrara, (1999). "Downscaled Climate and Streamflow Study of the Southwestern United States." Journal of the American Water Resources Association 35.6: 1525-37.

Shepard, D.S. (1984). "Computer mapping: The SYMAP interpolation algorithm, in Spatial Statistics and Models.", edited by G.L. Gaile and C.J. Willmott, pp. 133 145, D. Reidel, Norwell, Mass.

Stamm, J. F., E. F. Wood, and D. P. Lettenmaier, (1994). "Sensitivity of a Gcm Simulation of Global Climate to the Representation of Land-Surface Hydrology." Journal of Climate 7.8 (1994): 1218-39.

Tanaka, S. K., Tingju, Z., Lund, J. R., Howitt, R. E., Jenkins, M. W., Pulido, M. A., Tauber, M., Ritzema, R. S., and Ferreira, I. C., (2006). "Climate Warming and Water Management Adaptation for California," Climatic Change, 76, 361-387.

VanRheenen, N.T., A.W. Wood, R. N. Palmer, and D. P. Lettenmaier, (2004). “Potential Implications of PCM Climate Change Scenarios for Sacramento-Jan Joaquin River Basin Hydrology and Water Resources,” Climatic Change, 62, 257-281.

Vrac, M., M. Stein, and K. Hayhoe, (2007). "Statistical Downscaling of Precipitation through Nonhomogeneous Stochastic Weather Typing." Climate Research 34.3: 169-84.

Wilby, R. L., and T. M. L. Wigley, (1997). "Downscaling General Circulation Model Output: A Review of Methods and Limitations." Progress in Physical Geography 21.4: 530-48.

Wilks, D. S., and R. L. Wilby, (1999). "The Weather Generation Game: A Review of Stochastic Weather Models." Progress in Physical Geography 23.3: 329-57.

Wood, A. W., L. R. Leung, V. Sridhar and D. P. Lettenmaier, (2004). "Hydrologic Implications of Dynamical and Statistical Approaches to Downscaling Climate Model Outputs." Climatic Change 62.1-3: 189-216.

Xu, C. Y., (1999). "From Gcms to River Flow: A Review of Downscaling Methods and Hydrologic Modelling Approaches." Progress in Physical Geography 23.2: 229-49.

Xue, Y. K., Vasic, Ratko, Janjic, Zavisa, Mesinger, Fedor, and Mitchell, Kenneth E, (2007). "Assessment of Dynamic Downscaling of the Continental Us Regional Climate Using the Eta/Ssib Regional Climate Model." Journal of Climate 20.16: 4172-93.

Yao, H., and A. Georgakakos, (2001). "Assessment of Folsom Lake Response to Historical and Potential Future Climate Scenarios 2. Reservoir Management." Journal of Hydrology 249.1-4: 176-96.

List of Figures

List of Tables

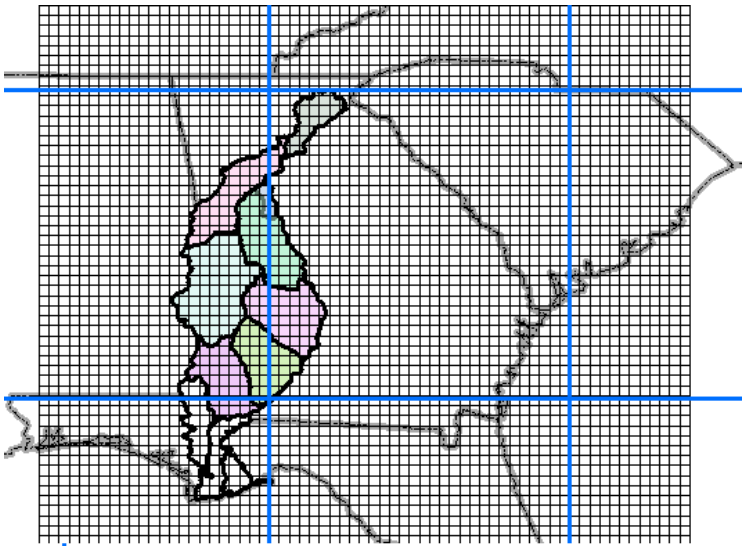

Figure 1: Spatial Resolutions of the Canadian GCM3.1 (blue) and Observational Data Sets (black) over the Southeast US

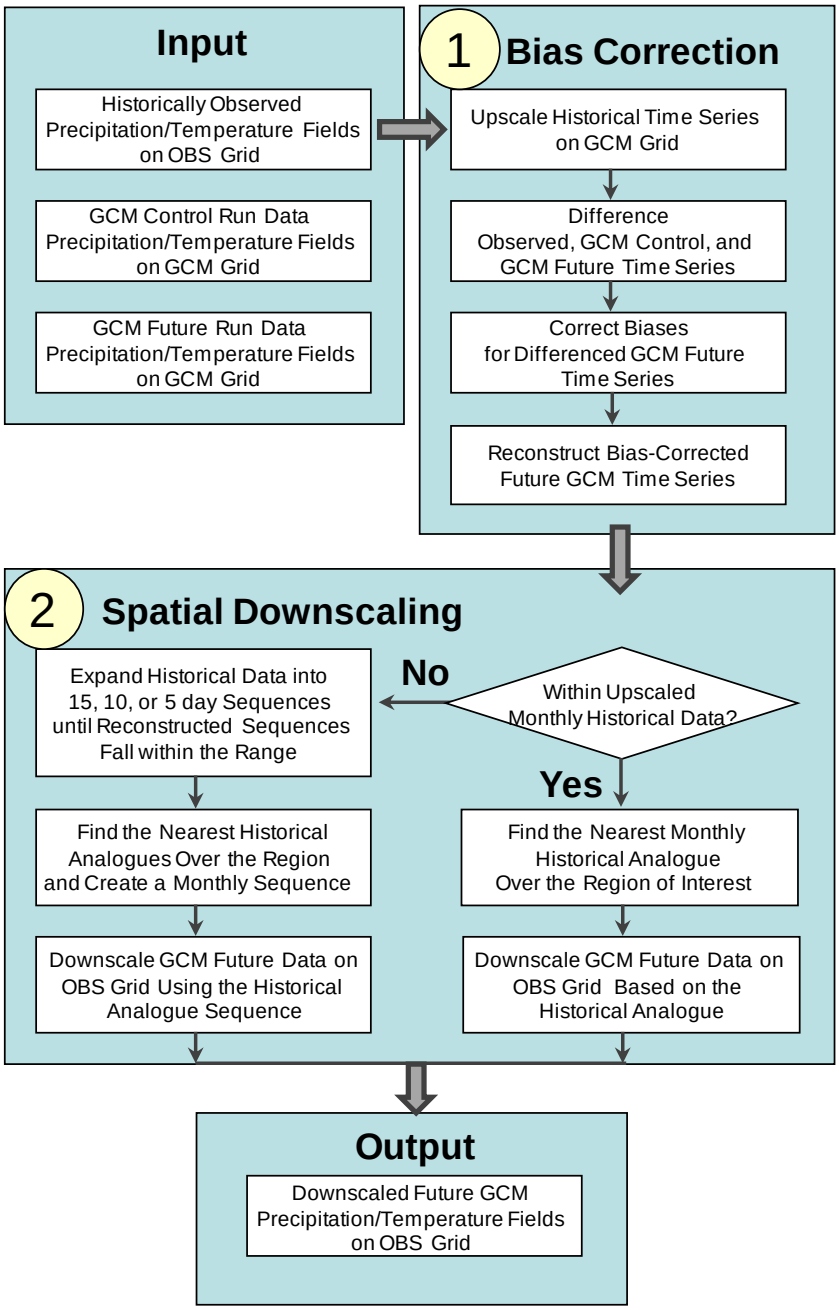

Figure 2: Joint Variable Spatial Downscaling (JVSD) Method Flow Chart

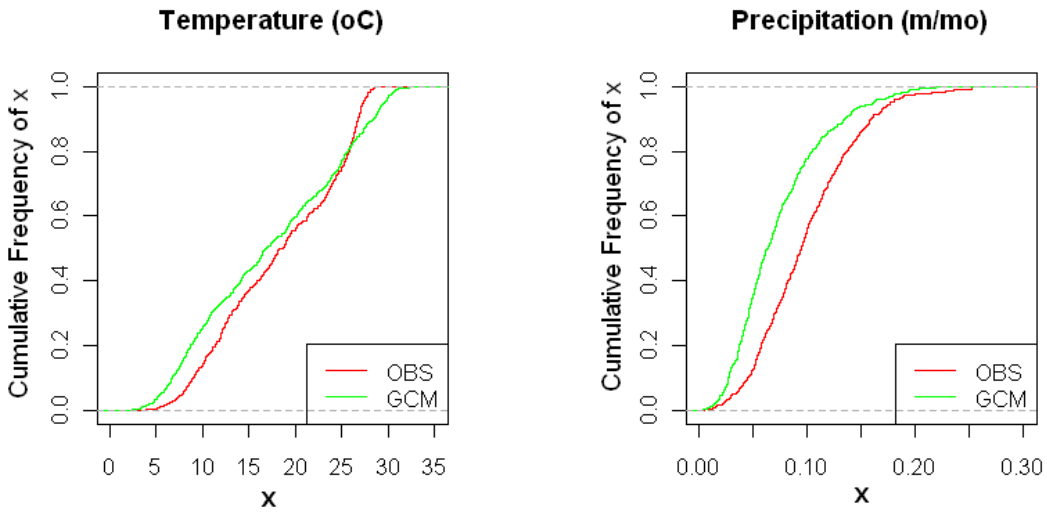

Figure 3: Typical Cumulative Frequency Curves of GCM Simulated and Observed Variables

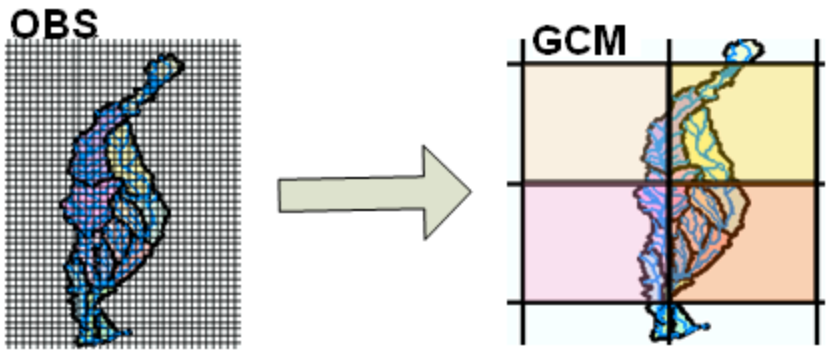

Figure 4: Schematic of Spatial Upscaling, From Observational Scale Grids (OBS) to GCM Scale Grids (GCM); Also Shown are the Main Sub-basins of the ACF River Basin

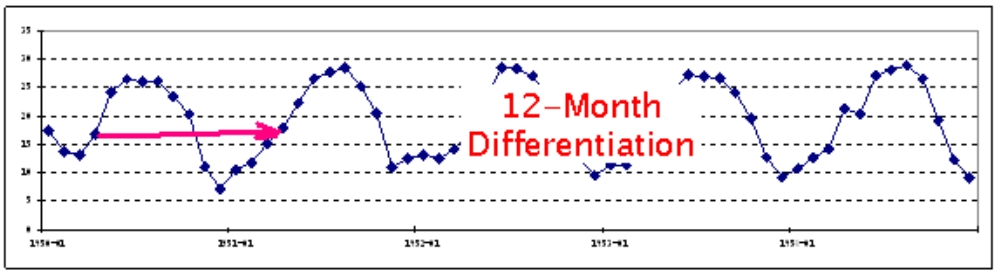

Figure 5: Example of Twelve-Month Differencing of the Original Time Series

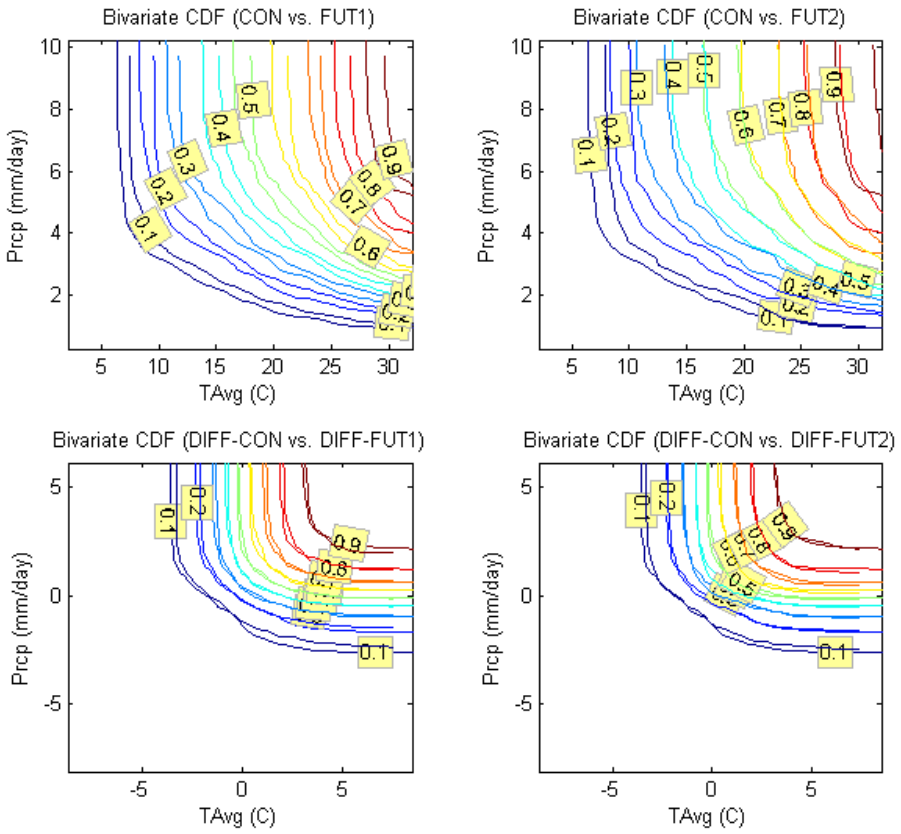

Figure 6: Bivariate Empirical Cumulative Frequency Curves for Original (Top) and Differenced (Bottom) Time Series of Temperature and Precipitation

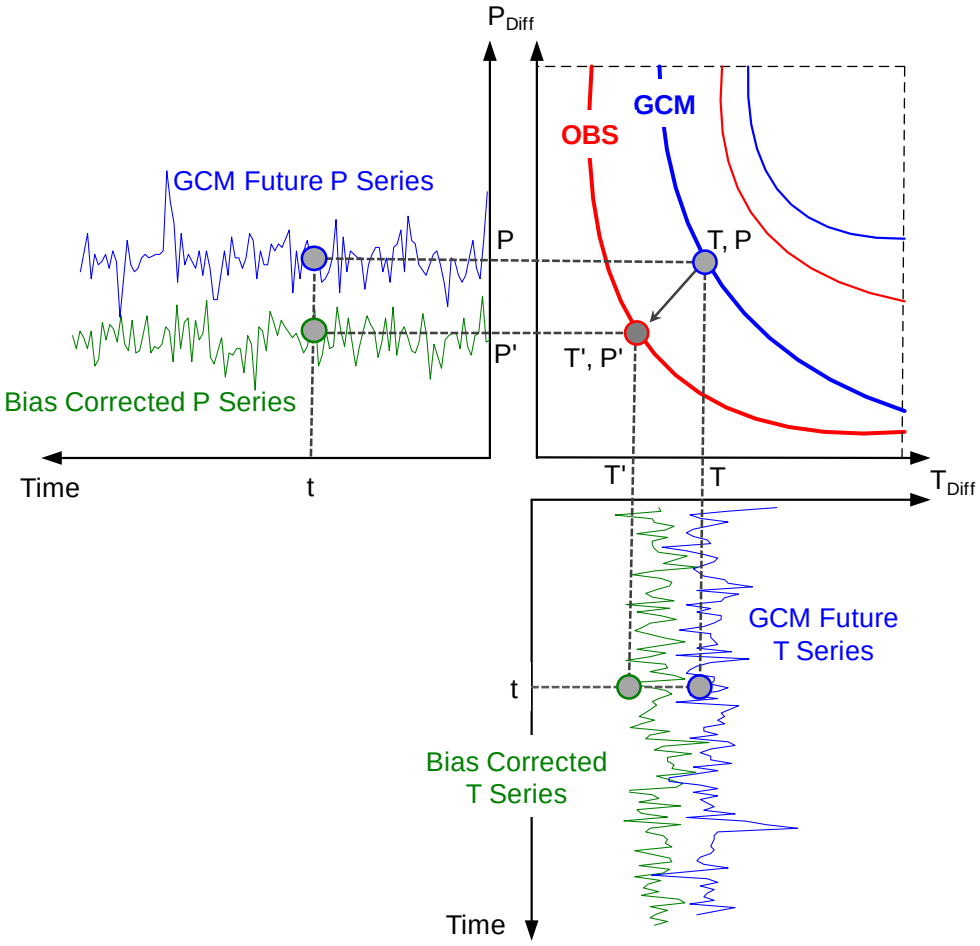

Figure 7: Joint Frequency Distribution Mapping

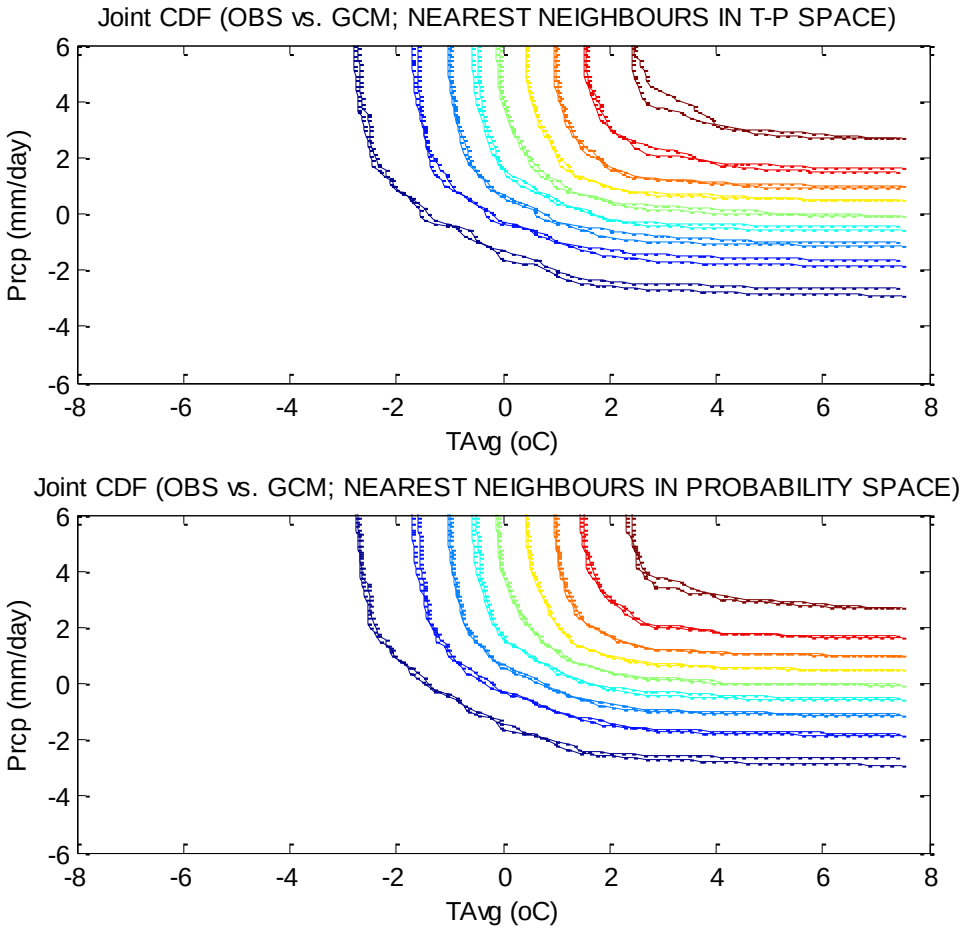

Figure 8: Comparison between two CDF mapping approaches for the CSIRO-MK3.5 GCM (Australia). The top graph compares the OBS versus the mapped GCM joint CDFs for the nearest neighbor approach in T-P space (9 iso-probability contours from 0.1 to 0.9 in 0.1 increments). The second graph displays the same results for the nearest neighbor approach in probability space.

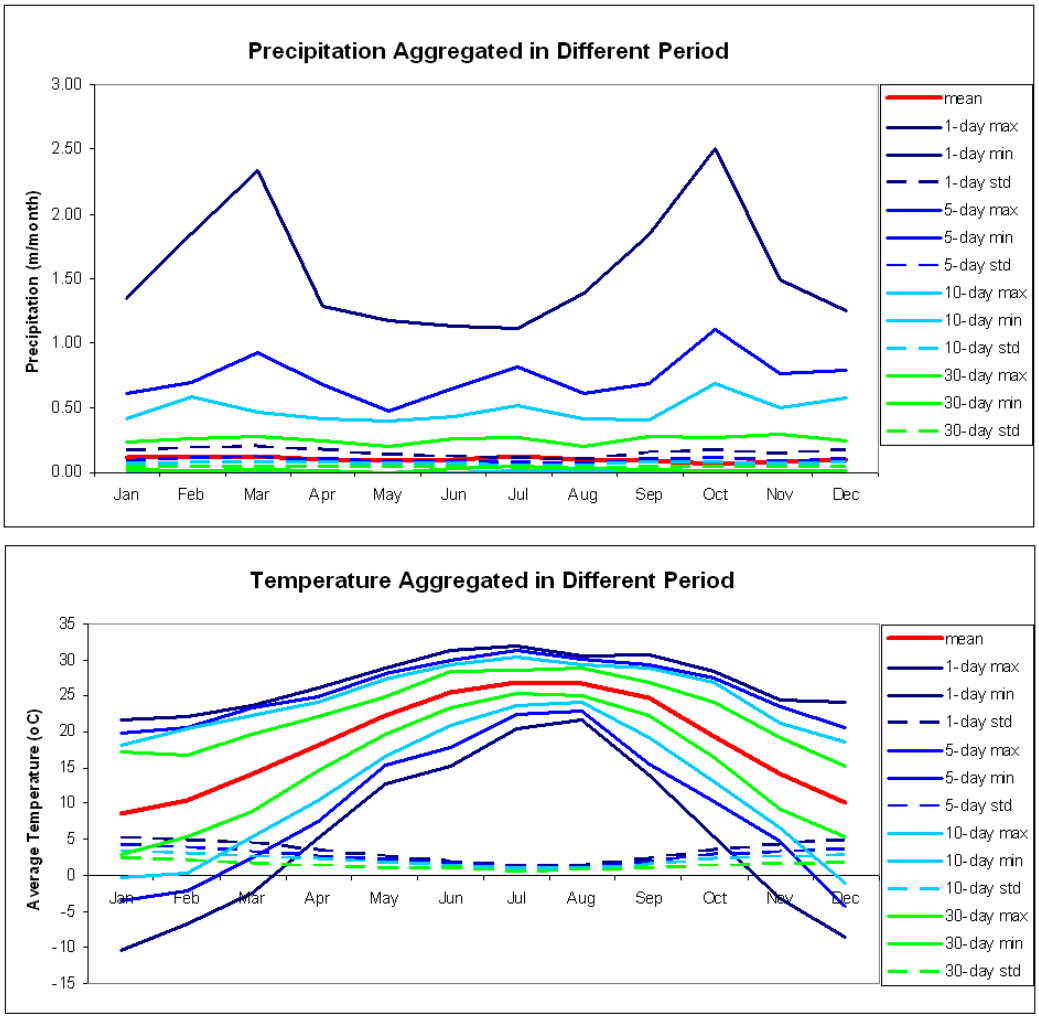

Figure 9: Data Range Expansion Example

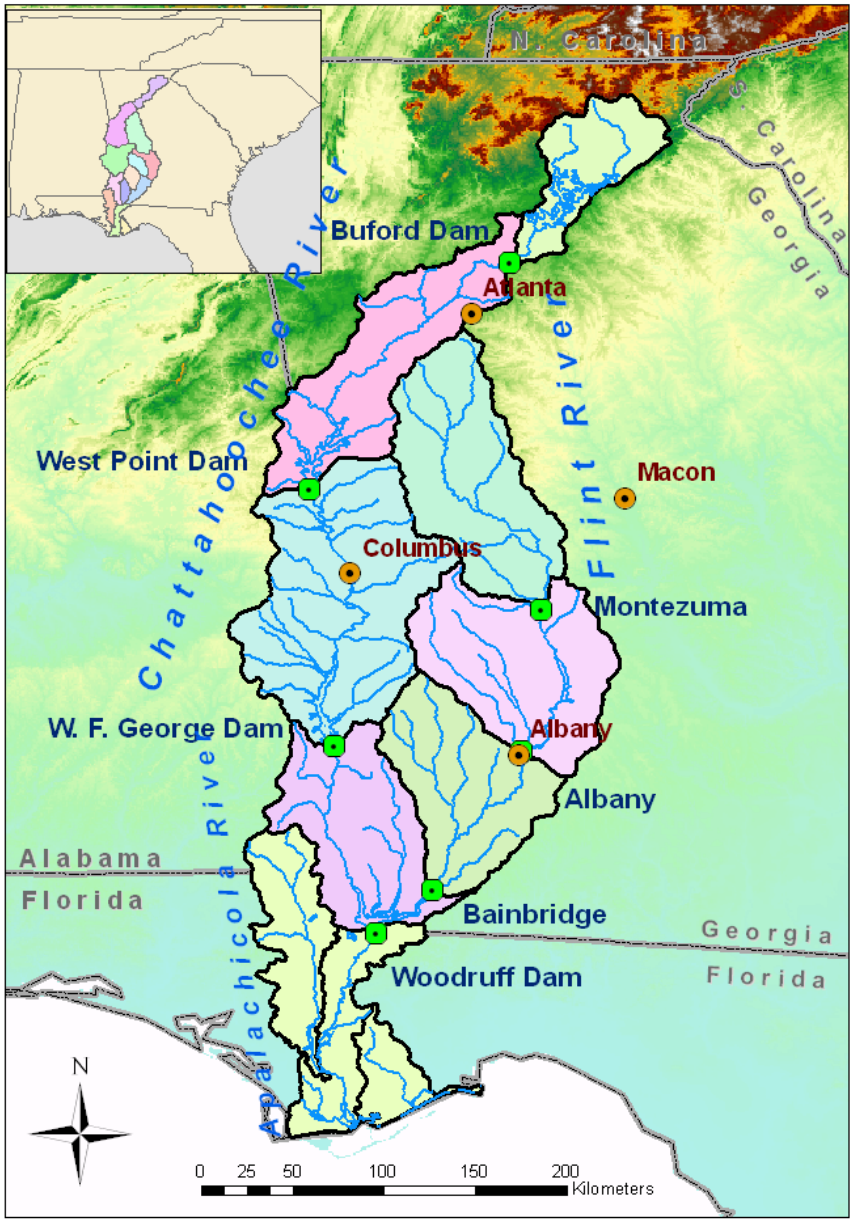

Figure 10: The Apalachicola-Chattahoochee-Flint (ACF) River System

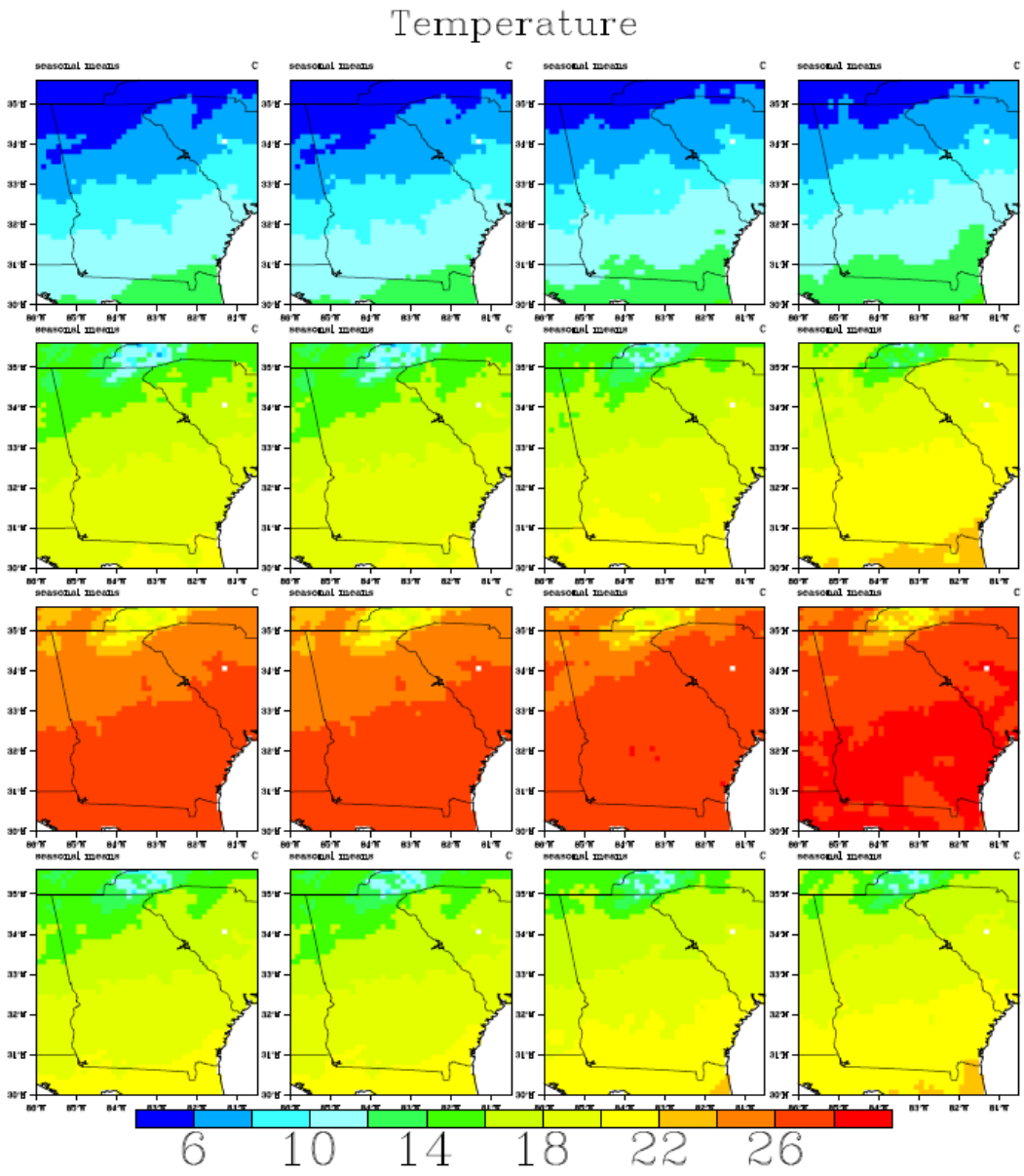

Figure 11: Spatial temperature distributions over the ACF basin and the southeast US. Monthly temperature fields are aggregated by season (DJF, MAM, JJA, and SON in rows 1, 2, 3, and 4 respectively). The columns depict observations for the period 01/1950 - 12/1999 (Column 1); JVSD downscaled data using input from the 20CM3 experiment for the period 01/1950 - 12/1999 (Column 2); JVSD downscaled data using input from the CGCM3.1-run1 A1B Scenario for the period 01/2000-12/2049 (Column 3); and JVSD downscaled data using input from the CGCM3.1-run1A1B Scenario for the period 01/2050-12/2099 (Column 4).

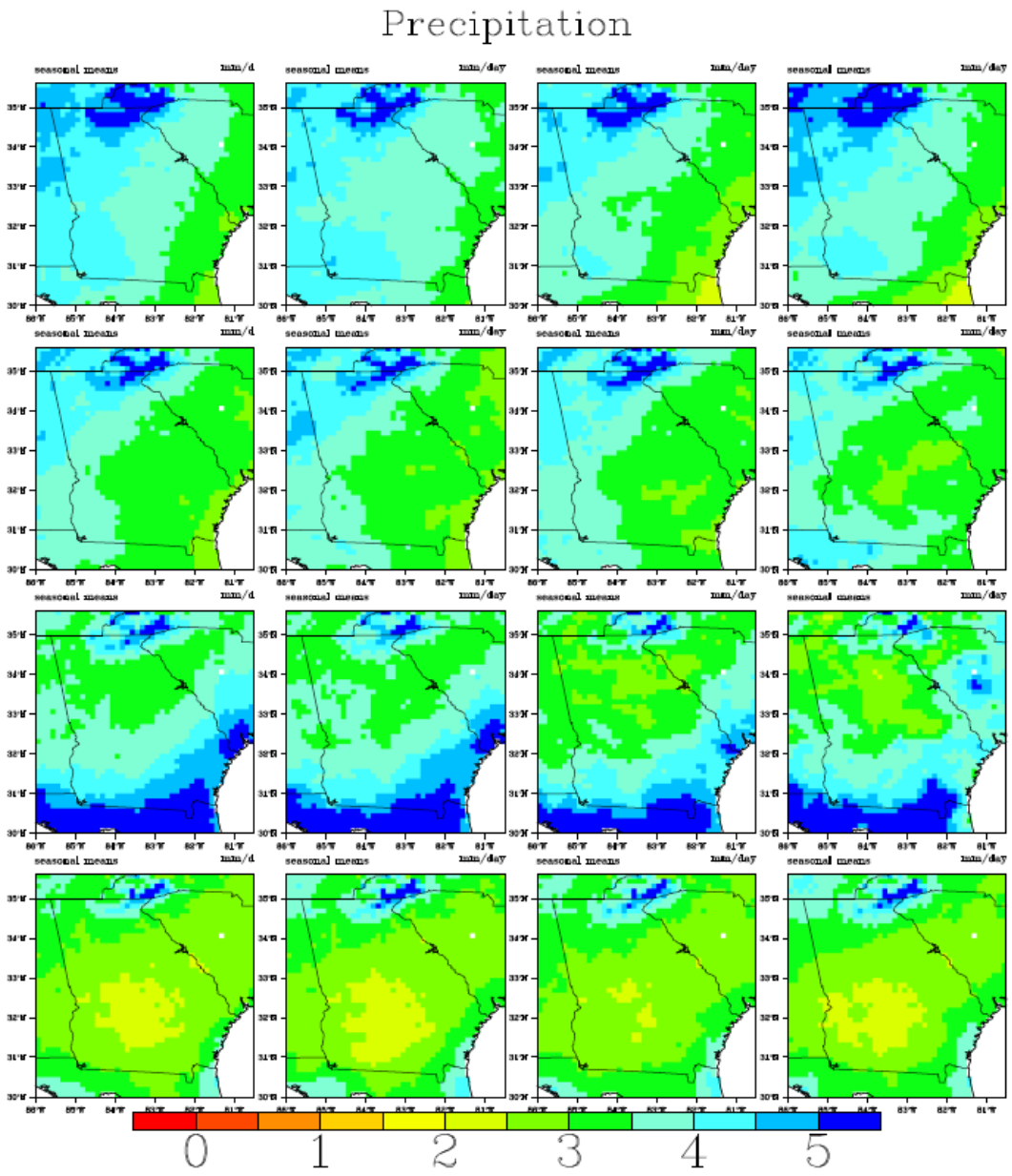

Figure 12: Spatial precipitation distributions over the ACF basin and the southeast US. Monthly precipitation fields are aggregated by season (DJF, MAM, JJA, and SON in rows 1, 2, 3, and 4 respectively). The columns depict observations for the period 01/1950 - 12/1999 (Column 1); JVSD downscaled data using input from the 20CM3 experiment for the period 01/1950 - 12/1999 (Column 2); JVSD downscaled data using input from the CGCM3.1-run1A1B Scenario for the period 01/2000-12/2049 (Column 3); and JVSD downscaled data using input from the CGCM3.1-run1 A1B Scenario for the period 01/2050-12/2099 (Column 4).

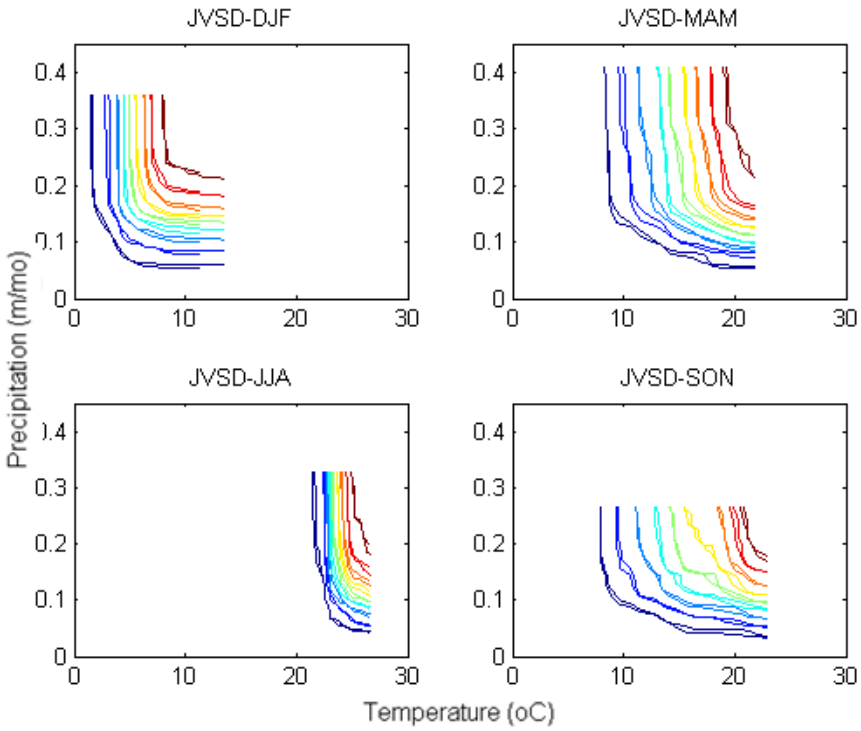

Figure 13: An example of joint CDFs of precipitation and temperature for each watershed and season corresponding to OBS and JVSD for Buford watershed from CGCM3.1 model.

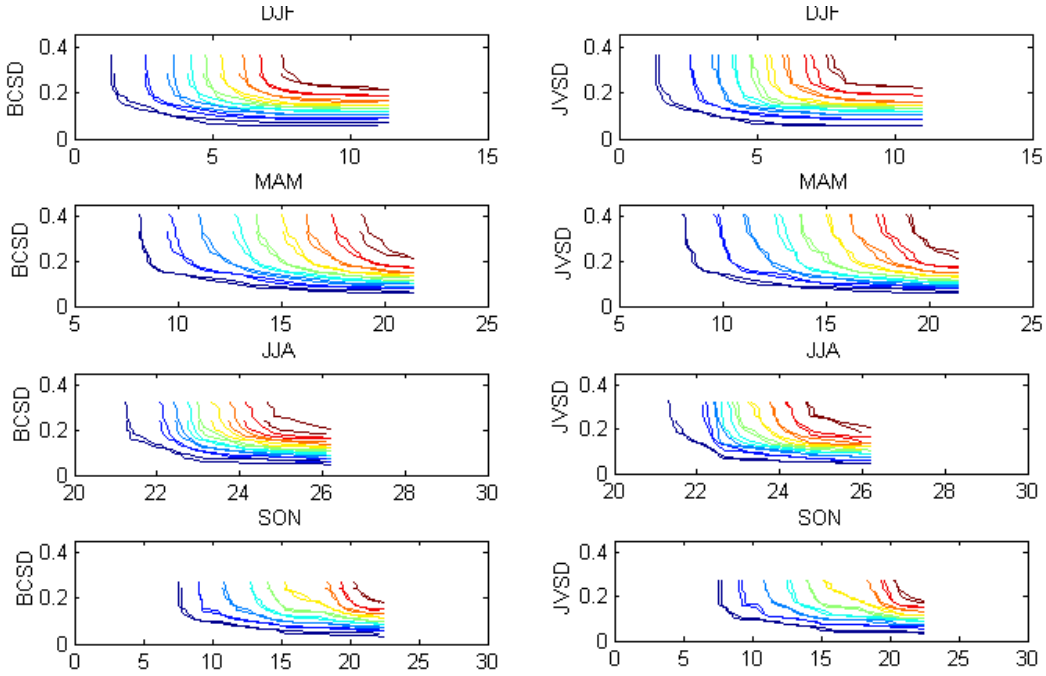

Figure 14: Joint CDF between precipitation and temperature for Buford watershed from observation, BCSD downscaling (left panel), and JVSD (right panel).

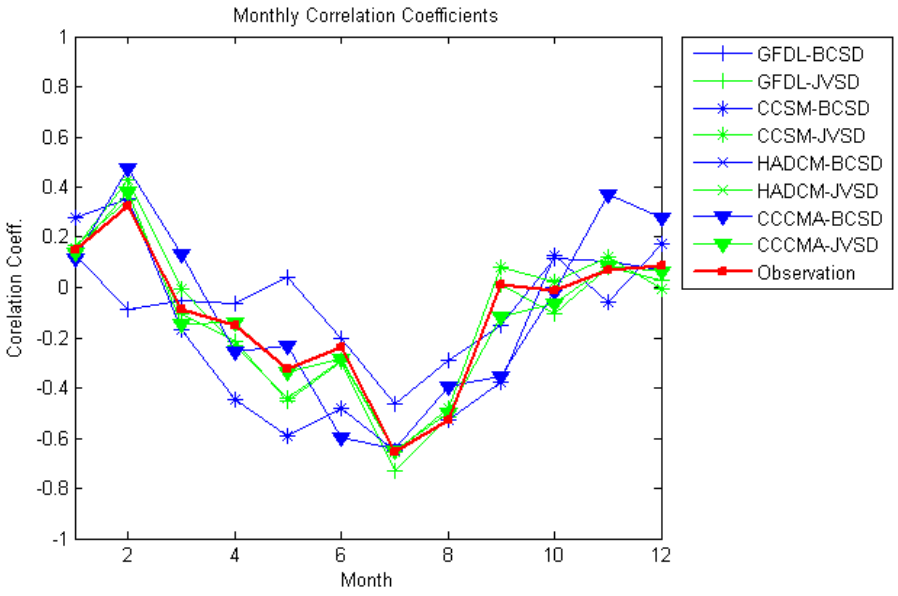

Figure 15: Monthly correlation coefficients between precipitation and temperature for Buford; observations (red), BCSD (blue), and JVSD (green).

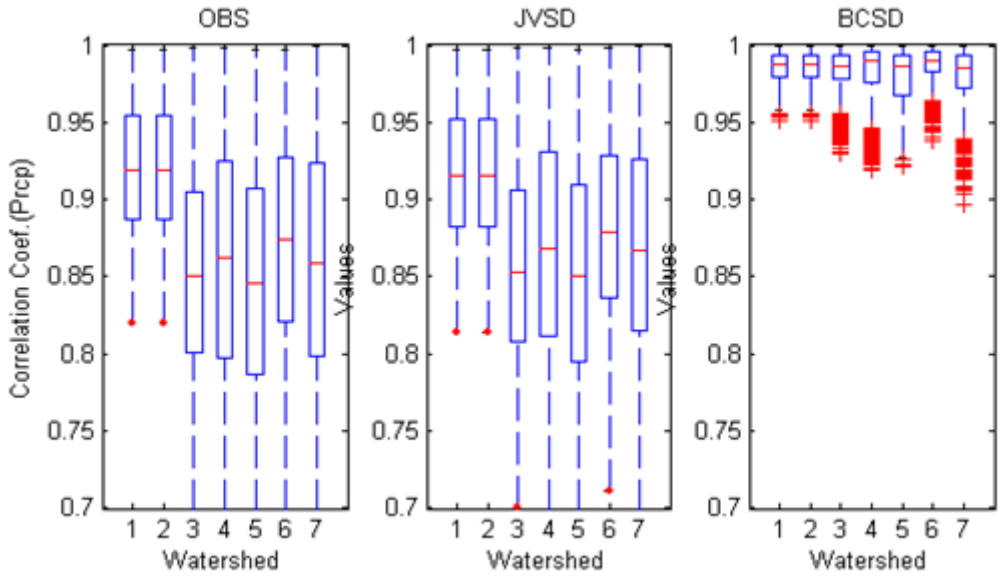

Figure 16: Box-plots of the pair-wise correlation coefficients of precipitation across the ACF sub-basins: *(1)*Buford, *(2)* West Point, *(3)* George, *(4)* Woodruff, *(5)* Montezuma, *(6)*Albany, and *(7)* Bainbridge.

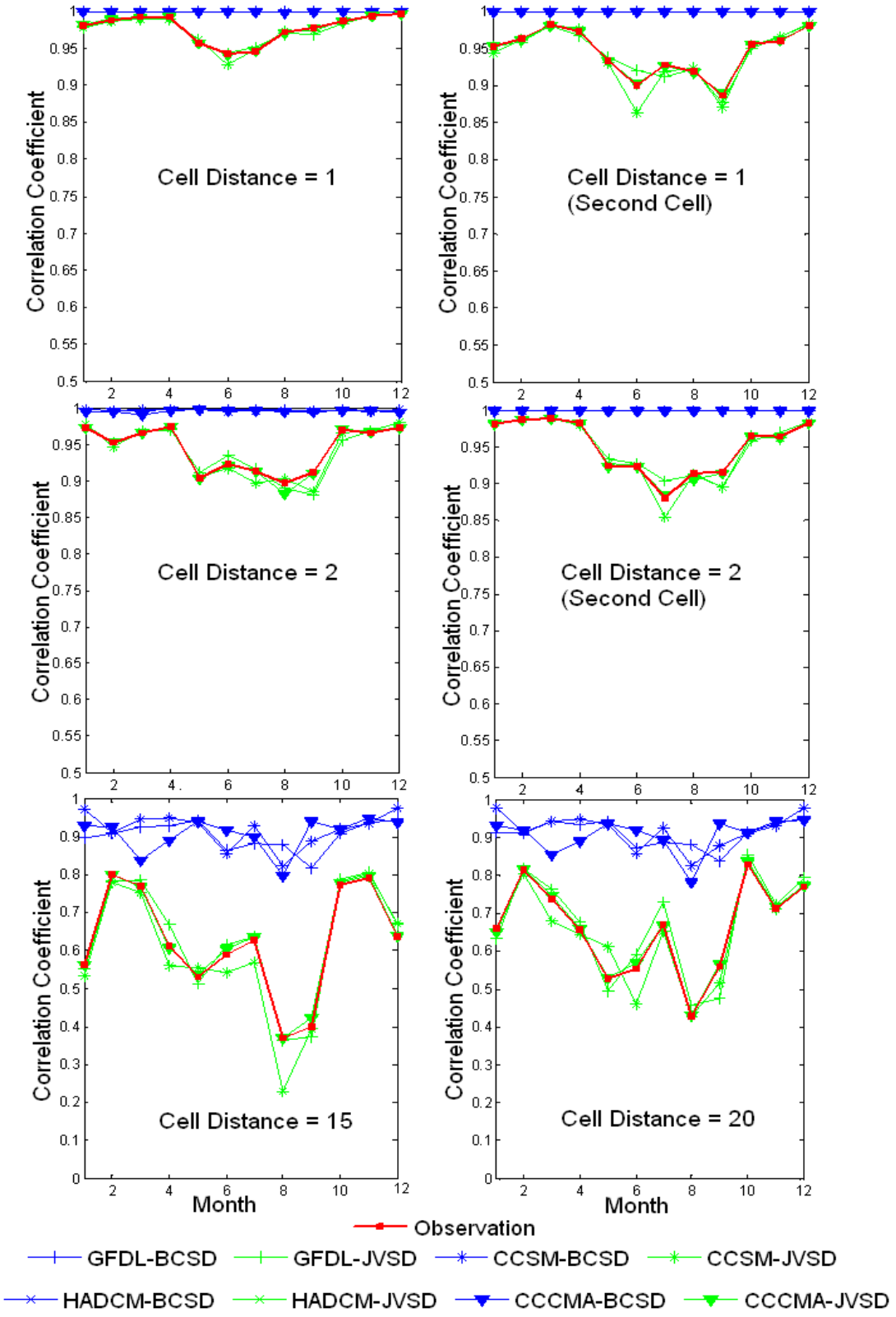

Figure 17: Spatial Correlation Comparison between Precipitation Observations (red), BCSD (blue), and JVSD (green) for four GCMs, various Grid Cell Distances, and Months. The cell pairs for the first four panels are selected from the Buford watershed. The cell pairs in the last two panels include one cell from the Buford watershed and a second cell from the West Point watershed.

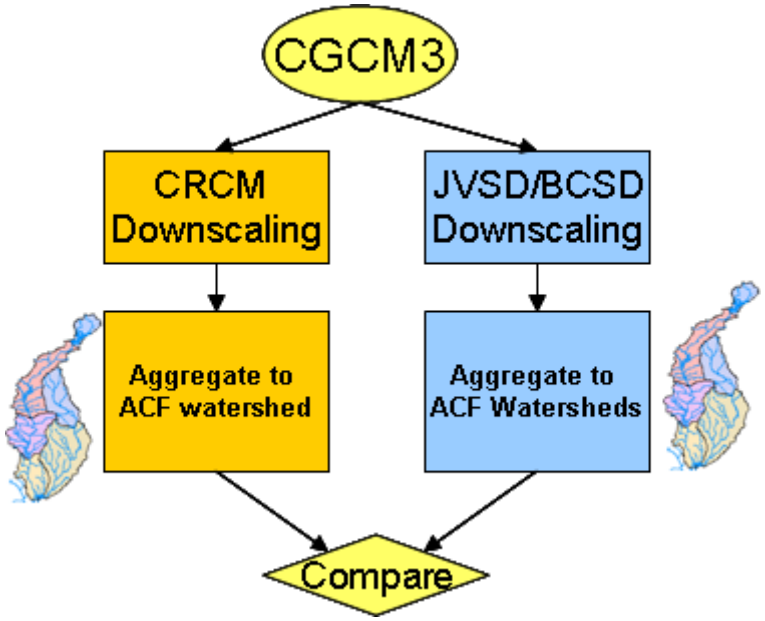

Figure 16: Comparison Process of JVSD with Dynamic Downscaling Methods from the NARCCAP Dataset (CRCM/CGCM3) for the Future Period 2041-2070.

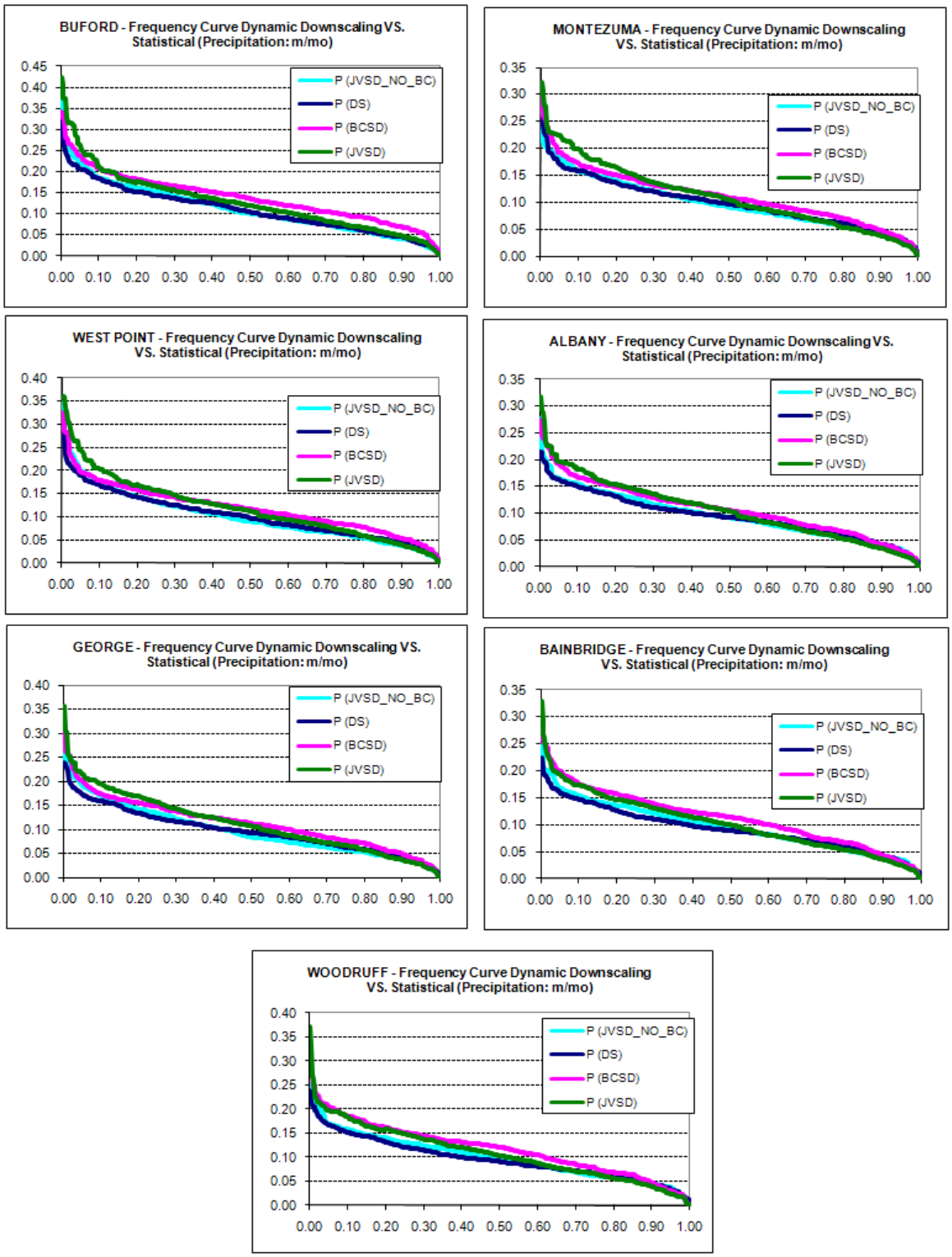

Figure 18: Comparisons of downscaled precipitation frequencies for ACF watersheds based on NARCCAP methods, BCSD, JVSD with no bias correction, and JVSD with bias correction.

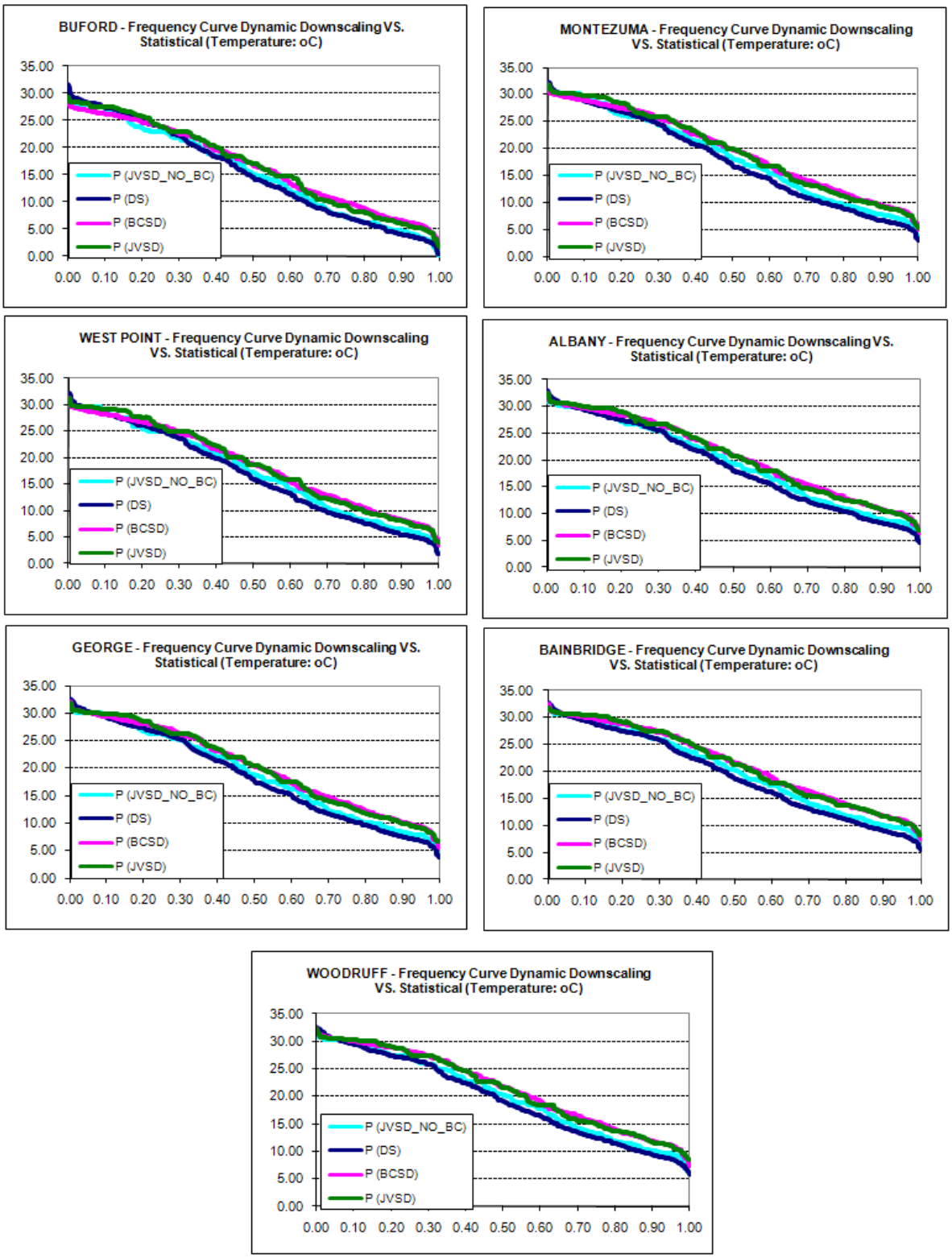

Figure 19: Comparisons of downscaled temperature frequencies for ACF watersheds based on NARCCAP methods, BCSD, JVSD with no bias correction, and JVSD with bias correction.

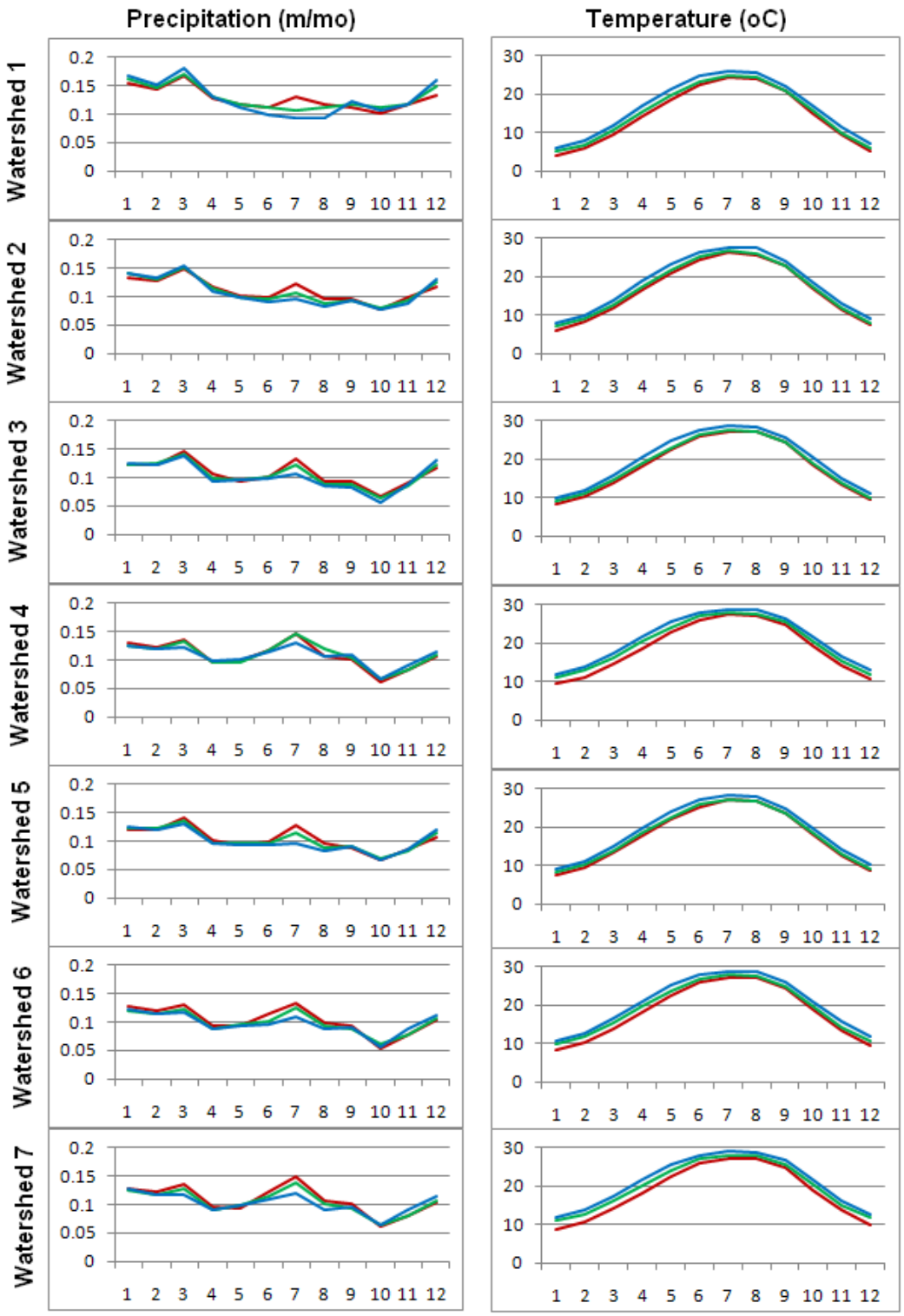

Figure 20: Climatologies of spatially aggregated precipitation and temperature for seven ACF watersheds: *(1)* Buford, *(2)* West Point, *(3)* George, *(4)* Woodruff, *(5)* Montezuma, *(6)* Albany, and *(7)* Bainbridge; Lines in

Red–Observations (1950-1999); Green–JVSD downscaled (2000- 2049); Blue–JVSD downscaled (2050-2099) under A1B Scenarios.

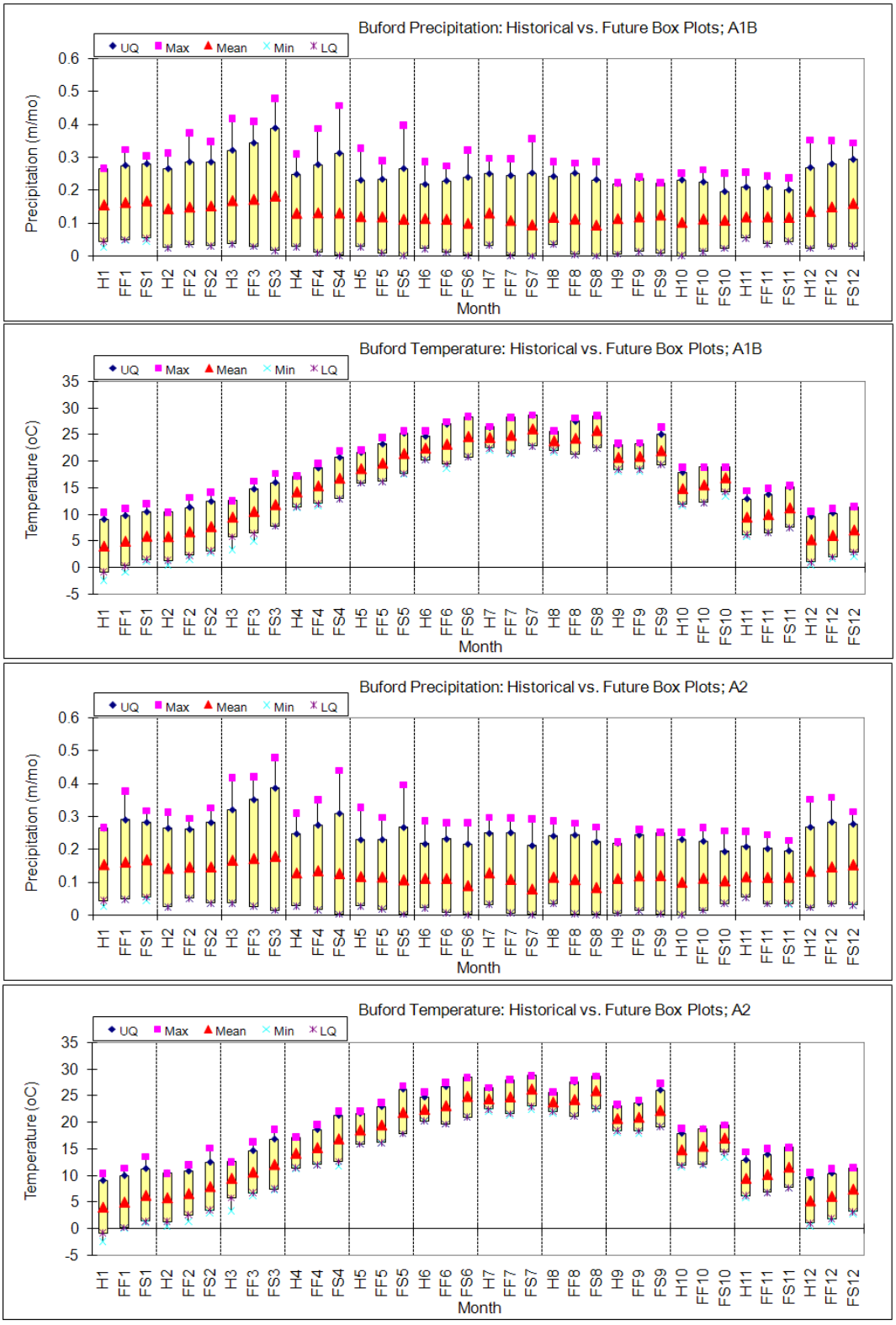

Figure 21: Box Plots of Monthly Historical vs. Future (A1B and A2) Watershed Precipitation and Temperature, Buford: H denotes the historical period (1950-1999); FF the first future period (2000-2049); and FS the second future period (2050-2099).

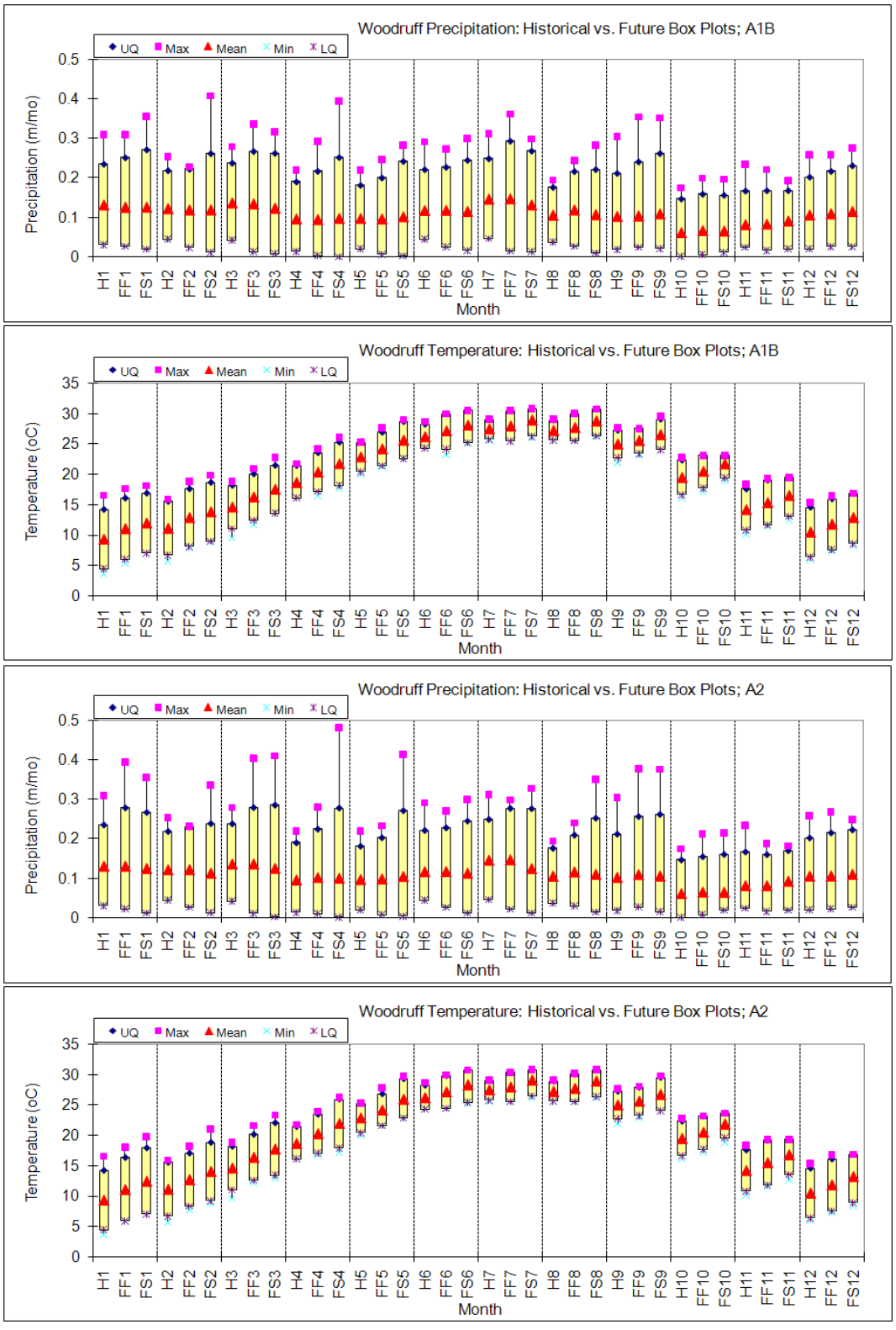

Figure 22: Box Plots of Monthly Historical vs. Future (A1B and A2) Watershed Precipitation and Temperature, Woodruff: H denotes the historical period (1950-1999); FF the first future period (2000-2049); and FS the second future period (2050-2099).

Table 1: General Characteristics of the ACF Sub-basins

ACF Sub-basins	Latitude (Centroid)	Longitude (Centroid)	Area (km^2)	Mean Elevation (m)	Min. Elevation (m)	Max. Elevation (m)
Buford	34°31’	-83°48’	2694	454	320	1250
West Point	33°40’	-84°44’	5189	270	137	455
George	32°20’	-85°01’	4787	143	46	396
Woodruff	31°13’	-84°58’	2141	64	22	167
Montezuma	32°55’	-84°24’	4507	213	85	394
Albany	32°01’	-84°11’	2605	115	53	235
Bainbridge	31°25’	-84°24’	1875	72	23	173

Table 2: Watershed coefficient of variability (CV) in seasonal precipitation and temperature for the ACF watersheds

Watershed	**Season**	**Precipitation**			**Temperature**		
		OBS	JVSD	BCSD	OBS	JVSD	BCSD
Buford	DJF	0.447	0.449	0.358	0.514	0.465	0.511
	MAM	0.510	0.515	0.379	0.191	0.198	0.188
	JJA	0.561	0.546	0.388	0.090	0.146	0.087
	SON	0.553	0.561	0.456	0.442	0.432	0.440
West Point	DJF	0.446	0.453	0.389	0.379	0.344	0.389
	MAM	0.534	0.531	0.442	0.169	0.176	0.442
	JJA	0.524	0.506	0.422	0.078	0.129	0.422
	SON	0.612	0.616	0.544	0.358	0.345	0.544
George	DJF	0.455	0.467	0.411	0.298	0.270	0.411
	MAM	0.552	0.538	0.464	0.153	0.159	0.464
	JJA	0.556	0.525	0.438	0.064	0.112	0.438
	SON	0.689	0.703	0.592	0.301	0.289	0.592
Woodruff	DJF	0.474	0.463	0.432	0.260	0.244	0.251
	MAM	0.577	0.533	0.493	0.138	0.140	0.136
	JJA	0.539	0.497	0.439	0.054	0.096	0.053
	SON	0.692	0.686	0.616	0.267	0.258	0.263
Montezuma	DJF	0.461	0.479	0.396	0.329	0.304	0.329
	MAM	0.526	0.522	0.442	0.159	0.166	0.158
	JJA	0.569	0.539	0.425	0.073	0.122	0.071
	SON	0.645	0.660	0.425	0.327	0.316	0.326
Bainbridge	DJF	0.486	0.480	0.561	0.274	0.251	0.268
	MAM	0.553	0.530	0.422	0.142	0.147	0.141
	JJA	0.547	0.496	0.467	0.059	0.106	0.056

	SON	0.708	0.703	0.596	0.279	0.269	0.277

Table 3: Evaluation of statistical differences among BCSD, JVSD(bias corrected), JVSD, and dynamic downscaling (DDS); ACF precipitation and temperature; "DIFF" denotes statistical difference and "-" denotes no statistical difference. Number of data values N=384.

K-S Test Statistic = $\max_x |F_1(x) - F_2(x)|$

Precipitation

	Buford	West Point	George	Montezuma	Albany	Bainbridge	Woodruff
JVSD-DDS	0.0599	0.0599	0.1094	0.0625	0.0547	0.0859	0.0859
JVSD(BC)-DDS	0.1224	0.1276	0.1589	0.1432	0.1615	0.1406	0.1458
BCSD-JVSD(BC)	0.1484	0.1294	0.1190	0.1124	0.1164	0.1192	0.1246

Temperature

	Buford	West Point	George	Montezuma	Albany	Bainbridge	Woodruff
JVSD-DDS	0.0703	0.0651	0.0729	0.0781	0.0703	0.0755	0.0651
JVSD(BC)-DDS	0.1146	0.1328	0.1328	0.1380	0.1406	0.1510	0.1380
BCSD-JVSD(BC)	0.1216	0.1068	0.0807	0.1016	0.0703	0.0755	0.0625

Significant level 0.05 ($K_{0.05}$ = $[-\frac{1}{2}(\frac{1}{N}+\frac{1}{N})\ln(\frac{\alpha}{2})]^{\frac{1}{2}} =$ **0.098)**

Precipitation

	Buford	West Point	George	Montezuma	Albany	Bainbridge	Woodruff
JVSD-DDS	-	-	DIFF	-	-	-	-
JVSD(BC)-DDS	DIFF	DIFF	DIFF	DIFF	DIFF	DIFF	DIFF
BCSD-JVSD(BC)	DIFF	DIFF	DIFF	DIFF	DIFF	DIFF	DIFF

Temperature

	Buford	West Point	George	Montezuma	Albany	Bainbridge	Woodruff
JVSD-DDS	-	-	-	-	-	-	-
JVSD(BC)-DDS	DIFF	DIFF	DIFF	DIFF	DIFF	DIFF	DIFF
BCSD-JVSD(BC)	DIFF	DIFF	-	DIFF	-	-	-

Significant level 0.01 ($K_{0.01}$ = $[-\frac{1}{2}(\frac{1}{N}+\frac{1}{N})\ln(\frac{\alpha}{2})]^{\frac{1}{2}} =$ **0.117)**

Precipitation

	Buford	West Point	George	Montezuma	Albany	Bainbridge	Woodruff
JVSD-DDS	-	-	-	-	-	-	-
JVSD(BC)-DDS	DIFF	DIFF	DIFF	DIFF	DIFF	DIFF	DIFF
BCSD-JVSD(BC)	DIFF	DIFF	DIFF	-	-	DIFF	DIFF

Temperature

	Buford	West Point	George	Montezuma	Albany	Bainbridge	Woodruff
JVSD-DDS	-	-	-	-	-	-	-
JVSD(BC)-DDS	-	DIFF	DIFF	DIFF	DIFF	DIFF	DIFF
BCSD-JVSD(BC)	DIFF	-	-	-	-	-	-

Information Transfer Program Introduction

None.

USGS Summer Intern Program

None.

Student Support					
Category	**Section 104 Base Grant**	**Section 104 NCGP Award**	**NIWR-USGS Internship**	**Supplemental Awards**	**Total**
Undergraduate	0	0	0	0	0
Masters	1	0	0	0	1
Ph.D.	2	2	0	0	4
Post-Doc.	0	0	0	0	0
Total	3	2	0	0	5

Notable Awards and Achievements

This project has supported one Ph.D. student, Kristen Kellock, in the UGA Interdisciplinary Toxicology Program. Kristen received the Best Student Presentation Award at the 2011 Georgia Water Resources Conference held in Athens, GA, April 11 13, 2011. Kristen published her findings in the Conference Proceedings (Kellock and Bringolf 2011).